Nanoparticle Growth and Transport in Gas Phase

A DISSERTATION
SUBMITTED TO THE FACULTY OF
UNIVERSITY OF MINNESOTA
BY

Hui Ouyang

IN PARTIAL FULFILLMENT OF THE REQUIREMENTS
FOR THE DEGREE OF
DOCTOR OF PHILOSOPHY

Professor Christopher J Hogan Jr.

August 2015

Acknowledgements

I feel incredibly lucky to have met Chris in the summer 2011 when I was still pregnant with my first child. Joining Hogan's Heroes is one of the best decisions I ever made in my life. I am very grateful to have Chris as my advisor, my mentor, and my best friend. It is a near impossible mission to get a PhD degree on time while being a mother of two babies, but we did it! (or almost☺, at the time of writing this). I still remember the day I told Chris that I was pregnant again (while I was doing experiments in the lab), as my dearest friend, the joy he had instead of consternation took away all my worries. Chris said that "I am very happy for you, but promise me that you will not quit your PhD program". At that moment, I was not sure whether this is possible for me to get a PhD degree or not. Now I am sure that without Chris, this would have been impossible. I am glad to have Chris, who has always been there to help me grow stronger in doing research as well as in being myself. I am lucky to work with- he cares about the education of young people deeply as well as about scientific research. His passion for education and science have strongly influence my views on these fields, and leads me to be a better educator to help other people grow and enjoy science even more. These four years in my PhD study are critical years in my life and have made me a stronger person as a mother, a daughter, and a wife. It would have been miserable without Chris' guidance and help in these years. I would not recommend any girl at their 20s to pursue a PhD degree while being a mother of two or even more children, if their advisor is not someone like Chris.

I want to thank Professor Peter McMurry for being my mentor, for letting me do experiments in ME 271, and also letting me borrow endless amounts of equipment for my other experiments in ME 4136. I enjoyed the conversations I had with him and I am very grateful to hear about his thoughts about life, career path, and future.

I give special thanks to Professor Pui's group, they always keep their door open to us and let us borrow and use spare instruments and parts. I literary built a coagulation experimental setup with almost all spare parts borrowed from Professor Pui's group. I also thank Professor Pui for his generous and warm greetings in the hallways.

I am very grateful to have the best set of lab mates. Dr. Carlos Larriba-Andaluz has been my unofficial "co-adviser" and is one of my best friends, he helped me to get my feet on the ground in doing laboratory experiments. I always knew things in the lab would be fine when he is around, and helped me to believe in myself. I give tons of thanks to him for all the help, warm hugs, and stress-releasing conversations. Dr. Derek Oberreit is my hero; he's capable of designing and building simple to use yet important parts. I also thank him for sharing thoughts on love and family. Dr. Thaseem Thajudeen is my sweetest friend who always looks out for me, like an older brother. I am thankful to have him to work with or just sit by as he is one of the nicest and most thoughtful people I have ever met. Dr. Ranganathan Gopalakrishnan is one of my closest friends and I enjoyed all the chats we had about science and life. Dr. Siqin He is one of my best

friends and a great coworker. I thank for her help with experiments and all the chats and happy reunions. I also thank SK, Vivek, Seongho, David and Jikku for sharing the office with me and brightening my day with all sorts of chats and laughs. I thank Hallie for the bonded girl friendship. I thank Dr. Anne Maisser, Chenxi and Xiaoshuang for all the nice meetings and occasions.

Special thanks to ME department staff. I thank Jennifer Dahal for helping me find a private room for nursing. I thank John Gardner for helping me with my degree documentation.

I thank CSCC community for providing a home for me where all friendship shines. I thank all my friends within and outside the US for supporting and encouraging me when I needed them through web chats or talks by my side.

Last but certainly not least, I thank my family for always supporting me. I thank my parents Meikai Ouyang (欧阳梅开) and Meizi Luo (罗美仔) for loving me so much, and helping me raising my children. I thank my husband, Zhenpeng Qin, for being patient and standing beside me. I thank my babies Alicia and Alvin, as you are my miracles. I thank my parents-in-law Cunlong Qin and Fanrong Kong for being kind to me and help me take care of my family.

In the end, thank you all for believing in me so that I can manage to have the family life I want and pursue my dream at the meantime.

Dedication

To my family and my love

Table of Contents

List of Tables

List of Figures

Chapter 1: Introduction

Nanoparticles, condensed phase species with characteristic lengths less than 100 nm, and nanoclusters, smaller nanoparticles containing $<10^4$ molecules, are encountered in a number of gas phase environments (aerosols), wherein they may form and grow from vapor phase precursors. A brief summary of the mechanisms leading to nanocluster/nanoparticles is provided in Figure 1.1. In both homogeneous (a single chemical compound) and heterogeneous (multiple chemical compounds) systems, vapor molecules form nanoclusters via collision controlled reactions, and nanoclusters similarly grow in size through collision with vapor molecules (vapor uptake). At the same time, clusters may dissociate via evaporation (which leads to an energy barrier to stable cluster formation), if the rate of collision controlled uptake exceeds the rate of dissociation (i.e. if the energy barrier is overcome), stable nanoclusters form. These nanoclusters may then grow (into nanoparticles), by either continued vapor uptake (condensation), or, if high enough in concentration, nanocluster-nanocluster collisions (coagulation/aggregation). Growth continues for nanoparticles through these same mechanisms.

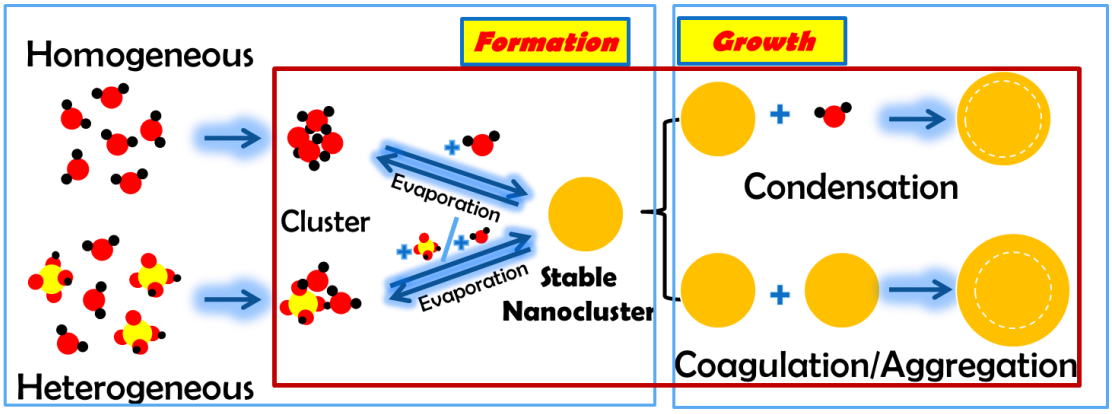

Figure 1.1 A schematic of nanoparticle formation and growth processes.

Though low in volume fraction in most systems, nanocluster/nanoparticle formation and growth can ultimately influence the properties of an aerosol. For example, nanoparticle growth and transport is critical in atmospheric chemistry and physics.

Nanoclusters form in New Particle Formation (NPF) events [1] from gaseous precursors and grow subsequently into nanoparticles, which can eventually be stable and large enough to act as cloud condensation nuclei (CCN) [2]. The concentration and distribution of atmosphere aerosol particles can hence have a direct impact on climate [3,4]. Nanoparticles also grow in combustion systems, as well as various high temperature nanoparticle synthesis systems through homogeneous/heterogeneous nucleation, with subsequent condensation, coagulation and agglomeration; growth in such circumstances has been reviewed by Wang [5] and others for [6] high temperature (non-combustion) gas phase synthesis, plasma, [7,8], and flame [9] systems. In all instances, nanoparticle growth and transport kinetics controls the formation of the nanoparticles and their eventual influence on their surrounding environment.

It is essential to evoke correct and precise models for nanocluster/nanoparticle growth in the gas phase. Various methods [10-12] have been developed to simulate the atmosphere aerosol growth and subsequent effects on the global radiation and climate. In almost all of these methods, nanoparticle growth and transport kinetics considering condensation and coagulation are included, and inaccurate nanoparticle growth rate models may lead to incorrect prediction of the overall impact of particles. Kinetic models of nanoparticle growth in combustion and high temperature reactors have also been developed [13,14]; in these situations as well accurate growth kinetics must be incorporated to predict the size distributions of particles produced.

Basic models for collision controlled reactions in the gas phase, as well as models of evaporation have been developed over the past century and incorporated into nanoparticle growth models. However, there are a number of features of nanocluster and nanoparticle formation and growth processes which are often omitted in models and require further investigation to be properly considered. Specifically, (1) the influence of nanocluster structure on their transport and growth, (2) the influence of nanocluster-nanocluster (or nanoparticle-nanoparticle) interactions on collision controlled reactions, (3) the dissociation rates and stability of nanoclusters, whose properties may deviate from

bulk matter, and (4) appropriate methods to link growth rate equations to the evolution of nanocluster/nanoparticle size distribution all must be considered in growth models. Typically, these features are either omitted or accounted for with simple approximations, not because they are not important, but because they are poorly understood. This dissertation focuses on these four topics, with the specific studies carried out described in the remaining portions of this chapter. Each of the four studies contains their own introduction, methods, results & discussion, and conclusion sections, and each is intended to serve as a stand-alone contribution to the study of nanocluster/nanoparticle transport and growth in the gas phase. At the same time, all studies are related to the evaluation of nanocluster/nanoparticle properties which can be inputs into growth and transport models for atmospheric and high temperature aerosols.

Chapter 2 focuses on measurements and modeling of how the structure of nanoclusters influences their transport. The growth and transport kinetics of condensed phase nanoscale species in the gas phase are size and morphology dependent as well as gas property dependent. Specifically, the diffusion coefficient *D* (utilized in describing transport via Fick's law [15]) and electrical mobility [16] (the proportionality constant between a particle's electrophoretic velocity and an external electric field it is immersed in), are defined via the equations:

$$D = \frac{kT}{f} \qquad\qquad Z_p = \frac{ze}{f} \qquad\qquad (1)$$

where D is the diffusion coefficient, Z_p is the electrical mobility, ze is the net charge on the particle, kT is the thermal energy, and f is the friction coefficient. The friction coefficient f for a sphere in the gas phase can be described in most circumstances by the Stokes-Millikan equation [17]:

$$f = \frac{6\pi\mu a_p}{1+Kn\left(1.257+0.4exp\left(-\frac{1.1}{Kn}\right)\right)} \qquad (2)$$

Where a_p is the particle radius, μ is the gas dynamic viscosity, and Kn is the Knudsen number, i.e. the ratio of the gas hard sphere mean free path to the particle radius. The coefficients in equation (2) derive from the measurements of Millikan [18] and are found to

agree with a number of other measurements. However, for nanoclusters, equation (2) is not expected to be accurate, because (a) the size effective of gas molecules is not negligible relative to the size of nanoclusters (they are assumed negligible in equation 2), (b) the coefficients based on the Millikan oil drop experiments do not necessarily apply for all materials, and (c) cluster gas molecule potential interaction (in particular the ion induced dipole potential for charge clusters) has non-negligible influence on the friction factor. For nanoclusters in atmospheric pressure (or lower pressure environments), Kn$\rightarrow\infty$, and, relaxing the spherical particle assumption, equation (2) can be written as:

$$f = \frac{4}{3}\rho_{gas}\sqrt{\frac{8kT}{\pi m_{red}}}\Omega \qquad (3)$$

where ρ_{gas} is the gas mass density, m_{red} is the gas molecule-nanocluster reduced mass, and Ω is the collision cross section. All parameters in equation (3) are clearly defined, with the exception of Ω; therefore, collision cross section calculation or inference is the key step in understanding nanocluster transport (i.e. Ω yields D and Z_p). In helium, a number of measurements[19,20] show that Ω agrees well with predictions considering structural models of nanocluster structure and specular scattering (elastic collisions from rigid surfaces with deterministic reemission angles) of gas molecules from nanocluster surfaces. However, diffuse scattering models (inelastic collisions with random reemission angles) are used to explain the measurements of Millikan, and measurements in air. Further, in Helium, ion-induced dipole influences are typically negligible. Additional experimental and theoretical efforts are required to link nanocluster and gas molecule structure to accurate predictions of Ω, as are described in this Chapter (which was adapted from: *The Collision Cross Sections of Iodide Salt Cluster Ions in Air via Differential Mobility Analysis-Mass Spectrometry,* Hui Ouyang, Carlos Larriba-Andaluz, Derek Oberreit, Christopher J. Hogan, *2013.,J. Am. Soc. Mass Spectrom. 24:1833-1847*).

Chapter 3 focuses on the theoretical development of collision rate expressions for nanoclusters/nanoparticles. In modeling collision growth, it is commonly assumed that there is no potential between colliding particles/clusters. However, van der Waals

potential exists in almost all circumstances and in many cases the effect is not negligible. For ionized species, the image potential between neutral-charged particle pair may also have an influence. To account for these potentials, the condensed matter approximation is frequently employed; this approximation results in potential energy functions which approach negative infinity at contact; such functions are difficult to utilize in reaction rate calculations. Coupled with singular potentials, as nanoclusters grow, the mass transfer regime in which collision growth occurs is dynamic. Collision limited nanoparticle growth is normally divided into three regimes [21]- the free molecular (ballistic), transition, and continuum (diffusive) regimes. A diffusive Knudsen number (Kn_D, distinct from the Knudsen number noted in the description of chapter 2) for a collision determines the regime in which a collision occurs; high diffusive Knudsen numbers are found in the ballistic limit and low diffusion Knudsen numbers in the continuum limit. In air, under standard atmosphere pressure and room temperature, as shown in figure 1.2, nanoclusters and nanoparticles have collisions with one another which occur at intermediate Kn_D, in the transition regime. For such collisions in the transition regime, gas dynamic approaches (as employed in molecular dynamics simulations and are applicable in the ballistic regime) as well as continuum approaches (Fick's law), do not apply. In deriving accurate collision rate expressions influence of both singular potentials and the transition regime are accounted in this Chapter (which is adapted from: *Nanoparticle Collisions in the Gas Phase in the Presence of Singular Contact Potentials*, Hui Ouyang, Ranganathan Gopalakrishnan, and Christopher J. Hogan, *2012. J. Chem. Phys. 137, 064316.*)

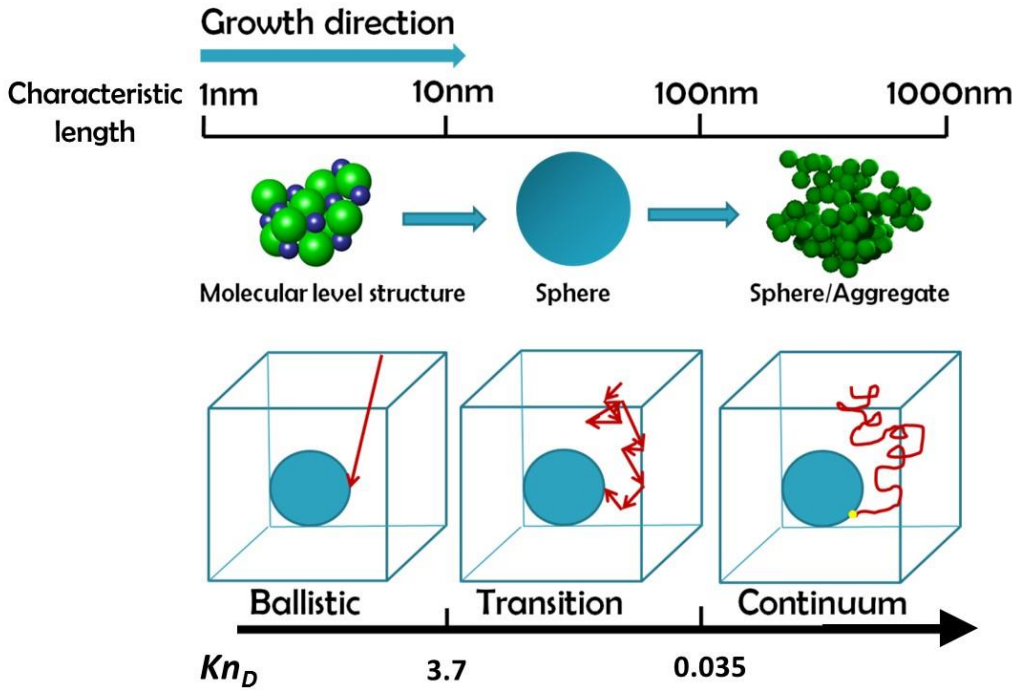

Figure 1.2 A depiction of the evolution of nanocluster-nanoparticle morphology as they grow via collisions. An approximate scale bar, which would apply for most materials, is provided under room temperature and standard pressure. In addition, a depiction of the three regimes of collisional growth is provided, with the Kn_D values giving roughly defining the ballistic-transition and transition-continuum regime boundaries. Overall, in analyzing nanoparticle growth, size, morphology, collision regime, and potential interactions need to be considered.

Chapter 4 focuses on measurements of the stability and extent of water uptake by dimethylamine-sulfuric acid nanoclusters. Dimethylamine and sulfuric acid have both been found to play a role in new particle formation events in atmosphere, hence the choice to study such nanoclusters. The dissociation and ability to uptake water of nanoclusters are equally important to nanocluster growth as the growth kinetics themselves; the net growth rate of nanoparticles is the difference between the forward (condensation and coagulation) and backward (evaporation) rates. The classically-derived Kelvin effect [22,23] is normally invoked to predict the vapor pressure of nanoclusters; knowledge of the vapor pressure enables prediction of the

dissociation/evaporation rate. However, as the Kelvin vapor pressure scales with the exponential of the inverse nanocluster radius, the dissociation rate predictions are typically extremely high with it [23], and are not consistent with field measurements of particle formation and growth [3,24]. To better understand the stability of nanoclusters, in this chapter the results of measurements with three different experimental systems, which were used to study the density, thermostability, as well as water uptake ability (hygroscopic/wetness) of dimethylamine-sulfuric acid clusters, are provided. This chapter has been published as: *IMS-MS and IMS-IMS Investigation of the Structure and Stability of Dimethylamine-Sulfuric Acid Nanoclusters*, Hui Ouyang, Siqin He, Carlos Larriba-Andaluz, Christopher J Hogan, *2015. J. Phys. Chem. A, 119 (10):2026–2036.*

Chapter 5 focuses on the development of simulation methods to incorporate growth kinetic relationships (such as the kinetic equations derived in chapter 3) to predict changes in nanoparticle number concentration and size distributions. In such simulations, a general dynamic equation (GDE) is used to describe the evolution of the particle size distribution (i.e. the number concentration per unit particle size, as a function of particle size). Coagulation, evaporation, other forms of particle generation and removal processes are considered in GDE. A considerable amount of effort has been made previously to solve GDEs, particularly in instances where it is coupled to fluid flow. Solution techniques include discrete models [25], sectional models [26], and moment models [13,27]. The rate equations for different processes (such as condensation and coagulation) are inputs into GDEs. Despite the use of numerically rigorous solution techniques, GDE predictions continue to be inaccurate in most situations. While some of this is still attributable to the numerical schemes applied (i.e. solution to GDEs, particularly when coupled with fluid flow models, requires a number of approximations), some of the inaccuracy, particularly for nanoclusters and nanoparticles, arises because of improperly employed models of growth (i.e. incorrect rate equations for coagulation or other forms of growth) [11] and inaccurate properties assumed [12] .

In this chapter, for coagulation only, the expressions developed in earlier chapters for particle growth are incorporated into a constant number Monte Carlo [28] based approach, with direct comparison made to measurements of the coagulation growth of Oleic acid particles as well as more precise (but computationally expensive) Brownian dynamics calculations [29] for coagulation. To solve the actual GDE, other forms of growth and removal processes (i.e. evaporation and deposition) will need to include in the future.

Chapter 2: The Collision Cross Sections of Iodide Salt Cluster Ions in Air via Differential Mobility Analysis-Mass Spectrometry

Abstract

To date, most collision cross section (CCS) predictions have invoked gas molecule impingement-reemission rules in which specular and elastic scattering of spherical gas molecules from rigid polyatomic surfaces are assumed. Although such predictions have been shown to agree well with CCSs measured in helium bath gas, a number of studies reveal that these predictions do not agree with CCSs for ions in diatomic gases, namely, air and molecular nitrogen. To further examine the validity of specular-elastic vs. diffuse-inelastic scattering models, we measured the CCSs of positively charged metal iodide cluster ions of the form $[MI]_n[M^+]_z$, where *M = Na*, *K*, *Rb*, or *Cs*, *n = 1-25*, and *z = 1-2*. Measurements were made in air via differential mobility analysis mass spectrometry (DMA-MS). The CCSs measured are compared to specular-elastic as well as diffuse-inelastic scattering model predictions with candidate ion structures determined from density functional theory. It is found that predictions from diffuse-inelastic collision models agree well (within 5%) with measurements from sodium iodide cluster ions, while specular-elastic collision model predictions are in better agreement with cesium iodide cluster ion measurements. The agreement with diffuse-inelastic and specular-elastic predictions decreases and increases, respectively, with increasing cation mass. However, even when diffuse-inelastic cluster ion predictions disagree with measurements, the disagreement is of a near-constant factor for all ions, indicating that a simple linear rescaling collapses predictions to measurements. Conversely, rescaling cannot be used to collapse specular-elastic predictions to measurements; hence, although the precise impingement reemission rules remain ambiguous, they are not specular-elastic.

2.1 Introduction

Predictions of collision cross sections (CCSs) with polyatomic ion candidate structures facilitate data interpretation in ion mobility spectrometry (IMS) [19,30,31]. In principle, comparison of predicted CCSs to those inferred from measurements enables identification of ion structures, and without precise CCS prediction, mobility measurement is more limited in its capabilities (e.g. CCSs are often linked to effective gas phase densities in the absence of model predictions [32-35]). However, comparison between measured and calculated CCSs can be performed if and only if the manner in which CCSs are calculated accurately reflects the manner in which gas molecules interact with ions. For this reason, the validity of the physics invoked in previously developed CCS calculation procedures [19,30,31] merits further examination.

The majority of IMS-MS studies in which comparison to structural models is performed use either an exact (elastic) hard sphere scattering (EHSS) [19] or a trajectory method (TM) [30] calculation procedure, both of which are incorporated into the freely available MOBCAL Fortran package [31]. In EHSS calculations, CCSs are determined with the gas molecule and all of the atoms within candidate structures modeled as spheres with prescribed radii. Conversely, TM calculations are performed considering Lennard-Jones potentials between gas molecules and structure atoms, with the inclusion of longer range potentials also possible. In both procedures, gas molecule trajectories near a structure are monitored, with the CCS approximated using methods described by Mason & McDaniel [36]. Importantly, without modification, both of these methods contain the implicit assumption that gas molecules are reemitted from structure surfaces at specular angles, with their impinging and reemitted kinetic energies equivalent, while the atoms within a structural model are held fixed at prescribed locations. In this regard, both EHSS and TM procedures invoke coarse-grained physics; in low-field mobility measurements ions are in thermal equilibrium with the surrounding bath gas and the atoms within the ion are vibrating with energies similar to the kinetic energies of impinging gas molecules. Therefore, although the total energy of the gas molecule-ion

system is conserved during collisions, impinging gas molecules need not be reemitted at the specular angle with respect to a fixed structural model (effectively diffuse reemission), and exchange between gas molecule translational energy and ion internal energy is possible (effectively inelastic collisions) [37].

Subsequent to their development, EHSS and TM calculations have been compared to measurements of ions of fairly unambiguous structures [19,30,38,39] with monoatomic helium as the background gas. Calculations consistently agree well with measurements under these conditions, for the TM procedure in particular. Based on this precedent, many studies invoke the assumption that the gas molecule impingement-reemission physics in TM calculations are valid under all conditions [40], and that in the event calculations and measurements do not agree with one another, it is appropriate to rescale Lennard-Jones parameters (i.e. the properties of the atoms in structures are adjusted to fit experimental measurements). However, more recently, with commercially available nitrogen background gas based IMS-MS systems (the Waters SYNAPT system, based on traveling wave IMS [41,42]), an interest in making IMS measurements with differential mobility analyzers [32,33,43], and helium conservation efforts, a large fraction of current IMS-MS based studies make use of diatomic nitrogen or air as the background gas. As noted by Shvartsburg& coworkers [37], there are significant differences in the gas molecule collision and reemission processes between helium and diatomic gas molecules. With the exception of hydrogen atoms, helium is significantly lighter than the atoms composing ions often examined via IMS-MS; hence at thermal equilibrium helium atoms may be moving at sufficient speeds that the use of fixed atom structural models with specular scattering effectively mimics the helium impingement-reemission process. Diatomic gas molecules, conversely, are similar in mass to most atoms within polyatomic ions; thus, they have speeds at thermal equilibrium similar in magnitude to the speed of atomic vibrational motion, which may have an influence on impingement-reemission. Moreover, polyatomic gas molecules themselves have vibrational and rotational degrees of freedom, and during collision the exchange of translational energy into vibrational and

rotational energy of not only of a polyatomic ion but also a diatomic gas molecule is possible.

There is in fact experimental evidence that collisions between polyatomic gas molecules and ions do occur in a manner which prohibits modeling them as fully specular and elastic with rigid ion structures. The differences in CCS which would be brought about by diffuse, inelastic collisions were first noted by Epstein [44], who found that the results of the Millikan oil drop experiments [17]are best explained through diffuse, inelastic collision models. More recently, Fernandez de la Mora and coworkers [33,35,45]have found that the CCSs of nearly spherical ions in the sub 10 nm diameter range (down to ~1.3 nm) are described well by Epstein's model. Also in line with these results, Kim and coworkers [46,47]determined that the CCSs of small (< 500 Da) organic ions can be predicted with TM procedures, but that TM calculations must be modified to consider the rotational and vibrational energy of diatomic gas molecules, thereby enabling reemission at non-specular angles and the possibly of exchange between modes of energy in calculations. Finally, in developing new CCS calculation routines with a control volume approach [48], our group has found that the measured CCSs of tetraalkylammonium ions [49], and multiply charged polyethylene glycol ions [50] can only be predicted accurately from correctly scaled structural models if non-specular, inelastic gas molecule impingement-reemission rules are invoked [51].

Taking into account the continued use of purely elastic, specular gas molecule scattering calculations for comparison to measurements, even in diatomic gases [52], there is a need to more clearly determine to what extent the traditionally used specular, elastic collision models and semi-empirical diffuse, inelastic models can predict CCSs. For this purpose, here we utilize a parallel plate differential mobility analyzer coupled to a time-of-flight mass spectrometer (DMA-MS) [53,54] to measure the CCSs of electrospray ionization generated sodium, potassium, rubidium, and cesium iodide cluster ions with the structures $[MI]_n[M^+]_z$, where $n = 1 - 25$ and $z = 1 - 2$. DMA measurements are made with nearly water-free "zero" air as the bath gas at atmospheric pressure and

temperatures in the 299-315 K range. CCSs are calculated from cluster ion model structures accounting for the influence of the ion-induced dipole potential between gas molecules and cluster ions, first with traditional specular, elastic gas molecule impingement and reemission rules (EHSS calculations), and second with semi-empirical wholly diffuse, inelastic gas molecule impingement and reemission rules (DHSS calculations) [48,51]. The sizes of the atoms in structures as well as the potential interaction between gas molecule and ion are not varied with the two scattering models applied; therefore this study can be viewed as the converse of prior IMS studies where a scattering model is assumed, and atomic sizes/short range potential interactions are varied. The results of both calculation procedures are shown to differ drastically from one another, noting the importance of the gas molecule impingement-reemission in CCS calculation, and both are compared to measured CCS values.

2.2 Materials and Methods

2.2.1 Differential Mobility Analysis-Mass Spectrometry

Solutions for electrospray ionization (ESI) were prepared using HPLC grade methanol as a solvent, with sodium, potassium, rubidium, and cesium iodide salts dissolved at concentrations of 10mM. All chemicals were purchased from Sigma-Aldrich (Saint Louis, MO) and used without further purification. Positive ESI was performed in a near-identical manner to that described by Hogan & Fernandez de la Mora [53,55], with a silica capillary of outer diameter of 360 μm, inner diameter of 40 μm, and a tapered outlet formed by grinding the capillary with fine grained sand paper. Sample solutions were placed inside a 1.5 mL screw cap vial (Dot Scientific, Burton, MI) which was pressurized 100-150 mbar above atmospheric pressure, driving sample solution into and through the capillary. A high purity 500 μm diameter silver wire placed inside the screw cap vial was used to apply voltage directly to the solution. The voltage applied was set to a constant level floating above the voltage applied to the DMA upper electrode. ESI was performed in cone-jet mode [56], with the mode of operation verified by visual examination

of the capillary tip with a magnifying lens, as well as by monitoring the current carried by produced drops [57]. During stable cone-jet operation this current was 100-200 nA, with a variation of +/- 5 nA during a given experiment.

The operation of parallel plate DMAs for the measurement of ESI generated ions, and the coupling of such DMAs to mass spectrometers is described in detail by Rus et al [54]. Briefly, in this study singly and multiply charged salt clusters ions, formed subsequent to the evaporation of methanol drops, were directed into the DMA inlet slit electrostatically, while a ~0.2 L min^{-1}counterflow of high purity, water free "zero" air (Air Gas, Ultra Zero < 1ppm, St. Paul, MN) prevented methanol vapor from entering the DMA. The DMA used was parallel plate model P5 (SEADM, Boecillio, Spain), which has resolving power of 50-70, an electrode to electrode (gap) distance of 1 cm, and an inlet to outlet distance of 4 cm (parallel to the direction of the sheath flow). The sheath flow (of high purity air) was operated in recirculating mode using a modified vacuum blower (Domel EC systems, Slovenia), with pressure inside the DMA classification region near atmospheric pressure. The temperature within the DMA was controlled via a fan based heat exchanger attached to sheath flow tubing. By controlling both the DMA blower speed (with higher speeds leading to higher temperatures) and the heat exchanger fans, in the DMA classification zone it was varied from 299 – 315 K, confirmed via measurement with a thermocouple (K-type) near the DMA upper electrode inlet. A dew point hygrometer (General Eastern Hygro M4) was also connected to the ESI chamber to determine the relative humidity of the DMA sheath gas (sampling the counterflow). Relative humidities for all experiments were below 1%. Between experiments, the counter of "zero" air was maintained and the DMA blower was operated continuously for a period of at least 8 hours prior to measurements. Experiments performed with gases of lower purity were observed to lead to appearance of contaminant ions in spectra; hence it was possible that under such conditions, contaminant vapor molecules transiently associated with cluster ions in the DMA shifting their mobilities. All attempts were made to avoid such contaminant influences, which we further note are not unique to the DMA-

MS system in this work, but are possible in all ion mobility spectrometers. To obtain mobility spectra, the voltage between the DMA electrodes was varied from 1000 to 3500 V in steps of 10 V. At each specified voltage, ions transmitted through the DMA entered the inlet of a QSTAR XL mass spectrometer (AB Sciex, Framingham, MA), where the time-of-flight section was used for mass measurement in the 20 – 10,000 Da *m/z* range. The "enhance all" option within Analyst 2.0 (the software package used for data acquisition with the QTSAR XL) was employed to transmit all ions in this *m/z* range as uniformly as possible. Accumulation times from 2 – 5 seconds were used to collect mass spectra at each voltage. At the QSTAR XL inlet, both declustering potentials were set to zero, while the focusing potential was set to 130 volts.

In the electrostatic field range examined, the mobilities measured by the DMA are those corresponding to the low field mobility limit (ion velocity <40 m/s, well below the mean thermal speed) and the DMA is a linear mobility spectrometer with a zero point intercept, with the applied voltage between electrodes directly proportional to the inverse mobility of the ions transmitted [53]. A single calibrant ion alone can thus link the applied voltage to the mobility of transmitted ions. For this purpose, we employed the tetraheptylammonium$^+$ (THA^+) ion, generated via ESI of a 5 mM solution of tetraheptylammonium bromide in methanol. The mobility of this ion at 293 K was measured by Ude& Fernandez de la Mora to be 0.97 $cm^2\ V^{-1}\ sec^{-1}$ in air near atmospheric pressure [49], with the collision cross sections inferred for tetraalkylammonium ions by Ude& Fernandez de la Mora in reasonable agreement with recent measurements by Bush et al [58] with a drift tube in N_2. As the temperature during our experiments was different than that of Ude& Fernandez de la Mora, the mobility of the THA^+ ion was adjusted by a factor $(T_{exp}/293\ K)^{1/2}$, where T_{exp} is the temperature within the DMA during the experiment under consideration. This adjustment is based on the assumption that polarization (i.e. the ion induced dipole potential between gas molecule and ion) minimally influences the mobility of THA^+; the mobility is shifted assuming that hard sphere potentials exist between THA^+ and gas molecules. While recently we have shown

(and further demonstrate here) that polarization slightly influences mobility in this range at atmospheric pressure [51], we note that the consideration of polarization in the temperature correction would only influence the measured mobilities by less than 4% percent and hence does not have any bearing on the conclusions drawn in this work. We also calibrated many spectra using the larger tetradecylammonium$^+$, tetradodecylammonium$^+$, and (THABr)THA$^+$ions, in each case with results near-identical to those using THA$^+$(differences of less than 2% in CCS). Further, we note because the temperature correction is small, use of the more commonly invoked linear temperature correction $(T_{exp}/293\ K)$ [36] also has little bearing on our results. With the THA$^+$ ion mobility denoted as Z_{THA} and with this ion transmitted through the DMA at an applied voltage V_{THA}, the mobilities of metal salt clusters ions Z_i were determined from the voltage they were transmitted at V_i through the relationship:

$$Z_i = \frac{V_{THA}}{V_i} Z_{THA} \quad (1)$$

Correspondingly, collision cross sections Ω for all measured ions were determined from mobilities:

$$\Omega = \left(\frac{\pi m_{red}}{8kT}\right)^{\frac{1}{2}} \frac{3ze}{4\rho_{gas} Z_i} \quad (2)$$

where z is the integer charge of the ion, e is the unit electron charge, m_{red} is the reduced mass of the ion-gas molecule (with a mass of 28.8 Da for air) system, ρ_{gas} is the bath gas mass density, k is Boltzmann's constant, and T is temperature. CCSs are hence determined as a function of temperature in the narrow temperature range examined for subsequent comparison to predictions.

2.2.2 Density Functional Theory Calculations

Metal iodide cluster ions are chosen for examination in this study for several reasons. First, the comparison of measured CCSs to those predicted from models in many studies suffers from the fact that the ion structures in the gas phase (e.g. for electrosprayed biomolecules) are difficult to predict; thus both the gas molecule

impingement and reemission rules and the candidate ion geometries have considerable ambiguity. For metal iodide cluster ions, local energy minimum structures can be reliably predicted via density functional theory (DFT), with more rigorous ab initio calculations of structures from prior work [59,60] available for comparison to DFT results. Second, Fernandez-Lima and coworkers [38] have similarly examined $[CsI]_nCs^+$ clusters via IMS-MS in helium bath gas, showing reasonable agreement between measurements and traditional EHSS and TM calculated CCSs. This prior precedent aids in validating both the ion structures and CCSs we calculate. Third, the prior measurements supporting the use of diffuse and inelastic scattering models in diatomic gases have been of organic ions exclusively [17,32,33,46,50,51,61]; comparison to inorganic ions, in which the cation and anion masses both exceed that of the impinging gas molecules may give rise to different results than these prior studies. Finally, while the structures of metal salt cluster ions can be predicted reliably, unlike the ions used in prior comparisons with similar goals [33,45], they are not near-spherical, have CCSs strongly influenced by the ion induced dipole potential in the size range examined, and further in the case of cesium iodide, small cluster ions are known to have structures which deviate considerably from bulk structures [62].

Candidate structures for the singly and doubly charged cluster ions detected with the DMA-MS were generated using the Gaussian 09 software package (Gaussian Inc., Wallingford, CT). The B3LYP density functional [63636363636363] was employed, which has been used successfully to determine structures of similar charged salt clusters previously [38,64], as was the basis set LANL2DZ, which applies Los Alamos ECP (effective core potential) plus DZ (double zeta) [65] for the elements in this study (*Na*, *K*, *Rb*, *Cs*, and *I*). Symmetry restrictions were not applied, and vibration frequencies were calculated. All structures presented in the *Results & Discussion* section showed positive frequencies, indicating they are truly local minima structures rather than transition states. Initial guesses of local minima structures of singly charged clusters were obtained from Aguado et al [60] ab initio calculations of $[NaI]_nNa^+$ and $[CsI]_nCs^+$ clusters or Fernandez-Lima et al

[38] DFT calculations of $[CsI]_nCs^+$ clusters. Initial structures for $[KI]_nK^+$ and $[RbI]_nRb^+$ were determined by replacing Na or Cs with K and Rb separately. Doubly charged clusters were initiated with "rocksalt" structures, which have been found previously to local minima for larger salt clusters [20,60,66]. These initial structures were determined by first finding local minima for neutral salt clusters with the desired number of cations or anions. Subsequently, either two anions were removed from or two cations were added to these structures, followed by further energy minimization.

2.2.3 Collision Cross Section Calculation

From DFT local energy minima structures, collision cross sections were calculated using the control volume method recently developed by Larriba [48,51]. In this calculation approach, CCSs are determined for fixed polyatomic structures via direct calculation of the rate of momentum transfer from impinging and reemitted gas molecules to a structure surface. Atoms may be modeled as hard spheres or via potential interactions with gas molecules, and the long range polarization potential between gas molecules and structures may be considered. Further, this calculation procedure permits the use of arbitrary gas molecule reemission rules, i.e. specular-elastic scattering as well as any variety of diffuse and inelastic reemission processes. In this study, as noted in the introduction both the gas molecule and all atoms were modeled as hard spheres, and calculations were first performed using specular, elastic reemission rules, akin to EHSS calculations [19] and denoted as such. Second, a diffuse and inelastic reemission rule was invoked, in which impinging gas molecules are reemitted at a random thermodynamically permissible angle from a structure surface (uniform distribution), and the reemitted speed is determined by sampling from a Maxwell-Boltzmann distribution with the mean temperature 8% lower than the system temperature. This set of collision rules, termed diffuse hard sphere scattering (DHSS) rules, was employed to mimic the influence of atomic vibrational and rotational motion within both structures and gas molecules with speeds relevant to collisions. The choice of reemission speed from a reduced temperature Maxwell-Boltzmann distribution is entirely empirical; this reemission rule leads to CCS

predictions in good agreement with the Millikan oil drop experiments [17], measurements of tetraalkylammonium ions [49], measurements of multiply charged polyethylene glycol ions in air in the kilo Dalton mass range [50], and measurements of sub 2 nm near-spherical ionic liquid drops [33] (with all noted measurements made in air or nitrogen near room temperature).

For appropriate CCS prediction, not only must a reasonable scattering law be invoked, but also the sizes of atoms and overall gas molecule and structures (i.e. the spacing between atoms) must accurately reflect the structures and gas molecules of interest at the measurement temperature. DFT determined structures were used without modification for CCS prediction. The atomic radii within each structure were approximated by the ionic radii for each species. Specifically, the radii used were: 1.16 $\dot{A}$ for sodium, 1.52 $\dot{A}$ for potassium, 1.66 $\dot{A}$ for rubidium, 1.81 $\dot{A}$ for cesium, and 2.06 $\dot{A}$ for iodide (anions). The choice of constant radii for all atoms is distinct from the approach employed commonly, such as by Wyttenbach et al. [59,67], who used regression equations developed from helium bath gas mobility measurements to determine atomic radii which are dependent on the number of atoms in an ion. Further, CCSs calculations were performed varying the size of cesium atoms (to 1.74 $\dot{A}$); it was found that this changed CCS predictions by < 2%, considerably less than the influence of scattering model. Based on the recent measurements of Fernandez de la Mora & coworkers near 300 K [33,45] and following the results of Larriba& Hogan [51], gas molecules were modeled as spheres with radii of 1.5 $\dot{A}$, which further leads to a sphere with a projected area near-equivalent to the orientationally averaged projected area (PA) of the structure of a nitrogen diatomic molecule provided by Niwa et al [68].

As noted in prior sections, the polarization potential has an influence on gas molecule trajectories in close proximity to a charge, and hence influences the CCSs of smaller (below 2 nm in characteristic size [48,69]) cluster ions. For a gas molecule of polarizability α_{pol}, the polarization potential U_{pol} is given as:

$$U_{pol} = -\frac{\alpha_{pol} z^2 e^2}{8\pi\varepsilon_0 r^4} \quad (3)$$

where ε_0 is the permittivity of free space and r is the scalar distance between the excess charge and the gas molecule position. To calculate this potential and the resulting force on gas molecules, the excess charge was placed at the geometric center of each structure examined. In the case of doubly charged ions, the charge was still placed at the center with its magnitude doubled as compared to singly charged ions. We acknowledge that this charge placement is a first approximation to the charge distribution on a structure, which is no doubt geometrically more complex, and further study will be necessary to rigorously determine spatial charge distributions and their influence on CCSs in polarizable gases. However, the influence of the spatial charge distribution on CCS calculations is expected to be small relative to the examined influence of gas molecule scattering rules. For example, the dipole moments of the sodium and cesium iodide structures examined were extracted from DFT calculations. Dipole moments ranged from 0-25 D and 10^{-2}-60 D for the singly and doubly charged clusters, respectively. During gas molecule impingement, the characteristic dipole-induced dipole energy with N_2 for these clusters relative to the thermal energy (at the measurement temperatures) is below 0.1, even for the structures of highest dipole moment (relative to their size). We do note, however, that dipole-induced dipole potential interactions are not necessarily negligible in all circumstances, and would likely influence gas molecule impingement at reduced temperature, or in gases of higher polarizability.

Polarization potentials were considered in both EHSS and DHSS calculations, and in all circumstances the input relative (bulk) speed between ion and bath gas was 40 m/s (a necessary input for momentum transfer calculations when long-range potentials and the non-truncated gas molecule velocity distributions are considered). The temperatures and pressures corresponding to experimental measurements were also direct inputs for calculations. In both EHSS and DHSS calculations many gas molecules were introduced into the control volume which did not impinge directly upon the structure but nonetheless transferred momentum, as their trajectories were altered via polarization. The momentum transferred by these gas molecules, which is independent of scattering model,

was accounted for via the calculations reported by Larriba & Hogan [48]. Using the results of these calculations for "grazing" gas molecules considerably sped up the CCS calculation procedure. The convergence of calculations was further enhanced by direct calculation of the drag tensor for structures, from which mobilities and CCSs values were extracted. As shown by Happel& Brenner [70], construction of the drag tensor only requires determination of momentum transfer to a structure for three perpendicular orientations. CCS calculations were performed sampling gas molecule speeds from both the full skewed Maxwell-Boltzmann distribution as well as from the linear perturbation distribution alone (the second term in the speed distribution after Chapman-Enskog linearization[71]). Results from only the latter are reported, although rigorously the full speed distribution should be considered when potential interactions influence gas molecule motion [48]. For all examined structures a negligible difference in results was found when the simplified distribution alone was used.

2.3 Results and Discussion

2.3.1 DMA-MS Spectra

Two-dimensional mass-mobility spectra collected with the DMA-MS at temperatures near 299 K are displayed in Figure 2.1 for all four types of salt cluster ions examined. On the abscissa of these plots is the applied voltage across the DMA electrodes, from which the mobility and collision cross section were inferred. On the ordinate, *n/z*, the number of neutral cation-anion pairs (*n*) per unit excess cation (*z*) is noted. For a given salt cluster, *n/z* can be calculated from *m/z* via the relationship:

$$\frac{n}{z} = \frac{\left(\frac{m}{z} - m_M\right)}{m_{MI}} \tag{4}$$

where m_M is the metal cation mass, m is the mass of the cluster and m_{MI} is the metal-iodide ion pair mass. Signal intensity for each ion is displayed via a logarithmic color scale, with red denoting the most intense signal and blue denoting the faintest signal

above a prescribed threshold. Plotting results in terms of *n/z* reveals distinct "bands" of line segments, where each line segment denotes a specific cluster ion and its length reflects the DMA resolution. The band in the lowest *n/z* range contains only ions with integer *n/z* values and hence corresponds to the singly charged cluster ions. Similarly, the next lowest *n/z* band contains ions which differ from their neighbors in *n/z* by steps of 0.5, and corresponds to doubly charged clusters. Both of these bands are labeled in spectra. In the $z = 1$ band, ions of identical mobility/transmitted voltage but different integer *n/z* appear. However, these ions are not indicative of differing structures for singly charged salt clusters, but are instead an artifact of neutral ion-pair loss ($[MI]_nM^+ \rightarrow [MI]_{n-1}M^+ + [MI]$, with examples labeled in the cesium iodide cluster ion plot) after ions exist the DMA outlet, but prior to mass measurement. This process is described in detail by Hogan & Fernandez de la Mora [55], and is a common occurrence during cluster ion examination via DMA-MS (as well as in drift-tube IMS-MS, as observed in measurements by Trimpin & Clemmer [72]). Apparent in Figure 2.1 spectra as well as in those presented in prior work, there is sufficient collisional activation energy in most mass spectrometer systems (after IMS) for multiple neutral loss reactions to occur prior to mass measurement, despite attempts to avoid it. In addition to neutral loss, a common occurrence for multiply charged cluster ions is collision energy driven ion evaporation reactions [53,73] of the form: $[MI]_n[M^+]_z \rightarrow [MI]_{n-1}[M^+]_{z-1} + [MI]M^+$ (example labeled in the potassium iodide cluster ion plot), which was also found to occur in our experiments for doubly charged clusters. Like neutral loss, ion evaporation appears to occur predominantly after ions exit the DMA outlet, but it is also found to occur when ions were transiting the DMA (both in this work and in prior studies). When charge loss within the DMA occurred, the mobility at which an ion was transmitted was intermediate to the mobility of the reactant ($[MI]_n[M^+]_z$) and the mobility of the product ($[MI]_{n-1}[M^+]_{z-1}$), leading to the appearance of long line segments at the *n/z* value of the product ion, whose lengths are not a function of DMA resolution. Such line segments are always apparent in spectra at $n/z = 13$ (though they are visible at other *n/z* as well), as the singly

charged 13-mer corresponds to a 3x3x3 cube for all examined ions and the doubly charged 14-mer is a less stable structure. The voltage corresponding to the left end of these line segments is the transmitted voltage for the reactant ions, i.e. the ions which were transmitted through the DMA stably, but underwent ion evaporation afterwards. Further, for many detected ions, ion evaporation within the DMA was minimal but prevalent after the DMA outlet, leading to the appearance of short, DMA resolving power-defined line segments at the voltage for the reactant but the spurious *n/z* for the product ion. For a selected few of these ions, it is possible to extract the mobilities and CCSs values for the reactants (for which $z = 2$) for comparison to CCS predictions. The bands of line segments formed by $z = 2 \rightarrow z = 1$ ion evaporation after the DMA are noted in all Figure 2.1 spectra. A final note on these spectra is that in each, at a relatively high mobility (transmitted voltages between 1300 to 1700 V in all cases) there are a series of line segments corresponding to singly charged ions (appearing only at integer *n/z* values, with an example labeled in the rubidium iodide cluster ion plot). These ions are attributable to neither neutral nor ion evaporation alone, and while they may be the result of these processes occurring in series, a distinct type of dissociation reaction, hitherto undescribed, may also bring about their appearance (e.g. these may result from a more symmetric fission process of the type $[MI]_n[M^+]_2 \rightarrow [MI]_a[M^+]_1 + [MI]_b[M^+]_1$, where $a > 1$ and $b > 1$).

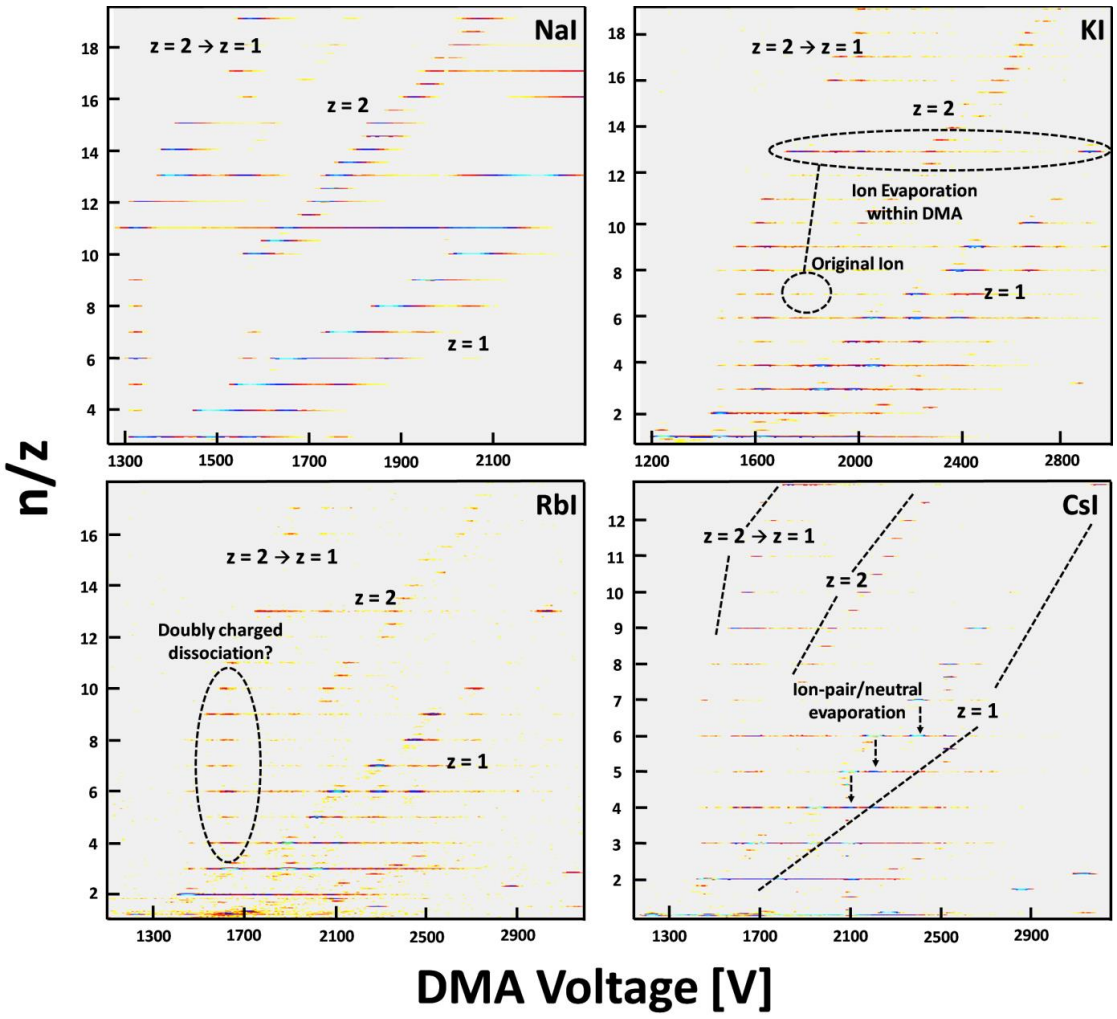

Figure 2.1 Contour plots displaying measured signal intensity (expressed via color intensity on a logarithmic scale, with blue the most intense and yellow the least intense) in DMA-MS experiments. *n/z* corresponds to the number of neutral ion-pairs per excess cation in detected cluster ions, and is calculated directly from mass-to-charge ratio. The DMA voltage applied is inversely proportional to the mobility of the ions transmitted. The sets of ions which were singly charged (z = 1), doubly charged (z =2), and which were doubly charged while transiting through the DMA but underwent charge loss prior to mass measurement (z = 2 →z = 1) are labeled in all contour plots, as are examples of observed dissociation processes (neutral evaporation, ion evaporation, and doubly charged ion dissociation).

Despite neutral and charge loss processes complicating spectra, it is possible to identify clearly the transmission voltages for singly charged cluster ions from *n = 1* to *13*

and doubly charged cluster ions from *n = 14* to *25*. For each examined ion of chemical composition $[MI]_n[M^+]_z$, only a single peak voltage was used to determine mobility and CCS; other line segments were attributable to either neutral loss or ion evaporation. The CCSs for all singly charged ions at all measurement temperatures and for doubly charged ions (which were only examined at the lowest achieved temperatures) are shown in table 2.1.

Table 2.1 The collision cross sections of the noted metal iodide salt clusters at all examined temperatures. Upper- clusters with a single excess cation (singly charged). Lower- clusters with two excess cations (doubly charged). Collision cross sections were inferred directly from DMA-MS measurements and the displayed values are in units of square Angstroms.

n	NaI			KI			RbI			CsI		
	26.4°C	**34.75 °C**	**41.95 °C**	**26.4°C**	**34.75 °C**	**42 °C**	**26.4°C**	**34.5°C**	**42 °C**	**26.4°C**	**34.5 °C**	**42.15 °C**
1	130.43	128.21	127.66	125.63	124.24	125.17	121.83	120.68	122.13	123.01	122.02	122.23
2	146.61	143.84	144.50	144.78	143.07	144.34	143.00	141.51	142.17	145.41	144.19	144.19
3	160.56	158.64	159.52	159.26	157.58	158.19	160.31	158.89	157.96	166.12	164.73	164.06
4	179.62	176.91	177.06	181.56	179.86	180.99	184.42	182.59	182.52	190.68	189.18	188.53
5	189.63	187.34	188.42	193.10	191.55	191.87	196.47	195.28	194.60	204.84	203.42	202.88
6	198.85	195.96	198.96	199.73	198.42	198.25	204.55	203.03	202.23	214.71	213.79	212.53
7	213.06	210.46	213.81	216.59	214.24	214.58	221.94	220.56	219.82	233.56	231.53	230.51
8	226.35	223.92	227.50	231.94	230.49	230.34	237.12	235.84	235.15	246.24	245.64	243.21
9	237.74	235.34	237.49	238.38	236.47	236.16	244.67	243.34	242.55	258.17	256.61	255.18
10	251.49	248.48	250.78	259.42	258.33	257.91	262.41	261.73	260.89	273.11	271.36	271.70
11	260.50	258.37	260.99	268.73	267.44	268.35	276.30	-	274.77	-	-	-
12	266.24	262.64	266.88	-	279.13	275.77	287.77	-	-	-	-	-
13	270.93	269.20	272.41	281.98	280.96	279.80	292.30	290.61	289.07	309.41	308.06	306.28

At 26.4°C:

n	NaI	KI	RbI	CsI
14	-	346.50	341.7	-
15	349.40	352.30	351.33	369.46
16	354.28	358.10	360.79	377.03
17	364.05	375.52	368.70	386.93
18	376.26	381.32	-	392.75

19	383.58	386.93	-	411.96
20	388.22	390.99	401.50	419.91
21	398.23	402.41	411.14	431.36
22	403.12	415.95	418.86	441.07
23	415.33	425.82	438.16	446.89
24	422.41	429.69	447.61	458.53
25	427.53	439.36	-	474.05

2.3.2 Density Functional Theory Structures

Figures 2.2 and 2.3 display calculated local minima structures (with the coordinates and energies for each structure provided in the Appendix B) of singly and doubly charged clusters with $[MI]_nM^+$ and $[MI]_n[M^+]_2$ respectively where *M = Na, K, Rb* and *Cs*. For singly charged clusters, *n* ranges from *1* to *13*, while clusters presented with *n>13* are all doubly charged. Atoms are represented by beads with size proportional to the ionic radius; thus, an increase in bead size can be observed from *Na* to *Cs* atom, while iodide atom is the same size for all clusters. In each cell, the structures of isomers are ordered based on their energy levels from left to right, beginning with the obtained ground state structure. Linear and planar local minimum structures were found for *n = 2-5*, though three dimensional structures were found to be the most stable/ground state structures, with the exceptions of $[RbI]_4Rb^+$ and $[CsI]_4Cs^+$, for which planar structures had the lowest energy. For n≥6, rocksalt structures were found for all ions, with a cubic crystal structure (3x3x3) as the ground state with *n=13* for all four salts. This cubic crystal rocksalt (NaCl-like) structure is the bulk crystal structure for *NaI*, *KI* and *RbI*. The bulk structure of *CsI* is a body-centered cubic crystal; however, as shown by Krückeberg et el [62], a phase change in $[CsI]_nCs^+$ from rocksalt type structure to the bulk structure is only found at uniquely *n=32*. For the doubly charged clusters, all structures obtained were again rocksalt cubic structures, with either missing corner atoms or incomplete layers bound to a cube, with the notable exceptions of $[CsI]_{14}[Cs^+]_2$ and $[CsI]_{15}[Cs^+]_2$, where contorted cube-like structures were obtained.

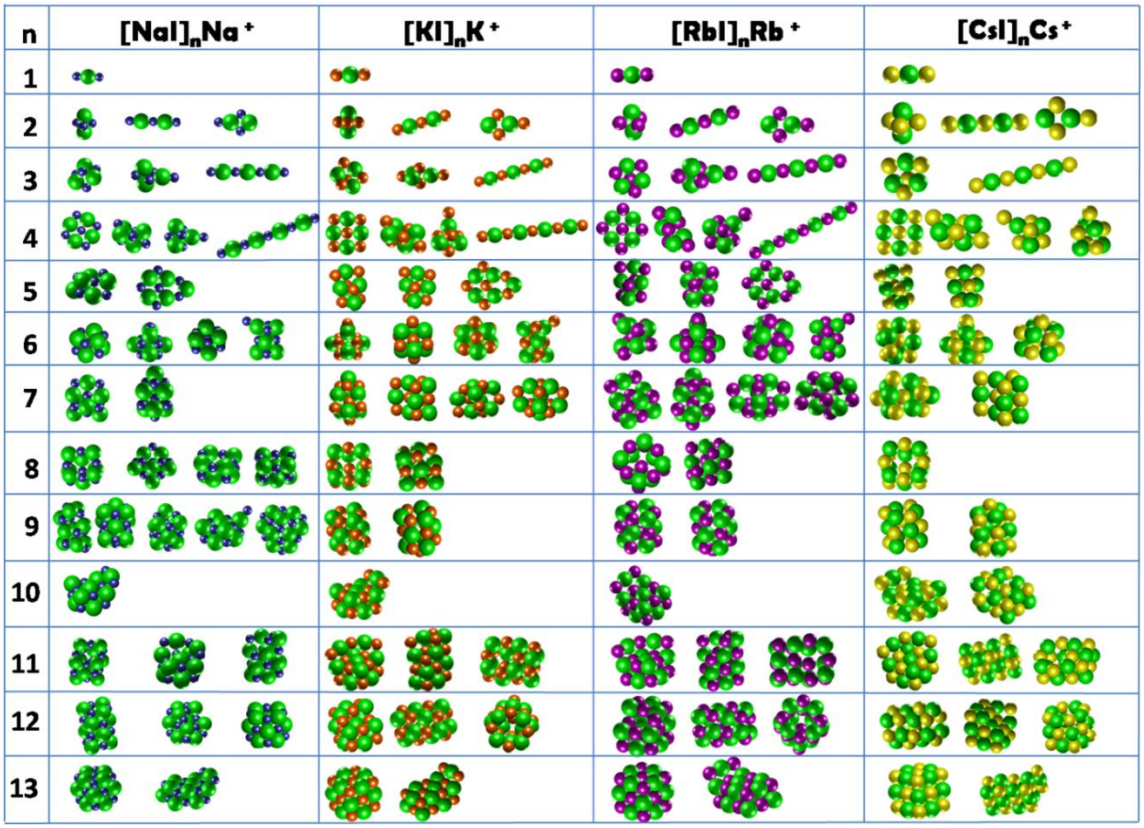

Figure 2.2 Depictions of the local energy minima structures found for **singly charged** metal iodide cluster ions via density functional theory. Iodide ions are denoted via green spheres, while sodium, potassium, rubidium, and cesium are denoted via blue, orange, purple, and yellow spheres respectively. The relative size of each sphere is proportional to the ionic radius of the cation/anion in question.

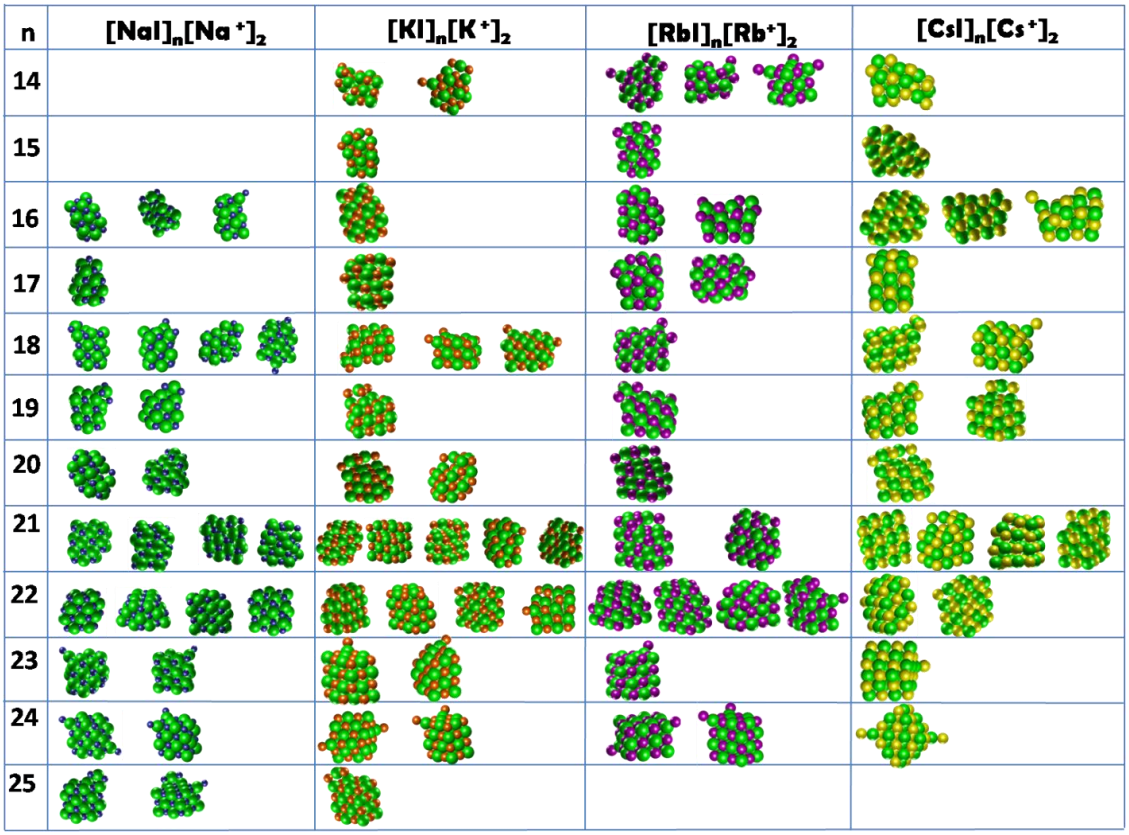

Figure 2.3 Depictions of the local energy minima structures found for **doubly charged** metal iodide cluster ions via density functional theory. Iodide ions are denoted via green spheres, while sodium, potassium, rubidium, and cesium are denoted via blue, orange, purple, and yellow spheres respectively. The relative size of each sphere is proportional to the ionic radius of the cation/anion in question.

2.3.3 Comparison to Helium Measurements and MOBCAL calculations

Using the same reported singly charged *CsI* structures from Fernandez-Lima et al [38] with *n = 1-7*, we first compare the results of EHSS calculations in this study to their results [38], which were obtained by producing $[CsI]_nCs^+$ clusters via laser ablation and measuring their CCSs in helium bath gas at in drift tube reduced pressure. A similar effort to that performed here was made in their work to compare measured CCSs to those predicted for DFT-determined energy minima, with traditional EHSS and TM methods in MOBCAL employed exclusively for this prediction. A comparison of the experimental,

EHSS calculated, and TM calculated CCSs reported by Fernandez-Lima et al to those calculated here using EHSS impingement-reemission rules is given in Table 2.2, where the values noted in each row correspond to calculations performed on similar structures. As helium has an extremely low polarizability and the measurements in question were made near room temperature, the influence of the ion-induced dipole potential was neglected in our calculations. The results of calculations with a probe (helium atom) radius of 0.5, 1.0, and 1.4$\dot{A}$ are provided, and it is found generally that those with a 1.4 $\dot{A}$ are in good agreement (within 10%) with both calculations (EHSS & TM) for most cases and measurements by Fernandez-Lima et al. This supports the validity of the calculations performed here, as separate DFT calculations and a distinct method of CCS predictions from MOBCAL were employed, yet agree well with prior work.

Table 2.2 A comparison of the CCS calculated and measured by Fernandez-Lima et al [38] for $[CsI]_nCs^+$ ions. Provided values are in units of $\dot{A}^2$. Under the "Fernandez-Limea et al. CCS Values" heading, **n** corresponding to the number of neutral ion-pairs in the cluster, with the roman numeral noting the exact structure reported by Fernandez-Lima et al, **EHSS** denotes elastic hard sphere scattering results from MOBCAL, **TM** denotes trajectory method calculation results, and **IM-MS** denotes the results of drift tube based ion mobility-mass spectrometry experiements. Under the "EHSS CCS Predictions (this Study)" heading, n again denotes the number of neutral ion-paris in the clusters, with the lower case letter corresponding to structure listed in Figure 2.2 (a- leftmost, b- second from the left, etc.), and r_g denotes the helium probe radius used in calculations.

Fernandez-Lima et al. CCS Values				**EHSS CCS Predictions (this Study)**			
n	**EHSS**	**TM**	**IM-MS**	**n**	**r_g=0.5$\dot{A}$**	**r_g =1.0$\dot{A}$**	**r_g =1.4$\dot{A}$**
1	72	67±8	85±13	1	42.4	54.5	**65.2**
2I	95	98±6	105±11	2a	66.0	81.9	**95.3**
2II	113	117±6		2b	67.0	81.5	**93.2**
2III	103	93±6		2c	66.7	82.8	**96.4**
3I	121	125±7	133±10	3a	86.2	104.1	**117.3**
4I	145	148±10	160±11	4a	107.5	126.8	**143.4**

4II	137	138±7		4b	102.4	120.7	**135.4**
5I	161	165±10	169±10	5a	122.1	142.6	**157.4**
5III	158	162±9		5b	119.6	138.4	**153.5**
6I	175	181±10	183±8	6c	137.8	158.6	**174.0**
7I	202	209±10	203±8	7b	152.3	179.8	**196.2**
7II	204	208±11		7a	157.8	174.0	**189.4**

2.3.4 Predicted vs. Measured Collision Cross Sections in Air

Figure 2.4 shows plots of the ratio $\Omega_{air}/\Omega_{calc}$, the CCS inferred from measurements in air to the CCS calculated for all four salt cluster ion types as a function of the number of neutral ion-pairs per cluster. $\Omega_{air}/\Omega_{calc}$ is plotted for all obtained local minimum structures except for the linear structures with *n=2, 3,* and *4*, which are not the ground state. In the temperature range examined, measured CCS values differ by 1-2% for most structures, thus only results at the lowest measurement temperatures are displayed. $\Omega_{air}/\Omega_{calc}$ ratios are shown for both EHSS (open circles) and DHSS (closed symbols) impingement-reemission rules, and in all cases the influence of polarization was considered. Guidelines at $\Omega_{air}/\Omega_{calc}$ = 1, 1.1, and 0.9 are provided in figure 2.4 plots for clarity. Immediately evident is the difference between EHSS and DHSS predictions; they differ from one another by 15-50% for the examined structures, with DHSS predicted CCSs systematically larger than EHSS predicted CCSs. Also clear is that while the ratio $\Omega_{air}/\Omega_{calc}$ is roughly independent of *n* for DHSS calculations, this ratio decreases with increasing *n* for all cluster ions for the EHSS model. The constancy of DHSS $\Omega_{air}/\Omega_{calc}$ ratio suggests that it may indeed be the correct scattering model for all ions in spite of the observed disagreements with measurements; a simple linear rescaling of dimensions in DFT-determined structures would bring the $\Omega_{air}/\Omega_{calc}$ close to unity for all *n*. Conversely, a systematic rescaling of structure dimensions cannot lead to agreement between EHSS predictions and measured CCSs, as $\Omega_{air}/\Omega_{calc}$ varies with *n* for all cluster ion types,

always above 1.2 at small *n* and progressively decreasing as *n* increases. This result hence refutes the notion that specular-elastic scattering models can be applied to predict CCSs accurate for all structures and all gases.

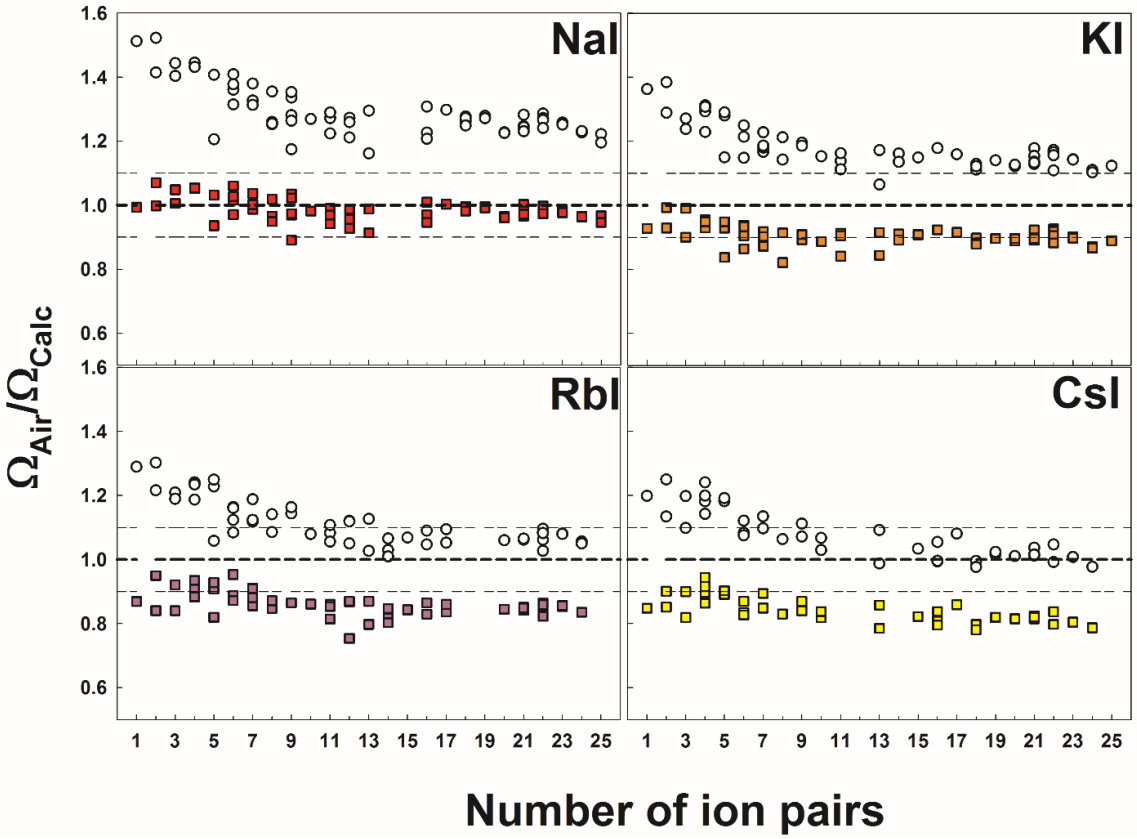

Figure 2.4 The ratio ($\Omega_{Air}/\Omega_{Calc}$) of DMA-MS measured CCS values in air to those calculated with EHSS (open circles) and DHSS (closed symbols) reemission rules as a function of the number of ion pairs in a cluster ion.

Without structure rescaling, which we note there is presently not ample evidence for and only remark upon it because of the constancy in the $\Omega_{air}/\Omega_{calc}$ ratio for DHSS calculations, another trend in the results is quite evident. As the cation mass in cluster ions decreases, DHSS calculations are in better agreement with measurements, while at larger cation mass EHSS calculations are in better agreement with measurements at large *n*. For example, for *NaI* clusters, DHSS calculated CCSs for at least one energy

minimum structure are within 5% of the measured CCS at all *n*, and are within 10% of measured values for all candidate structures. Meanwhile, doubly charged, larger *n RbI* and *CsI* cluster ion CCS measurements are in better agreement with EHSS predictions. Lastly, *KI* CCS measurements are underpredicted by the EHSS model and proportionally overpredicted by the DHSS model. In total, measurements do demonstrate that EHSS calculations cannot accurately predict CCSs in air for all ions, but at the same time they do not support universal use of DHSS models. This is in contrast to findings for the CCSs of organic ions in air, for which, to date, DHSS predictions have agreed well [51]. However, qualitatively, a similar result is found. In both cases it appears that when the gas molecule mass is close to or larger than the individual masses of a significant number of atoms within a polyatomic ion (e.g. the mass of diatomic nitrogen compared to the masses of sodium, carbon, or oxygen atoms), gas molecule impingement and reemission is diffuse and inelastic, while when the gas molecule mass is less than these atomic masses (e.g. the mass of helium compared to the masses of carbon and oxygen as well as the mass of diatomic nitrogen and oxygen compared to the mass of cesium), impingement and reemission appear less diffuse. These findings hence further highlight the need for continued fundamental study of the gas molecule impingement-reemission process from ion surfaces, as the two limiting models lead to evidently different CCS predictions in the nanometer size range, mitigating the ability with which IMS-MS can be used to infer ion structure.

Until gas molecule scattering models are improved upon, the most tractable approaches for relating ion structures to diatomic gas CCSs are likely those of Bush and coworkers [42,58], who have correlated diatomic nitrogen measured CCSs to those measured in helium bath gas, and of Fernandez de la Mora and coworkers, who, for ion structures that are near spherical, have estimated CCS based on an estimation of ion density [33,35,45]. However, both of these approaches require modification for sufficiently small sized or highly charged ions at room temperature or lower temperatures, i.e. when the polarization potential significantly influences the collision cross section. The influence of the

polarization potential on CCSs of salt cluster ions is displayed in Figure 2.5a, which is a plot of the ratio of the measured CCS to the orientationally averaged projected area (which are calculated for all DFT structures), Ω_{air}/PA, as a function of the dimensionless polarization energy to thermal energy ratio, Ψ_{pol}:

$$\Psi_{pol} = \frac{\pi \alpha_{pol} z^2 e^2}{8 \varepsilon_0 P A^2} \quad (5)$$

Wholly inelastic, diffuse scattering alone can only lead to CCS values ~40% larger than the orientationally averaged projected area [44,48], yet as Ψ_{pol} increases, Ω_{air}/PA exceeds 1.5, and approaches 2.0 at Ψ_{pol} = 1.0. The construction of a calibration curve linking CCSs measured in helium bath gas (which is minimally influenced by polarization) to CCSs measured in a polarizable gas under conditions such as these is not possible unless CCSs can be expressed as the product of the CCSs under hard sphere conditions and a dimensionless factor correcting for polarization influences, which would need to be applicable for ions of all shapes. Without expressing the CCS in this manner, a calibration curve relating CCSs in polarizable gases to CCSs in a nonpolarizable gas developed through measurement cannot be extrapolated to temperatures other than the calibration measurement temperature, and the charge state of an examined ion must be exactly equal to the charge state of an equivalent CCS ion used for calibration curve construction (i.e. calibration ions must have the same value of Ψ_{pol} as ions to which the calibration procedure is applied). Similarly, estimations of CCS based upon ion density would need to be corrected for polarization influences under these conditions.

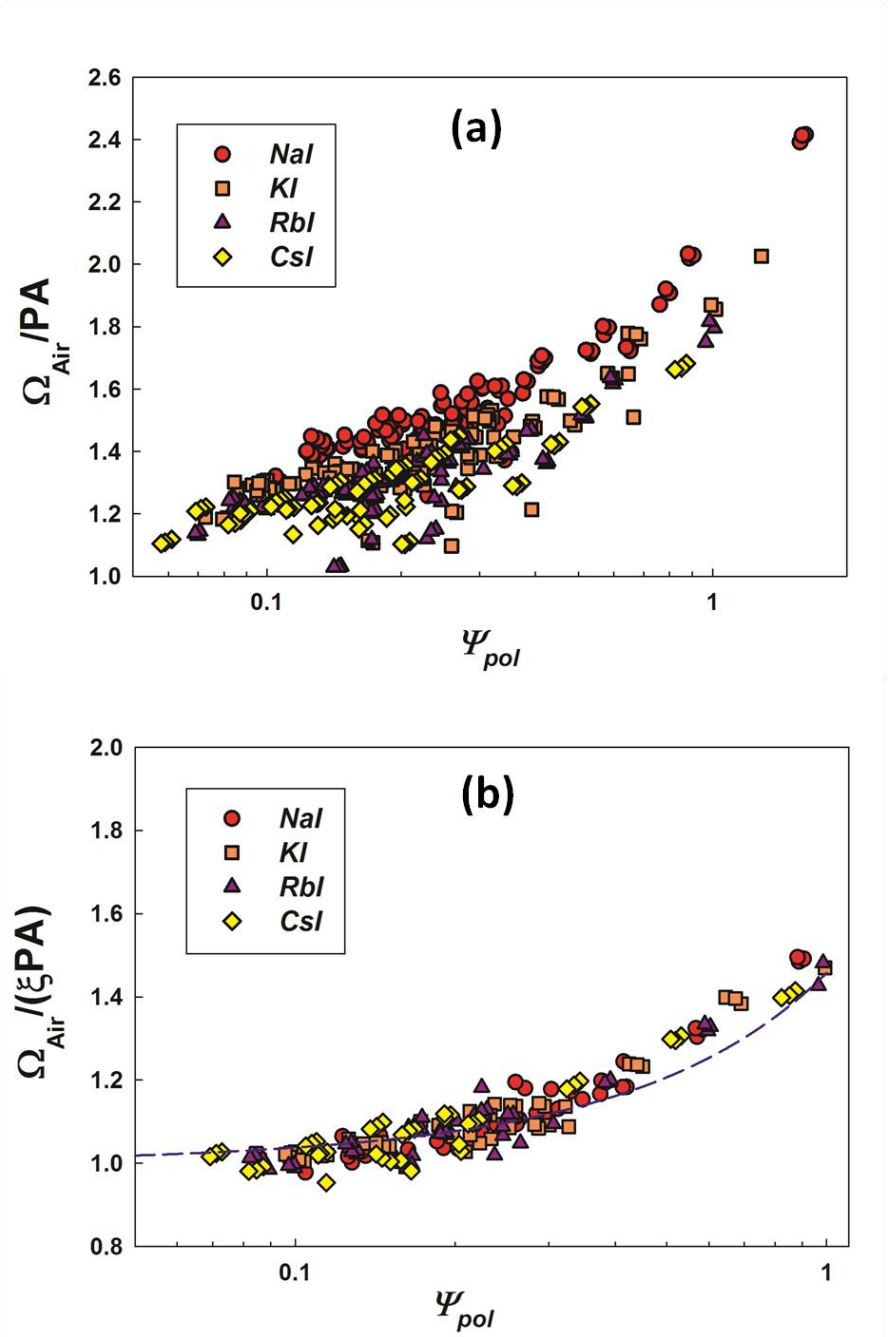

Figure 2.5 (a.) The ratio Ω_{air}/PA as a function of Ψ_{pol}, determined for singly and doubly charged salt clusters via DMA-MS measurements. **(b.)** The value of the polarization enhancement factor, $\mathcal{E} = \Omega_{air}/(\xi PA)$ as a function of Ψ_{pol}, where "best fit" values of ξ have been selected for each type of salt cluster. The guideline represents the expected

values of $\mathcal{L}$ for a sphere at ξ = 1.25 (solid). Plotted points correspond to ground state structures only.

A dimensionless polarization correction factor, $\mathcal{L}$, dependent on Ψ_{pol}, can be extracted from calculation results based on a sphere and compared to predicted values [48,51]. For extraction, we note that prior work [32,33,42,45,51,74,75] suggests the relationship $\Omega \approx \mathcal{L}\,\xi$PA can be used to simply approximate the CCS of an ion, where ξ is a dimensionless momentum scattering coefficient. This approximate relation is further supported by our measurements through the near constant value of $\Omega_{air}/\Omega_{calc}$ for DHSS calculations. However, unlike prior studies, in which the Stokes-Millikan value of ξ = 1.36 was either arrived at or assumed, different values of ξ appear to apply for different salt cluster species, evidenced by the variation in the $\Omega_{air}/\Omega_{calc}$ ratio for different cluster ions. Noting that the Stokes-Millikan value of ξ = 1.36 agrees well with measurements of *NaI* cluster, values of ξ for salt clusters can be found by plotting the value $\Omega_{air}/(1.36PA)$ for the *NaI* cluster ions (using the ground state structures only for PA calculation) as a function of Ψ_{pol} and fitting the data to a second order polynomial.

Subsequently, to find the "best fit" values of the momentum scattering coefficients, ξ for *KI*, *RbI*, and *CsI* clusters is stated as following. The momentum scattering coefficient for *NaI* is fixed as ξ_{Na} = 1.36 is the expected value from the Stokes-Millikan equation as well as from DHSS calculations, and for *NaI* cluster ions, matches experimental results well. The ratios of the experimental CCSs to the product of the momentum scattering coefficient and projected area, denoted as y_{Na} ($y_{Na}=\Omega_{air}/(\xi_{Na}PA)$), are calculated for all ground state structures of *NaI* clusters and using measurements at different temperatures. The function $f(\Psi_{pol}) = -0.1231\Psi_{\mathrm{pol}}^2 + 0.7348\Psi_{\mathrm{pol}} + 0.9345$ is found to fit all discrete values of y_{Na} with respect to the polarization potential Ψ_{pol}, with an R^2 equal to 0.97. This function is subsequently used to fit discrete values of y_K of ground state structures of *KI*; ξ_K is determined by finding the minimum value of the residual sum of squares, $RSS = \sum_{i=1}^{n}(y_K - f(\Psi_{pol}))^2$ (where n is the total number of

ground states of *KI* clusters for three different temperatures). Theoretically, $y_K = \mathcal{L} = a + b/\xi_K$ (equation 6 in the main text), hence $\frac{\partial(RSS)}{\partial(1/\xi_K)} = 2\sum_{i=1}^{n}(a_n + b_n/\xi_K - f(\Psi_{pol})) \cdot b_n$. Taking $\frac{\partial(RSS)}{\partial(1/\xi_K)} = 0$ leads to the minimum value of RSS and reveals ξ_K through the equation $1/\xi_K = \frac{\sum_{i=1}^{n}(f(\Psi_{pol})-a_n)b_n}{\sum_{i=1}^{n} b_n^2}$ (leading to ξ_K=1.272 based on our results). This procedure is similarly performed for *RbI* and *CsI* ground state structure clusters, revealing ξ_{Rb} = 1.2265 and ξ_{Cs}= 1.1887. In the end, the value of $\Omega_{air}/(\xi PA)$ as a function of Ψ_{pol} for the remaining salt cluster ions (again using only ground state structures) is collapsed to the regression equation for *NaI* ions by determination of the best fit ξ for each salt type. $\mathcal{L}=\Omega/(\xi PA)$ is plotted as a function of Ψ_{pol} in Figure 2.5b with these values of ξ. Also plotted is the function inferred for a sphere directly from scattering computations [48,51] at $\psi_{pol} < 1$:

$$\mathcal{L} \simeq 1 + \psi_{pol}\left(0.322 + \frac{1}{\xi}\left(0.0625 + 0.1212\psi_{pol}\right)\right) \quad (6)$$

Equation (6) is plotted with ξ = 1.25, an average value for all salt clusters. Strong agreement is found between the equation result and the results of measurements/calculations, suggesting that despite the non-spherical shapes of the examined cluster ions and the observed deviation from the Stokes-Millikan momentum scattering coefficient, $\Omega \approx \mathcal{L}\,\xi PA$ agrees well with measurements.

As has been performed in prior studies [45], the results of DMA-MS measurements were also compared to Stokes-Millikan based predictions under the assumption that salt cluster ions have densities (ρ) similar to bulk densities (though this is known to be inaccurate) and geometries close to spherical. These assumptions lead to the relationship:

$$\Omega = 1.36\mathcal{L}\pi\left(r_v + r_g\right)^2 \quad (7)$$

where r_v is the volume equivalent radius of the cluster ion: $r_v = [3m_{ion}/(4\pi\rho)]^{1/3}$ (m_{ion} is the ion mass). Unlike in prior work, the parameter $\mathcal{L}$ has been introduced into equation 7 in an effort to account for polarization influences (with $\mathcal{L}$ computed using equation 6 and

$\xi = 1.36$). Selecting bulk salt cluster densities at 300 K (3,670 kg $m^{-3}$for *NaI*, 3,120 kg m^{-3} for *KI*, 3,110 kg m^{-3} for *RbI*, and 4,510 kg m^{-3} for *CsI)*, ratio $\Omega_{air}/\Omega_{SM\text{-}POL}$, which is the DMA-MS measured CCS divided by the predicted CCS from equation 7, is shown as a function of the number of ion-pairs per cluster ion in Figure 2.6. In spite of the extreme simplifications involved with equation 7 implementation, the ratio $\Omega_{air}/\Omega_{SM\text{-}POL}$ is bounded between 0.9 and 1.1 for all salt ions except *NaI (*and several *RbI* clusters), indicating that the Stokes-Millikan equation, when modified to account for polarization, estimates CCS values as well as do many of the more detailed scattering procedures. The somewhat close agreement between equation (7) and measurements, however, appears to be due to a fortuitous cancellation of several effects: (a) cluster ions are not spheres, (b) except for *NaI* they appear to have differing values of ξ than 1.36, (c) their densities are not necessarily the bulk values, and (d) the manner in which polarization influences gas

molecule trajectories about them may not be entirely accounted for by equation (6).

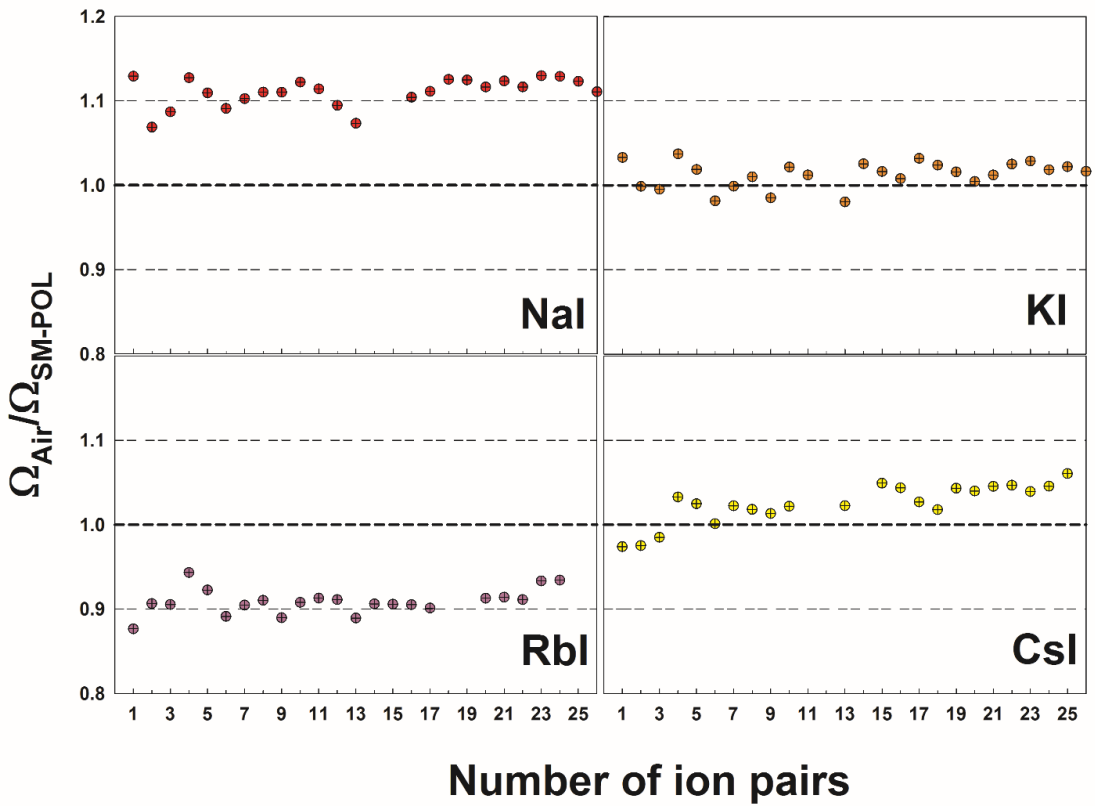

Figure 2.6 The ratio $\Omega_{air}/\Omega_{SM\text{-}POL}$ as a function of the number of ion pairs per cluster ion. $\Omega_{SM\text{-}POL}$ values were determined via equation (7), with bulk densities at 300 K assumed for each ion type.

Finally, while the measurements made do not make clear the precise manner in which diatomic gas molecules scattering from ion surfaces occur, they do demonstrate clearly that simple projection approximations cannot be used to estimate mobility, even with modest accuracy. Figure 2.7 displays plots of again the ratio $\Omega_{air}/\Omega_{calc}$ for DHSS calculations (closed circles) and also with Ω_{calc} treated as equivalent to the to the orientiationally averaged projected area (open triangles) of the cluster ions with gas molecules, both as functions of the number of ion-pairs in cluster ions. Ω_{air}/PA exceeds 1.3 in most circumstances, and exceeds 1.5 for the smallest ions. Such large

disagreement cannot be mitigated by resizing atoms within structures at any *n*, and at the smallest *n* values the CCS is strongly influenced by grazing gas molecule collisions, limiting the applicability of the PA method.

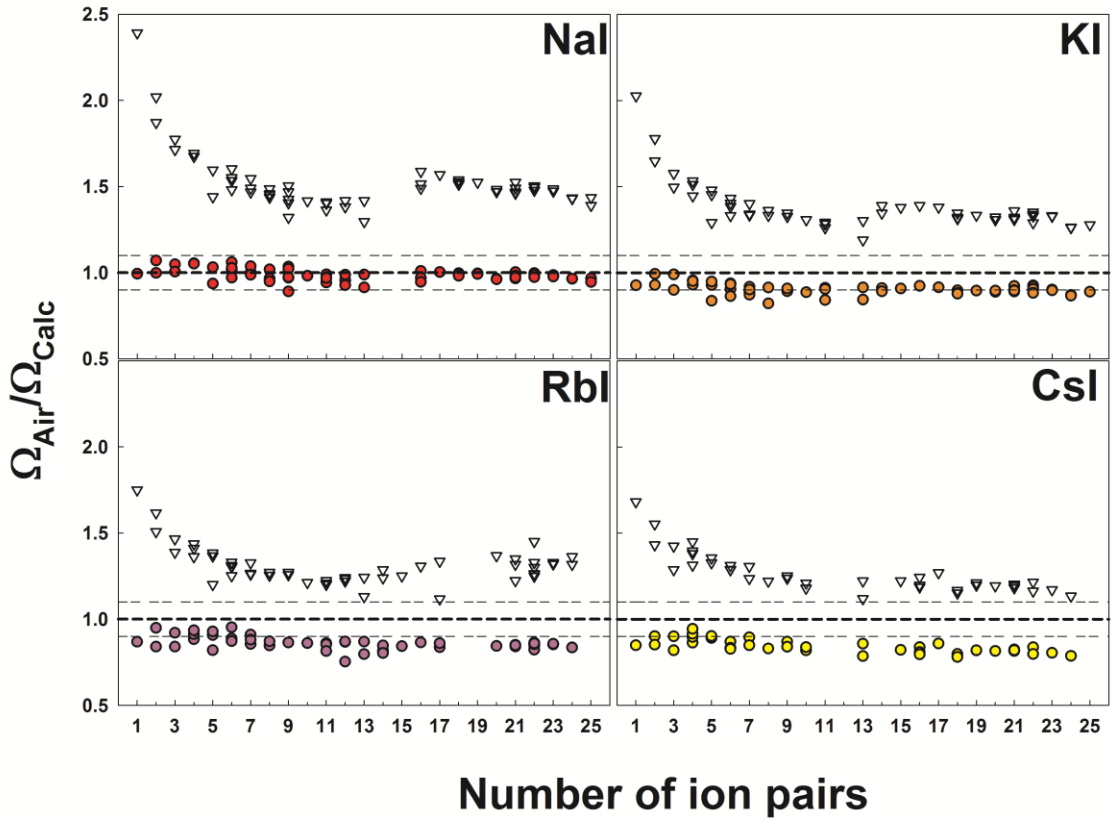

Figure 2.7 The ratio $\Omega_{Air}/\Omega_{Calc}$ of DMA-MS for DHSS calculations (closed circles) and the projection approximation (open triangles) as a function of the number of ion-pairs in each cluster.

2.4 Conclusions

The measurements and calculations performed for this work indicate that the gas molecule impingement-reemission process in polyatomic gases is yet ambiguous. Nonetheless, measurements reveal clearly that neither can gas molecule impingement-reemission rule be described as specular and elastic under all conditions, nor can CCSs be estimated from projection approximations in diatomic gases. Further, with the exception of *NaI* ions, the cluster ions measured are found to have CCSs which are overestimated

by DHSS scattering calculations with impingement-reemission rules designed to agree with prior measurements of organic ions. However, for each ion type, a near constant ratio $\Omega_{air}/\Omega_{calc}$ is obtained with DHSS scattering models, enabling determination of a value of ξ, the momentum scattering coefficient, for each cluster ion type, and demonstrating that the relationship $\Omega \approx \xi PA$ agrees well with measurements. This is in line with prior measurements in diatomic gases. While the inferred ξ values here do not agree with the Stokes-Millikan inferred value of $\xi = 1.36$, better convergence to this value would be brought about by linear rescaling of the determined local minimum structures. Overall, this study highlights the need to elucidate proper impingement-reemission laws for gas molecule scattering calculations if IMS-MS is to be of continued utility in quantitative structural characterization of gas phase ions in polyatomic gases.

Acknowledgements

This work was supported by NSF grant CHE-1011810. C. L. acknowledges support from the Ramon Areces Foundation and D. O. acknowledges support from a NSF Graduate Research Fellowship. We also thank the Minnesota Supercomputing Institute for providing the computational resources needed for density functional theory calculations.

Chapter 3: Nanoparticle Collisions in the Gas Phase in the Presence of Singular Contact Potentials

Abstract

Collisional growth and ionization is commonplace for gas phase nanoparticles (i.e. in aerosols). Because collisions involving nanoparticles in systems near atmospheric pressure occur in the mass transfer transition regime, and because attractive singular contact potentials (which arise when modeling nanoparticles as condensed matter and for which the potential energy approaches $-\infty$ when two entities contact) often have a non-negligible influence on gas phase collision processes, however, collision rate calculations for nanoparticles in the gas phase are not straightforward. We use mean first passage time calculations to develop a simple relationship for collision rate calculation in the gas phase, accounting for the influences of both the transition regime and singular contact potentials (specifically the non-retarded van der Waals and image potentials). In the presented analysis, methods to determine the degree of enhancement in collision rate due to attractive singular potentials in the continuum (diffusive) regime, η_C, and the degree of enhancement in the free molecular (ballistic) regime, η_{FM}, are first reviewed. Accounting for these enhancement factors, with mean first passage time calculations it is found that the collision rate for gas phase nanoparticles with other gas phase entities can be determined from a relationship between the dimensionless collision rate coefficient, H, and the diffusive Knudsen number, Kn_D, i.e. the ratio of the collision persistence distance to the collision length scale. This coincides with the $H(Kn_D)$ relationship found to appropriately describe collisions between entities interacting via a hard-sphere potential, but with η_C and η_{FM} incorporated into the definitions of both H and Kn_D, respectively. The $H(Kn_D)$ relationship is compared to the predictions of flux matching theory, used prevalently in prior work for collision rate calculation, and through this comparison it is found that at high potential energy to thermal energy ratios, flux matching theory predictions underestimate the true collision rate. Finally, a series of experimental

measurements of nanoparticle-nanoparticle collision rates are compared to the determined $H(Kn_D)$ expression, considering that nanoparticles interact via non-retarded van der Waals potentials. Very good agreement is found with collision rates inferred from experiments, with almost all measured values from four separate studies within 25% of model predictions

3.1 Introduction

The physicochemical properties of nanoparticles in the gas phase (aerosol nanoparticles) are largely governed by collisions [76]. For example, nanoparticle size distribution functions and chemical compositions are altered by nanoparticle-nanoparticle collisions and irreversible coalescence (coagulation), as well as by collisions and reversible coalescence with vapor molecules (condensation). The net charge on nanoparticles, as well, is controlled by collisions with gas phase ions and this further influences nanoparticle transport in aerosols. It is thus frequently necessary to study theoretically and numerically the collision rates (the number of collisions per unit volume per unit time) between nanoparticles and other nanoparticles, vapor molecules, and ions [77-87]. However, even under conditions where nanoparticles and other colliding entities may be approximated as perfect spheres, several complexities arise during collision rate calculation. First, the persistence distances of gas phase nanoparticles [21,88] (the characteristic ballistic distances traveled by nanoparticles due to thermal motion) fall within the 10-300 nm range in atmospheric pressure environments, similar in size to the radii of nanoparticles themselves. For this reason, nanoparticle collisions in the gas phase often occur within the mass transfer transition regime [21,88-92], wherein neither continuum (diffusive) nor free molecular (ballistic) transport kinetics can reliably predict collision rates. Second, although collisions are driven in large part by thermal motion, attractive potential interactions between colliding entities in the gas phase have a non-negligible influence on the collision rate under almost all circumstances [77,87,93,94]. Of particular concern are the impacts of singular contact potentials [80,95] which arise when modeling nanoparticles as condensed matter. These singular potentials, for which the

potential energy approaches -∞ when entities contact one another, include the van der Waals potential [82,83,96] present between all colliding entities, and the image potential [97] between net neutral nanoparticles and charged entities. In most prior examinations of nanoparticle collisions, either the transition regime nature of the collision process or the effects of singular potentials are accounted for, but with few notable exceptions [77,82,84,85,93,98,99], the simultaneous consideration of both of these factors is not commonplace.

Compounding these concerns, recent studies [88,92,100] have suggested that the most prevalently used approach to examine collisions in the transition regime, the flux matching theory of Fuchs [76,101], leads to incorrect collision rate predictions when non-hard sphere interactions are considered. Therefore, at present, a clear method for gas phase nanoparticle collision rate calculation is not established. In this work, we develop a simple and accurate method to calculate the collision rate for gas-phase nanoparticles in the mass transfer transition regime, accounting for singular contact potentials. In doing so we employ a combination of dimensional analysis and mean first passage time simulations, an approach which has proven successful in developing collision rate expressions for both spherical [21] and non-spherical [90,102] entities in the transition regime, as well as for entities interacting via a Coulombic potential [88]. While we specifically examine collisions between entities interacting via the non-retarded van der Waals potential and the image potential, we propose that the expression developed here can be applied to collision rate calculation for entities interacting via any potential which is sufficiently short range in nature [87,94]. The predictions of this collision rate expression are compared to the predictions of flux matching theory[101], revealing the shortcomings of flux matching theory when attractive potential energy is present, and to experimental measurements of aerosol nanoparticle collision rates [89,103-105].

3.2 Theoretical Approach

3.2.1 Collisions in the Continuum and Free Molecular Regimes

Except in rare circumstances, the concentration of nanoparticles in gas phase systems is low and the dilute approximation applies. The collision rate (R_{ij}) between entities of type *i* and type *j* can thus be expressed as:

$$R_{ij} = \beta_{ij} n_i n_j \tag{1}$$

where n_i and n_j are the number concentrations of type *i* and type *j* entities, respectively, and β_{ij} is the collision rate coefficient (collision kernel), which must be determined properly to account for the influences of both the transition regime and singular contact potentials. We focus on the latter first, restricting analysis to the continuum and free molecular limits. In the continuum limit, the collision kernel for two spherical particles with radii a_i and a_j and friction factors f_i and f_j, respectively, can be expressed as [76]:

$$\beta_{ij} = 4\pi \frac{kT}{f_{ij}} \left(a_i + a_j\right) \eta_C \tag{2a}$$

where *T* is the system temperature (assumed to be in thermal equilibrium), *k* is Boltzmann's constant, and f_{ij}, the reduced friction factor, is given by the equation:

$$f_{ij} = \frac{f_i f_j}{f_i + f_j} \tag{2b}$$

η_C in equation (2a) is the continuum regime enhancement factor, defined as the factor increase or decrease in the collision rate due to a radially-varying potential interaction between colliding entities, $\phi(r)$ (where *r* is the scalar difference between the centers of the entities). A general expression for the this enhancement factor is given by Fuchs [76]:

$$\eta_C = \left[\int_1^\infty \exp\left(\frac{\phi\left(r^*\right)}{kT} \right) r^{*-2} dr^* \right]^{-1} \tag{3}$$

where $r^* = r/(a_i+a_j)$. For the non-retarded van der Waals potential, $\phi(r^*)$ is expressed as:

$$\frac{\phi(r^*)}{kT} = -\frac{\psi_{VDW}}{6}\left(\frac{2\omega(1-\omega)}{r^{*2}-1} + \frac{2\omega(1-\omega)}{r^{*2}-(2\omega-1)^2} + \ln\left[\frac{r^{*2}-1}{r^{*2}-(2\omega-1)^2}\right]\right) \quad (4a)$$

where $\Psi_{VDW} = A/(kT)$ is the dimensionless van der Waals energy (A is the material dependent Hamaker constant) and ω is the ratio $a_i/(a_i+a_j)$. As noted in the introduction section, this potential energy is present between all colliding entities in the gas phase, and in the absence of net charge it is the dominant form of potential energy influencing collisions (though there is recent evidence that for nanoparticles with strong dipole moments, the dipole-dipole attractive potential may have a stronger influence than the van der Waals potential [87,94]). Conversely, the image potential is frequently the dominant form of potential energy in collisions between net neutral particles and ions, where the approximation that the ion is a point mass applies (i.e. $a_j = 0$). In this instance $\phi(r^*)$ is given by the expression:

$$\frac{\phi(r^*)}{kT} = -\frac{\psi_I}{2r^{*2}\left(r^{*2}-1\right)} \quad (4b)$$

In equation (4b), Ψ_I is the dimensionless image potential energy, expressed as:

$$\psi_I = \left(\frac{\varepsilon_p - 1}{\varepsilon_p - 2}\right)\frac{e^2}{4\pi\varepsilon_0 kTa_i} \quad (4c)$$

where ε_p is the particle dielectric constant, e is the unit electron charge, and ε_0 is the permittivity of free space. While with equations (4a) and (4b), $\phi(1) \rightarrow -\infty$, the integral in equation (3) still converges for these potential functions, enabling calculation of η_C. For $\omega = 0.5$ (equal sized colliding particles) Figure 3.1a shows η_C in the range $0 < \Psi_{VDW} < 300$ and $0 < \Psi_I < 300$ as determined with integration using both equations (4a) and (4b), respectively. Tables displaying η_C values for both the van der Waals and image potential (at various Ψ_{VDW} and $\omega = 0.5$ for the van der Waals potential and at various Ψ_I for the image potential, respectively) are given in the Appendix A[106106106], as are regression equations to approximately determine η_C. $\eta_C > 1$ indicates that the presence of both

potentials enhances the rate of coagulation, as expected as both potentials are monotonically attractive.

The continuum limit expression for the collision rate, however, only applies when sum of the radii of the colliding entities is substantially larger than the collision persistence distance [88,90,102], as is the case in colloidal suspensions. In the opposite limit, the free molecular limit, colliding entities migrate with purely ballistic motion until collision, and the collision kernel is given by the expression [106,107]:

$$\beta_{ij} = \sqrt{\frac{8\pi kT}{m_{ij}}}\left(a_i + a_j\right)^2 \eta_{FM} \tag{5a}$$

where m_{ij} is the reduced mass, given by the equation:

$$m_{ij} = \frac{m_i m_j}{m_i + m_j} \tag{5b}$$

with m_i and m_j the masses of entities i and j, respectively. Comparable to η_C, η_{FM} is the free molecular enhancement factor. Regardless of the functional form of the potential, under conditions of thermal equilibrium (Maxwell-Boltzmann distributed kinetic energies), η_{FM} can be calculated from the equation:

$$\eta_{FM} = 2\int_0^\infty e^{-\nu^2}\nu^3 b_{crit}{}^2(\nu)d\nu \tag{6a}$$

where $b_{crit}(\nu)$ is the dimensionless critical impact parameter [107,108] (normalized by a_i+a_j) for collision between two entities, which depends upon the dimensionless speed, ν (normalized by $[2kT/m_{ij}]^{1/2}$). For non-singular (bounded) attractive potentials, determination of $b_{crit}(\nu)$ is rather straightforward [106]. However, for singular contact potentials, conflicting methods have been proposed either to determine $b_{crit}(\nu)$ or to find η_{FM}. Here, we propose that $b_{crit}(\nu)$ can be determined with the method described subsequently, and we compare this method to three existing approaches for η_{FM} calculation. For two entities approaching one another with dimensionless speed ν at dimensionless impact parameter b and interacting via attractive a potential function $\phi(r^*)$,

there are only two possible outcomes: either these entities collide, or they do not contact one another. In instances where collision does not occur, there exists a (dimensionless) distance of closest approach for these two entities, r_{min}. By conservation of energy and angular momentum, the following relationship defines r_{min}:

$$b = r_{\min}\sqrt{1+\frac{|\phi(r_{\min})|}{kT\nu^2}} \tag{6b}$$

If equation (6b) reveals an $r_{min} > 1$ for a given ν, b, and $\phi(r^*)$, then $b \geq b_{crit}(\nu)$ and collision does indeed not occur under these conditions. However, if $r_{min} < 1$ or a real r_{min} cannot be found, then collision must occur with the set of b, ν, and $\phi(r^*)$, and $b < b_{crit}(\nu)$ (i.e. a non-collision event does not occur). Therefore, $b_{crit}(\nu)$ can be found by determining r_{min} for a number of varying b; $b_{crit}(\nu)$ is taken to be the smallest value of b at and above which r_{min} is found to be a real number > 1, and below which r_{min} is a complex number or is a real number < 1.

For monotonically attractive potentials, $b_{crit}(\nu) \geq 1$ always holds valid. This calculation procedure is a more general form of the method applied by Fuchs & Sutugin [89], who found $b_{crit}(\nu)$ identically, but rather than apply this relationship in equation (6a), neglected the distribution of speeds between colliding entities and assumed that entities approach each other at identical relative speeds during all collisions. With this simplification, the free molecular enhancement factor from Fuchs & Sutugin, η^{FS}_{FM} is expressed as:

$$\eta^{FS}_{FM} = b_{crit}{}^2\left(\sqrt{\frac{3}{2}}\right) \tag{6c}$$

Alternative to both equation (6a) and equation (6c), Marlow and coworkers [78,79,95] have developed methods for η_{FM} calculation for both singular and non-singular contact potentials, which have been applied in a number of prior studies [84,86,109]. For singular potentials this expression for the enhancement factor, η^{M}_{FM}, is given as [80,84,109]:

$$\eta_{FM}^{M} = \frac{1}{2kT}\int_{1}^{0} r^{*2}\,\frac{d}{d\left(\frac{1}{r^*}\right)}\left(\frac{1}{r^*}\frac{d\phi\left(r^*\right)}{d\left(\frac{1}{r^*}\right)}\right)\exp\left[\frac{1}{2r^*}\frac{d\phi\left(r^*\right)}{d\left(\frac{1}{r^*}\right)}-\phi\left(r^*\right)\right]d\left(\frac{1}{r^*}\right) \qquad (6d)$$

Despite the fact that equation (6d) is derived accounting for the initial distribution of colliding entity kinetic energies (unlike the Fuchs-Sutugin method) [79], there is some concern with its use based on the results of prior studies. Ravi and Girshick [86] report that the enhancement factor from an analogous equation to (6d) for non-singular potentials considering a neutral nanoparticle and a charged nanoparticle (using the modified image potential from Huang et al [84]) is higher in some circumstances than the enhancement factor for two coulombically interacting, oppositely charged particles, which is calculated using the traditional orbital motion approach [106]. This suggests that equation (6d) and its analog overestimate the free molecular enhancement factor; the collision rate for entities attracting one another via a sufficiently strong long range potential, such as the Coulomb potential, should be considerably larger than the collision rate for attracting one another via a short range potential (e.g. the image potential). In addition, in examining the non-retarded van der Waals potential, Zhang et al [87] find that equation (6d) predictions are larger than free molecular enhancement factors inferred from trajectory calculations. A final distinct method of free molecular enhancement factor calculation is given by Sceats [77] (η^{S}_{FM}), which leads to the equations:

$$\eta_{FM}^{S} = \Lambda^2 \exp\left[-\frac{\phi(\Lambda)}{kT}\right]; \qquad \frac{\Lambda}{2}\frac{d\phi\left(r^*\right)}{dr^*}\bigg|_{r^*=\Lambda} = kT \qquad (6e)$$

Equations (6a), (6c), (6d), and (6e) determined enhancement factors are plotted in figures 3.1b and 3.1c for the van der Waals potential (ω = 0.5) and the image potential, respectively. Tables and regression equations for η_{FM} calculated from equation (6a) are further shown in the Appendix A. As expected from the results of prior work, the enhancement factor determined with equation (6d) is considerably larger than enhancement factors determined with alternative approaches in all circumstances. The

approach of Sceats [77] (equation 6e) also leads to enhancement factors larger than those from equation (6a) and (6c), which only differ from one another slightly. In total, these calculations indicate there is a need to independently determine collision rates and enhancement factors in the free molecular regime, as currently available methods lead to highly variable results.

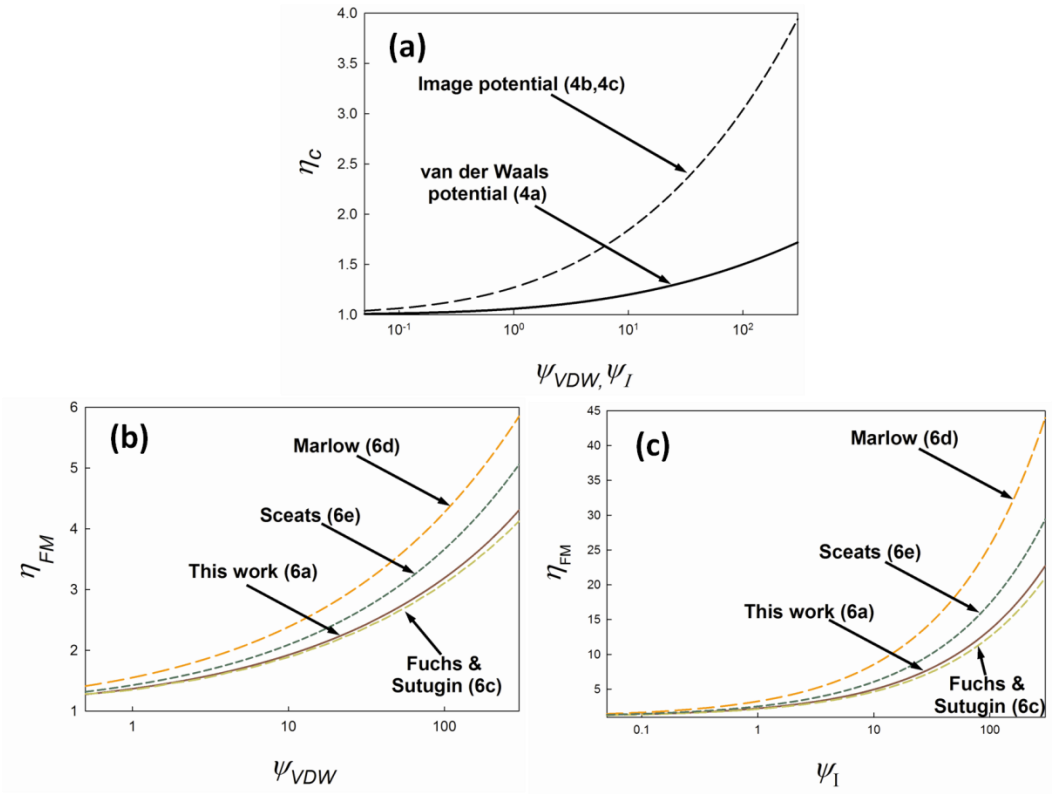

Figure 3.1 (a) The continuum enhancement factors for both the van der Waals and image potentials as functions of Ψ_{VDW} ($\omega = 0.5$) and Ψ_I, respectively. (**b.**) The free molecular enhancement factor for the van der Waals potential as a function of Ψ_{VDW} ($\omega = 0.5$). (**c.**) The free molecular enhancement factor for the image potential as a function of Ψ_I. Free molecular enhancement factors are calculated through the four approaches noted in the main text.

3.2.2 Collisions in the Transition Regime

Calculation of the collision kernel in the transition regime is less straightforward than are calculations in the continuum and free molecular limits. We thus use dimensional analysis to find appropriate parameters for description of the transition regime collision kernel. Following the arguments of Gopalakrishnan and Hogan [88], a dimensionless form of the collision kernel can be expressed as:

$$H = \frac{\beta m_{ij} \eta_C}{f_{ij}\left(a_i + a_j\right)^3 \left(\eta_{FM}\right)^2} \tag{7a}$$

and a ratio of the collision persistence distance to collision size, i.e. the diffusive Knudsen number, Kn_D, is given as:

$$Kn_D = \frac{\sqrt{kTm_{ij}}\,\eta_C}{f_{ij}\left(a_i + a_j\right)\eta_{FM}} \tag{7b}$$

When $Kn_D \rightarrow 0$, the continuum limit expression applies, and conversely as $Kn_D \rightarrow \infty$, collisions occur in the free molecular limit. Therefore, with equations (2a) and (5a) as valid dimensional equations, dimensionlessly it is found that:

$$H = 4\pi Kn_D^2 \qquad \text{as } Kn_D \rightarrow 0 \tag{7c}$$

$$H = \sqrt{8\pi}\, Kn_D \qquad \text{as } Kn_D \rightarrow \infty \tag{7d}$$

In the intermediate Kn_D range, for collisions between both spherical and non-spherical particles in the absence of potential energy (for which $\eta_C = \eta_{FM} = 1$), prior mean first passage time calculations [21,88,90,102] reveal that the $H(Kn_D)$ can be described by the equation:

$$H = \frac{4\pi Kn_D^2 + C_1 Kn_D^3 + \sqrt{8\pi} C_2 Kn_D^4}{1 + C_3 Kn_D + C_4 Kn_D^2 + C_2 Kn_D^3} \tag{7e}$$

where C_1 =25.836, C_2 = 11.211, C_3 = 3.502, and C_4 = 7.211. Equation (7e) converges to equations (7c) and (7d) in the $Kn_D \rightarrow 0$ and $Kn_D \rightarrow \infty$ limits, respectively, and is in excellent agreement with expressions arising from alternative analyses [76,110] of collisions between spherical entities. For collisions in the presence of repulsive Coulombic

potential energy, mean first passage time calculations also agree well with equation (7e) [88]. However, in the presence of attractive Coulombic potential energy, the validity of equation (7e) is found to break down when the ratio of the potential energy to thermal energy at collision becomes sufficiently large. With singular contact potentials, the ratio of potential energy to thermal energy at contact is infinite under all circumstances; thus, there is a clear need to compare equation (7e) to mean first passage time calculations performed in the presence of singular contact potential energy.

The mean first passage time approach employed here derives originally from the work of Narsimhan & Ruckenstein [93,99], with details on these calculations provided in our earlier studies [21,88,90,102]. Briefly, to initiate calculations, a motionless, spherical collector of dimensionless radius 1 is placed in the center of a cubical simulation domain (with a side length of 50-100). A point mass is placed at a random location on the surface of the domain, and its motion within the domain is monitored via a dimensionless form of the Ermak & Buckholtz solution to the Langevin equation[111].

With $\vec{v}$ and $\vec{r}$ defined as the velocity and position vectors of the point mass, respectively, and with $\vec{v}^{*} = \dfrac{m_{ij}\vec{v}}{f_{ij}\left(a_i + a_j\right)}$ as well as $\vec{r}^{*} = \dfrac{\vec{r}}{\left(a_i + a_j\right)}$, the solution of the Langevin equation for the point mass in the presence of van der Waals potentials can be written dimensionlessly as[111]:

$$\vec{v}^{*}\left(\tau+\Delta\tau\right) = \vec{v}^{*}\left(\tau\right)\exp\left(-\Delta\tau\right) - \psi_{VDW}\,\mathrm{F}^{*}_{\mathrm{VDW}}\left[\mathrm{r}^{*},\omega\right]\mathrm{Kn}_{\mathrm{D}}^{2}\,\frac{\eta_{FM}^{2}}{\eta_{C}^{2}}\left(1-\exp\left(-\Delta\tau\right)\right)\hat{r} + \vec{A}_1 \qquad (8a)$$

$$\vec{r}^{*}\left(\tau+\Delta\tau\right) = \vec{r}^{*}\left(\tau\right) + \left(\vec{v}^{*}\left(\tau+\Delta\tau\right) + \vec{v}^{*}\left(\tau\right) + 2\psi_{VDW}\,\mathrm{F}^{*}_{\mathrm{VDW}}\left[\mathrm{r}^{*},\omega\right]\mathrm{Kn}_{\mathrm{D}}^{2}\,\frac{\eta_{FM}^{2}}{\eta_{C}^{2}}\hat{r}\right)\left(\frac{1-\exp\left(-\Delta\tau\right)}{1+\exp\left(-\Delta\tau\right)}\right)$$

$$-\psi_{VDW}\,\mathrm{F}^{*}_{\mathrm{VDW}}\left[\mathrm{r}^{*},\omega\right]\mathrm{Kn}_{\mathrm{D}}^{2}\,\frac{\eta_{FM}^{2}}{\eta_{C}^{2}}\hat{r}\,\Delta\tau + \vec{A}_2 \qquad (8b)$$

where τ is the nondimensionalized time ($\tau = (f_{ij}/m_{ij})t$) and $\Delta\tau$ is small change in τ; thus $\vec{v}^{*}\left(\tau+\Delta\tau\right)$, $\vec{x}^{*}\left(\tau+\Delta\tau\right)$, $\vec{v}^{*}\left(\tau\right)$, and $\vec{x}^{*}\left(\tau\right)$ denote the point mass dimensionless velocities

and positions at dimensionless times τ and $\tau + \Delta\tau$,respectively. The vector $\hat{r}$ and the scalar r^* denote a unit vector in radial direction and the dimensionless distance of the point mass from the origin in the simulation domain, respectively. $\vec{A}_1$ and $\vec{A}_2$ are both Gaussian distributed random vectors with zero mean and variances given in equations (A1c) and (A1d), respectively:

$$\left\langle \vec{A}_1^{\,2} \right\rangle = 3\mathrm{Kn}_\mathrm{D}^2 \frac{\eta_{FM}^2}{\eta_C^2}\left(1-\exp\left(-2\Delta\tau\right)\right) \tag{8c}$$

$$\left\langle \vec{A}_2^{\,2} \right\rangle = 6\mathrm{Kn}_\mathrm{D}^2 \frac{\eta_{FM}^2}{\eta_C^2}\left(\Delta\tau - 2\left(\frac{1-\exp\left(-\Delta\tau\right)}{1+\exp\left(-\Delta\tau\right)}\right)\right) \tag{8d}$$

Finally, F^*_{VDW} is the dimensionless van der Waals force between colliding entities, which is expressed as:

$$\mathrm{F}^*_{\mathrm{VDW}}\left[\mathrm{r}^*,\omega\right] = \frac{1}{6}\left[\frac{4\omega(1-\omega)r^*}{\left(r^{*2}-1\right)^2} + \frac{4\omega(1-\omega)r^*}{\left(r^{*2}-\left(2\omega-1\right)^2\right)^2} - \frac{8\omega(1-\omega)r^*}{\left(r^{*2}-1\right)\left(r^{*2}-\left(2\omega-1\right)^2\right)}\right] \tag{8e}$$

For the image potential, the dimensionless equations of motion of are similarly expressed as:

$$\vec{v}^*(\tau+\Delta\tau) = \vec{v}^*(\tau)\exp\left(-\Delta\tau\right) - \psi_I \mathrm{F}_\mathrm{I}^*\left[\mathrm{r}^*\right]\mathrm{Kn}_\mathrm{D}^2 \frac{\eta_{FM}^2}{\eta_C^2}\left(1-\exp\left(-\Delta\tau\right)\right)\hat{r} + \vec{A}_1 \tag{9a}$$

$$\vec{r}^*(\tau+\Delta\tau) = \vec{r}^*(\tau) + \left(\vec{v}^*(\tau+\Delta\tau) + \vec{v}^*(\tau) + 2\psi_I \mathrm{F}_\mathrm{I}^*\left[\mathrm{r}^*\right]\mathrm{Kn}_\mathrm{D}^2 \frac{\eta_{FM}^2}{\eta_C^2}\hat{r}\right)\left(\frac{1-\exp\left(-\Delta\tau\right)}{1+\exp\left(-\Delta\tau\right)}\right)$$

$$-\psi_I \mathrm{F}_\mathrm{I}^*\left[\mathrm{r}^*\right]\mathrm{Kn}_\mathrm{D}^2 \frac{\eta_{FM}^2}{\eta_C^2}\hat{r}\,\Delta\tau + \vec{A}_2 \tag{9b}$$

and the dimensionless image force, F^*_I is expressed as:

$$\mathrm{F}_\mathrm{I}^*\left[\mathrm{r}^*\right] = \frac{\left(2r^{*2}-1\right)}{\left(r^{*2}-1\right)^2 r^{*3}} \tag{9c}$$

Periodic boundary conditions are employed on the simulation domain surface. Motion is influenced by the point mass's inertia, diffusion, and if present, the external forces arising from a potential energy field. As noted by Gopalakrishnan & Hogan [88], to

account for these processes the only required inputs for each calculation are a dimensionless time step, Kn_D, and dimensionless parameters describing the potential function (Ψ_{VDW} and ω =0.5 for the van der Waals potential energy and Ψ_I for the image potential energy). In this study the dimensionless time step used is $0.005(r^*/Kn_D)^2$, where r^* is the scalar distance from the point mass location to the center of the simulation domain. Motion is monitored until the point mass collides with the central collector, at which point the dimensionless time required for this collision, τ_i, is recorded, and the process is repeated. After 5,000-15,000 collisions have been monitored in this manner, the dimensionless collision kernel is determined with the equation:

$$H = \frac{s^3 \eta_C}{\left(\eta_{FM}\right)^2 \sum_{i=1}^{n} \tau_i} \tag{10}$$

where s is the simulation domain side length, n is the total number of collisions monitored, and η_C and η_{FM} are calculated using the prescribed Ψ_{VDW} and ω (van der Waals potential) or Ψ_I (image potential).

With the use of a Langevin equation, an implicit assumption made is that the mass of both entities is significantly greater than the mass of the surrounding gas molecules. This assumption is reasonable in aerosols, and comparison of Langevin equation based calculations [21] to a solution to the Boltzmann equation for collisions under conditions where the moving entity is massless [112] reveals that influence of gas molecule mass on collision processes is small. The simplification of the system to two entities, one a collector and the other a moving point mass, also places several restrictions on our results. First, as discussed by Veshchunov [92,113], our results describe collisions occurring in the dilute kinetic regime, i.e. between each collision, there is ample time for gas phase entities to redistribute themselves uniformly prior to the occurrence of subsequent collisions. While this is in contrast with the diffusion regime, wherein concentration gradients of smaller entities surround larger entities and which is usually examined in the continuum regime, the collision kernel in the kinetic and diffusion regimes coincide for

three dimensional processes [91,92]. Second, the use of a single equation to monitor the relative motion between two entities restricts results to conditions where $\theta_f = f_i/(f_i+f_j)$ and $\theta_m = m_i/(m_i+m_j)$ are equivalent. Nonetheless, our results apply exactly for colliding entities of disparate sizes ($\theta_f = \theta_m = 0$) as well as for equal sized colliding entities ($\theta_f = \theta_m = 0.5$), and are approximately valid in most realistic circumstances [21].

3.3 Results and Discussion

3.3.1 Mean First Passage Time Calculations

Mean first passage time calculations are performed at various Kn_D in the 0.001-15 range. For the van der Waals potential, Ψ_{VDW} is varied from 0.3 to 300 at $\omega = 0.5$, and for the image potential Ψ_I is also varied from 0.3 to 300. This range for both potential energy to thermal energy ratios spans the values encountered for nanoparticles in systems at $T > 300$ K. Calculated $H(Kn_D)$ values accounting for van der Waals and image potentials are shown in Figures 3.2a and 3.2b, respectively. η_{FM} is calculated with equations (6a) and (6b) for all displayed results. Also displayed in both plots are curves corresponding to the continuum limit (equation (7c)), the free molecular limit (equation (7d)), and equation (7e), the $H(Kn_D)$ relationship found from prior mean first passage time calculations. For all examined Ψ_{VDW}, Ψ_I, and Kn_D, mean first passage time calculated $H(Kn_D)$ values agree well with the continuum and free molecular limit expressions at low and high Kn_D, respectively. Furthermore, with few exceptions, across the entire Kn_D range they are within 5% of the predictions of equation (7e). These results thus indicate that the influence of singular contact potentials is accounted for entirely by the incorporation of η_C and η_{FM} into the definitions of both H and Kn_D, and vastly simplifies calculation of the collision kernel accounting for singular contact potentials in the transition regime. This is in contrast to results found for the attractive Coulomb potential [88,100,114], and suggests that the reason the $H(Kn_D)$ relationship breaks down for the Coulomb potential is related to the long range nature of this potential, as opposed to

ratio of the potential energy to thermal energy at contact. For most sufficiently short ranged potentials (e.g. dipole-dipole potentials [87,94]), both singular and non-singular, we suggest that the $H(Kn_D)$ relationship examined here will hold valid.

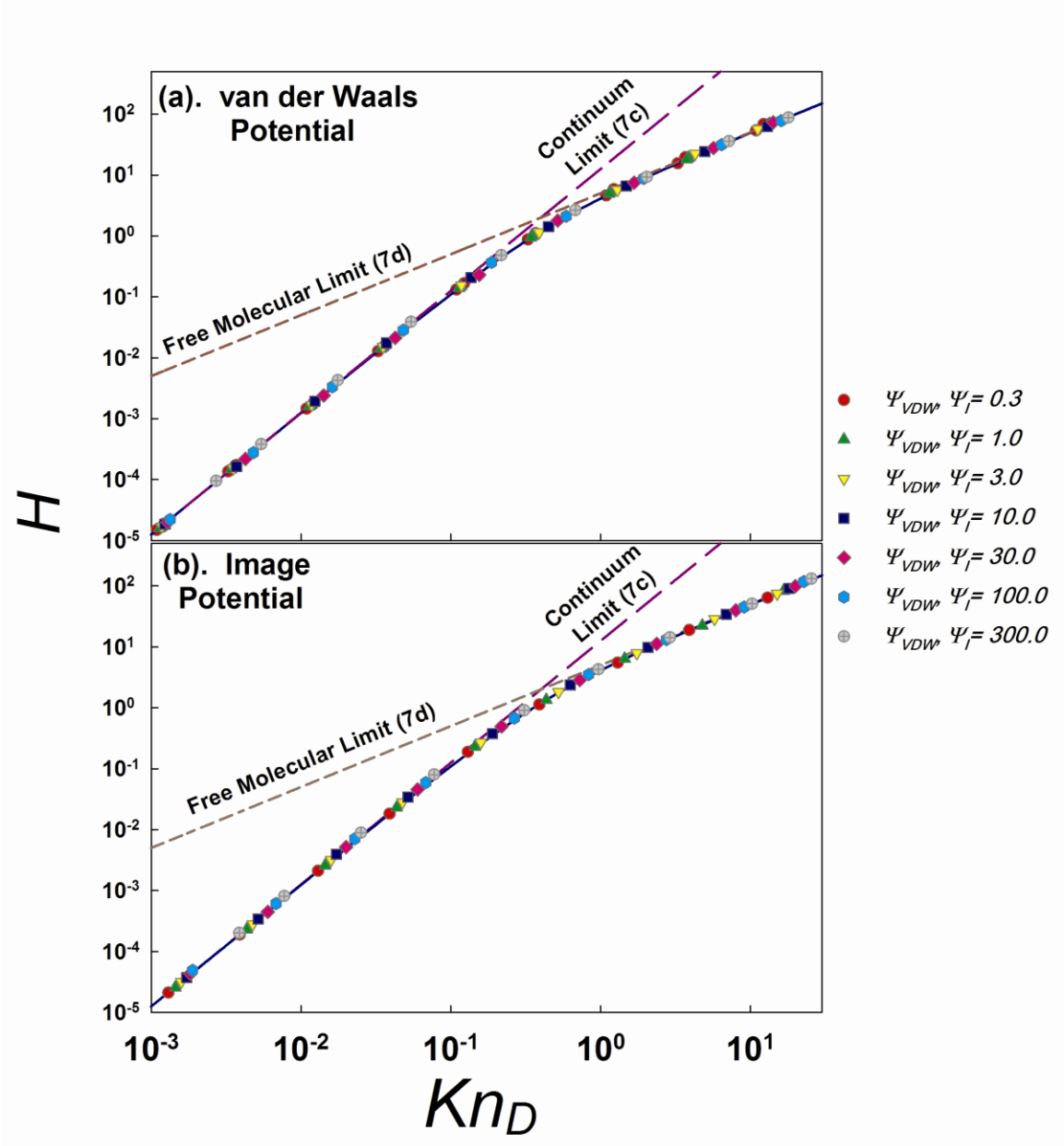

Figure 3.2 Mean first passage time calculated H(KnD) values for **(a.)** the van der Waals potential (ω = 0.5) and **(b.)** the image potential at various potential energy to thermal energy ratios. Also shown are the expected curves in the continuum limit (long dash),

free molecular limit (short dash), and the previously determined regression expression (equation 7e, solid blue line).

Also important to note is that the definition of Kn_D utilized depends upon both η_C and η_{FM}. For both potentials examined, $\eta_{FM} > \eta_C$ in all circumstances, with the ratio η_{FM}/η_C increasing with increasing Ψ_{VDW} and Ψ_I. Therefore, these potentials effectively reduce Kn_D, and collisions expected to occur in the free molecular regime in the absence of potentials do indeed occur in the transition regime when potential energy is present. For example, in the absence of potentials, Kn_D for the collision of two 5 nm radius particles with densities of $4000\ kg\ m^{-3}$ at atmospheric pressure and room temperature is 5.5. However, in the presence of van der Waals potentials at $\Psi_{VDW} = 30$, Kn_D is shifted to 3.0, and if one of these particles has a single excess charge with $\Psi_I = 5.56$, Kn_D is shifted to 2.3. While the original hard sphere-calculated Kn_D suggests the collision of these two particles is a free molecular process, the shifts in Kn_D brought about by potentials indicate that free molecular kinetics cannot be invoked to model this collision [102].

3.3.2 The Free Molecular Enhancement Factor

The results of mean first passage time calculations are independent of the chosen form for the free molecular enhancement factor; η_{FM} is simply used for nondimensionalization and does not naturally appear in the solution to the Langevin equation. Therefore, mean first passage time calculations enable us to examine the validity of the noted η_{FM} calculation procedures. That the $H(Kn_D)$ values agree well with equation (7d) as $Kn_D \rightarrow \infty$ when equations (6a) and (6b) are utilized suggests that these equations are indeed appropriate for evaluating η_{FM}. Moreover, the deviation which arises when other forms of η_{FM} are employed is made apparent with the same calculation results. If the result $H^1(Kn^1_D)$ is found with η^1_{FM} used for nondimensionalization, then with η^2_{FM} used in nondimensionalization, $H^2(Kn^2_D)$ can be determined from $H^1(Kn^1_D)$ with the equations:

$$H^2 = H^1 \left(\frac{\eta^1_{FM}}{\eta^2_{FM}} \right)^2 \tag{11a}$$

$$Kn^2_D = Kn^1_D \frac{\eta^1_{FM}}{\eta^2_{FM}} \tag{11b}$$

Figures 3.3a (van der Waals potential) and 3b (image potential) show the values of $(H-H_{7e})/H_{7e}$ as a function of Kn_D (where H_{7e} is the H calculated from equation 7e) for H and Kn_D from mean first passage time calculations and with varying calculation procedures for η_{FM}. While with equations (6a) and (6b) defining η_{FM}, the value $(H-H_{7e})/H_{7e}$ oscillates close to zero, the use of equations (6c) (η^{FS}_{FM}), (6e) (η^{S}_{FM}), and (6d) (η^{M}_{FM}), lead to progressively larger absolute values of $(H-H_{7e})/H_{7e}$ at all displayed Kn_D. Deviations further increase with increasing magnitudes of the potential to thermal energy ratio, approaching -0.5 for the case of η^{M}_{FM} at the largest Ψ_{VDW} and Ψ_I values.

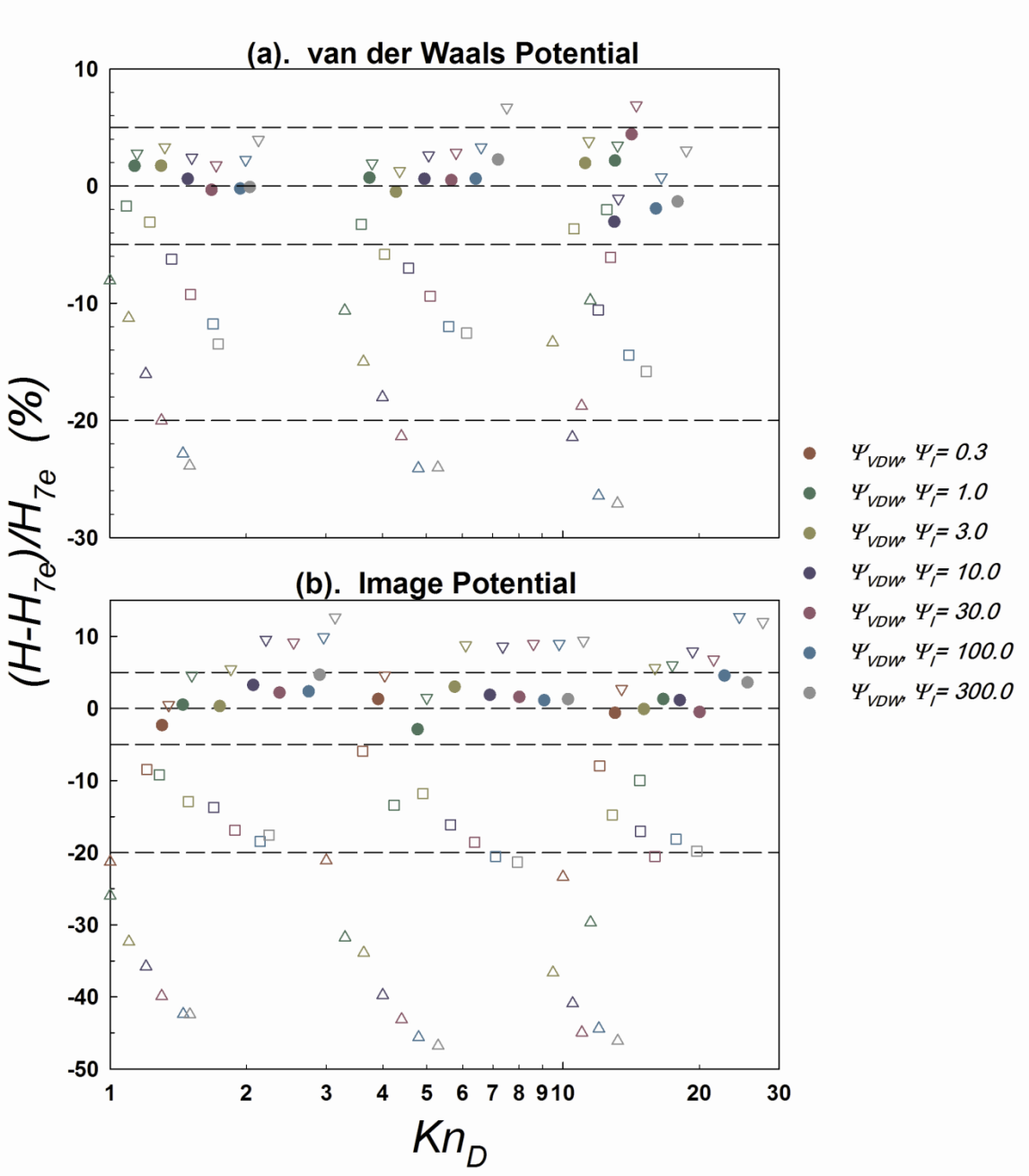

Figure 3.3 The difference between calculated $H(Kn_D)$ values and those predicted by equation 7e as a function of Kn_D considering **(a.)** the van der Waals potential (ω = 0.5) and **(b.)** the image potential at various potential energy to thermal energy ratios (shown via color). Dimensionless H and Kn_D coordinates shown are determined using free molecular enhancement factors calculated with equation (6a) (closed circles), the

approach of Fuchs & Sutugin (6c) (open, downward triangles), the approach of Marlow (6d) (open, upward triangles), and the approach of Sceats (6e) (open squares).

3.3.3 Comparison to Flux Matching Theory

In most prior works focusing on gas-phase nanoparticle collisions [84,103-105,115,116], the flux matching theory of Fuchs [76,101,117] or a variation of this approach [114,118] is utilized for calculations of collision rates. The origins of equation (7e) are completely distinct from flux matching theory (unlike the approach employed in several prior Brownian dynamics calculations [119]), and therefore comparison of equation (7e) to the predictions of flux matching theory in the presence of van der Waals and image potentials is warranted. As in mean first passage time calculations, in flux matching theory, transport of one colliding entity (analogous to the moving point mass) to another (analogous to the collector) is monitored. When the entities are far from one another, continuum transport mechanics is utilized to monitor motion. However, when the center to center distance between colliding entities is less than the radius of a "limiting sphere", free molecular mechanics are used to describe motion. On the surface of this limiting sphere, the flux of moving entities from the outer continuum is equated with the flux entering the inner free molecular space. Following Fuchs's 1963 description [101] of flux matching theory and calculating the limiting sphere radius with parameters specified by Adachi et al [115], the dimensionless collision kernel arising from flux matching theory can be calculated with the following equations:

$$H = \frac{4\pi K n_D^2}{\frac{\sqrt{2\pi} K n_D \eta_f}{\alpha \delta^2} \exp\left(\frac{\phi(\delta^*)}{kT}\right) + \frac{\eta_C}{\eta_\ell}} \tag{12a}$$

$$\delta^* = \frac{1}{\lambda^2}\left(\frac{(1+\lambda)^5}{5} - \frac{(1+\lambda)^2(1+\lambda)^3}{3} + \frac{2(1+\lambda^2)^{5/2}}{15}\right) \tag{12b}$$

$$\eta_\ell = \left[\int_{\delta^*}^{\infty} \exp\left(\frac{\phi(r^*)}{kT}\right) r^{*-2} dr^*\right]^{-1} \tag{12c}$$

$$\lambda = 1.329\sqrt{\frac{\pi}{8}}\frac{Kn_D\eta_{FM}}{\eta_C} \tag{12d}$$

$$\alpha = \left(\frac{b_{\min}}{\delta^*}\right)^2 \tag{12e}$$

Similar to b_{crit} in η_{FM} calculations, b_{min} is the critical impact parameter below which point masses that reach the limiting sphere surface will collide with the central collector. It is determined as the minimum value of b in the equation:

$$b = r^*\sqrt{1+\frac{2}{3}\left[\frac{\phi(\delta^*)}{kT}-\frac{\phi(r^*)}{kT}\right]} \tag{12f}$$

for r^* between 1 and δ^* (the limiting sphere radius). In the absence of potential interactions, flux matching theory predictions are in good agreement (within 5-10%) of equation (7e) [21]. However, with attractive Coulomb potentials considered, flux matching theory predictions appear to vastly underestimate the collision rate at high potential to thermal energy ratios [88,100]. Figures 3.4a (van der Waals potential) and 4b (image potential) show $H(Kn_D)$ results from flux matching theory at various Ψ_{VDW} and Ψ_I, respectively. Apparent in these figures, underestimation of the collision rate is also found at moderate and high values of Ψ_{VDW} and Ψ_I in the transition regime ($0.035 < Kn_D < 3.7$, note that by construction, flux matching theory correctly predicts the collision rate in the continuum limit and is approximately correct in the free molecular limit for these potentials). For example, at $\Psi_{VDW} > 10$, flux matching theory predictions are 20 - 40% smaller than the expected $H(Kn_D)$ relationship about $Kn_D = 0.2 – 0.3$ and in the same Kn_D range with the image potential for $\Psi_I > 1$ flux matching predictions are 20 - 70% than expected values. Noted previously [88], the failure of flux matching theory in the presence of attractive forces is attributable to several factors. First, in Fuchs's flux matching approach all entities on the limiting sphere surface begin at the mean thermal speed. Strong attractive potentials may indeed lead to entities moving much faster at this surface. Second, the assumption of uniformly distributed impact parameters on the

limiting sphere surface is also made, yet impact parameters are also skewed by the potential. Finally, without modification [120], in flux matching theory gas molecule collisions with moving entities inside the limiting sphere radius are ignored, although these may reduce kinetic energy and promote entity-entity collisions. Conversely, in mean first passage time calculations, the concept of a limiting sphere is not invoked; thus, they are insensitive to these shortcomings in flux matching theory. In total, we suggest that the $H(Kn_D)$ relationship given in equation (7e), with H defined by equation (7a), Kn_D defined by equation (7b), η_C defined by equation (3), and η_{FM} defined by equations (6a) and (6b) enables more accurate calculation of transition regime collision rates than does flux matching theory at moderate and high potential to thermal energy ratios.

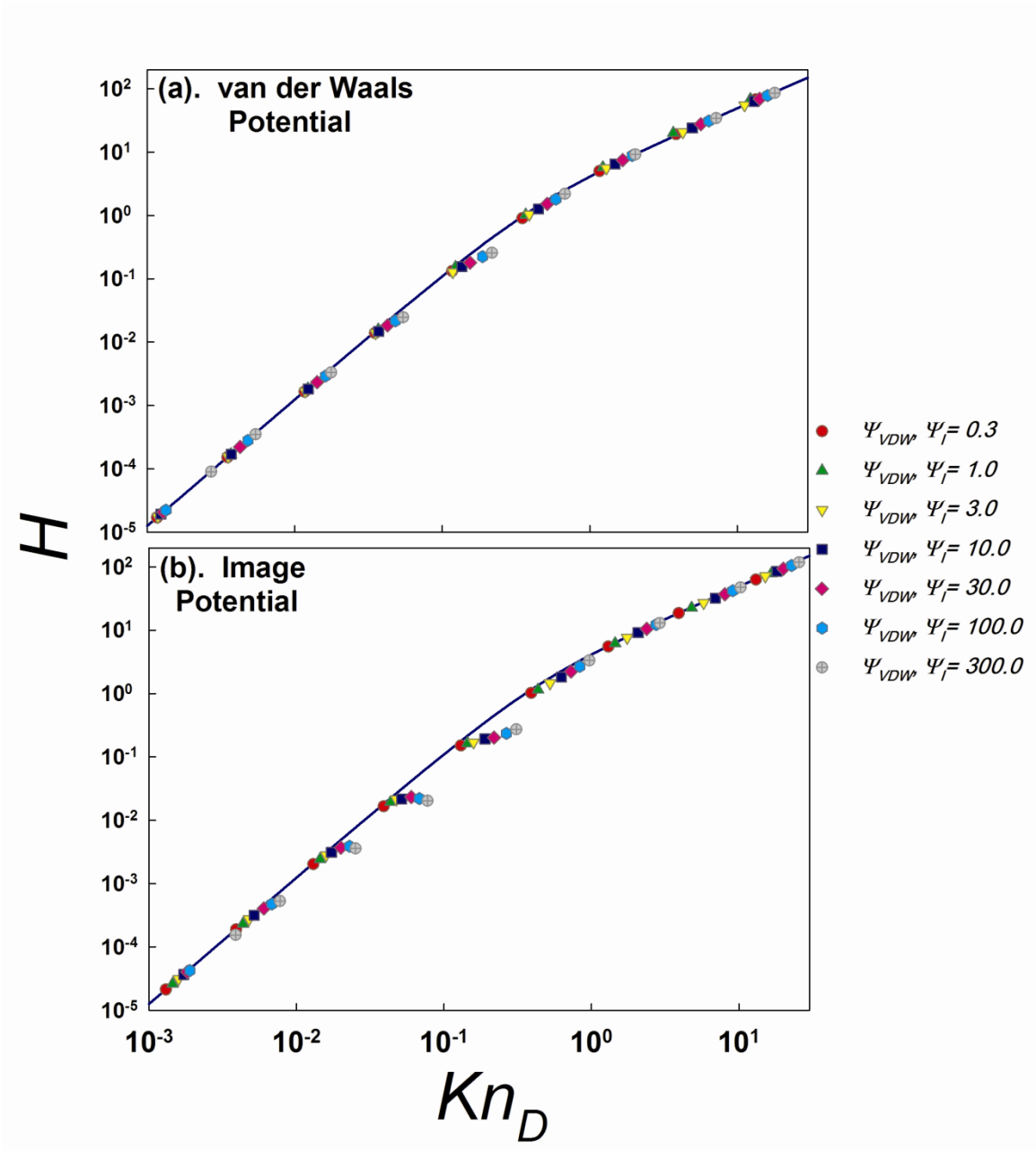

Figure 3.4 Flux-matching theory calculated $H(Kn_D)$ values and those predicted by equation (7e) (solid blue line) considering **(a.)** the van der Waals potential ($\omega = 0.5$) and **(b.)** the image potential at various potential energy to thermal energy ratios.

3.3.4 Comparison to Experimental Measurements

Because nanoparticle-nanoparticle collisions and nanoparticle-ion collisions lead to polydispersity in the size and charge distributions of gas-phase nanoparticles [121], precise experimental determination of collision rates is often difficult. Nonetheless, we can compare the predictions of equation (7e) accounting for van der Waals potentials to the measured nanoparticle-nanoparticle collision (coagulation) rates inferred from experiments by Chan & Mozurkewich [103] (H_2SO_4-H_2O droplets, with Ψ_{VDW} = 16.0), Okuyama et al [104] (NaCl and $ZnCl_2$ nanoparticles, with Ψ_{VDW} = 21.8 known for NaCl and also assumed for $ZnCl_2$), Wagner & Kerker [105] (DEHS droplets, with Ψ_{VDW} = 10.0 used as an approximate value), and Fuchs & Sutugin [89] (NaCl nanoparticles, Ψ_{VDW} = 21.8). For all of these studies, the colliding nanoparticles are neutral and of approximately equal size. H and Kn_D values are computed using the reported dimensional collision kernels, nanoparticle radii, the Stokes-Millikan equation to infer friction factors [18] (requiring the hard sphere mean free path of the gas molecules and the gas dynamic viscosity), the bulk densities of the nanoparticle materials, the background gas temperature, and the noted Ψ_{VDW} values, with η_C and η_{FM} computed using equations (3) and (6a), respectively. A compilation of these data is shown in Figure 3.5. Also shown are the continuum and free molecular expected curves, as well as equation (7e). With the exception of few data points, experimental results are within 25% of equation (7e) predicted values. This agreement is quite encouraging given the complexities of inferring collision kernels from measurements for particles of a specific size, and supports the validity of equation (7e). However, it is also clear in Figure 3.5 that there is a dearth of data collected in the actual transition regime for mass transfer, which is in contrast to the noted purpose of several of the referenced experimental studies [103,105]. The particles examined in these works are smaller in size than the mean free path of the surrounding gas; thus the Knudsen numbers (ratio of gas mean free path to particle radii) exceed unity. Although this leads to momentum transfer occurring in the transition and free molecular regimes [75], it does not guarantee that collisions, which are a mass transfer process and depend upon Kn_D, will be

transition regime processes. Moreover, as noted previously in this work, with singular contact potentials the ratio $\eta_{FM}/\eta_C > 1$ and is close to 2, even in instances of modest Ψ_{VDW} (i.e, the examined experimental results). The mere existence of attractive potential interactions thus leads to collisions occurring in a transport regime closer to the continuum limit than the free molecular limit. These prior studies, therefore, do not afford examination of the nature of transition regime collisions, but rather they examine near-continuum regime collisions in the presence of slip (non-continuum momentum transfer) and potential interactions. As a final note, a number of experimental results are not included in this comparison, primarily because the reported collision kernels are inferred from measurements of polydisperse particles [122]. Clearly, further experimentation will be necessary to verify the predictions of the theory presented here.

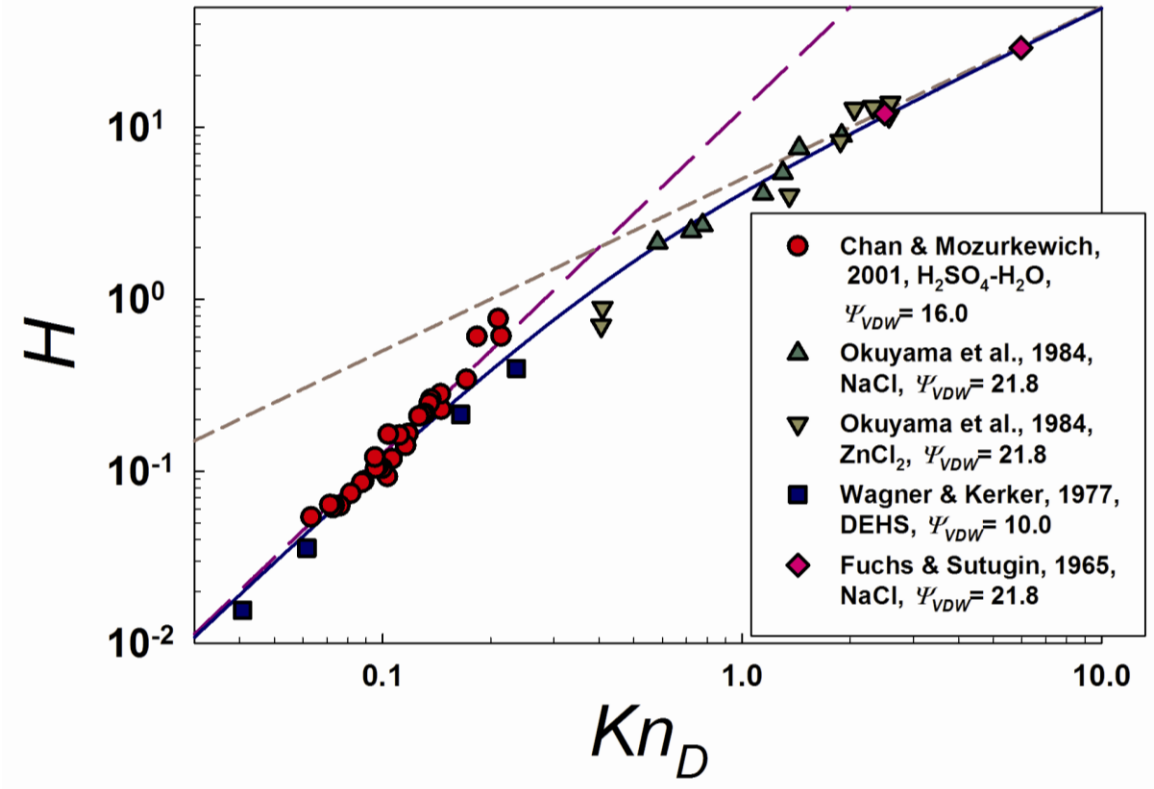

Figure 3.5 *H(Kn$_D$)* values inferred from experimental measurements. For comparison, the continuum limit (long dash) and free molecular limit (short dash) expected curves, as well as the predictions of equation (7e) (solid line), are plotted.

3.4 Conclusions

The collisions of gas-phase nanoparticles in the mass transfer continuum, free molecular, and transition regimes accounting for singular contact potentials are studied via dimensional analysis and mean first passage time calculations. Results of this analysis are subsequently used to examine various proposed expressions for the free molecular regime enhancement factor and the limits of flux matching theory, and compared to experimental measurements of nanoparticle coagulation rates. Based on this work we conclude that the most appropriate approach for free molecular enhancement factor calculation is that displayed in equations (6a) and (6b) in this work, in which the distribution of colliding entity kinetic energies is considered and the enhancement factor is calculated with *a priori* determination of the critical impact parameter as a function of colliding entity relative speed. From mean first passage time calculations, it is found that a regression equation (equation 7e) for the dimensionless collision kernel H as a function of the diffusive Knudsen number Kn_D determined in the absence of potential interactions aptly describes collisions in the presence of singular potentials (such as the van der Waals and image potential), provided that the continuum and free molecular enhancements are incorporated into the definitions of both H and Kn_D. Use of this regression expression should vastly simplify collision rate calculations for gas-phase nanoparticles, enabling both transition regime and potential energy influences to be considered in future analyses. The more complex, yet conventional approach utilizing flux matching theory is found to break down at moderate and large potential to thermal energy ratios in the transition regime, which further promotes use of the mean first passage time inferred regression expression. Comparison to experimental data also supports the approximate validity of equation (7e), and cautions that the presence of singular potentials leads to collisions which tend to occur in the mass transfer continuum regime. This particular influence of potential interactions is not made clear in prior work on collisions, and is perhaps the most important influence that singular potentials have on gas-phase nanoparticles.

Acknowledgements

The authors thank the Minnesota Supercomputing Institute (MSI) for providing the high performance computing hardware used in mean first passage time calculations. Support for this work was provided by NSF-CHE-1011810.

Chapter 4: IMS-MS and IMS-IMS Investigation of the Structure and Stability of Dimethylamine-Sulfuric Acid Nanoclusters

Abstract

Recent studies of new particle formation events in the atmosphere suggest that nanoclusters, i.e the species formed during the early stages of growth and composed of 10^1-10^3 molecules, often consist of amines and sulfuric acid. The physicochemical properties of sub-10 nm amine-sulfuric acid clusters are hence of interest. In this work we measure the density, thermostability, and extent of water uptake of < 8.5 nm effective diameter dimethylamine-sulfuric (DMAS) nanoclusters in the gas phase, produced via positive electrospray ionization. Specifically, we employ three systems to investigate DMAS properties; ion mobility spectrometry (IMS, with a parallel-plate differential mobility analyzer) is coupled with mass spectrometry to measure masses and collision cross sections for < 100kDa positively charged nanoclusters, two differential mobility analyzers in series (IMS-IMS) are used to examine thermostability, and finally a differential mobility analyzer coupled to a recently developed atmospheric drift tube ion mobility spectrometer (also IMS-IMS) is used for water uptake measurements. IMS-MS measurements reveal that dry DMAS nanoclusters have densities of ~1567kg/m^3 near 300 K, independent of the ratio of dimethylamine to sulfuric acid originally present in the electrospray solution. IMS-IMS thermostability studies reveal that partial pressures of DMAS nanoclusters are dependent upon the electrospray solution concentration ratio, R= $[H_2SO_4]/[(CH_3)_2NH]$. Extrapolating measurements, we estimate that dry DMAS nanoclusters have surface vapor pressures of order 10^{-4} Pa near 300 K, with the surface vapor pressure increasing with increasing values of R through most of the probed concentration range. This suggests that sulfuric acid dissociates from nanoclusters, and that nanocluster surface vapor pressures are enhanced by capillarity effects (the Kelvin effect). Meanwhile, IMS-IMS water uptake measurements show clearly that DMAS nanoclusters uptake water at relative humidity beyond 10% near 300 K, and that larger clusters uptake water to a larger extent. In total our results suggest that dry DMAS

nanoclusters (in the 5-8.5 nm size range in diameter) would not be stable under ambient conditions; however, DMAS nanoclusters would likely be hydrated in the ambient (in some cases above 20% water by mass), which could serve to reduce surface vapor pressures and stabilize them from dissociation.

Introduction

There is strong evidence that new particle formation events in the ambient atmosphere lead to the formation of clusters composed of amines in combination sulfuric acid [123-125]; though amines have lower atmospheric concentrations than ammonia [126], because of their stronger basicity than ammonia [127], amine-sulfuric acid clusters are more stable in ambient conditions than are ammonium sulfate/ammonium bisulfate clusters. In particular, dimethylamine molecules ($(CH_3)_2NH$) in combination with sulfuric acid molecules (H_2SO_4) form condensed phase species (dimethylamine-sulfuric acid clusters, DMAS, which are combinations of dimethylammonium sulfate and/or dimethylammonium bisulfate), which have been found to be more stable than their methylamine- and trimethylamine-sulfuric acid cluster counterparts [127,128]. As a result, DMAS are highly likely to be the seeds for nanoparticle growth in many new particle formation events in the atmosphere [123,129,130].

Of considerable interest are thus the physicochemical properties of DMAS in the 1- 10 nm size range. Such entities are typically composed of 10^1-10^3 molecules, and are henceforth refer to as nanoclusters here. Though in the initial stages of new particle formation clusters composed of a smaller number of molecules ($<10^1$) form [127,131], these smaller clusters must grow into nanoclusters, and it is nanocluster properties (namely their density, thermostability, and capacity to uptake water) which govern subsequent growth to larger nanoparticles, i.e. to eventually act as CCN (cloud condensation nuclei), the nanoclusters must not dissociate under atmospherically relevant conditions and further must be able to grow by vapor uptake (via condensation). When input into models of condensational particle growth in the ambient atmosphere [132,133], nanocluster physicochemical properties will have a direct influence on the model output particle growth rate. Of concern for nanoclusters is that although modeling them as spheres is

likely acceptable, the properties of nanoclusters can, and presumably do, deviate from bulk properties as well as the properties of larger nano- to submicrometer particles, with such deviations not necessarily predictable from classically derived theories (though such theories are used almost universally in modeling nanocluster growth [132]). For example, the capillarity model, i.e. the Kelvin effect [22,23], leads to the prediction that nanoclusters are much less thermo stable than larger species of the same chemical composition and have substantially higher vapor pressures than their bulk counterparts. While qualitatively this is true, the capillarity model is based upon a bulk definition of surface tension; simulations [134] show that for pure phase nanoclusters whose radii are ≤7 van der Waals radii, quantitatively the capillarity model leads to extremely inaccurate vapor pressure predictions. Additional deviations from the capillarity model are to be expected for the vapor pressures of multicomponent nanoclusters, such as DMAS. Furthermore, size dependencies/deviations from bulk behavior are also expected, and have been observed for the density, [135] and extent of water uptake of nanoclusters [136,137].

DMAS nanoclusters and larger nanoparticles have been studied experimentally and theoretically by several different approaches. An overview of the properties of amines and studies of atmospheric amine chemistry was recently provided by Qiu & Zhang [138]. Specifically for DMAS particles, Qiu & Zhang also measured the thermostability, density, and extent of water vapor uptake for particles in the 80nm to 240nm size (diameter) range [128]. Ab initio calculations have been performed by several research groups to study the formation of neutral or charged DMAS clusters with or without water molecules [130,131,139,140]. However, experimental measurements in the nanocluster size range are lacking (beyond measurements of clusters composed of ≤10 sulfuric acids, above a size of ~1.1nm in diameter). In this study, we thus focus on measurements of the properties of DMAS nanoclusters in the size (effective diameter) range of 2 nm - 8.5nm, produced in a laboratory setting via electrospray ionization (ESI). Of specific interest are the density, thermostability, and extent of water uptake by such nanoclusters, properties which are amenable to laboratory investigation. Three unique

measurement systems are employed for measurements of these properties, which are described in detail in the subsequent sections: for density measurement ion mobility spectrometry-mass spectrometry with a high resolution differential mobility analyzer coupled to a mass spectrometer is applied [135,141-143]; for thermostability a tandem differential mobility analyzer system [144,145] using modest-to-high resolution differential mobility analyzers [146] is utilized; and for heterogeneous water uptake experiments, a differential mobility analyzer-drift tube mobility analysis system is applied [137,147]. The overarching goal of this work is to better understand what the properties of DMAS nanoclusters would be under atmospherically relevant conditions.

4.2 Experimental Methods

4.2.1 Materials

As a source of gas phase DMAS nanoclusters we used ESI of methanol based solutions, which, upon methanol evaporation, yielded nanoclusters. Solutions were prepared by adding sulfuric acid (99.999%) and dimethylamine (40 wt. % in H_2O) to HPLC grade methanol. All chemicals were purchased from Sigma-Aldrich (Saint Louis, MO, USA). Variable molar concentrations of sulfuric acid and dimethylamine were used, which are denoted as $[H_2SO_4]$ and $[(CH_3)_2NH]$ respectively. Seven molar concentration ratios, $R = \frac{[H_2SO_4]}{[(CH_3)_2NH]}$ were employed, specifically, *R = 10,5,4,3,2, 1, & 0.5*. These solutions were used for nanocluster generation with all three employed measurement systems.

For ESI, a 40µm ID silica capillary (360µm OD, Polymicro Technologies, Phoenix, AZ, USA) was used, as is described previously in cluster ion generation experiments [135,141]. An applied pressure was used to drive the solution through the capillary, while a positive voltage was applied directly to the solution to run the electrospray in a cone-jet mode [148], which was observed to be stable visually with a magnifying lens. DMAS nanoclusters with either single or multiple excess positive

charges were formed via ESI; for IMS-MS measurement, the ESI voltage was floated over the outer electrode of the parallel-plate differential mobility analyzer employed and no charge reduction scheme was employed prior to measurements. Conversely, for tandem differential mobility analyzer experiments and differential mobility-analyzer-drift tube experiments a 0.5 mCi Po-210 source was used to reduce the charge level of nanoclusters; after charge reduction most nanoclusters were neutral and those that were observed were singly charged [149].

4.2.2 Differential Mobility Analysis – Mass Spectrometry

Differential mobility analysis-mass spectrometry [143], a form of ion mobility spectrometry-mass spectrometry (IMS-MS) [150] was used for measurement of the collision cross sections of mass-identified nanoclusters in air. From these measurements nanocluster densities can be inferred [45,151]. The parallel plate differential mobility analyzer (model p5 SEADM, Boecillio, Spain, with a resolving power in mobility near 60) and QSTAR XL time-of-flight mass spectrometer (Applied Biosystems, Framingham,MA, USA) combination has been described in detail previously [135,141,143] and was operated in a similar manner to these prior works. Briefly, to specify the mobilities of the nanoclusters which can traverse the differential mobility analyzer, a potential difference was generated between the two electrodes by applying a voltage on the outer electrode. Singly and multiply charged nanoclusters were drawn into the classification region electrostatically, with the inlet operated in counterflow mode (~0.1 l min^{-1} of counterflow). High purity air (Air Gas, Ultra Zero Gas 1 ppm, St. Paul, MN, USA) was used as the sheath flow gas, and the sheath flow was operated in recirculating mode using a vacuum blower (Domel Inc., Železniki, Slovenia) with the sheath gas temperature in the measurement zone near 303 K and close to atmospheric pressure. ~0.2 l min^{-1} was drawn into the mass spectrometer inlet (at the outlet of the classification region of the mobility analyzer), to continuously supply air for the outlet and the counterflow a mass flow controller (MKS instruments, Andover, MA, USA) was set at 0.3 l min^{-1}.

To collect combined mass-mobility spectra, a potential difference of 1000 V – 4000 V was applied in steps of 10V, and mass spectra were collected at each voltage for an accumulation time of 2 s. For mass spectra measurements, the quadrupole mass filters were operated in radiofrequency only mode, and the time-of-flight section was employed. Between the mobility analyzer outlet and the first quadrupole of the mass spectrometer, there are several applied declustering and focusing potential differences; all of these differences were set to minimal values to mitigate the dissociation of nanoclusters in the mass spectrometer inlet (i.e. to reduce collision induced dissociation). Prior IMS-MS measurements where the IMS was operated at atmospheric pressure have revealed that in the inlets (where ions/nanoclusters are exposed to high pressure drop as well as strong electric fields) of mass spectrometers with atmospheric pressure ionization, collision induced dissociation of nanoclusters is commonplace [135,142,152].

As in prior studies using high sheath flow rate (in excess of 100 l min^{-1}) parallel-plate differential mobility analyzers, we did not measure the sheath flow rate directly. Instead, as differential mobility analyzers are linear spectrometers (i.e. the applied voltage is linearly proportional to the inverse mobility of the selected ions/nanoclusters), we employed a single point calibration technique. Prior to all experiments, we measured the electrical mobility of the tetraheptylammonium$^+$ (THA^+) ion, produced via ESI of a tetraheptylammonium bromide-methanol solution. The mobility of this ion (Z_{THA}), measured by Ude & Fernandez de la Mora [153] at 293 K was used to determine mobility of observed nanoclusters (Z_{nc}) through the relationship: $Z_{nc} = \frac{V_{THA}}{V_{nc}} \cdot Z_{THA}$, where V_{THA} is the applied voltage at which the THA^+ ion was maximally transmitted, and V_{nc} is the voltage at which the nanocluster in question was maximally transmitted. Neglecting the influence of the ion-induced dipole potential, for calibration, Z_{THA} was adjusted from Ude& Fernandez de la Mora's measured value because of the difference in temperatures used in measured here and in their work (303 K vs. 293 K, leading to a 1.6% shift in the mobility).

4.2.3 IMS-IMS Investigation of Thermostability.

Tandem differential mobility analysis, a form of IMS-IMS [154], has been successfully used in thermostability studies for over two decades [144,155]. We applied a similar measurement principle here, using two differential mobility analyzers of modest to high resolving power (typically above 20) for measurements. The tandem differential mobility analysis system employed is depicted in Figure 4.1a. In it, industrial grade dry nitrogen was used as a carrier gas, and DMAS nanoclusters were generated as described by an electrospray, with subsequent charge reduction in a Po-210 source. A flow of dry nitrogen was subsequently mixed with the generated nanocluster flow, with a 3.87 l min^{-1} of aerosol flow entering the first differential mobility analyzer (labelled as IMS-1in Figure 4.1a).

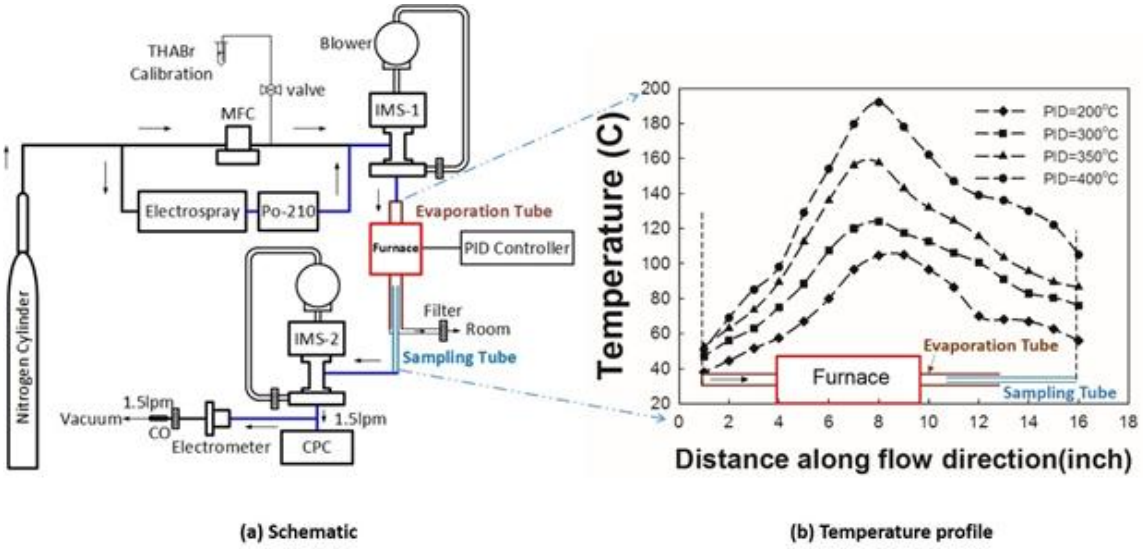

Figure 4.1 (a) A depiction of the tandem differential mobility analyzer system employed in thermostability experiments (IMS: differential mobility analyzer; CPC: condensation particle counter; Po-210: bipolar ion source). **(b)**The temperature profiles measured axially in the microfurnace chamber. The position of the furnace heating chamber and the sampling tube are also depicted.

Both differential mobility analyzers were cylindrical ½-mini models (Nanoengineering Corp., Boca Raton, FL, USA), the design of which is described by Fernandez de la Mora & Kozlowski [146]. In both, a negative voltage was applied to the

inner electrode where the aerosol exit slit is located, while the outer electrode is grounded. Positively charged nanoclusters were hence selected and measured. The sheath flows were operated in a recirculating mode with Domel Inc. vacuum blowers, and again, the THA^+ ion was used for calibration. The first differential mobility analyzer was operated at a fixed voltage to transmit nanoclusters of a specific mobility (and hence radius, as nearly all charged nanoclusters were singly charged). To evaluate thermostability, a microfurnace (UltraCoil Robust Radiator, Micropyretics Heaters International Inc., Cincinnati, OH, USA) was placed between the two differential mobility analyzers, and nanoclusters transmitted through the first differential mobility analyzer were sent through the microfurnace via a 12inch long sintered silicon carbide round tube (the evaporation tube) with ½ inch outer diameter (OD) and 3/8 inch inner diameter (ID) (Ortech Inc., Sacramento, CA, USA). Nanocluster evaporation occurred in the heated zone of the microfurnace, which was a 1.5 inch in diameter and 3.5 inch in length cylindrical chamber. Two insulating caps with the thicknesses of 0.75 inch were used to seal the heating chamber, and a PID controller was connected to a thermocouple embedded in the heated zone. The temperature profile was varied in the furnace by adjusting PID controller values. Four specific temperatures were set with the PID controller, 200^{o}C, 300^{o}C, 350^{o}C, and 400^{o}C. However, because the flow within the silicon carbide tube was laminar, and heating was non-uniform, an axial temperature profile was developed in the silicon carbide tube, i.e. the PID controller set temperature was not the temperature in the evaporation tube. Temperature profiles along the length of the evaporation tube were hence measured for all experiments and are displayed in Figure 4.1b. The temperature increased first and then decreased, with the highest temperature appearing at an axial location two-thirds downstream in the microfurnace (because of convective heat transfer). After the evaporation tube, an alumina sampling tube, which only sampled the center streamlines of the evaporation tube (3 l min^{-1} sampled), transmitted particles exiting the microfurnace to the second differential mobility analyzer (IMS-2). The second differential mobility analyzer was operated with a stepping applied

voltage in the 0 V to 4000 V range, with a step rate of 10 V s^{-1}, in order to determine to what extent the selected nanoclusters evaporated when passing through the microfurnace. The flow at the second differential mobility analyzer outlet was split, with half entering a condensation particle counter (CPC, TSI model 3776, Shoreview, MN, USA) and the other half entering a custom made Faraday cage electrometer. The CPC was used primarily for thermostability measurements (nanocluster detection), while the electrometer was used for THA^+detection, and hence mobility calibration (which was repeated at all PID controller set temperatures).

4.2.4 IMS-IMS Investigation of Water Uptake

While tandem differential mobility analyzers can be used to examine the sorption of vapor molecules to nanoparticles, maintaining high sheath flow rates at constant vapor concentrations (i.e. constant relative humidities) can be difficult. As an alternative, our group has recently developed a drift tube ion mobility spectrometer (DT-IMS, described in detail previously [147]) which can be uniquely coupled to a CPC for nanoparticle and nanocluster measurements. When using the DT-IMS in tandem with a differential mobility analyzer upstream, by controlling the relative humidity of its counterflow (~0.2 l min^{-1}), shifts in nanocluster mobilities brought about by vapor uptake can be directly observed. Following the experimental setup described by Oberreit et al [137], ESI generated and charge reduced DMAS nanoclusters were first passed through a ½-mini differential mobility analyzer, which was again operated at a constant applied voltage to isolate nanoclusters of a specific mobility. The selected nanoclusters then entered the DT-IMS, which was operated with clean air as the counterflow and humidified with a custom flowrate controlled nebulizer-heater system. The relative humidity in the DT-IMS was calculated from dew point and temperature measurements with a hygrometer (General Eastern Hygro M4, Fairfield, CT, USA) and a K type thermocouple.

Without any applied voltage, all nanoclusters entering the DT-IMS were immediately swept out of the inlet by the counterflow. However, upon timed application of a voltage (3 kV in this study) at the inlet, a near-linear electric field forms axially,

driving positively charged nanoclusters down the tube at a speed equal to the difference between their electrophoretic velocities and the counterflow velocity. Therefore, nanocluster arrival times at the CPC placed downstream of the DT-IMS are solely a function of nanocluster mobilities. Specifically, the inverse mobility (Z_{nc}^{-1}) of a nanocluster is linked to its arrival time (t_a) as measured by a CPC via the equation: $Z_{nc}^{-1} = at_a + b$, where a and b are constants dependent upon the delay time in CPC detection, the counterflow velocity, the applied voltage, and the drift tube geometry. To minimize signal broadening, a fast response CPC (WCPC, Model 3786, TSI, Shoreview, MN, USA) was employed in all measurements.

The differential mobility analyzer-DTIMS system enabled the investigation of water vapor uptake by nanoclusters via observation of uptake facilitated shifts in inverse mobilities, which was directly inferred from shifts in mobility classified nanocluster arrival time distributions. Again, we used ESI generated THA^+ to calibrate the ½-mini differential mobility analyzer, and subsequently, mobility classified particles were used to determine the values of a and b in DT-IMS calibration. For uptake experiments, five voltages were applied to the ½-mini differential mobility analyzer (5 nanocluster sizes) and arrival time distributions were measured correspondingly for 10 different relative humidity settings in the 3%-52% range.

4.3 Results and Discussion

4.3.1 Nanocluster Collision Cross Sections and Inferred Densities

IMS-MS measurements directly lead to mass-mobility spectra, in which measured signal intensity is a function of both mass-to-charge ratio (*m/z*) and inverse mobility (*$1/Z_{nc}$*, which is directly proportional to the applied voltage in the differential mobility analyzer). In these experiments five solutions with different molar ratios, $R = \frac{[H_2SO_4]}{[(CH_3)_2NH]}$ were used to generate DMAS nanoclusters, and each gave rise to their own mass-mobility spectra. Such data can be represented via contour plots; a contour plot for *R = 1* is

displayed in Figure 4.2. In it, signal intensity for each ion is displayed via a logarithmic color scale, with blue denoting the most intense signal and yellow denoting the faintest signal above a prescribed threshold. Signal intensities were mass averaged over 0.3 Da. In the contour plot, short line segments appear; each line segment denotes an ion of a specific *m/z* and $1/Z_{nc}$, and the width of the line represents the resolution of the ion mobility spectrometer. As discussed in detail previously, line segments for electrospray generated nanoclusters are grouped into charge-state specific bands [33,135,141,156]. Bands for seven charge states (z=1 to 7) are labeled in the figure. For several of the singly charged nanoclusters, a zoomed-in plot is inserted in Figure 4.2.

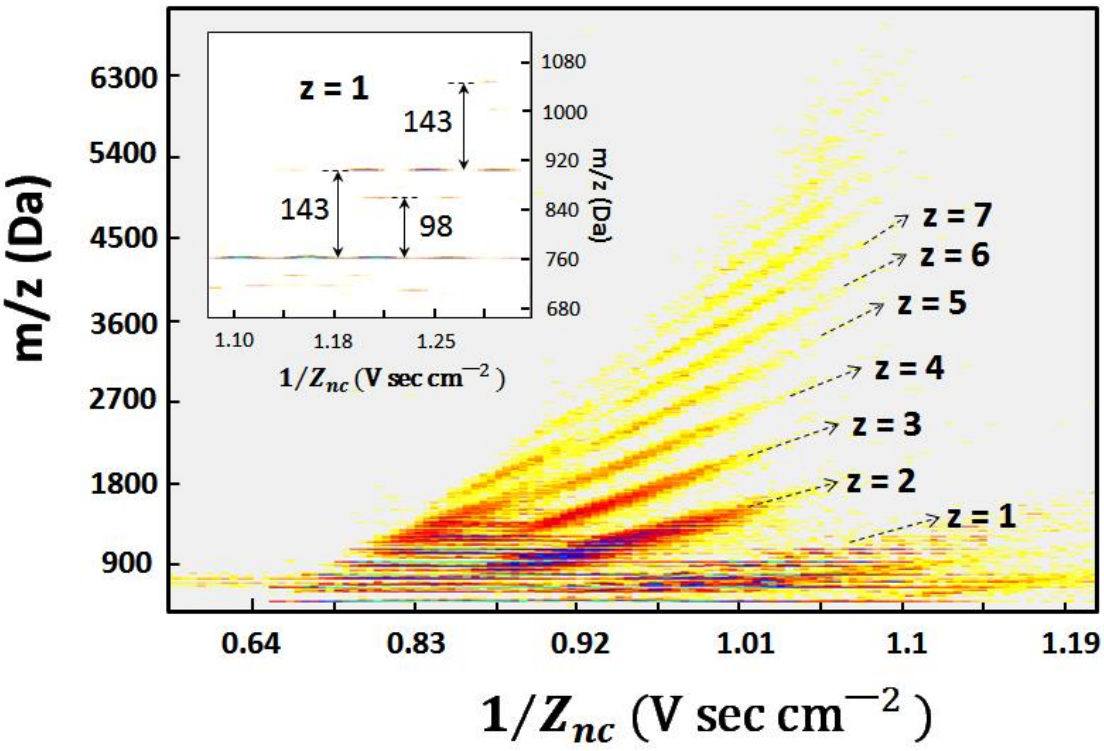

Figure 4.2 A mass-mobility contour plot inferred from IMS-MS measurement of multiply charged DMAS nanolcusters,with measured signal intensity expressed via color intensity on a logarithmic scale, with blue the most intense and yellow the least intense. Bands of ions of different charge states are labelled, from *z = 1* to *7*.

Apparent in this plot is that nanoclusters differ in *m/z* from one another by either 98 or 143 Da. For doubly charged species, the mass differences observed are half of

these values; together these indicate that nanoclusters are composed predominantly of $[(CH_3)_2NH{\cdot}H_2SO_4]$ and $[H_2SO_4]$ base units. In several instances, nanoclusters of the same *m/z* ratio but varying inverse mobility appear. Such line segments are attributable to neutral ion-pair ($[(CH_3)_2NH{\cdot}H_2SO_4]$ or $[H_2SO_4]$) evaporation in the inlet of the mass spectrometer (after mobility classification) [142]. Charge loss in the mass spectrometer inlet (in particular for z = 2 nanoclusters) additionally complicates spectra, giving rise to wider line segments which appear at neither the *m/z* nor the inverse mobility of the parent nanoclusters [141]. Fortunately, neutral evaporation and charge loss are minimal for most multiply charged nanoclusters, hence the *m/z* and $1/Z_{nc}$ values, as well as *z*, are readily determined from measurements for these nanoclusters. Subsequently, collision cross sections (CCSs, Ω) can be calculated for nanoclusters from mass-mobility data:

$$\Omega = \left(\frac{\pi m_{red}}{8kT}\right)^{0.5} \frac{3ze}{4\rho_{gas} Z_{nc}} \tag{1a}$$

where m_{red} is the reduced mass of the nanocluster-gas molecule pair (approximated as the gas molecule mass for all nanoclusters, 28.8 Da), *k* is Boltzmann's constant, *T* is temperature, *e* is the elementary charge, and ρ_{gas} is the bath gas mass density. In examining smaller clusters, structural analysis via IMS is best accomplished via comparison of measured CCSs to predictions based upon gas molecule scattering calculations [135,151,152,157,158]; the asphericity of such entities, combined with the non-negligible influence of the ion-induced dipole potential (for measurements in air) and some ambiguity in the manner in which gas molecules impinge and are reemitted from clusters surfaces (i.e. diffuse versus specular) often prohibits the use of simple relationships to link the CCS to physical structure. However, nanoclusters are sufficiently large, such that they can be modeled as spheres [33]. For spherical entities in diatomic gases [152], considering the free-molecular limit of the Stokes-Millikan equation [45,121,151,157] as well as the influence of the polarization potential between gas molecule and charged nanocluster [69], the following relationship can be applied to link the CCS to a nanocluster's radius, r_{nc}:

$$\Omega = \xi \cdot \pi \cdot \left(r_{nc} + r_{gas}\right)^2 \cdot L \quad (1b)$$

where r_{gas} is the effective gas molecule radius (1.5 Å for air near 300 K [33]), ξ is a dimensionless momentum scattering coefficient, found to be ≈ 1.36 in many instances and taken to be so here (though exception have been observed [135]), and L is a dimensionless polarization correction factor (a correction factor of the ion induced-dipole potential), the calculation of which is described in detail by Larriba-Andaluz& Hogan [151]:

$$L = \left[1 + \phi_e\left(\frac{1}{3.1} + \frac{1}{\xi}\left(\frac{1}{16} + \frac{4}{33}\phi_e\right)\right)\right] \text{ if } \phi_e \leq 1 \quad (1c)$$

$$L = \left[1 + \phi_e\left(\frac{1}{4} - \frac{2.3}{1000}\phi_e + \frac{1}{\xi}\left(\frac{9}{56} - \frac{6.8}{1000}\phi_e\right)\right)\right] \text{ if } \phi_e > 1 \quad (1d)$$

where $\phi_e = U_{pol}/kT$ (potential energy to thermal energy ratio), and $U_{pol} = -\alpha z^2 e^2/(8\pi\epsilon\epsilon_0(r_{nc} + r_{gas})^4)$, with ε_0 the permittivity of free space, ε the dielectric constant of the background gas, and α the polarizability of the background gas molecules (~1.7 Å^3 in air).

For each nanocluster measured, we infer r_{nc} with equations (1a-1d). Additionally, in figure 4.3, the masses of all multiply charged nanoclusters are plotted as functions of $\Omega^{3/2}$; for these clusters, polarization influences (though considered in r_{nc} inference) are small, and additionally r_{nc} is considerably larger than r_{gas}. Therefore, $\Omega^{3/2}$ scales approximately with nanocluster volume, and the observed linear relationship between nanocluster mass and $\Omega^{3/2}$ suggests that the measured nanoclusters are of a constant density, which is found relatively independent of the sulfuric acid to dimethylamine concentration ratio R in ESI solutions. As discussed in prior studies [33], high resolution ion mobility spectrometry of mass identified ions enables density inference to within several percent; however, density inference alone does enable quantification of nanocluster internal structure or surface structure changes which may be brought about by changing R ratios. Via linear regression with all data in Figure 4.3, we infer a density, $\rho_{DMAS} = m_{nc}/(\frac{4}{3}\pi r_{nc}^3)$, of 1567 kg m^{-3}. Although this value is slightly higher than the 97 nm diameter particle DMAS density reported by Qiu & Zhang [128]

(1408 kg m^{-3}), it is bounded by bulk densities of dimethylamine (670kg m^{-3}) and sulfuric acid (1840 kg m^{-3}), and further increases in density for nanoclusters (due to capillarity effects, provided charged clusters are not Coulombically stretched) [33] are expected.

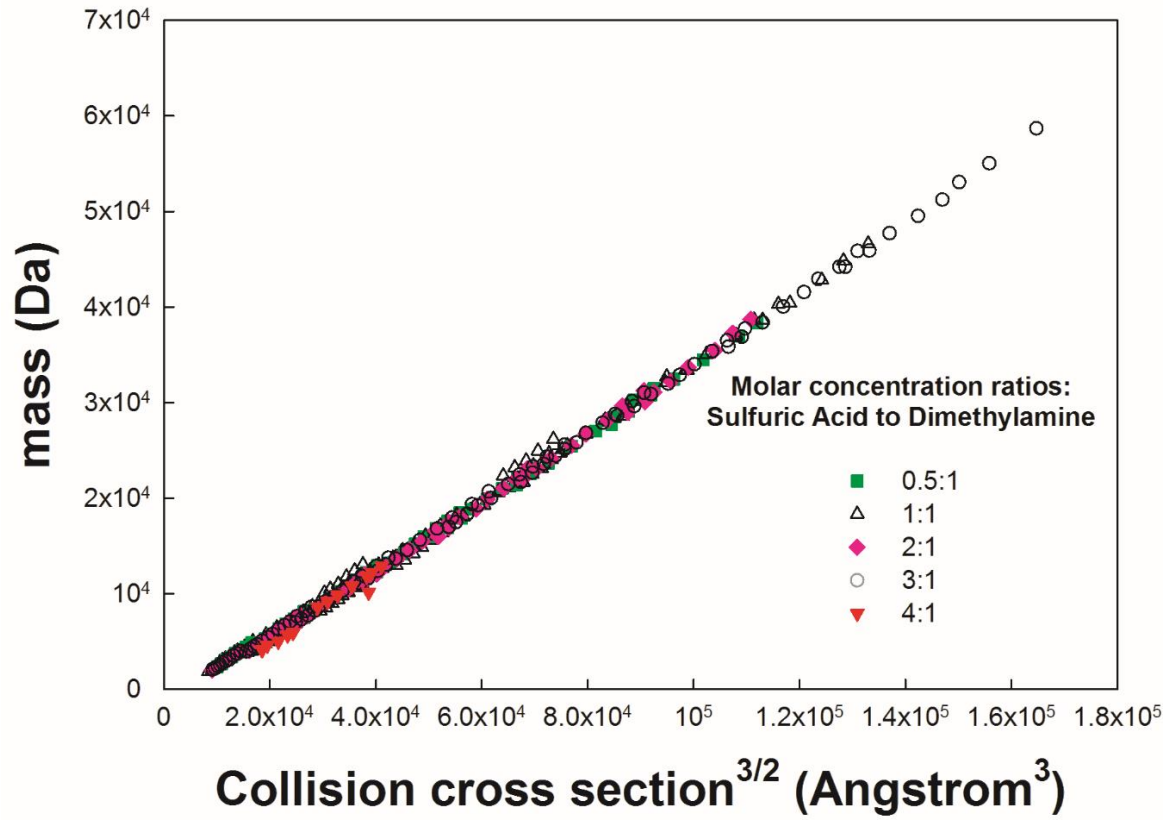

Figure 4.3 The measured mass of nanoclusters as a function of their collision cross-sections to the 3/2 power, which is approximately proportional to nanocluster volume. Different symbols represent different molar concentration ratios of initial solution used in ESI solutions.

4.3.2 Nanocluster Thermostability

For tandem differential mobility analysis experiments, we additionally use equation (1b) to infer nanocluster radii, r_{nc} for the nanoclusters transmitted by both the first and second differential mobility analyzers, respectively. For all results, $L = 1$ was assumed, as for the singly charged nanoclusters examined in these experiments, polarization influences are negligible. Measurements result in plots of measured signal intensity (CPC signal) as a function of r_{nc} for each selected $r_{nc,0}$ by the first differential

mobility analyzer and each set temperature profile in the furnace. Such plots are displayed in figure 4.4 for $r_{nc,0}$ = *3.00 nm, 3.30 nm, 3.66 nm, &3.95 nm* with 4 different PID settings. Evidenced in this figure, in all instances, as the PID set temperature was increased (1) the absolute detected signal decreased, (2) distributions became noticeably broader and asymmetric, and (3) peaks in distributions shifted to smaller inferred radii. The first observation is attributable to thermophoretic deposition in the furnace, while the second and third are attributable to evaporation (monomer dissociation) of nanoclusters at elevated temperatures, with broadening presumably arising because of variations in temperature-time history by transmitted nanoclusters (spatial effects). Although attempts were made to minimize such broadening and spatial influences on the evaporation process by sampling along the evaporation tube centerline only, such effects are difficult to completely mitigate [145] in a system for sub 10 nm charged entities.

While we nonetheless proceed to infer surface vapor pressures for nanoclusters (P_{nc}) from these measurements, we caution that the absolute values obtained have not been corrected considering a detailed analysis of the temperature profile in the evaporation tube and the nanocluster trajectories (i.e. an averaging approaching is taken), and further the analysis approach itself utilizes several approximations. However, we will only focus on estimating the surface vapor pressures to within an order of magnitude, which such approximations should not mitigate.

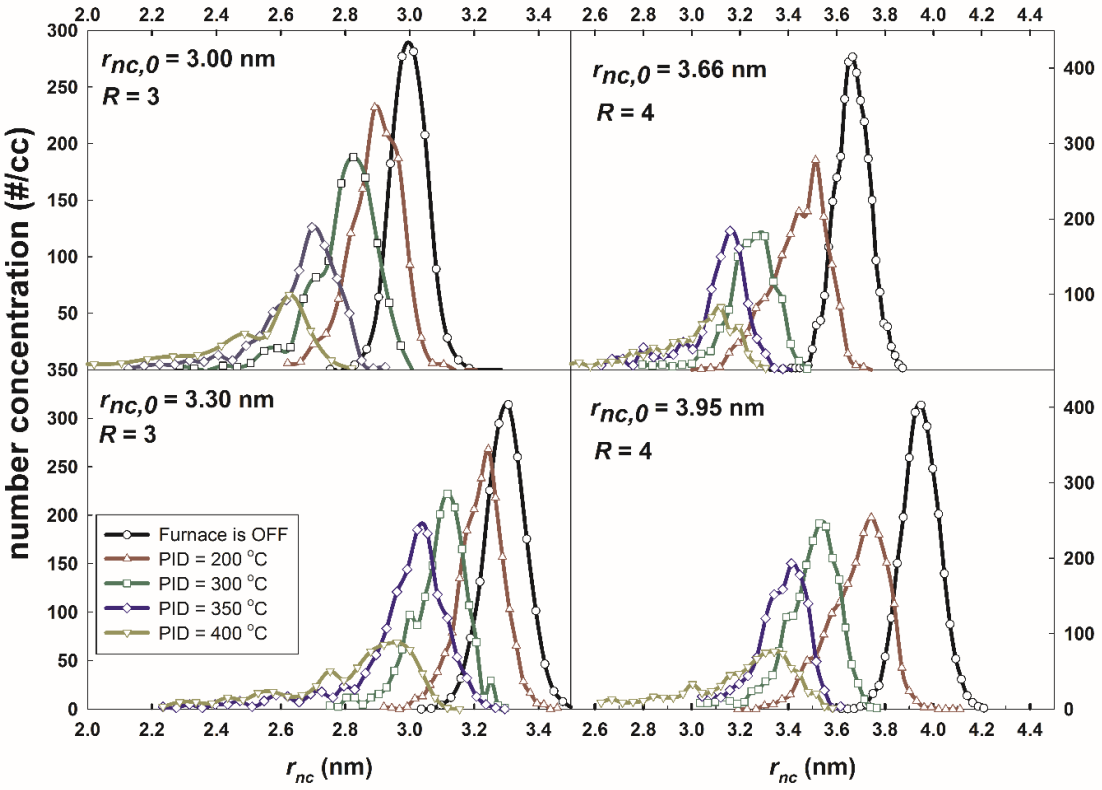

Figure 4.4 Nanocluster number concentrations, as measured by a CPC, measured as function of r_{nc} based on the second differential mobility analyzer settings in tandem differential mobility experiments, for different temperatures (distinguished by PID setting) and for four initial radii.

To analyze tandem differential mobility analyzer data, we determine the peak r_{nc} values for each measured distribution and assume that all of these nanoclusters were transmitted through the evaporation tube with near identical residence times (t). The number of vapor molecules evaporating from the surface of a single nanocluster per unit time (the evaporation rate, $\frac{dN}{dt}$, in units of molecules per second) is given by the equation:

$$\frac{dN}{dt} = -\beta n_{v,nc} \tag{2a}$$

where $n_{v,nc}$ is the vapor molecule number concentration on the surface of a nanocluster, and β is the collision kernel/collision rate coefficient, which for nanoclusters in the

ballistic regime can be approximated as $\sqrt{\frac{8kT}{\pi m_v}} \cdot \pi r_{nc}^2$, where $\sqrt{\frac{8kT}{\pi m_v}}$ is the mean thermal speed of the evaporating vapor molecules, and m_v is the mass of vapor (assumed to be 98 Da, the mass of sulfuric acid, for reasons elaborated upon later on).

The surface concentration of vapor molecules, in turn, can be converted to a nanocluster surface vapor pressure via the relationship $n_v = \frac{P_{nc}}{kT}$. With the number of vapor molecules in a nanocluster given by $\frac{\rho V_{nc}}{m_v}$, where V_{nc} is the nanocluster volume (assuming they are spheres $V_{nc} = \frac{4}{3}\pi r_{nc}^3$) and ρ the density (measured in IMS-MS experiments), it then follows that $\frac{dN}{dt} = \frac{\rho}{m_v}\frac{dV_{nc}}{dt}$. This relationship coupled with the assumption that the density and vapor molecule mass are nanocluster size invariant leads to:

$$\frac{dV_{nc}(t)}{dt} = -\sqrt{\frac{8kT(t)}{\pi m_v}} \cdot \pi r_{nc}^2 \cdot \frac{P_{nc}(T, r_{nc})}{kT(t)} \cdot \frac{m_v}{\rho} \qquad (2b)$$

In equation (2b), the nanocluster volume and the temperature are denoted as functions of time, while the nanocluster vapor pressure is denoted as a function of temperature and the nanocluser radius. Measurements provide the initial and final nanocluster volume, respectively, and the temperature-time relationship for the centerline of the evaporation tube was measured as discussed previously (at 16 discrete axial distances). These two pieces of information, combined with equation (2b), enable inference of $P_{nc}(T, r_{nc})$. Isolating dV_{nc} on the left-hand side of equation (2b) and integrating over the residence time t in the furnace leads to:

$$\frac{4}{3}\pi\left(r_{nc,0}^3 - r_{nc,f}^3\right) = \Delta V \approx \frac{r_{nc,0}^2}{\rho} \cdot \sqrt{\frac{8\pi m_v}{k}} \cdot \int_0^t \frac{P_{nc}(T, r_{nc,0})}{\sqrt{T(t)}} dt \qquad (2c)$$

where $r_{nc,f}$ is the final peak radius of the transmitted nanoclusters and ΔV is the volume change due to evaporation. In integrating (2b), for simplicity we assume that $r_{nc}^2 \approx r_{nc,0}^2$, i.e. the projected area of an evaporating nanocluster did not change substantially during experiments. In addition, vapor pressures inferred are assumed to apply for clusters of radius $r_{nc,0}$.

To subsequently determine $P_{nc}(T)$, for each $r_{nc,0}$ we used the fitting function:

$$P_{nc}(T) = \exp(A^2 - \frac{B^2}{T} - \frac{C^2}{T^{1.5}} - \frac{D^2}{T^{0.5}}) \quad (2d)$$

where *A,B,C,* and *D* are fitting coefficients, the temperature *T* is in Kelvin, and the resulting pressure is in Pascals. This function is similar in construction to the Antoine equation [159] or Riedel equation [160], though it is simply used because of its flexibility in fitting our results and not derived from thermodynamic relationships (i.e. the third and fourth terms are ad-hoc corrections, introduced only to provide flexibility in fitting results). With substitution of equation (2d) into equation (2c), combined with the trapezoidal rule for integration, equation (2c) can be rearranged to give:

$$\Delta V_i \cdot \frac{\rho}{\pi r_{nc,0}^2} \cdot \sqrt{\frac{\pi k}{8 m_v}} \approx \sum_{j=1}^{15} \left\{ \left(\frac{\exp\left(A^2 - \frac{B^2}{T_{j,i}} - \frac{C^2}{T_{j,i}^{1.5}} - \frac{D^2}{T_{j,i}^{0.5}}\right)}{T_{j,i}^{0.5}} + \frac{\exp\left(A^2 - \frac{B^2}{T_{j+1,i}} - \frac{C^2}{T_{j+1,i}^{1.5}} - \frac{D^2}{T_{j+1,i}^{0.5}}\right)}{T_{j+1,i}^{0.5}} \right) / 2 \cdot \delta t \right\}$$

(2e)

where *I* =1,2,3, and 4 denotes the four PID set values (200ºC, 300ºC, 350ºC, and 400ºC, respectively), $T_{j,i}$ denotes the temperature measured at location *j* for PID setting *i*, and $\delta t = t/15$. To find the "best-fit" values of A, B, C, and D, for which the left-hand side and right-hand side of equation (2e) are approximately equal for all PID settings, we use the solver add-in of Microsoft Excel (version 2010). A global error is defined as $e_G = \sum_{i=1}^{4} \left(1 - \frac{a_i}{b_i}\right)^2$, where a_i and b_i are left-hand and right-hand sides of equation (2e) respectively. Local errors were also similarly calculated as $e_i = |1 - a_i/b_i|$. Using initial guesses of *A=1,B=10,C=100,* and *D=10,* under all circumstances, the solver minimizes e_G while keeping all e_i less than 15% as a constraint, with the exception of the PID setting of 200º C, for which no constraint is placed. Different initial guess values led to a negligible change in the resulting P_{nc} values, and this fitting procedure is applied for six separate initial sizes, and seven values of *R*, hence 42 separate coefficient sets.

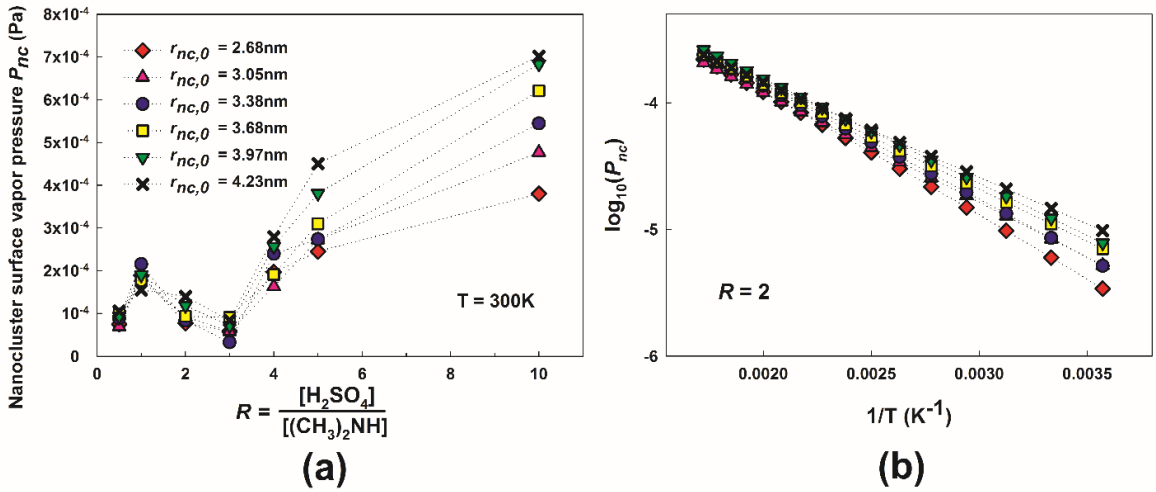

Figure 4.5 (a) Extrapolated surface vapor pressures, P_{nc}, as a function of $R = \frac{[H_2SO_4]}{[(CH_3)_2NH]}$. **(b.)** $\log_{10}(P_{nc})$ inferred from experiments, based on fitting equation (2d) to experimental results, as a function of 1/T. Different symbols represent different initial particle radii: diamonds (2.68 nm), upward triangles (3.05 nm), circles (3.38 nm), squares (3.68 nm), downward triangles (3.97 nm) and crosses (4.23 nm).

Table 4.1 Inferred coefficients *A,B,C&D* for different initial solution molar ratios *R*.

R=0.5

$r_{nc,0}$	2.7nm	3.07nm	3.39nm	3.69nm	3.98nm	4.24nm
A	0.14	0.81	0.71	0.58	0.59	0.59
B	5.41	10.66	10.55	10.73	10.83	10.83
C	131.45	133.37	118.91	120.39	131.91	131.43
D	10.28	10.56	10.8	10.52	10.1	10.02

R=1.0

$r_{nc,0}$	2.71nm	3.07nm	3.4nm	3.71nm	3.99nm	4.26nm
A	0.04	0.54	0.52	0.82	0.82	0.81
B	1.48	9.85	9.88	9.84	9.93	10.11

C	41.15	46.82	43.43	74.9	80.58	98.64
D	11.95	11.88	11.79	11.7	11.52	11.17

R=2.0

$r_{nc,0}$	2.66nm	3.03nm	3.35nm	3.66nm	3.94nm	4.19nm
A	0.75	0.64	0.63	0.57	0.81	0.85
B	10.48	10.62	10.81	10.89	10.44	10.21
C	117.58	113.33	132.95	133.93	118.68	104.83
D	11.02	10.89	10.19	9.99	10.71	11.11

R=3.0

$r_{nc,0}$	2.66nm	3.02nm	3.34nm	3.66nm	3.93nm	4.2nm
A	0.93	0.9	1.1	0.64	0.72	0.64
B	10.57	10.61	10.74	10.8	10.79	10.94
C	141.02	142.21	175.61	133.39	155.41	150.87
D	10.62	10.51	9.5	10.2	9.47	9.44

R=4.0

$r_{nc,0}$	2.69nm	3.06nm	3.39nm	3.7nm	3.98nm	4.23nm
A	0.01	0.78	0.91	0.86	0.85	1.04
B	0.01	10.35	10.19	10.22	10.29	9.82
C	115.56	109.98	107.15	106.91	110.2	88.22
D	10.58	10.96	11.15	11	10.83	11.6

R=5.0

$r_{nc,0}$	2.69nm	3.06nm	3.4nm	3.7nm	3.98nm	4.24nm

A	-0.01	0	0.21	0.18	0.13	0.02
B	5.99	8.13	10.03	10.02	10	-4.4
C	95.96	98.12	100.02	100.01	100	114.61
D	10.84	10.62	10.46	10.35	10.26	9.97

R=10.0

$r_{nc,0}$	2.66nm	3.04nm	3.37nm	3.68nm	3.96nm	4.23nm
A	-0.23	-0.45	0	0	0.01	0.01
B	1.15	-4.55	0	0	9.95	0
C	65.08	44.24	52.51	43.15	99.96	64.68
D	11.1	11.33	11.05	11.05	9.67	10.65

Table 4.1 shows lists of inferred values *A*, *B*, *C*, &*D* for all measured $r_{nc,0}$ and *R* values. Based upon these values, in Figure 4.5a we plot the values of P_{nc} extrapolated to 300 K as a function of *R*, and in Figure 4.5b we plot P_{nc} (quantified by $log_{10}(P_{nc})$) as a function of inverse temperature. Nanocluster vapor pressures near 300 K, are of order 10^{-4}-10^{-3} Pa for nearly all circumstances. These values, are substantially higher (by multiple orders of magnitude) than ammonium sulfate surface vapor pressures inferred by Marti et al [161] for larger nanoparticles (50-300 nm diameters) under dry conditions, and even larger than surface vapor pressure of larger DMAS particles inferred by Lavi et al [162], who found that DMAS particles have lower vapor pressures than ammonium sulfate submicrometer particles. However, our surface vapor pressure extrapolations are only an order of magnitude larger than the vapor pressure of 50-300 nm sulfuric acid-water nanoparticles (76% sulfuric acid by mass) estimated by Marti et al (of order 10^{-5} Pa). At atmospheric pressure, our extrapolated vapor pressures correspond to nanocluster surface vapor concentrations in the ppbv (parts per billion by volume) range. Ambient sulfuric acid concentrations are typically in the pptv (parts per trillion by volume range) [125,163],

and dimethylamine concentrations are expected to be in a similar, sub-ppbv range [163]. Despite the approximations employed in analysis as well as the extrapolation used to 300 K, our error in vapor pressure estimation is presumably not several orders of magnitude, and our measurements strongly suggest the surface vapor pressures of dry DMAS nanoclusters are higher than ambient vapor pressures for their constituents. We also note the vapor pressures inferred are sensitive to the choice of m_v, but not to an extent which alters the order of P_{nc} values. Such high surface vapor pressures suggest that it is excess sulfuric acid evaporating from dry clusters, and likely arise because of a Kelvin model-like behavior for nanoclusters; the Kelvin effect [121] predicts that the vapor pressure at the surface of a nanocluster will increase over the bulk value by a factor of $exp\left(\frac{2\gamma m_v}{\rho kTr_{nc}}\right)$, where γ is the effective surface energy density of the nanocluster (i.e. the surface tension, expected to high for ionically bond systems). High surface energy densities can thus lead surface vapor pressures enhanced by several orders of magnitude over bulk values (hence our measurements are in-line with the vapor pressure estimations of Marti et al [161] for larger, nearly dry sulfuric acid particles), creating a barrier to dry nanocluster growth. The observation of high surface vapor pressures for nanoclusters is further supported by attempts to analyze R = 0 (pure dimethylamine) and R = ∞ (pure sulfuric acid) nanoclusters; in these circumstances nanoclusters evaporate almost completely at room temperature prior to transmission through ion mobility spectrometers, such we could not detect clusters from pure dimethylamine or pure sulfuric acid solutions. Interestingly, a clear nanocluster size dependency of the vapor pressure (increasing vapor pressure with decreasing size) is not observed in the nanocluster size range examined, in fact at large R values an increase in P_{nc} with increasing radius is observed. This is likely because of compounding influences of size dependent chemical composition (from the nanocluster formation process in these experiments) and direct size influences on the surface vapor pressure, and because the size range examined itself was relatively narrow. An increase in P_{nc} is additionally observed with increasing R, and hence increasing sulfuric acid

content, further evidence that sulfuric acid is the major evaporating species from DMAS nanoclusters.

4.3.3 Nanocluster Water Vapor Uptake

While our thermostability measurements suggest that dry DMAS nanoclusters (r_{nc}= 2.5-4 nm) may not grow by condensation purely of sulfuric acid and dimethylamine under ambient conditions, our results do not preclude DMAS constituents from being the primary species involved in the earlier stages of new particle formation (as smaller clusters have been found stable) [124,127]. Further, as pure, dry DMAS nanoclusters were examined, our results do not preclude other species from condensing onto DMAS and reducing surface vapor pressures, thus stabilizing them. One such species that could stabilize nanoclusters, is water vapor. It has been shown (again by Marti et al [161]) that the sorption of water vapor by particles composed of sulfuric acid or ammonium sulfate decreases by orders of magnitude, even in instances where the extent of sorption leads to particles which are still primarily sulfuric acid or ammonium sulfate. We therefore use differential mobility analyzer-DT-IMS experiments [137,147] to examine the extent of water uptake by DMAS nanoclusters as function of nanocluster dry radius. Arrival time distributions, in which CPC inferred nanocluster counts per second are plotted as functions of time required for nanoclusters to arrive at the CPC, are shown in Figure 4.6(a-e) for R = 2 nanoclusters with 5 selected initial sizes and at 10 separate relative humidities. Evident is the shift in spectra to longer arrival times with increasing relative humidity for all initial nanocluster radii. As a negative control experiment, electrospray generated cesium iodide nanoclusters [135] were also measured (results not shown), and no change in the arrival time distributions was observed for these nanoclusters at any relative humidity in the range examined. The shift in arrival time brought about by increasing relative humidity is thus indicative of a decrease in the electrical mobility of DMAS nanoclusters (i.e. water vapor did not change the DT-IMS calibration curve), which, in turn, is indicative of water uptake by these nanoclusters. Water uptake by larger alkylammonium salts has been observed in prior studies [128,162]; thus our

observation of water uptake by nanoclusters under sub-saturated conditions is not surprising. To quantify the extent of uptake, following prior work [164] we calculated the growth factor (GF) for all nanoclusters as a function of relative humidity (RH), via the equation:

$$\mathrm{GF} = \frac{(r_{nc}+r_{gas})_{RH}}{(r_{nc}+r_{gas})_{RH=3.7\%}} \quad (3)$$

We include the gas molecule radius in GF calculations for consistency with Oberreit et al [137], and r_{nc} in equation (3) is inferred using equation (1) as well as the DT-IMS calibration curve with the peak in arrival time distributions. The baseline relative humidity of 3.7% was the lowest humidity achievable in experiments. Growth factors as functions of relative humidity are shown in Figure 4.6f. For nanoclusters of all measured initial radii, growth factors increase with increasing relative humidity, but remain in the 0.98 – 1.13 range. With the exception of the smallest nanoclusters examined (r_{nc} = *1.55 nm*), we find that for a given relative humidity, growth factors increase slightly with initial nanocluster radius, suggesting that larger nanoclusters uptake proportionally more water vapor. For example, at a relative humidity of 29%, measurements suggest that nanclusters with initial radii of 2.1 nm uptake ~174 water vapor molecules on average (based on the change in volume) and correspondingly are ~8.2% water by mass, while initially 3.05 nm radius nanoclusters uptake ~659 water molecules and are 9.9% water by mass. At the highest relative humidity examined, measurements suggest that initially 3.05 nm nanoclusters uptake ~1860 water molecules and are ~23.7% water by mass. Overall, the evidence for water uptake under conditions resembling ambient air is clear in these IMS-IMS experiments, hence such nanoclusters should be modeled as partially hydrated species. However, as has been found quantum mechanical calculations for smaller DMAS clusters [140], the extent of hydration is insufficient to permit modeling nanoclusters as aqueous droplets containing dissolved cations and anions. Future work, both experimental and computational, will be necessary to better resolve the internal structures of such hydrated nanoclusters.

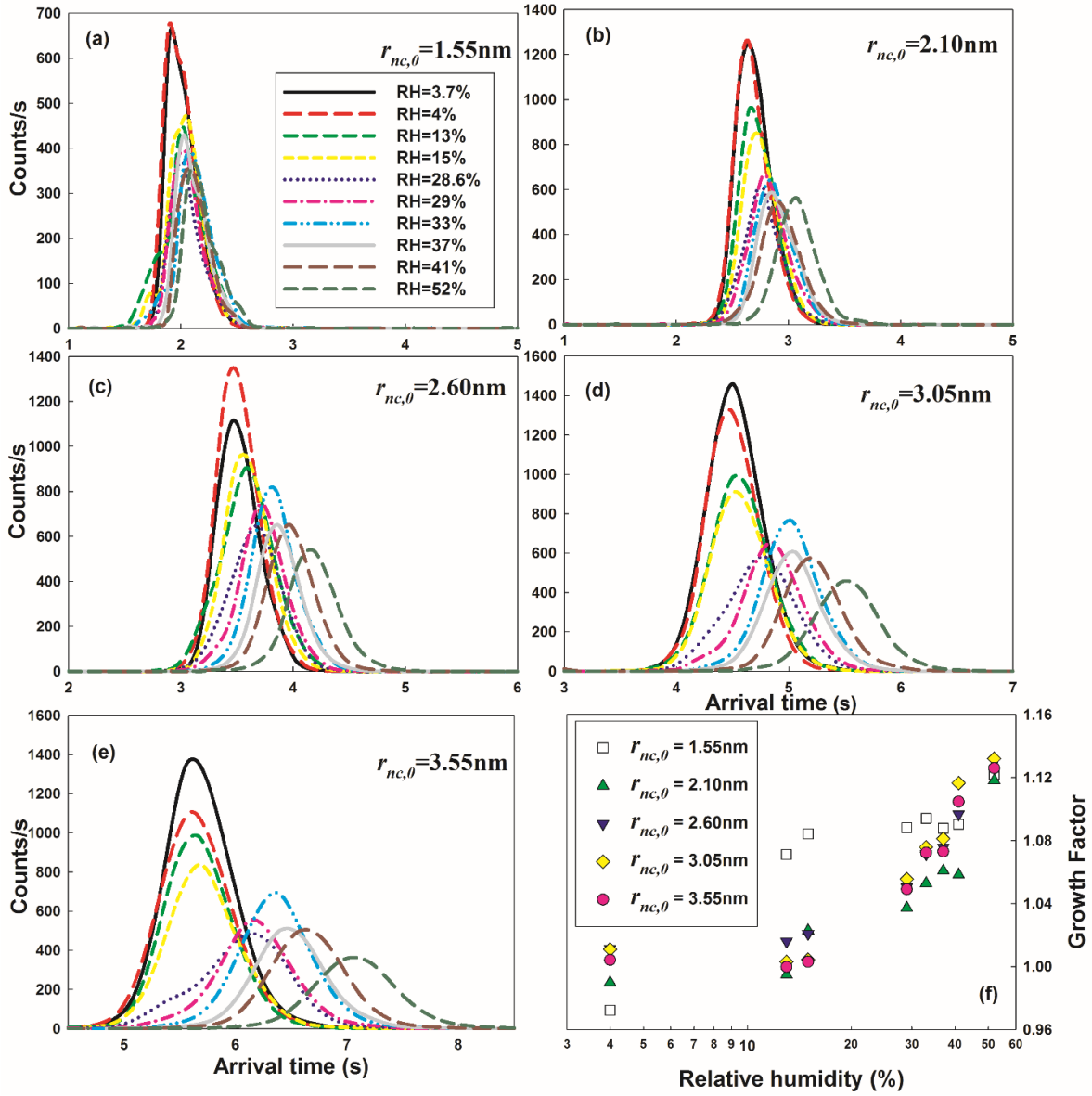

Figure 4.6 (a-e) Arrival time distributions for 5 separate dry nanocluster radii and with 10 separate relative humidities (RHs) in the drift tube ion mobility spectrometer. **(f.)** The inferred growth factor for nanoclusters of 5 different dry radii as a function of relative humidity.

4.4 Conclusions

A series of ion mobility spectrometry based measurements have been performed to study the physicochemical properties of dimethylamine-sulfuric acid (DMAS)

nanoclusters in effective diameter range <8.5nm ($2*r_{nc}$). Independent of the ratio of sulfuric acid to dimethylamine in electrospray solutions used in cluster generation, from IMS-MS measurements we find that the average density of dry DMAS nanoclusters is ~1567 kg m^{-3}, which is inferred from IMS-MS results through the polarization corrected free molecular limit of the Stokes-Millikan equation [151]. This value is slightly (~10%) higher than has been reported for larger DMAS nanoparticles and submicrometer particles [128,162], suggesting that the nanoclusters studied here may have contained excess sulfuric acid (note that for the multiply charged nanoclusters in IMS-MS analysis, adducts prevent clear chemical identification from mass measurements alone). Thermostability measurement inferred vapor pressures for DMAS nanoclusters suggest that their surface vapor pressures near 300 K are orders of magnitude higher than the vapor pressures of sulfuric acid or dimethylamine in ambient air [163,165], and are an order of magnitude higher than the vapor pressure found for larger sulfuric acid nanoparticles [161]. Measurements hence suggest that it is excess sulfuric acid which dissociates from nanoclusters (as the vapor pressure increases with increasing sulfuric acid vapor pressure) and capillarity effects (i.e. the Kelvin effect) enhance DMAS nanocluster vapor pressure to an extent where dry nanoclusters would not necessarily be stable in the ambient. However, IMS-IMS measurements of water uptake show that DMAS nanoclusters uptake water and are hydrated at relative humidities beyond 10% (near 300 K). Such water uptake likely serves to stabilize nanoclusters (reducing surface vapor pressures). The measurements reported here are for an important size range between that of clusters and nanoparticles. However, these latter two size ranges are studied much more frequently than nanoclusters; mass spectrometry lends itself to cluster analysis [124,125], while differential mobility analysis (and various forms aerosol mass spectrometry [1,166]) are applicable to larger nanoparticles and submicrometer particles. Unfortunately nanocluster concentrations are often too low to detect via cluster mass spectrometry or by aerosol mass spectrometry in the ambient. Nonetheless as the properties of species in this size range ultimately affect particle growth in the ambient (i.e. all particles originating in

new particle formation events were once nanoclusters) it is important to develop techniques amenable to nanocluster characterization. The tandem techniques utilized here may find continued utility in nanocluster analysis.

Acknowledgements

This work was supported by National Science Foundation Grant No: CHE-1011810. H. O. acknowledges support from a University of Minnesota Doctoral Dissertation Fellowship. C.L.A. acknowledges support from a Ramon Areces Foundation Fellowship.

Chapter 5: Constant Number Monte Carlo Simulation of Non-Continuum Coagulation & Aggregation

Abstract

In various gas phase systems, coagulation/aggregation is an essential growth mechanism for nanoparticles growth. Nanoparticles growth through collisions often fall into the transition regime. And the interaction potentials (van der Waals potential) between colliding entities might enhance/reduce the growth rate. To accurately capture and predict the nanoparticle growth through coagulation/aggregation, transition regime and potentials are needed to incorporate into simulation models. Yet both effects are often too simplified or not considered at all. In this study, a Constant Number Monte Carlo (CNMC) method is utilized to simulate coagulation and possible aggregation to predict the evolution of size distribution and even the morphology of outcome nanoparticles. Average Knudsen number $\overline{Kn}$ and average diffusive Knudsen number $\overline{Kn_D}$ of the system determines which model to use for growth simulation, as growth is a dynamic process, thus it is important to monitor the evolution of $\overline{Kn}$ and $\overline{Kn_D}$ to evoke correct models for different growth stages. Collision kernel developed previously for transition regime is incorporated into the code. Comparisons are made to trajectory based Langevin Dynamics Simulations. The evolution of $\overline{Kn}$ and $\overline{Kn_D}$ of the system for both models agree well with each other. Oleic acid coagulation experiments were performed with a coagulation chamber which couples to scanning mobility particle sizer system, and both size distribution and the evolution of $\overline{Kn_D}$ with respect to $\overline{Kn}$ of the system show good agreements. By monitoring $\overline{Kn}$ and $\overline{Kn_D}$, the dynamic growth process through coagulation from free molecular to transition and further into continuum regime is revealed without the restriction of the same regime for the entire growth process. Van der Waals potentials is also incorporated into CNMC to account for interactions, and other forms of interaction is also possible to be included providing with known enhancement factors built into the coagulation rate. For coagulation, a single evolution curve of $\frac{d\overline{Kn}}{d(\ln(\overline{Kn_D}))}$ as a function of average Knudsen number $\overline{Kn}$ is observed regardless of the

various different initial coagulation starting points, and it is the same evolution curve even with the presence of different strength of van der Waals potentials. An extension to aggregation simulation with CNMC is also discussed at the end for future work.

5.1 Introduction

Particle-particle collision driven growth in the gas phase, which leads to coagulation (sticking and complete coalescence of the colliding particles) or aggregation (sticking with incomplete coalescence), is industrially important process; high temperature flow reactor and flame systems, as well as thermal and non-thermal plasma systems can be used for the scalable production of a variety of inorganic materials, and collisional growth is a key feature of all such systems [7,167]. To better predict the output product in gas phase synthesis systems, it is necessary to develop models of collisional growth and incorporate such models into predictions of produced particle size distributions and morphology [85,168-170]. While considerable effort has been devoted to this purpose over the past several decades, there are still features of collisional growth process which have been difficult to incorporate into growth models. These features, which are outlined subsequently, serve as motivation for this study, whose goal is to develop an improved constant number Monte Carlo model of particle coagulation and aggregation, applicable to gas phase synthesis reactors.

Accurate models of particle growth require proper consideration of three main physical phenomena: (1) the non-continuum transport of particles as they collide with one another [171] , (2) the influence particle-particle potential interactions have on collisions [172], and (3) both the effect of particle morphology [173] on the collision rate and the evolution of particle morphology as growth occurs [90,174]. Issue (1) arises because in the early stages of growth in the gas phase (from vapor phase precursors) particles are nanometer sized or submicrometer sized entities, and are surrounded by gas with a mean free path which is also tens of nanometers or larger. In this instance, the Knudsen numbers (Kn) of particles, defined as the ratio of the gas hard sphere mean free path to characteristic

particle size, are substantially greater than zero, hence continuum transport theory must not be used to predict the drag force on particles and particle diffusion coefficients. More importantly, under these conditions, the relative thermal persistence distances of particles, which, for two particles is proportional to the sum of their diffusion coefficients divided by the sum of their mean thermal speeds, are also several nanometers or larger (increasing with decreasing pressure). The ratio of the persistence distance to the combined particle size (collision distance) for most particle pairs is defined as the diffusive Knudsen number (Kn_D). It is also typically greater than zero early in gas phase processes, and for this reason collisional growth in the gas phase cannot be modeled with purely diffusive equations (i.e. equations based upon Fick's Law). Noted by Thajudeen et al [29,174,175], as growth in the gas phase occurs, the distribution of particle Knudsen numbers (Kn) and diffusive Knudsen numbers (Kn_D) continue to evolve, and this evolution needs to be accurately incorporated into particle growth models. Issue (2) becomes critical as van der Waals potentials [176] and coulombic potentials [17717177178179179179] can enhance/diminish collision rates. Issue (3) arises when particles do not fully coalesce with one another upon collision, leading to the formation of aggregates. Both aggregate formation and the resulting influence aggregate morphology has on subsequent aggregate-aggregate collisions must be considered, in conjunction with transition regime and potential interaction influences.

The most exact method to account for all of these effects involves the use of particle trajectory models, wherein non-continuum equations of motion are solved numerically for all particles within a population. Along these lines, a number of studies have used trajectory based simulations, often using the Langevin equation or approximations to it, to model the evolution of particles in the gas phase [29,111,178]. Notably, Thajudeen et al [29] performed Langevin Dynamics Simulation (LDS) for coagulation and aggregation to reveal the evolution of average Knudsen number and average diffusive Knudsen number. The simulation is performed in a cubic domain and each particle is tracked by dimensionless Langevin equation. Although computationally

expensive and the limited number of monomers in an aggregates (<300), it will serve as a validation for current work for both coagulation and aggregation. Regrettably, the computational requirements of trajectory models limit their use to either limited time scales (i.e. the early stages of growth) or they too must incorporate coarse-grained physics of the growth process. A more computationally feasible alternative to trajectory models are population balance equations, utilized in a number of prior studies [169,179-181] and highlighted in a special issue of *Chemical Engineering Science* in 2002 ("***Population balance modelling of particulate systems***"). In population balance models, the number concentrations of particles of varying size and/or morphology are monitored with respect to one another through a series of differential equations. Specifically, the kinetics of coagulation is described by Smoluchowski theory [182], which predicts particle number concentrations as a function of size over time through solution to a number of integrodifferential equations that can be solved analytically only in a few cases. For aerosol systems, numerical methods are hence often employed to simulate coagulation. Monte Carlo simulations of coagulation have become increasing popular, since they can efficiently and accurately simulate systems with large number of particles, can be performed without assumptions about the shape of the size distribution of particles (as are used in lognormal distribution models or coarse sectional models), do not require simulation of particle motion (such as the simulations in the previous section). Different Monte Carlo simulation techniques have been used to simulate coagulation, including time-driven /event-driven Direct Simulation Monte Carlo (DSMC) [181,183], in which the volume of simulation domain is held constant (with the total number of particles decreasing over time by collisions), and constant number Monte Carlo [28,184], in which the number of tracked particles is held constant while the simulation volume grows. In DSMC, eventually the number of particles in the system will decrease to a point where accuracy of simulation is in question and the simulation has to terminate when the system reduces to a single particle. This can be corrected by using constant-number Monte Carlo simulation, which has been used to successfully simulate multicomponent and multi-

process systems [170,180,185]; thus, we employ it here in examining growth dynamics with our new transition regime collision rate equation with and without van der Waals potential.

To better simulate collisional nanoparticle growth through coagulation and aggregation with incorporation of transition kinetics, potential influence and particle morphology, this study is divided into three sections followed by a short conclusions for this chapter. Firstly, coagulation simulation with CNMC is presented with a description of the method, comparisons to Langevin Dynamics Simulation and coagulation experiments, and finally simulation results. Secondly, coagulation considering the singular contact van der Waals potential is handled. Last but not least, the extension to aggregation with CNMC for future work is discussed.

5.2 Coagulation

5.2.1 Methods

5.2.1.1 Constant Number Monte Carlo (CNMC)

Constant number Monte Carlo is employed to simulate particle growth via coagulation, i.e. to solve the Smoluchowski coagulation equation with and without the van der Waals potential interactions between colliding entities. In this study of coagulation, the domain is assumed to comprise only spherical particles and only binary collisions are considered. The coalescence coefficient is assumed to be 100%, such that when two spherical particles collide, a new larger spherical particle is formed with total mass being conserved. It is also assumed that particles always bind to one another upon collision, such that the collision rate equals the coagulation rate. Based on the colliding system (potential strength) and material properties of colliding entities (initial size and density), $Kn_{D_{ij}}$ between particle i and particle j can be calculated by $Kn_{D_{ij}} = \frac{(kTm_{ij})^{1/2}\eta_C}{f_{ij}(a_i+a_j)\eta_{FM}}$ and H_{ij} can be calculated by $H_{ij} = \frac{4\pi Kn_{D_{ij}}^2 + C_1 Kn_{D_{ij}}^3 + (8\pi)^{\frac{1}{2}} C_2 Kn_{D_{ij}}^4}{1 + C_3 Kn_{D_{ij}} + C_4 Kn_{D_{ij}}^2 + C_2 Kn_{D_{ij}}^3}$. The collision kernel with dimension β_{ij} is giving by $\beta_{ij} = \frac{H_{ij} f_{ij} (a_i+a_j)^3 \eta_{FM}^2}{m_{ij}\eta_C}$. β_{11} is defined as

the collision kernel between two monomers with the same initial radius a_0. Once all collision kernels β_{ij} of all possible colliding pairs in the system are calculated, dimensionless relative coagulation kernel k_{ij} is defined by $k_{ij} = \frac{\beta_{ij}}{\beta_{11}}$. For cases where there is no van der Waals potential, $\eta_C = \eta_{FM} = 1$.

Simulations begin with monodisperse spherical particles with radius a_0, with the total number of particles *N=10000*, initial total number concentration C_0 at temperature T=300k and under standard atmospheric pressure. At each step, a random number *r* is drawn from a uniform distribution (0,1). A random pair of particles *i* and *j* is picked, and the coagulation kernel k_{ij} of this pair is calculated from which the probability $p_{ij} = k_{ij}/k_{max}$ is determined, where k_{max} is the maximum coagulation kernel among the whole system (k_{max} is used instead of using $\sum k_{ij}$ in the denominator to increase the acceptance rate and speed up computations). If the calculated probability is smaller than *r*, coagulation between particles *i* and *j* is accepted. If not, a new pair is selected and the process is repeated until coagulation happens in that time step. The newly formed particle, with its size determined via conservation of mass of the colliding pairs, is stored in the position of old particle *i* while a randomly selected particle *k* from the existing distribution of particles is copied into the element vacated by particle *j*. Each particle size after collision is recorded and for each particle, the Knudsen number Kn_i is calculated as $Kn_i = \lambda/a_i$ where λ is the mean free path of background gas. Kn_i governs momentum transfer to particles; the friction factor for a spherical particle is determined as $f = 6\pi\mu a_i/C_C(Kn_i)$, where $C_C(Kn_i)$ is the slip correction factor determined from the Millikan oil drop measurements. Therefore, Kn_i is an input into collision rate calculations, and determines Kn_D. Coagulation leads to a system of particles evolving in both Kn_i (a single particle parameter) and Kn_D (a two particle parameter), and the evolution of the distribution of these numbers can describe a coagulating system. Therefore, to monitor particle growth, average Knudsen number $\overline{Kn}$ and average diffusive Knudsen number $\overline{Kn_D}$ of the system after each time step will be calculated through $\overline{Kn} = \frac{\sum_{i=1}^{N} Kn_i}{N}$ and

$\overline{Kn_D} = \frac{2\sum_{i=1}^{N}\sum_{j=i+1}^{N} Kn_{D_{ij}}}{N(N-1)}$. The total time passed t_κ after the κ^{th} coagulation event is given by $t_\kappa = \sum_{i=1}^{\kappa} \Delta t_\kappa$ where $\Delta t_\kappa = \frac{2\tau_C}{\langle k_{ij} \rangle} \cdot \frac{1}{N}\left(\frac{N}{N-1}\right)^{\kappa}$ and $\tau_C = \frac{1}{\beta_{11} C_0}$ is a dimensionless time, $\langle k_{ij} \rangle = \sum_i^N \sum_{j \neq i}^N \frac{\beta_{ij} c_i c_j}{\beta_{11} C^2} = \frac{\sum_i^N \sum_{j \neq i}^N k_{ij}}{N(N-1)}$ is the dimensionless ensemble average kernel with $k_{ij} = \frac{\beta_{ij}}{\beta_{11}}$.

5.2.1.2 Coagulation Experiment

Coagulation experiments were also performed with oleic acid droplets for direct comparison with CNMC coagulation simulations, as for neutral oleic acid in air the van der Waals influence is negligiable (low Hamaker constant). Figure 5.1(a) shows the experimental schematic. To generate oleic acid droplets, a TSI electrospray (TSI, Minneapolis) and TSI atomizer (TSI, Minneapolis) were used separately. Both of them can generate monomodal polydisperse size distributions with a smaller mean size and narrower distribution producible with electrospray. Different solutions are used for these two aerosol generators. For the atomizer, oleic acid solutions were prepared by adding oleic acid to methanol with resulting oleic acid molar fractions of 0.05% and 0.08%. With the electrospray, ammonium acetate was also added to make the solution electrically conducting, and the oleic acid mole fractions were as 2.5% and 5%. Atomizer generated aerosols passed through an activated carbon diffusion dryer to capture extra methanol. A homemade electric precipitator (ESP) was used to remove charged particles downstream, prior to the coagulation chamber. Neutral Oleic acid droplets entered the coagulation chamber, which was a steel cylinder chamber with two cone shape ends. Due to the expansion of the flow near the entrance, even though with a low flow velocity, vortices were likely induced near the chamber walls and the particles traversing the edge of the chamber experience different coagulation time than those traveling along the centerline. To minimize this complication brought about by chamber geometry, a sampling scheme with two concentric stainless steel tubes was used; 1.2 lpm of pure

clean nitrogen for dilution was supplied to the outer tube with 10mm inner diameter and then only 0.3 lpm aerosol from the coagulation chamber is drawn into the inner tube with a 6.4mm outer diameter (4.2cm inner diameter) while in total 1.5 lpm diluted aerosol is used for detection and the remaining aerosol exhaust exit the chamber at the chamber outlet. The dilution along with short transport tubes between the coagulation chamber and downstream detectors was to minimize particle deposition during transportation. A TSI differential mobility analyzer was coupled to a TSI condensation particle counter for size distribution measurements. The sampling tubes were fixed at the centerline of the chamber to only pick up aerosols traveling along these centerlines. Two sampling points were examined, and are denoted as sampling point A and B in figure 5.1; these points were used as the initial and final distributions for comparison to simulations. With the sampler positioned at point B, the fluid flow streamlines, simulated via FLUENT, are shown in figure 5.1b. These simulations suggest that with dilution and centerline sampling, the particles sampled travel along the center streamlines only without being entrained into vortices. Characteristic size distributions from experiments are plotted in figure 5.1c for atomizer generated aerosol. Monomodal size distributions shift from left to right as particles grow larger through coagulation. Although the total number concentration drops due to coagulation, the number concentration of larger particles increased which indicts particle growth, and the particle volume concentration is roughly conserved. Each sampling took place at least 10mins after particle generation through electrospray or atomizer, assuming oleic acid vapor reach equilibrium within the coagulation chamber such that evaporation has negligible effect on the coagulation results.

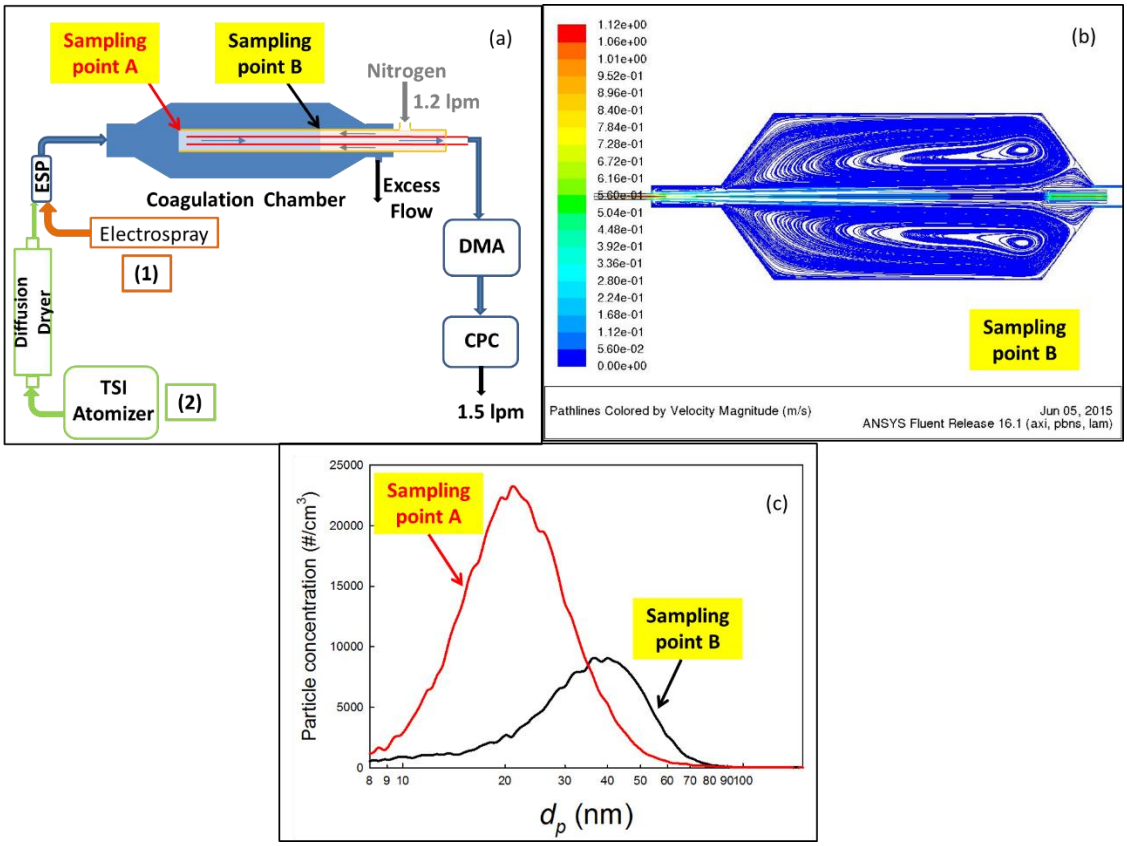

Figure 5.1 (a) Experimental setup: ESP (Electric Precipitator), DMA(Differential Mobility Analyzer), CPC(Condensation Particle Counter); **(b)** Contour plot of streamlines from CFD simulations at sampling point B, streamlines colored by velocity magnitude; **(c)** Size distribution for two stages of coagulation as initial (point A) and end (point B).

5.2.2 Results

Without potentials, $\eta_C = \eta_{FM} = 1$, and different initial states of Kn_0 and Kn_{D_0} were assigned to different simulations by varying initial monomer size and material density of the particles (changing their initial mass). Again, at each timestep, average Knudsen number $\overline{Kn}$ and average diffusive Knudsen number $\overline{Kn_D}$ were calculated. Coagulation can also be simulated by Langevin Dynamics Simulation (LDS). Thajudeen et al (2015) simulated coagulation by placing N=10000 particles/monomers in a cubic

box and monitor the motion of each particle by a Langevin equation. Thajudeen et al (2015) also calculated $\overline{Kn}$ and $\overline{Kn_D}$ from simultions, enabling comparison to CNMC calculations with the same Kn_0 and $Kn_{D\,0}$. Figure 5.2 shows the evolution of $\overline{Kn}$ and $\overline{Kn_D}$ as particles growing through coagulation both through Langevin Dynamics Simulation (red square) and through Constant Number Monte Carlo (CNMC) simulation (green circle) in this study. Both simulation methods reveal the same pathway for $\overline{Kn}$ and $\overline{Kn_D}$ as two lines collapsed with each other. This demonstrates that the CNMC method is indeed capable of simulating coagulation with implementation of a collision kernal appropriate for all regimes (free molecular, transition and continuum). As in the Langevin Dynamics Simulation, the total number of particle in the fixed simultion box decreases as coagulation proceeds, eventually there will be not enough particles to represent the whole system. As shown in figure 5.2, in LDS the coagulation can only go to $\overline{Kn} \approx 0.9$ and $\overline{Kn_D} \approx 0.2$ with fewer scattered datapoints suffering from higher uncertainty. Conversely, CNMC can simulate coagulation with a much better range without sacrificing accuracy, in this case $\overline{Kn}$ and $\overline{Kn_D}$ goes to 0.001 before the termination of calculation in figure 5.2.

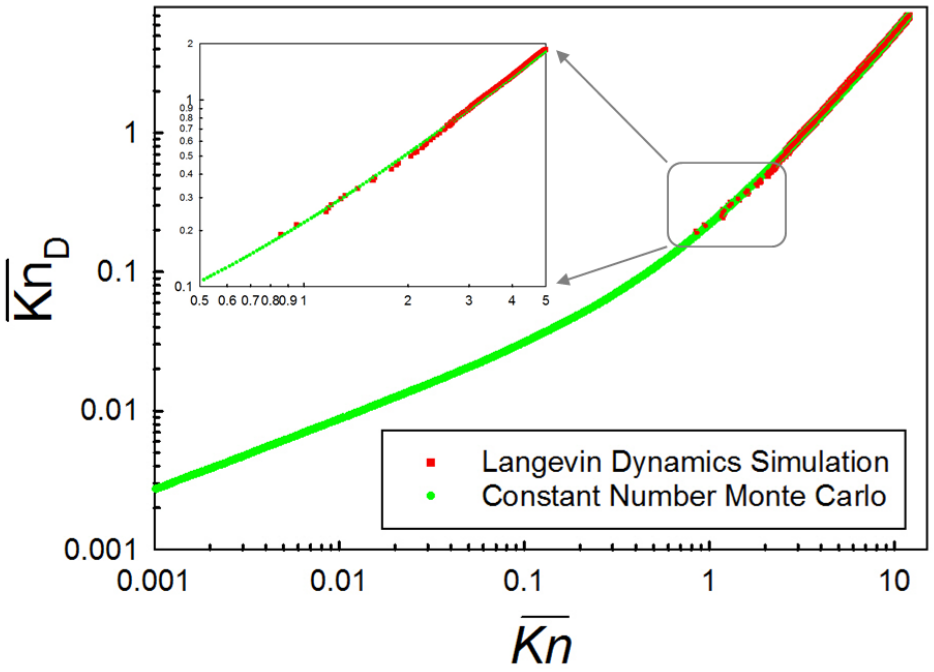

Figure 5.2 The evolution of average diffusive Knudesen number with respect to the averagre Knudsen number for a coagulation case starting with monomode monodispersed aerosols with initial average values as Kn_0 = 7.0 and Kn_{D0}=12.0. Red squares are results from Langevin Dynamics Simulation and Green circle are from this study with Constant Number Monte Carlo simulation. A zoom-in subplot in also provided at the up-left cornor.

Size distributions are also extracted from CNMC simulations and compared to experimental measurements. Figure 5.3 shows three sets of experimentally measured size distributions (with the initial size distribution and final size distribution colored black and red, respectiely), with all distributions are normalized by the maximum value. The tables on the right of the Figure 5.3 display the average Knudsen number $\overline{Kn}$ and average diffusive Knudsen number $\overline{Kn_D}$, respectively, for each size distribution. To calculate these $\overline{Kn}$ and $\overline{Kn_D}$ values, each experimental size distribution was converted to a frequency function f_i for a number of size bins and with the total number of particles N_{total}, the number of particles N_i was calculated $N_i = N_{total} * f_i$ in each size bin i. The $\overline{Kn}$ and $\overline{Kn_D}$ for experiments were calculated the same way as in simulations, i.e. $\overline{Kn} =$

$\frac{\sum_{j=1}^{N_{total}} Kn_j}{N}$ and $\overline{Kn_D} = \frac{2\sum_{j=1}^{N_{total}} \sum_{k=j+1}^{N_{total}} Kn_{D\,jk}}{N_{total}(N_{total}-1)}$. For experimental Knudsen number calculation, the total number of particles N_{total} and number of bins were varied to ensure that the choice of bin size did not influence $\overline{Kn}$ and $\overline{Kn_D}$.

The initial distributions input into CNMC simulations are also ploted as open circles in figure 5.3, as are distributions from later time steps. The initial experimental distribution in 5.3 (a) & (b) have almost identical initial mode values (21nm and 21.6nm) but slightly different distribution shapes, which is captured by their differing average $\overline{Kn}$ and $\overline{Kn_D}$ values. The coagulation growth from these two distributions results in similar distribution shapes but with different mode values (39nm and 43nm), and different calculated $\overline{Kn}$ and $\overline{Kn_D}$ values, demonstrating that slight differences in initial size distribution do have consequences in size distribution evolution. Blue dashed lines denote the size distributions which have the closest $\overline{Kn}$ and $\overline{Kn_D}$ values (within 5% difference) compared to the experimental end point. These simulated size distributions (blue dashed lines) also recover the shape of the experimentall measured size distributions, which are slightly asymmetric with a longer tail at the lower size range. However, although the average $\overline{Kn}$ and $\overline{Kn_D}$ value are almost identical to experiments, the peak values from simulations are consistently at smaller diameters than experiments shifts. This might be due to the intrumental limits in recovering the size distributions near the detection limit of the instrument employed, diffusive and inertial losses of particles, or oleic acid evaporation, which are not considered in simulations. Size distributions at later time steps from simulations are also ploted in figure 5.3 (green short dash lines), which have the same peak (mode) diameter values as the experiments. In these cases the average $\overline{Kn}$ and $\overline{Kn_D}$ values deviate by 13%~17% from the experimental values. In total, this comparison reveals that the CNMC method does a reasonable job in mimicking the experimentally observed evolution of size distribution functions for aerosol particles in the tranistion regime.

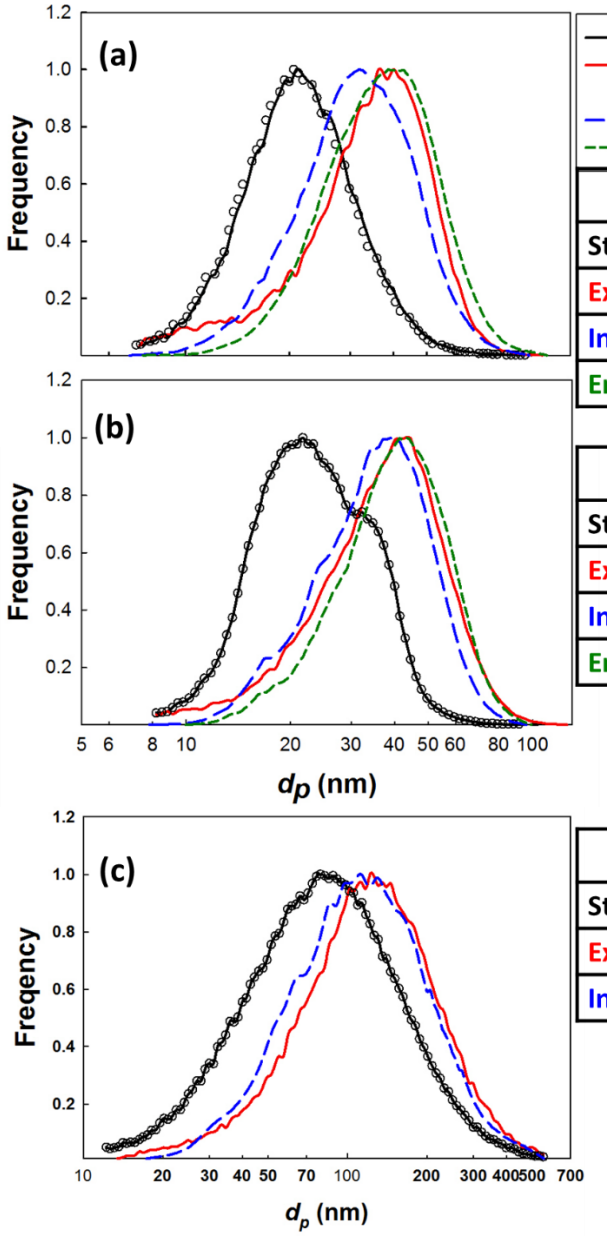

(a)	$\overline{Kn}$	$\overline{Kn_D}$
Start/Initial	6.49	0.78
Experimental End	4.86	0.48
Intermediate Time Step	4.82	0.49
End Time Step	4.07	0.39

(b)	$\overline{Kn}$	$\overline{Kn_D}$
Start/Initial	7.06	0.86
Experimental End	4.37	0.42
Intermediate Time Step	4.34	0.43
End Time Step	3.81	0.35

(c)	$\overline{Kn}$	$\overline{Kn_D}$
Start/Initial	2.22	0.15
Experimental End	1.49	8.95e-2
Intermediate Time Step	1.46	8.95e-2

Figure 5.3 Size distributions from experiments and simulations. Solid lines represent the size distributio from Oleic acid coagulation experiments with black is the initial distribution and red is the final distribution; Open circles are initial distribution in CNMC simulation. Blue dashed line and green short dash line are from CNMC at earlier and later time step. The corresponding average Knudsen numbers ($\overline{Kn}$ and $\overline{Kn_D}$) are also shown in the up-right subtable.

We find that the evolution of $\overline{Kn}$ and $\overline{Kn_D}$ in both experiments and simulations is a simple yet meaningful way to monitor growth of particles in the transition regime. In simulating coagulation with varying initial Kn_0 and $Kn_{D,0}$, we obtain curves similar to the curve in 5.2, with varying Kn_0 and $Kn_{D,0}$ values simply shifting curves. Interestingly, with monomodal initial distributions, intersecting curves are not observed, suggesting that all results, if normalized properly, may be collapsed to a single curve describing the evolution of Kn_0 and $Kn_{D,0}$ with respect to one another, via coagulation. As shown in figure 5.4, in which each symbol represents one simulation result point and the same symbols represent a continuously growing system from higher Kn value, irrespective of the different starting state of the systems, $\overline{Kn}$ is found to be solely a function of $\frac{d\overline{Kn}}{d(\ln(\overline{Kn_D}))}$, where $\frac{d\overline{Kn}}{d(\ln(\overline{Kn_D}))}$ is calculated by $\frac{\overline{Kn}_{i+1}-\overline{Kn}_i}{\ln(\overline{Kn_D}_{i+1})-\ln(\overline{Kn_D}_i)}$ while i is selected timesteps from the simulation. Furthermore, three regimes can be observed following the curvature of the curve which are free molecular ($Kn > 7.1$), transition ($0.04 < Kn < 7.1$) and continuum regime ($Kn < 0.04$) in momentum transfer.

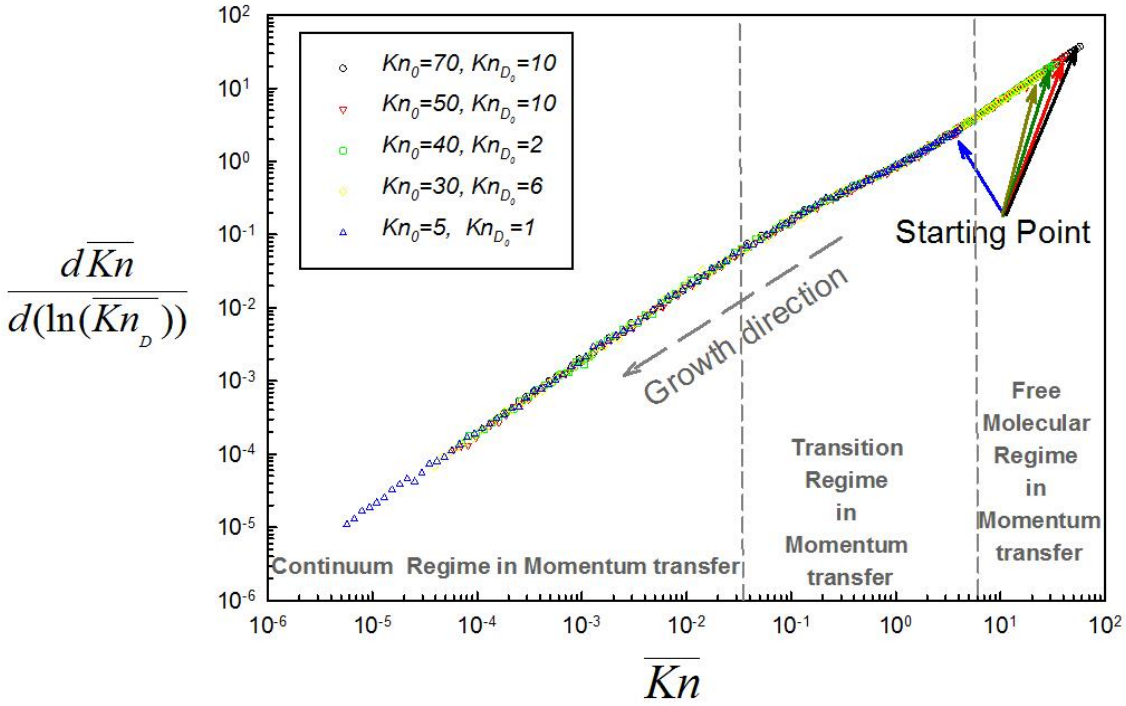

Figure 5.4 The results of preliminary Monte Carlo simulations, in terms of $\overline{Kn}$ versus $\frac{d\overline{Kn}}{d(\ln(\overline{Kn_D}))}$. Without the van der Waals potential, the average Knudsen number $\overline{Kn}$ as a function of $\frac{d\overline{Kn}}{d(\ln(\overline{Kn_D}))}$ is displayed for different systems starting with different initial values of Kn_0 and Kn_{D_0} and monodisperse particles.

$\frac{d\overline{Kn}}{d(\ln(\overline{Kn_D}))}$ can also be calculated from oleic acid coagulation experiments. As coagulation stages recorded from coagulation experiments are close to each other and the change rate of average Knudsen number to the natrual log of average diffusive Knudsen number can be calculated by $\frac{d\overline{Kn}}{d(\ln(\overline{Kn_D}))} \approx \frac{\overline{Kn}_{end}-\overline{Kn}_{initial}}{\ln(\overline{Kn_D}_{end})-\ln(\overline{Kn_D}_{initial})}$, where subscript 'initial' corresponding to distribution from sampling point A in experiment where 'end' is from sampling point B (Figure 5.1). Finally, all data points extrapolated from experiments are ploted on figure 5.5. Smallest grey dots represent simulation results. Each set of experiment provides a single data point and ploted on figure 5.5 with different shapes and colors. Experiments cover the near transition and free molecular regime and they all match simulation results quite well. We thus conclude that evolution of average Knudsen number and diffusive Knudsen number follows a universal curve, i.e. $\frac{d\overline{Kn}}{d(\ln(\overline{Kn_D}))} = f(\overline{Kn})$. With this curve, as well as knowledge of Kn_0 and $Kn_{D,0}$, it is then possible to infer $\overline{Kn_D}$ simply from $\overline{Kn}$, provided the system is isothermal and monomodal.

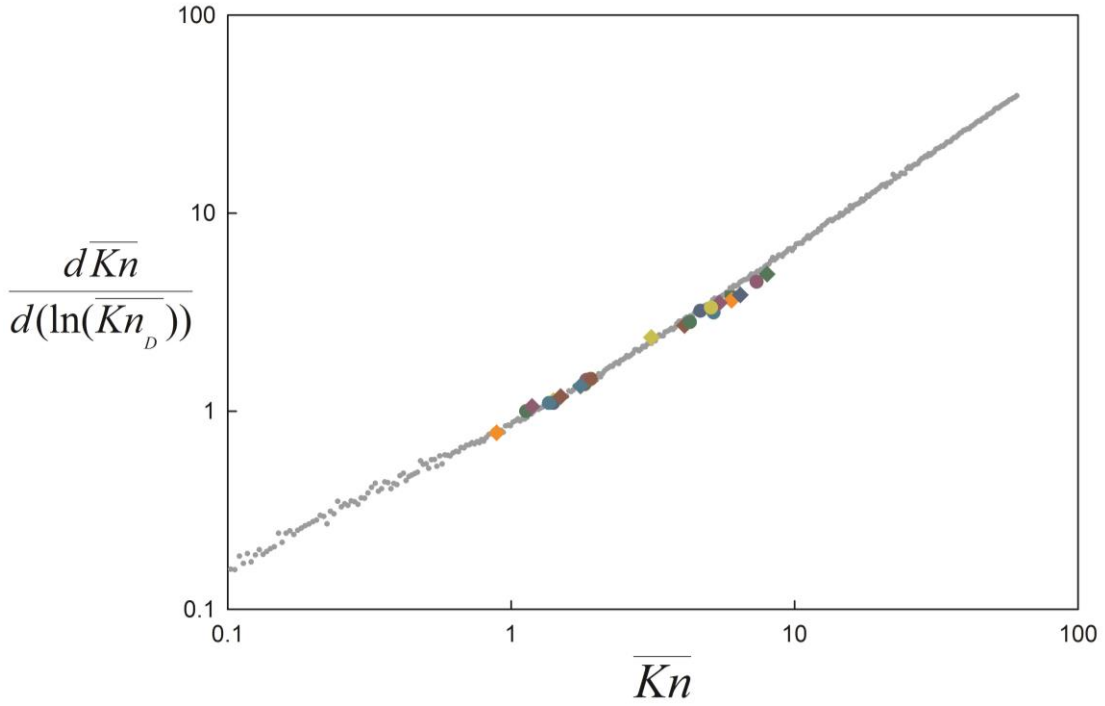

Figure 5.5 Small grey points are simulation results and equivalent to Figure 5.4; Other larger points in different colors and shapes are experimental results and each data point represent one coagulation event with different oleic acid concentration of solution.

5.3 Coagulation with van der Waals Potentials

Further examination of this relationship in the presence of potentials between colliding entities will enable full description of how growing particle populations evolve. To account for the van der Waals (VDW) potential, enhancement factors as described previously in this dissertation must be input into the collision kernal and are further needed for diffusive Knudsen number calculation as $Kn_{D_{ij}} = \frac{(kTm_{ij})^{1/2}\eta_C}{f_{ij}(a_i+a_j)\eta_{FM}}$. The enhancement factors for the van der Waals potential are a function of the particle sizes for colliding pair. For equal size particles they have been calculated and shown in Chapter 3 as well as Appendix A . For unequal size pair where the colliding entities have different diameters, the enhancement factors are shown in figure 5.6 for two different potential strengths, Ψ_{VDW} = 1.0 and 10.0. Free molecular enhancement factors are

typically higher than continuum enhancement factors for the same potential magnitude. The enhancement factors increase as $\Pi_i=\frac{a_i}{a_i+a_j}$ ($0< \Pi_i <1$) increases to 0.5, then decreases symetrically with the maximum value at the middle where Π_i =0.5, i.e. where the two colliding entities have identical radius.

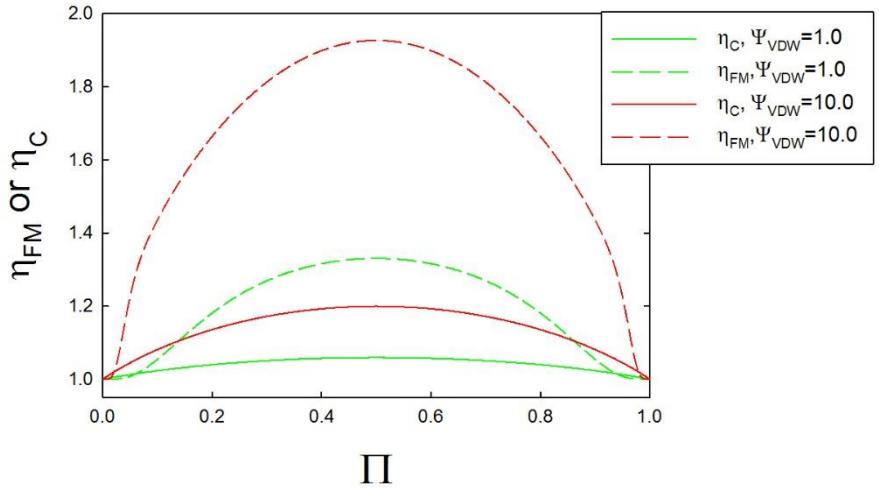

Figure 5.6 Enhancement factors for van der Waals (VDW) potential as a function of particles size ratio $\Pi=\frac{a_i}{a_i+a_j}$ of the collidiong pairs particle *i* and particle *j* with radius a_i and a_j. Solid lines represent continuum enhancement factor η_C while dash lines represent free moleular enhancement factor η_{FM}. Colors are represent different strength of the potential with red (Ψ_{VDW} = 10.0) and green (Ψ_{VDW} = 1.0)

With enhancement factor built into the constant number Monte Carlo simulation for coagulation, the evolution of $\overline{Kn}$ and $\overline{Kn_D}$ with van der Waals potential can be monitored as well. Figure 5.7 shows again $\frac{d\overline{Kn}}{d(\ln(\overline{Kn_D}))}$ as a function of $\overline{Kn}$ with and without potentials. Again, without and with van der Waals potential (Ψ_{VDW} = 0.0 & 10.0), the evolutioin of $\frac{d\overline{Kn}}{d(\ln(\overline{Kn_D}))}$ as a function of $\overline{Kn}$ appeal to be exactly the same, provided enhancement factors are built into the definition of $Kn_{D_{ij}}=\frac{(kTm_{ij})^{1/2}\eta_C}{f_{ij}(a_i+a_j)\eta_{FM}}$. This suggests that the universal function $\frac{d\overline{Kn}}{d(\ln(\overline{Kn_D}))}=f(\overline{Kn})$ can be applied even when potential interactions are present between colliding particles, and in this instance,

monitoring $\overline{Kn}$ evolution as well as the particle size distribution provides information about the strength of the potential interactions.

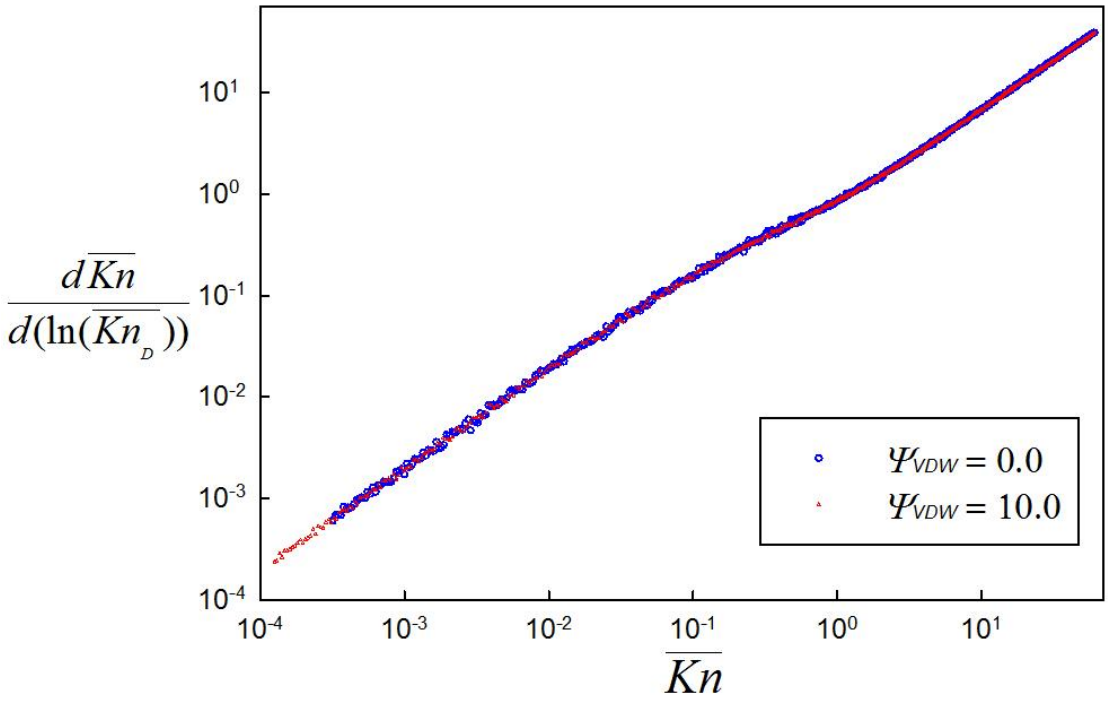

Figure 5.7 $\overline{Kn}$ and $\overline{Kn_D}$ revolution in the coagulation growth with (red triangle Ψ_{VDW} = 10.0) and without (blue circles Ψ_{VDW} = 0.0) the van der Waals potential.

5.4 Notes on Aggregation through CNMC for Future Work

While we do not examine aggregation directly here, we remark on the applicability of the CNMC method to aggregation. Aggregates typically contain different numbers of primary monomers (as i^{th} aggregate has N_i monomers). Each monomer attaches to each other by near point contact, which represents a zero percent coalescence coefficient. To describe the transport properties of aggregates, two parameters have been found applicable in prior work: (1) Rs_i as Smoluchowski radius [29,90,174,186] is the

characteristic length of the particle instead of radius a_i for sphere; (2) PA_i as the orientationly average projected area.

For aggregates the Knudsen number *Kn* and diffustive Knudsen number Kn_D are defined as $Kn_i = \frac{\pi\lambda Rs_i}{PA_i}$ and $Kn_{D\,ij} = \frac{(m_{ij}kT)^{0.5}\pi Rs_{ij}}{f_{ij}PA_{ij}}$ [29,174,187], where Rs_{ij} is the combined Smoluchowski radius, PA_{ij} is the combined orientational averaged projected area, f_{ij} is the reduced friction factor with $f_i = \frac{6\pi\mu Rs_i}{1+Kn_i[1.257+0.4\exp\left(-\frac{1.1}{Kn_i}\right)]}$. The dimentionless collision kernel H_{ij} for aggregation still takes the same formula $H_{ij} = \frac{4\pi Kn_{D_{ij}}^2 + C_1 Kn_{D_{ij}}^3 + (8\pi)^{\frac{1}{2}} C_2 Kn_{D_{ij}}^4}{1+C_3 Kn_{D_{ij}} + C_4 Kn_{D_{ij}}^2 + C_2 Kn_{D_{ij}}^3}$ as for collisions in all regimes (free molecular, transition and continuum regime) which has been valided by mean first passenge time calculations [29,174,187]. The collision kernel β_{ij} can be calculated for a given diffusive Knudsen number Kn_{Dij} as $\beta_{ij} = \frac{H_{ij}f_{ij}PA_{ij}^2}{\pi^2 m_{ij}Rs_{ij}}$ and β_{11} is defined as the primary monomer-monomer collision kernel which is same as for coagulation.

To model aggregation in CNMC, Rs_i, Rs_{ij}, PA_i and PA_{ij} are needed to describe the shape and transport of the aggregates. With internal coordinates available for each primary monomers in the aggregate, Rs_i, Rs_{ij}, PA_i and PA_{ij} can be calculated numerically, which has been illustrated in detail in Gopalakrishnan and Thajudeen's work [29,174,187]. When two aggregates collide, the shape of the new formed aggregate is described by Rs_{new} and PA_{new}. In Langevin Dynamics Simulations where the motion of the aggregates (motion of center of the mass) is monitored, it is easy to get the internal coordinates of

each monomer in the new formed aggregate. While in Constant Number Monte Carlo simulation, the motion of the aggregate is eliminated thus makes it difficult to find the shape of the new formed aggregate. To solve this and evetually to make CNMC method applicable to aggreation, a series of separate calculations will need to be performed prior to aggregation simulation to find Rs_i, Rs_{ij}, PA_i, PA_{ij}, Rs_{new} and PA_{new} independently, such that this information can be input into CNMC calculations a priori. Once such information is available, it will be possible to monitor aggregate evolution without any additional aggregate descriptors besides R_S and PA values.

5.5 Conclusions

A constant number Monte Carlo (CNMC) code is developed to simulate coagulation driven particle growth, which is computationally much less expensive compared to Langevin Dynamics Simulation, but enables examination of transition regime coagulation and can consider particle-particle interactions. Along with the size distribution, the evolution of average the Knudsen number $\overline{Kn}$ and average diffusive Knudsen number $\overline{Kn_D}$ are monitored with CNMC calculations, and comparisons are made to both experimental and LDS simulation results. This evolution also will be an important parameter to reveal the coagulation process. CNMC calculations are found to agree reasonably well with experiments, and with them the evolution of $\overline{Kn}$ and $\overline{Kn_D}$ are found describable with a single curve (the change rate of $\overline{Kn}$ with respect to $ln(\overline{Kn_D})$ as function of $\overline{Kn}$) under all circumstanes, including case with the van der Waals potential considered. In total, we believe continued refinement of the CNMC approach will enabled more detailed modeling of aerosol size distributions in a computationally inexpensive manner.

Chapter 6: Conclusions and Future Directions

This dissertation presents and discusses the results of several studies on the properties and growth kinetics of nanoclusters/nanoparticles. A combination of experiments, numerical simulation, and theory was utilized. The overarching goal was to develop tools to determine parameters needed in nanoparticle growth and transport models, including the mobility/diffusion coefficient (which derive from the collision cross section), the collision limited growth rate (considering potential interactions), the thermostability and extent of water uptake by amine-bisulfate salt clusters, and finally a method to predict nanoparticle size distributions considering potential interactions or non-spherical particle shapes. While for each of these studies, a conclusions section was provided in their corresponding chapters, in this section, additional conclusions and directions for future work are noted.

The studies performed in Chapter 2 show that at the atomic/molecular scale, momentum transfer from gas molecules cannot be described by simple specular or diffuse models for situations; results suggest that the manner in which gas molecules impinge upon and are reemitted from a surface are dependent on the ratio of the gas molecule mass to the masses of atoms within the structure. Further support for this finding was recently discussed by Larriba-Andaluz et al [188]; they found that N_2 scattering from ionic liquid surfaces was largely diffuse, while He scattering was largely specular (i.e. they performed the converse to the study described in Chapter 2 in that they varied the gas molecule mass). While the study described in Chapter 2 does not resolve the proper

impingement-reemission rules to invoke in gas molecule trajectory simulations in all circumstances, the measurements performed do suggest that the influences ion-induced dipole potential can be accounted for by utilizing a theoretically derived correction factor. Recently, additional support for use of this correction factor was provided by Fernandez-Garcia & Fernandez de la Mora, whose measurements of ionic liquid clusters in CO_2 at variable temperature [189] also agree well with the correction factor examine in Chapter 2. Future work in understanding momentum transfer on the molecular scale should focus on a number of features of the process that remain poorly understood. In addition to additional measurements to uncover the proper impingement-reemission law to apply in particular circumstances, the influences of ion-dipole interactions should be examined in instances where gas is extremely humid. Measurements in Chapter 2 were additionally focused on objects moving at low speed relative to the mean thermal speed; higher speed objects, encountered in plasmas, should also be examined. Finally, again for plasma environments, the influences of momentum transfer between negatively charged clusters and positive ions (ion drag) should be examined; though simple models for ion drag exist, they are limited to particular circumstances.

The work presented in Chapter 3 shows that a simple expression can be applied to collision rate calculation in the transition (i.e. for all Kn_D) considering singular contact potentials. Importantly, the derivation presented shows that the diffusive Knudsen number itself is influenced by the strength of the potentials present, hence the regime in which a collision occurs is not a function solely of the sizes of the colliding entities.

Work by Gopalakrishnan et al and Thajudeen et al [174,190] has additionally shown that this function can be applied to collisions between non-spherical particles and ions of the same charge, and between two non-spherical particles which interact by hard-sphere potentials. Future work will be needed to develop a complete collision rate expression for two non-spherical particles considering both Coulomb interactions and higher order electrostatic effects (including van der Waals potentials). In addition, Gopalakrishnan & Hogan [88] (as well as others, Gatti & Kortshagen [100]) show that instances of strong, long range attractive interactions between particles, the dimensionless collision rate expression utilized here fails to correctly recover the collision rate in the transition regime. Future work will also be necessary find a simple method for collision rate calculation in this circumstance, which also correctly recovers the collision rate in the absence of potentials and in both the ballistic and continuum limits.

Based on the results of Chapter 4, it is possible to evaluate the thermostability and extent of vapor uptake (not only water) of chemically well characterized nanoclusters through the combination of IMS-MS and IMS-IMS measurements. This approach should couple well with observations of growth in the ambient atmosphere; through observational (field) studies, the chemical composition (or possible chemical composition) of nanoclusters can be determined. In laboratory studies, through the use of electrosprays or chamber reactors, nanoclusters of controlled chemical composition can be produced, and the chemical compositions of such nanoclusters can be checked via IMS-MS measurements. Subsequently, thermostability and vapor uptake studies can be

carried out via IMS-IMS measurements. Such studies provide information on whether the nanoclusters examined would be stable under atmospheric conditions (or the conditions of interest). Key to utilizing this approach is the realization that the thermodynamic properties of nanoclusters are solely dependent on their chemical composition; these properties need not be examined under precisely identical circumstances to those encountered in the atmosphere (though atmospheric conditions govern their actual chemical composition).

Chapter 5 shows that the constant number Monte Carlo method can be used as a simple approach to consider nanoparticle growth via collisions, with the prediction size distributions in good agreement with experimental measurements. Still, the development of approach to solve the GDE (not coagulation only), when coupled with fluid flow and heat transfer models, is an ongoing process, and modifications to the method presented will be needed to couple it with other transport models. In addition, partial coalescence of particles (sintering) would eventually need to be incorporated into growth models, as in high temperature systems, partial coalescence is frequently observed.

In total, this dissertation focuses on several aspects of nanocluster/nanoparticle transport and growth, and presents several advances over prior studies on these topics. At the same time, the studies presented show that this is a topic in need of continued investigation, both to develop better fundamental relationships to describe nanoparticle transport parameters and subsequently, to utilize such relationships in models of realistic systems (the ambient atmosphere, engines, waste incinerators, etc.). Future work should

not only focus on fundamental studies of transport, but also translating the results of fundamental studies, such that new findings extend beyond academic interest.

Bibliography

[1] J. N. Smith, K. C. Barsanti, H. R. Friedli, M. Ehn, M. Kulmala, D. R. Collins, J. H. Scheckman, B. J. Williams, and P. H. McMurry, P Natl Acad Sci USA **107** (15), 6634 (2010).

[2] I. Riipinen, T. Yli-Juuti, J. R. Pierce, T. Petaja, D. R. Worsnop, M. Kulmala, and N. M. Donahue, Nature Geoscience **5** (7), 453 (2012).

[3] P. H. McMurry, M. Fink, H. Sakurai, M. R. Stolzenburg, R. L. Mauldin, J. Smith, F. Eisele, K. Moore, S. Sjostedt, D. Tanner, L. G. Huey, J. B. Nowak, E. Edgerton, and D. Voisin, Journal of Geophysical Research-Atmospheres **110** (D22) (2005).

[4] V. M. Kerminen, H. Lihavainen, M. Komppula, Y. Viisanen, and M. Kulmala, Geophysical Research Letters **32** (14) (2005).

[5] Hai Wang, Proceedings of the Combustion Institute **33** (1), 41 (2011).

[6] F. E. Kruis, H. Fissan, and A. Peled, Journal of Aerosol Science **29** (5-6), 511 (1998); M. T. Swihart, Current Opinion in Colloid & Interface Science **8** (1), 127 (2003).

[7] D. Vollath, Kona-Powder and Particle **25**, 39 (2007).

[8] D. Vollath, Journal of Nanoparticle Research **10**, 39 (2008); Davide Mariotti and R Mohan Sankaran, Journal of Physics D: Applied Physics **43** (32), 323001 (2010).

[9] D. E. Rosner, Industrial & Engineering Chemistry Research **44** (16), 6045 (2005).

[10] SL Gong, LA Barrie, J‐P Blanchet, K Von Salzen, U Lohmann, G Lesins, L Spacek, LM Zhang, E Girard, and H Lin, Journal of Geophysical Research: Atmospheres (1984–2012) **108** (D1), AAC 3 (2003); D. V. Spracklen, K. J. Pringle, K. S. Carslaw, M. P. Chipperfield, and G. W. Mann, Atmospheric Chemistry and Physics **5**, 2227 (2005); W. M. Gong, C. Stroud, and L. M. Zhang, Atmosphere **2** (4), 567 (2011); Y. Peng, K. von Salzen, and J. Li, Atmospheric Chemistry and Physics **12** (15), 6891 (2012); L. Huang, S. L. Gong, M. Gordon, J. Liggio, R. Staebler, C. A. Stroud, G. Lu, C. Mihele, J. R. Brook, and C. Q. Jia, Atmospheric Chemistry and Physics **14** (23), 12631 (2014); Z. L. Wang, H. Zhang, and P. Lu, Journal of Geophysical Research-Atmospheres **119** (13) (2014).

[11] D. V. Spracklen, K. J. Pringle, K. S. Carslaw, M. P. Chipperfield, and G. W. Mann, Atmospheric Chemistry and Physics **5**, 3233 (2005).

[12] E. Vignati, M. Karl, M. Krol, J. Wilson, P. Stier, and F. Cavalli, Atmospheric Chemistry and Physics **10** (6), 2595 (2010).

[13] Daniele L Marchisio and Rodney O Fox, Journal of Aerosol Science **36** (1), 43 (2005); Bin Zhao, Zhiwei Yang, Murray V Johnston, Hai Wang, Anthony S Wexler, Michael Balthasar, and Markus Kraft, Combustion and Flame **133** (1), 173 (2003).

[14] Neal Morgan, Markus Kraft, Michael Balthasar, David Wong, Michael Frenklach, and Pablo Mitchell, Proceedings of the Combustion Institute **31** (1), 693 (2007).
[15] Adolf Fick, (Annalen der Physik, 1855), Vol. 170, pp. 59.
[16] E. O. Knutson and K. T. Whitby, Journal of Aerosol Science **6** (6), 443 (1975).
[17] R. A. Millikan, Physical Review **22**, 1 (1923).
[18] C. N. Davies, Proceedings of the Physical Society **57**, 259 (1945).
[19] A. A. Shvartsburg and M. F. Jarrold, Chem Phys Lett **261** (1-2), 86 (1996).
[20] P. Dugourd, R. R. Hudgins, and M. F. Jarrold, Chem Phys Lett **267** (1-2), 186 (1997).
[21] R. Gopalakrishnan and C. J. Hogan, Aerosol Sci Tech **45**, 1499 (2011).
[22] S.W. Thomson, Phil Mag Lett (4), 448 (1871).
[23] K. M. Zhang and A. S. Wexler, J Geophys Res-Atmos **107** (D21) (2002).
[24] P. H. McMurry, K. S. Woo, R. Weber, D. R. Chen, and D. Y. H. Pui, Philosophical Transactions of the Royal Society of London Series a-Mathematical Physical and Engineering Sciences **358** (1775), 2625 (2000); R. J. Weber, P. H. McMurry, L. Mauldin, D. J. Tanner, F. L. Eisele, F. J. Brechtel, S. M. Kreidenweis, G. L. Kok, R. D. Schillawski, and D. Baumgardner, Journal of Geophysical Research-Atmospheres **103** (D13), 16385 (1998); M. Kulmala, L. Laakso, K. E. J. Lehtinen, I. Riipinen, M. Dal Maso, T. Anttila, V. M. Kerminen, U. Horrak, M. Vana, and H. Tammet, Atmospheric Chemistry and Physics **4**, 2553 (2004).
[25] Fred Gelbard and John H. Seinfeld, Journal of Colloid and Interface Science **68** (2), 363 (1979).
[26] Fred Gelbard, Yoram Tambour, and John H. Seinfeld, Journal of Colloid and Interface Science **76** (2), 541 (1980); Wu Jin Jwang and Richard C. Flagan, Journal of Colloid and Interface Science **123** (2), 339 (1988); Paul S. Hill, Deep Sea Research Part I: Oceanographic Research Papers **43** (5), 679 (1996); Z. Sun, R. L. Axelbaum, and B. H. Chao, Proceedings of the Combustion Institute **29** (1), 1063 (2002); Karl Netzell, Harry Lehtiniemi, and Fabian Mauss, Proceedings of the Combustion Institute **31** (1), 667 (2007).
[27] Michael Frenklach and Stephen J. Harris, Journal of Colloid and Interface Science **118** (1), 252 (1987); D. L. Marchisio, J. T. Pikturna, R. O. Fox, R. D. Vigil, and A. A. Barresi, Aiche Journal **49** (5), 1266 (2003); M Balthasar and M Kraft, Combustion and Flame **133** (3), 289 (2003).
[28] M. Smith and T. Matsoukas, Chem Eng Sci **53** (9), 1777 (1998).
[29] T. Thajudeen, S. Deshmukh, and C. J. Hogan, Aerosol Science and Technology **49** (2), 115 (2015).
[30] M. F. Mesleh, J. M. Hunter, A. A. Shvartsburg, G. C. Schatz, and M. F. Jarrold, J Phys Chem-Us **100** (40), 16082 (1996).
[31] A. A. Shvartsburg, S. V. Mashkevich, E. S. Baker, and R. D. Smith, J Phys Chem A **111** (10), 2002 (2007).
[32] C. J. Hogan and J. Fernandez de la Mora, J Am Soc Mass Spectr **22**, 158 (2011).

[33] C. Larriba, C. J. Hogan, M. Attoui, R. Borrajo, J. Fernandez-Garcia, and J. Fernandez de la Mora, Aerosol Sci Tech **45**, 453 (2011).
[34] A. E. Counterman, S. J. Valentine, C. A. Srebalus, S. C. Henderson, C. S. Hoaglund, and D. E. Clemmer, J Am Soc Mass Spectr **9** (8), 743 (1998).
[35] D. A. Saucy, S. Ude, I. W. Lenggoro, and J. Fernandez de la Mora, Anal Chem **76** (4), 1045 (2004); B. K. Ku, J. Fernandez de la Mora, D. A. Saucy, and J. N. Alexander, Anal Chem **76** (3), 814 (2004).
[36] E. W. McDaniel and E. A. Mason, *The Mobility and Diffusion of Ions in Gases*. (1973).
[37] A. A. Shvartsburg, S. V. Mashkevich, and K. W. M. Siu, J Phys Chem A **104** (42), 9448 (2000).
[38] F. A. Fernandez-Lima, C. Becker, K. Gillig, W. K. Russell, M. A. C. Nascimento, and D. H. Russell, J Phys Chem A **112** (44), 11061 (2008).
[39] Toralf Beitz, Robert Laudien, Hans-Gerd Löhmannsröben, and Bernd Kallies, The Journal of Physical Chemistry A **110** (10), 3514 (2006); B. S. Kinnear, D. T. Kaleta, M. Kohtani, R. R. Hudgins, and M. F. Jarrold, J Am Chem Soc **122** (38), 9243 (2000); B. Liu, Z. Y. Lu, B. C. Pan, C. Z. Wang, K. M. Ho, A. A. Shvartsburg, and M. F. Jarrold, J Chem Phys **109** (21), 9401 (1998); A. A. Shvartsburg and M. F. Jarrold, Phys Rev A **60** (2), 1235 (1999); F. A. Fernandez-Lima, H. Wei, Y. Q. Gao, and D. H. Russell, J Phys Chem A **113** (29), 8221 (2009).
[40] C. Bleiholder, T. Wyttenbach, and M. T. Bowers, Int J Mass Spectrom **308** (1), 1 (2011); Thomas Wyttenbach, Christian Bleiholder, and Michael T. Bowers, Anal Chem **85** (4), 2191 (2013).
[41] K. Thalassinos, S. E. Slade, K. R. Jennings, J. H. Scrivens, K. Giles, J. Wildgoose, J. Hoyes, R. H. Bateman, and M. T. Bowers, Int J Mass Spectrom **236** (1-3), 55 (2004); A. A. Shvartsburg and R. D. Smith, Anal Chem **80** (24), 9689 (2008).
[42] M. F. Bush, Z. Hall, K. Giles, J. Hoyes, C. V. Robinson, and B. T. Ruotolo, Anal Chem **82**, 9557 (2010).
[43] P. Martinez-Lozano and J. Rus, Journal of the American Society for Mass Spectrometry **21** (7), 1129 (2010); J. K. Jiang, M. Attoui, M. Heim, N. A. Brunelli, P. H. McMurry, G. Kasper, R. C. Flagan, K. Giapis, and G. Mouret, Aerosol Sci Tech **45** (4), 480 (2011).
[44] P. S. Epstein, Physical Review **23**, 710 (1924).
[45] B. K. Ku and J. Fernandez de la Mora, Aerosol Sci Tech **43** (3), 241 (2009).
[46] I. Campuzano, M. F. Bush, C. V. Robinson, C. Beaumont, K. Richardson, H. Kim, and H. I. Kim, Anal Chem **84** (2), 1026 (2012).
[47] H. I. Kim, H. Kim, E. S. Pang, E. K. Ryu, L. W. Beegle, J. A. Loo, W. A. Goddard, and I. Kanik, Anal Chem **81** (20), 8289 (2009).
[48] C. Larriba and C. J. Hogan, Journal of Computational Physics **In Press** (2013).
[49] S. Ude and J. Fernandez de la Mora, J Aerosol Sci **36** (10), 1224 (2005).

[50] C. Larriba and J. Fernandez de la Mora, The Journal of Physical Chemistry B **116**, 593 (2012).
[51] C. Larriba and C. J. Hogan, The Journal of Physical Chemistry A **117**, 3887 (2013).
[52] B. T. Ruotolo, K. Giles, I. Campuzano, A. M. Sandercock, R. H. Bateman, and C. V. Robinson, Science **310**, 1658 (2005); B. T. Ruotolo, J. L. P. Benesch, A. M. Sandercock, S. J. Hyung, and C. V. Robinson, Nat Protoc **3** (7), 1139 (2008); C. A. Scarff, K. Thalassinos, G. R. Hilton, and J. H. Scrivens, Rapid Commun Mass Sp **22** (20), 3297 (2008); C. Uetrecht, R. J. Rose, E. van Duijn, K. Lorenzen, and A. J. R. Heck, Chem Soc Rev **39**, 1633 (2010); E. van Duijn, A. Barendregt, S. Synowsky, C. Versluis, and A. J. R. Heck, J Am Chem Soc **131** (4), 1452 (2009); J. V. Hamilton, J. B. Renaud, and P. M. Mayer, Rapid Commun Mass Sp **26** (14), 1591 (2012); T. W. Knapman, J. T. Berryman, I. Campuzano, S. A. Harris, and A. E. Ashcroft, Int J Mass Spectrom **298** (1-3), 17 (2010).
[53] C. J. Hogan and J. Fernandez de la Mora, Phys Chem Chem Phys **11** (36), 8079 (2009).
[54] J. Rus, D. Moro, J. A. Sillero, J. Royuela, A. Casado, F. Estevez-Molinero, and J. Fernandez de la Mora, Int J Mass Spectrom **298**, 30 (2010).
[55] C. J. Hogan and J. Fernandez de la Mora, J Am Soc Mass Spectr **21** (8), 1382 (2010).
[56] M. Cloupeau and B. Prunet-foch, J Electrostat **22** (2), 135 (1989).
[57] J. Fernandez de la Mora and I. G. Loscertales, J Fluid Mech **260**, 155 (1994).
[58] M. F. Bush, I. D. G. Campuzano, and C. V. Robinson, Anal Chem **84** (16), 7124 (2012).
[59] A. Aguado, A. Ayuela, J. M. Lopez, and J. A. Alonso, Phys Rev B **56** (23), 15353 (1997).
[60] A. Aguado, A. Ayuela, J. M. Lopez, and J. A. Alonso, Phys Rev B **58** (15), 9972 (1998).
[61] J. H. Kim, G. W. Mulholland, S. R. Kukuck, and D. Y. H. Pui, J Res Natl Inst Stan **110** (1), 31 (2005); A. J. Borysik and C. V. Robinson, Phys Chem Chem Phys **14** (42), 14439 (2012).
[62] S. Kruckeberg, D. Schooss, M. Maier-Borst, and J. H. Parks, Phys Rev Lett **85** (21), 4494 (2000).
[63] A. D. Becke, J Chem Phys **98** (7), 5648 (1993).
[64] J. A. Bradshaw, S. L. Gordon, A. J. Leavitt, and R. L. Whetten, J Phys Chem A **116** (1), 27 (2012).
[65] P. J. Hay and W. R. Wadt, J Chem Phys **82** (1), 270 (1985); P. J. Hay and W. R. Wadt, J Chem Phys **82** (1), 299 (1985); W. R. Wadt and P. J. Hay, J Chem Phys **82** (1), 284 (1985).
[66] A. Aguado, J. Phys. Chem. B **105** (14), 2761 (2001).

[67] T. Wyttenbach, J. E. Bushnell, and M. T. Bowers, J Am Chem Soc **120** (20), 5098 (1998); T. Wyttenbach, M. Witt, and M. T. Bowers, J Am Chem Soc **122** (14), 3458 (2000).
[68] Miki Niwa, Kiyoshi Yamazaki, and Yuichi Murakami, Ind Eng Chem Res **30** (1), 38 (1991).
[69] H. Tammet, J Aerosol Sci **26** (3), 459 (1995).
[70] J. Happel and H. Brenner, *Low Reynolds Number Hydrodynamics*. (Martinus Nijhoff Publishers, The Hague, The Netherlands, 1983).
[71] S. Chapman and T. G. Cowling, *The Mathematical Theory of Non-uniform Gases*. (Cambridge University Press, Cambridge, UK, 1991).
[72] S. Trimpin and D. E. Clemmer, Anal Chem **80** (23), 9073 (2008).
[73] M. Gamero-Castano and J. Fernandez de la Mora, J Mass Spectrom **35** (7), 790 (2000); J. V. Iribarne and B. A. Thomson, J Chem Phys **64** (6), 2287 (1976).
[74] P. Chan and B. Dahneke, J Appl Phys **52**, 3106 (1981).
[75] C. Zhang, T. Thajudeen, C. Larriba, T. E. Schwartzentruber, and C. J. Hogan, Aerosol Sci Tech **46**, 1065 (2012).
[76] N. A. Fuchs, *The mechanics of aerosols*, Rev. and enl. ed. (Macmillan, New York,, 1964), pp.xiv.
[77] M. G. Sceats, J Colloid Interf Sci **129**, 105 (1989).
[78] A. S. Amadon and W. H. Marlow, Phys Rev A **43** (10), 5483 (1991).
[79] A. S. Amadon and W. H. Marlow, Phys Rev A **43** (10), 5493 (1991).
[80] W. H. Marlow, J Chem Phys **73** (12), 6284 (1980).
[81] W. H. Marlow, Surf Sci **106** (1-3), 529 (1981); W. H. Marlow, J Colloid Interf Sci **87** (1), 209 (1982); U. Kortshagen and U. Bhandarkar, Phys Rev E **60** (1), 887 (1999).
[82] M. K. Alam, Aerosol Sci Tech **6**, 41 (1987).
[83] V. M. Kerminen, Aerosol Sci Tech **20** (2), 207 (1994); J. Chun and D. L. Koch, J Aerosol Sci **37** (4), 471 (2006).
[84] D. D. Huang, J. H. Seinfeld, and K. Okuyama, J Colloid Interf Sci **141** (1), 191 (1991).
[85] L. Isella and Y. Drossinos, Physical Review E **82**, 011404 (2010).
[86] L. Ravi and S. L. Girshick, Phys Rev E **79**, 026408 (2009).
[87] Y. Zhang, S. Li, W. Yan, Q. Yao, and D. Tse, The Journal of Chemical Physics **134**, 084501 (2011).
[88] R. Gopalakrishnan and C. J. Hogan, Phys Rev E **85**, 026410 (2012).
[89] N. A. Fuchs and A. G. Sutugin, Journal of Colloid Science **20**, 492 (1965).
[90] R. Gopalakrishnan, T. Thajudeen, and C. J. Hogan, J Chem Phys **135**, 054302 (2011).
[91] M. S. Veshchunov, J Aerosol Sci **41** (10), 895 (2010).
[92] M. S. Veshchunov and I. B. Azarov, J Aerosol Sci **47**, 70 (2012).
[93] G. Narsimhan and E. Ruckenstein, J Colloid Interf Sci **107** (1), 174 (1985).

[94] W. Yan, S. Li, Y. Zhang, Q. Yao, and S. D. Tse, J Phys Chem C **114**, 10755 (2010).
[95] W. H. Marlow, J Chem Phys **73** (12), 6288 (1980).
[96] V. Arunachalam, R. R. Lucchese, and W. H. Marlow, Phys Rev E **60** (2), 2051 (1999); V. Arunachalam, W. H. Marlow, and J. X. Lu, Phys Rev E **58** (3), 3451 (1998); D. Langbein, J Phys Chem Solids **32** (1), 133 (1971); A.;Burtscher Schmidt-Ott, H., J Colloid Interf Sci **89** (2), 5 (1982); J. Visser, Adv Colloid Interfac **3** (4), 32 (1972).
[97] J. R. Brock, J Appl Phys **41**, 843 (1970).
[98] D. D. Huang and J. H. Seinfeld, J Colloid Interf Sci **139** (1), 213 (1990); M. G. Sceats, J Chem Phys **84**, 5206 (1986); J. M. Dawes and M. G. Sceats, J Chem Phys **88**, 5489 (1988).
[99] G. Narsimhan and E. Ruckenstein, J Colloid Interf Sci **104**, 344 (1985).
[100] M. Gatti and U. Kortshagen, Phys Rev E **78** (4), 046402 (2008).
[101] N.A. Fuchs, Geofis. Pura Appl. **51**, 185 (1963).
[102] T. Thajudeen, R. Gopalakrishnan, and C. J. Hogan, Aerosol Sci Tech **In Press** (2012).
[103] T. W. Chan and M. Mozurkewich, J Aerosol Sci **32**, 321 (2001).
[104] K. Okuyama, Y. Kousaka, and K. Hayashi, J Colloid Interf Sci **101** (1), 98 (1984).
[105] P. E. Wagner and M. Kerker, J Chem Phys **66**, 638 (1977).
[106] J. E. Allen, Phys Scripta **45** (5), 497 (1992).
[107] W. G. Vincenti and C. H. Kruger, *Introduction to Physical Gas Dynamics*. (Krieger, Huntington, NY, 1975).
[108] E. A. Mason and E. W. McDaniel, *Transport Properties of Ions in Gases*. (Wiley, New York, 1988).
[109] V. Premnath, D. Oberreit, and C. J. Hogan, Aerosol Sci Tech **45**, 712 (2011).
[110] N. A. Fuchs and A. G. Sutugin, *Highly dispersed aerosols*. (Ann Arbor Science Publishers, Ann Arbor,, 1970), p.105 p; S. K. Loyalka, J Chem. Physics **58** (1) (1973); B. E. Dahneke, in *Theory of Dispersed Multiphase Flow*, edited by R.E. Meyer (Academic Press, New York, 1983).
[111] D. L. Ermak and H. Buckholz, Journal of Computational Physics **35** (2), 169 (1980).
[112] D. C. Sahni, Journal of Nuclear Energy **20**, 915 (1966).
[113] M. S. Veshchunov, J Exp Theor Phys+ **114**, 631 (2012).
[114] L. G. D'yachkov, A. G. Khrapak, S. A. Khrapak, and G. E. Morfill, Phys Plasmas **14** (4), 042102 (2007).
[115] M. Adachi, Y. Kousaka, and K. Okuyama, J Aerosol Sci **16** (2), 109 (1985).
[116] A. Maisels, F. E. Kruis, and H. Fissan, J Colloid Interf Sci **255** (2), 332 (2002).
[117] P. G. Wright, Discussions of the Faraday Society **30**, 100 (1960).
[118] A. A. Lushnikov and M. Kulmala, Phys Rev E **70** (4), 046413 (2004).

[119] A. V. Filippov, J Aerosol Sci **24** (4), 423 (1993); G. Biskos, E. Mastorakos, and N. Collings, J Aerosol Sci **35** (6), 707 (2004).
[120] W. A. Hoppel and G. M. Frick, Aerosol Sci Tech **5** (1), 1 (1986).
[121] S.K. Friedlander, *Smoke, dust, and haze*. (Oxford University Press New York, 2000).
[122] S. N. Shon, G. Kasper, and D. T. Shaw, J Colloid Interf Sci **73** (1), 233 (1980); N. Egilmez and C. N. Davies, Proceedings of the Royal Society of London Series a-Mathematical Physical and Engineering Sciences **380** (1778), 99 (1982); C. N. Davies, J Aerosol Sci **10** (2), 151 (1979).
[123] P. Paasonen, T. Olenius, O. Kupiainen, T. Kurten, T. Petaja, W. Birmili, A. Hamed, M. Hu, L. G. Huey, C. Plass-Duelmer, J. N. Smith, A. Wiedensohler, V. Loukonen, M. J. McGrath, I. K. Ortega, A. Laaksonen, H. Vehkamaki, V. M. Kerminen, and M. Kulmala, Atmos Chem Phys **12** (19), 9113 (2012).
[124] A. Kurten, T. Jokinen, M. Simon, M. Sipila, N. Sarnela, H. Junninen, A. Adamov, J. Almeida, A. Amorim, F. Bianchi, M. Breitenlechner, J. Dommen, N. M. Donahue, J. Duplissy, S. Ehrhart, R. C. Flagan, A. Franchin, J. Hakala, A. Hansel, M. Heinritzi, M. Hutterli, J. Kangasluoma, J. Kirkby, A. Laaksonen, K. Lehtipalo, M. Leiminger, V. Makhmutov, S. Mathot, A. Onnela, T. Petaja, A. P. Praplan, F. Riccobono, M. P. Rissanen, L. Rondo, S. Schobesberger, J. H. Seinfeld, G. Steiner, A. Tome, J. Trostl, P. M. Winkler, C. Williamson, D. Wimmer, P. L. Ye, U. Baltensperger, K. S. Carslaw, M. Kulmala, D. R. Worsnop, and J. Curtius, P Natl Acad Sci USA **111** (42), 15019 (2014).
[125] J. Zhao, J. N. Smith, F. L. Eisele, M. Chen, C. Kuang, and P. H. McMurry, Atmos Chem Phys **11** (21), 10823 (2011).
[126] A. Sorooshian, S. N. Murphy, S. Hersey, H. Gates, L. T. Padro, A. Nenes, F. J. Brechtel, H. Jonsson, R. C. Flagan, and J. H. Seinfeld, Atmos Chem Phys **8** (17), 5489 (2008); X. L. Ge, A. S. Wexler, and S. L. Clegg, Atmos Environ **45** (3), 524 (2011).
[127] C. N. Jen, P. H. McMurry, and D. R. Hanson, J Geophys Res-Atmos **119** (12), 7502 (2014).
[128] C. Qiu and R. Y. Zhang, Environ Sci Technol **46** (8), 4474 (2012).
[129] T. Kurten, V. Loukonen, H. Vehkamaki, and M. Kulmala, Atmos Chem Phys **8** (14), 4095 (2008); B. R. Bzdek, D. P. Ridge, and M. V. Johnston, Atmos Chem Phys **11** (16), 8735 (2011); T. Petaja, M. Sipila, P. Paasonen, T. Nieminen, T. Kurten, I. K. Ortega, F. Stratmann, H. Vehkamaki, T. Berndt, and M. Kulmala, Phys Rev Lett **106** (22) (2011).
[130] V. Loukonen, T. Kurten, I. K. Ortega, H. Vehkamaki, A. A. H. Padua, K. Sellegri, and M. Kulmala, Atmos Chem Phys **10** (10), 4961 (2010).
[131] H. Henschel, J. C. A. Navarro, T. Yli-Juuti, O. Kupiainen-Määttä, T. Olenius, I. K. Ortega, S. L. Clegg, T. Kurtén, I. Riipinen, and H. Vehkamäki, The Journal of Physical Chemistry A **118** (14), 2599 (2014).

[132] M. Kulmala, V. M. Kerminen, T. Anttila, A. Laaksonen, and C. D. O'Dowd, J Geophys Res-Atmos **109** (D4) (2004).
[133] N. M. Donahue, E. R. Trump, J. R. Pierce, and I. Riipinen, Geophys Res Lett **38** (2011).
[134] S. M. Thompson, K. E. Gubbins, J. P. R. B. Walton, R. A. R. Chantry, and J. S. Rowlinson, The Journal of Chemical Physics **81** (1), 530 (1984).
[135] H. Ouyang, C. Larriba-Andaluz, D. R. Oberreit, and C. J. Hogan, J Am Soc Mass Spectr **24** (12), 1833 (2013).
[136] K. Park, J. S. Kim, and A. L. Miller, J Nanopart Res **11** (1), 175 (2009); G. Biskos, A. Malinowski, L. M. Russell, P. R. Buseck, and S. T. Martin, Aerosol Sci Tech **40** (2), 97 (2006).
[137] D. R. Oberreit, P. H. McMurry, and C. J. Hogan, Phys Chem Chem Phys **16** (15), 6968 (2014).
[138] C. Qiu and R. Y. Zhang, Phys Chem Chem Phys **15** (16), 5738 (2013).
[139] J. W. DePalma, B. R. Bzdek, D. J. Doren, and M. V. Johnston, J Phys Chem A **116** (3), 1030 (2012); I. K. Ortega, Olenius, T., Kupiainen-Määttä, O., Loukonen, V., Kurtén, T., and Vehkamäki, H., Atmos. Chem. Phys. **14**, 13 (2014); I. K. Ortega, O. Kupiainen, T. Kurten, T. Olenius, O. Wilkman, M. J. McGrath, V. Loukonen, and H. Vehkamaki, Atmos Chem Phys **12** (1), 225 (2012).
[140] J. W. DePalma, D. J. Doren, and M. V. Johnston, J Phys Chem A **118** (29), 5464 (2014).
[141] C. J. Hogan and J. F. de la Mora, Phys Chem Chem Phys **11** (36), 8079 (2009).
[142] C. J. Hogan and J. F. de la Mora, J Am Soc Mass Spectr **21** (8), 1382 (2010).
[143] J. Rus, D. Moro, J. A. Sillero, J. Royuela, A. Casado, F. Estevez-Molinero, and J. F. de la Mora, Int J Mass Spectrom **298** (1-3), 30 (2010).
[144] D. J. Rader and P. H. Mcmurry, J Aerosol Sci **17** (5), 771 (1986).
[145] P. Villani, D. Picard, V. Michaud, P. Laj, and A. Wiedensohler, Aerosol Sci Tech **42** (9), 729 (2008).
[146] J. Fernandez de la Mora and J. Kozlowski, J Aerosol Sci **57**, 45 (2013).
[147] D. R. Oberreit, P. H. McMurry, and C. J. Hogan, Aerosol Sci Tech **48** (1), 108 (2014).
[148] M. Cloupeau and B. Prunetfoch, J Electrostat **22** (2), 135 (1989).
[149] D. R. Chen, D. Y. H. Pui, and S. L. Kaufman, J Aerosol Sci **26** (6), 963 (1995); M. Scalf, M. S. Westphall, and L. M. Smith, Anal Chem **72** (1), 52 (2000).
[150] S. K. Guharay, P. Dwivedi, and H. H. Hill, Ieee T Plasma Sci **36** (4), 1458 (2008); A. B. Kanu, P. Dwivedi, M. Tam, L. Matz, and H. H. Hill, J Mass Spectrom **43** (1), 1 (2008).
[151] C. Larriba and C. J. Hogan, J Phys Chem A **117** (19), 3887 (2013).
[152] C. Larriba, J. Fernandez de la Mora, and D. E. Clemmer, J Am Soc Mass Spectr **25** (8), 1332 (2014).
[153] S. Ude and J. F. de la Mora, J Aerosol Sci **36** (10), 1224 (2005).

[154] S. L. Koeniger, S. I. Merenbloom, S. J. Valentine, M. F. Jarrold, H. R. Udseth, R. D. Smith, and D. E. Clemmer, Anal Chem **78** (12), 4161 (2006).
[155] D. J. Rader, P. H. Mcmurry, and S. Smith, Aerosol Sci Tech **6** (3), 247 (1987); K. Park, D. Dutcher, M. Emery, J. Pagels, H. Sakurai, J. Scheckman, S. Qian, M. R. Stolzenburg, X. Wang, J. Yang, and P. H. McMurry, Aerosol Sci Tech **42** (10), 801 (2008).
[156] J. Fernández-García and J. Fernández de la Mora, J Am Soc Mass Spectr **24** (12), 1872 (2013); J. Fernández-García and J. Fernández de la Mora, Phys Chem Chem Phys **16** (38), 20500 (2014).
[157] C. Larriba and C. J. Hogan, J Comput Phys **251**, 344 (2013).
[158] C. Larriba-Andaluz, J. Fernandez-Garcia, C. J. Hogan, and D. E. Clemmer, **Submitted** (2014); A. Kumar, S. Kang, C. Larriba-Andaluz, H. Ouyang, C. J. Hogan, and R. M. Sankaran, Nanotechnology **25**, 385601 (2014); C. Larriba-Andaluz and C. J. Hogan, J Chem Phys **141**, 194107 (2014).
[159] C. Antoine, Comptes Rendus des Séances de l'Académie des Sciences **107**, 681 (1888).
[160] Alessandro Vetere, Ind Eng Chem Res **30** (11), 2487 (1991).
[161] J. J. Marti, A. Jefferson, X. P. Cai, C. Richert, P. H. McMurry, and F. Eisele, J Geophys Res-Atmos **102** (D3), 3725 (1997).
[162] A. Lavi, N. Bluvshtein, E. Segre, L. Segev, M. Flores, and Y. Rudich, J Phys Chem C **117** (43), 22412 (2013).
[163] J. Almeida, S. Schobesberger, A. Kurten, I. K. Ortega, O. Kupiainen-Maatta, A. P. Praplan, A. Adamov, A. Amorim, F. Bianchi, M. Breitenlechner, A. David, J. Dommen, N. M. Donahue, A. Downard, E. Dunne, J. Duplissy, S. Ehrhart, R. C. Flagan, A. Franchin, R. Guida, J. Hakala, A. Hansel, M. Heinritzi, H. Henschel, T. Jokinen, H. Junninen, M. Kajos, J. Kangasluoma, H. Keskinen, A. Kupc, T. Kurten, A. N. Kvashin, A. Laaksonen, K. Lehtipalo, M. Leiminger, J. Leppa, V. Loukonen, V. Makhmutov, S. Mathot, M. J. McGrath, T. Nieminen, T. Olenius, A. Onnela, T. Petaja, F. Riccobono, I. Riipinen, M. Rissanen, L. Rondo, T. Ruuskanen, F. D. Santos, N. Sarnela, S. Schallhart, R. Schnitzhofer, J. H. Seinfeld, M. Simon, M. Sipila, Y. Stozhkov, F. Stratmann, A. Tome, J. Trostl, G. Tsagkogeorgas, P. Vaattovaara, Y. Viisanen, A. Virtanen, A. Vrtala, P. E. Wagner, E. Weingartner, H. Wex, C. Williamson, D. Wimmer, P. L. Ye, T. Yli-Juuti, K. S. Carslaw, M. Kulmala, J. Curtius, U. Baltensperger, D. R. Worsnop, H. Vehkamaki, and J. Kirkby, Nature **502** (7471), 359 (2013).
[164] P. H. McMurry and M. R. Stolzenburg, Atmos Environ **23** (2), 497 (1989); B. Y. H. Liu, D. Y. H. Pui, K. T. Whitby, D. B. Kittelson, Y. Kousaka, and R. L. McKenzie, Atmos Environ **12** (1-3), 99 (1978).
[165] J. Zhao, F. L. Eisele, M. Titcombe, C. G. Kuang, and P. H. McMurry, J Geophys Res-Atmos **115** (2010).
[166] M. R. Canagaratna, J. T. Jayne, J. L. Jimenez, J. D. Allan, M. R. Alfarra, Q. Zhang, T. B. Onasch, F. Drewnick, H. Coe, A. Middlebrook, A. Delia, L. R.

Williams, A. M. Trimborn, M. J. Northway, P. F. DeCarlo, C. E. Kolb, P. Davidovits, and D. R. Worsnop, Mass Spectrom. Rev. **26** (2), 185 (2007).

[167] S. E. Pratsinis, Progress in Energy and Combustion Science **24** (3), 197 (1998); H. K. Kammler, L. Madler, and S. E. Pratsinis, Chemical Engineering & Technology **24** (6), 583 (2001); C. B. Almquist and P. Biswas, Journal of Catalysis **212** (2), 145 (2002); O. I. Arabi-Katbi, K. Wegner, and S. E. Pratsinis, Annales De Chimie-Science Des Materiaux **27** (6), 37 (2002); W. J. Stark and S. E. Pratsinis, Powder Technology **126** (2), 103 (2002); S. L. Girshick, Journal of Nanoparticle Research **10** (6), 935 (2008); J. L. H. Chau and C. C. Kao, Journal of Non-Crystalline Solids **355** (50-51), 2448 (2009); Uwe Kortshagen, Journal of Physics D-Applied Physics **42** (11) (2009); M. Mamak, S. Y. Choi, U. Stadler, R. Dolbec, M. Boulos, and S. Petrov, Journal of Materials Chemistry **20** (44), 9855 (2010); J. X. Fang, Y. Wang, M. Attoui, T. S. Chadha, J. R. Ray, W. N. Wang, Y. S. Jun, and P. Biswas, Analytical Chemistry **86** (15), 7523 (2014); Jingkun Jiang, Da-Ren Chen, and Pratim Biswas, Nanotechnology **18** (28) (2007).

[168] D. Meimaroglou, A. I. Roussos, and C. Kiparissides, Chemical Engineering Science **61** (17), 5620 (2006); G. Inci, A. Arnold, A. Kronenburg, and R. Weeber, Aerosol Science and Technology **48** (8), 842 (2014); R. B. Diemer and J. H. Olson, Chemical Engineering Science **57** (12), 2211 (2002); M. Z. Yu, J. Z. Lin, and T. L. Chan, Powder Technology **181** (1), 9 (2008).

[169] R. B. Diemer and J. H. Olson, Chemical Engineering Science **57** (12), 2193 (2002).

[170] H. Zhao, A. Maisels, T. Matsoukas, and C. Zheng, Powder Technol **173** (1), 38 (2007).

[171] V. A. Nemchinsky and M. Shigeta, Modelling and Simulation in Materials Science and Engineering **20** (4) (2012).

[172] H. K. Ma, T. J. Pan, and P. T. Cheng, Aerosol and Air Quality Research **14** (1), 251 (2014).

[173] D. X. Zhou and A. A. Keller, Water Research **44** (9), 2948 (2010).

[174] T. Thajudeen, R. Gopalakrishnan, and C. J. Hogan, Aerosol Science and Technology **46** (11), 1174 (2012).

[175] W. R. Heinson, F. Pierce, C. M. Sorensen, and A. Chakrabarti, Aerosol Science and Technology **48** (7), 738 (2014).

[176] Hui Ouyang, Ranganathan Gopalakrishnan, and Christopher J. Hogan, Jr., Journal of Chemical Physics **137** (6) (2012).

[177] R. Gopalakrishnan, T. Thajudeen, H. Ouyang, and C. J. Hogan, Journal of Aerosol Science **64**, 60 (2013).

[178] L. Isella and Y. Drossinos, Physical Review E **82** (1), 15 (2010).

[179] Shraddha Shekar, Alastair J. Smith, William J. Menz, Markus Sander, and Markus Kraft, Journal of Aerosol Science **44**, 83 (2012); A. A. Turkin, M. V. Dutka, Y. T. Pei, D. I. Vainshtein, and J. T. M. De Hosson, Journal of Applied Physics **111** (12), 11 (2012); J. W. Su, Z. L. Gu, Y. Li, S. Y. Feng, and X. Y. Xu,

Chemical Engineering Science **62** (21), 5897 (2007); Chemical Engineering Science **57** (12), 2123 (2002); Benjamin J. McCoy, Chemical Engineering Science **57** (12), 2279 (2002); H. Mühlenweg, A. Gutsch, A. Schild, and S. E. Pratsinis, Chemical Engineering Science **57** (12), 2305 (2002); S. Tsantilis, H. K. Kammler, and S. E. Pratsinis, Chemical Engineering Science **57** (12), 2139 (2002); S. K. Friedlander and C. S. Wang, Journal of Colloid and Interface Science **22** (2), 126 (1966).

180 S. Khalili, Y. L. Lin, A. Armaou, and T. Matsoukas, Aiche J. **56** (12), 3137 (2010).

181 H. B. Zhao and C. G. Zheng, J Comput Phys **228** (5), 1412 (2009); A. Maisels, F. E. Kruis, and H. Fissan, Chem Eng Sci **59** (11), 2231 (2004); F. E. Kruis, A. Maisels, and H. Fissan, Aiche J. **46** (9), 1735 (2000).

182 Marian von Smoluchowski, Z. physikalische Chemie **92**, 40 (1917); Reinhard Lang and NguyenXuan Xanh, Z. Wahrscheinlichkeitstheorie verw Gebiete **54** (3), 227 (1980).

183 Z. Sun, R. L. Axelbaum, and J. I. Huertas, Aerosol Sci Tech **38** (10), 963 (2004).

184 K. Lee and T. Matsoukas, Powder Technol **110** (1-2), 82 (2000); Y. L. Lin, K. Lee, and T. Matsoukas, Chem Eng Sci **57** (12), 2241 (2002).

185 J. A. Gantt and E. P. Gatzke, Aiche J. **52** (9), 3067 (2006); H. H. Liu, S. Surawanvijit, R. Rallo, G. Orkoulas, and Y. Cohen, Environ. Sci. Technol. **45** (21), 9284 (2011); C. L. Marshall, P. Rajniak, and T. Matsoukas, Chem. Eng. Res. Des. **89** (5A), 545 (2011).

186 T. Thajudeen, S. Jeon, and C. J. Hogan, Journal of Aerosol Science **80**, 45 (2015); C. L. Zhang, T. Thajudeen, C. Larriba, T. E. Schwartzentruber, and C. J. Hogan, Aerosol Science and Technology **46** (10), 1065 (2012).

187 R. Gopalakrishnan, T. Thajudeen, and C. J. Hogan, Journal of Chemical Physics **135** (9) (2011).

188 Carlos Larriba-Andaluz, Juan Fernandez-Garcia, Michael A. Ewing, Christopher J. Hogan, and David E. Clemmer, Physical chemistry chemical physics : PCCP **17** (22), 15019 (2015).

189 J. Fernandez-Garcia and J. F. de la Mora, Physical Chemistry Chemical Physics **16** (38), 20500 (2014).

190 R. Gopalakrishnan, T. Thajudeen, and C. J. Hogan, Journal of Chemical Physics **135** (5) (2011).

Appendix A - Enhancement Factor Correlations

Table A1: van der Waals with $\omega = 0.5$

$$\eta_C = 1 + 0.0586\Psi_{VDW}^{0.5704} \qquad 0 < \Psi_{VDW} \leq 4.5$$

$$\eta_C = (0.9976 - 0.0725\ln(\Psi_{VDW}))^{-1} \quad 4.5 < \Psi_{VDW} \leq 300$$

$$\eta_{FM} = 1 + 0.3636\Psi_{VDW}^{0.4202} \quad 0 < \Psi_{VDW} \leq 4.5$$

$$\eta_{FM} = 1 + 0.3757\Psi_{VDW}^{0.3913} \quad 4.5 < \Psi_{VDW} \leq 300$$

Ψ_{VDW}	η_C	η_{FM}	13	1.224281	2.0218	26	1.301231	2.3287	39	1.354008	2.5483
0.5	1.038533	1.2744	13.5	1.22806	2.0366	26.5	1.303578	2.3382	39.5	1.355764	2.5556
1	1.05919	1.3674	14	1.231746	2.0511	27	1.305893	2.3476	40	1.357504	2.5629
1.5	1.075052	1.4344	14.5	1.235342	2.0653	27.5	1.308178	2.3569	40.5	1.359227	2.5701
2	1.088272	1.4886	15	1.238855	2.0792	28	1.310434	2.3661	41	1.360936	2.5773
2.5	1.099756	1.5348	15.5	1.242288	2.0927	28.5	1.312661	2.3752	41.5	1.362629	2.5844
3	1.109986	1.5755	16	1.245646	2.106	29	1.31486	2.3842	42	1.364307	2.5914
3.5	1.119259	1.6121	16.5	1.248933	2.119	29.5	1.317032	2.3931	42.5	1.365971	2.5984
4	1.127771	1.6455	17	1.252151	2.1318	30	1.319178	2.4019	43	1.36762	2.6053
4.5	1.135659	1.6763	17.5	1.255304	2.1443	30.5	1.321298	2.4105	43.5	1.369256	2.6122
5	1.143025	1.7051	18	1.258396	2.1566	31	1.323394	2.4191	44	1.370877	2.6191
5.5	1.149947	1.732	18.5	1.261428	2.1686	31.5	1.325465	2.4277	44.5	1.372486	2.6259
6	1.156484	1.7575	19	1.264403	2.1805	32	1.327513	2.4361	45	1.374081	2.6326
6.5	1.162685	1.7816	19.5	1.267325	2.1922	32.5	1.329538	2.4444	45.5	1.375663	2.6393
7	1.168588	1.8045	20	1.270194	2.2036	33	1.33154	2.4527	46	1.377232	2.6459
7.5	1.174226	1.8264	20.5	1.273014	2.2149	33.5	1.33352	2.4609	46.5	1.378789	2.6525
8	1.179625	1.8474	21	1.275786	2.226	34	1.33548	2.4713	47	1.380333	2.6591
8.5	1.184809	1.8676	21.5	1.278512	2.237	34.5	1.337418	2.4793	47.5	1.381866	2.6656
9	1.189797	1.887	22	1.281193	2.2477	35	1.339337	2.4872	48	1.383387	2.6721
9.5	1.194606	1.9057	22.5	1.283832	2.2583	35.5	1.341235	2.4951	48.5	1.384896	2.6785
10	1.19925	1.9238	23	1.28643	2.2688	36	1.343114	2.5029	49	1.386393	2.6849
10.5	1.203742	1.9414	23.5	1.288988	2.2791	36.5	1.344975	2.5106	49.5	1.38788	2.6912
11	1.208094	1.9584	24	1.291508	2.2893	37	1.346817	2.5183	50	1.389355	2.6975
11.5	1.212315	1.9749	24.5	1.293991	2.2993	37.5	1.348641	2.5259	50.5	1.39082	2.7037
12	1.216415	1.9909	25	1.296439	2.3092	38	1.350447	2.5334	51	1.392273	2.71
12.5	1.220401	2.0066	25.5	1.298851	2.319	38.5	1.352236	2.5409	51.5	1.393717	2.7161

52	1.39515	2.7223	71	1.443296	2.9318	90	1.482559	3.108	109	1.515968	3.2619
52.5	1.396572	2.7284	71.5	1.444425	2.9368	90.5	1.483504	3.1123	109.5	1.516785	3.2657
53	1.397985	2.7344	72	1.445548	2.9418	91	1.484445	3.1166	110	1.517599	3.2695
53.5	1.399388	2.7405	72.5	1.446666	2.9468	91.5	1.485382	3.1208	110.5	1.518411	3.2733
54	1.400782	2.7464	73	1.447777	2.9517	92	1.486315	3.1251	111	1.519219	3.2771
54.5	1.402165	2.7524	73.5	1.448883	2.9566	92.5	1.487244	3.1293	111.5	1.520025	3.2809
55	1.40354	2.7583	74	1.449984	2.9615	93	1.48817	3.1336	112	1.520828	3.2847
55.5	1.404905	2.7642	74.5	1.451078	2.9664	93.5	1.489091	3.1378	112.5	1.521629	3.2884
56	1.406261	2.77	75	1.452168	2.9712	94	1.490009	3.142	113	1.522426	3.2921
56.5	1.407608	2.7759	75.5	1.453252	2.976	94.5	1.490924	3.1462	113.5	1.523221	3.2959
57	1.408947	2.7816	76	1.45433	2.9808	95	1.491834	3.1503	114	1.524014	3.2996
57.5	1.410276	2.7874	76.5	1.455403	2.9856	95.5	1.492741	3.1545	114.5	1.524803	3.3033
58	1.411597	2.7931	77	1.456471	2.9904	96	1.493645	3.1586	115	1.52559	3.307
58.5	1.41291	2.7988	77.5	1.457533	2.9951	96.5	1.494544	3.1628	115.5	1.526375	3.3107
59	1.414214	2.8045	78	1.458591	2.9999	97	1.495441	3.1669	116	1.527157	3.3144
59.5	1.41551	2.8101	78.5	1.459643	3.0046	97.5	1.496334	3.171	116.5	1.527936	3.3181
60	1.416798	2.8157	79	1.460691	3.0093	98	1.497223	3.1751	117	1.528713	3.3217
60.5	1.418078	2.8212	79.5	1.461733	3.0139	98.5	1.498109	3.1791	117.5	1.529487	3.3254
61	1.41935	2.8268	80	1.46277	3.0186	99	1.498991	3.1832	118	1.530259	3.329
61.5	1.420615	2.8323	80.5	1.463803	3.0232	99.5	1.49987	3.1873	118.5	1.531028	3.3326
62	1.421871	2.8378	81	1.464831	3.0278	100	1.500746	3.1913	119	1.531795	3.3363
62.5	1.423121	2.8432	81.5	1.465854	3.0324	100.5	1.501619	3.1953	119.5	1.532559	3.3399
63	1.424362	2.8486	82	1.466872	3.037	101	1.502488	3.1993	120	1.533321	3.3435
63.5	1.425597	2.854	82.5	1.467885	3.0416	101.5	1.503354	3.2033	120.5	1.53408	3.3471
64	1.426824	2.8594	83	1.468894	3.0461	102	1.504216	3.2073	121	1.534837	3.3507
64.5	1.428044	2.8647	83.5	1.469899	3.0506	102.5	1.505076	3.2113	121.5	1.535592	3.3542
65	1.429257	2.87	84	1.470898	3.0551	103	1.505932	3.2153	122	1.536344	3.3578
65.5	1.430463	2.8753	84.5	1.471894	3.0596	103.5	1.506785	3.2192	122.5	1.537094	3.3614
66	1.431663	2.8806	85	1.472885	3.0641	104	1.507635	3.2232	123	1.537841	3.3649
66.5	1.432855	2.8858	85.5	1.473871	3.0686	104.5	1.508482	3.2271	123.5	1.538586	3.3685
67	1.434041	2.891	86	1.474853	3.073	105	1.509325	3.231	124	1.539329	3.372
67.5	1.43522	2.8962	86.5	1.475831	3.0774	105.5	1.510166	3.2349	124.5	1.54007	3.3755
68	1.436393	2.9014	87	1.476805	3.0818	106	1.511004	3.2388	125	1.540808	3.379
68.5	1.437559	2.9065	87.5	1.477774	3.0862	106.5	1.511838	3.2427	125.5	1.541544	3.3825
69	1.438719	2.9116	88	1.478739	3.0906	107	1.51267	3.2466	126	1.542278	3.386
69.5	1.439872	2.9167	88.5	1.4797	3.095	107.5	1.513499	3.2504	126.5	1.54301	3.3895
70	1.441019	2.9218	89	1.480657	3.0993	108	1.514325	3.2543	127	1.543739	3.393
70.5	1.442161	2.9268	89.5	1.48161	3.1037	108.5	1.515148	3.2581	127.5	1.544466	3.3965

128	1.545191	3.3999
128.5	1.545914	3.4034
129	1.546635	3.4069
129.5	1.547353	3.4103
130	1.54807	3.4137
130.5	1.548784	3.4171
131	1.549496	3.4206
131.5	1.550206	3.424
132	1.550914	3.4274
132.5	1.55162	3.4308
133	1.552324	3.4341
133.5	1.553026	3.4375
134	1.553726	3.4409
134.5	1.554424	3.4442
135	1.55512	3.4476
135.5	1.555814	3.4509
136	1.556506	3.4543
136.5	1.557196	3.4576
137	1.557884	3.4609
137.5	1.55857	3.4643
138	1.559254	3.4676
138.5	1.559937	3.4709
139	1.560617	3.4742
139.5	1.561296	3.4774
140	1.561972	3.4807
140.5	1.562647	3.484
141	1.56332	3.4873
141.5	1.563991	3.4905
142	1.564661	3.4938
142.5	1.565328	3.497
143	1.565994	3.5003
143.5	1.566658	3.5035
144	1.56732	3.5067
144.5	1.56798	3.5099
145	1.568639	3.5131
145.5	1.569296	3.5163
146	1.569951	3.5195
146.5	1.570604	3.5227

147	1.571256	3.5259
147.5	1.571906	3.5291
148	1.572554	3.5323
148.5	1.573201	3.5354
149	1.573846	3.5386
149.5	1.574489	3.5417
150	1.575131	3.5449
150.5	1.575771	3.548
151	1.576409	3.5512
151.5	1.577046	3.5543
152	1.577681	3.5574
152.5	1.578315	3.5605
153	1.578946	3.5636
153.5	1.579577	3.5667
154	1.580205	3.5698
154.5	1.580833	3.5729
155	1.581458	3.576
155.5	1.582082	3.5791
156	1.582705	3.5822
156.5	1.583326	3.5852
157	1.583945	3.5883
157.5	1.584563	3.5913
158	1.585179	3.5944
158.5	1.585794	3.5974
159	1.586408	3.6005
159.5	1.587019	3.6035
160	1.58763	3.6065
160.5	1.588239	3.6096
161	1.588846	3.6126
161.5	1.589452	3.6156
162	1.590057	3.6186
162.5	1.59066	3.6216
163	1.591262	3.6246
163.5	1.591862	3.6276
164	1.592461	3.6306
164.5	1.593058	3.6335
165	1.593654	3.6365
165.5	1.594249	3.6395

166	1.594842	3.6424
166.5	1.595434	3.6454
167	1.596025	3.6483
167.5	1.596614	3.6513
168	1.597202	3.6542
168.5	1.597788	3.6572
169	1.598373	3.6601
169.5	1.598957	3.663
170	1.599539	3.6659
170.5	1.60012	3.6689
171	1.6007	3.6718
171.5	1.601279	3.6747
172	1.601856	3.6776
172.5	1.602432	3.6805
173	1.603006	3.6834
173.5	1.60358	3.6862
174	1.604152	3.6891
174.5	1.604722	3.692
175	1.605292	3.6949
175.5	1.60586	3.6977
176	1.606427	3.7006
176.5	1.606993	3.7035
177	1.607557	3.7063
177.5	1.608121	3.7092
178	1.608683	3.712
178.5	1.609243	3.7148
179	1.609803	3.7177
179.5	1.610361	3.7205
180	1.610919	3.7233
180.5	1.611475	3.7261
181	1.612029	3.729
181.5	1.612583	3.7318
182	1.613135	3.7346
182.5	1.613687	3.7374
183	1.614237	3.7402
183.5	1.614786	3.743
184	1.615333	3.7458
184.5	1.61588	3.7485

185	1.616425	3.7513
185.5	1.61697	3.7541
186	1.617513	3.7569
186.5	1.618055	3.7596
187	1.618596	3.7624
187.5	1.619136	3.7652
188	1.619674	3.7679
188.5	1.620212	3.7707
189	1.620748	3.7734
189.5	1.621284	3.7761
190	1.621818	3.7789
190.5	1.622351	3.7816
191	1.622883	3.7843
191.5	1.623414	3.7871
192	1.623944	3.7898
192.5	1.624473	3.7925
193	1.625001	3.7952
193.5	1.625528	3.7979
194	1.626053	3.8006
194.5	1.626578	3.8033
195	1.627101	3.806
195.5	1.627624	3.8087
196	1.628146	3.8114
196.5	1.628666	3.8141
197	1.629185	3.8168
197.5	1.629704	3.8195
198	1.630221	3.8221
198.5	1.630738	3.8248
199	1.631253	3.8275
199.5	1.631767	3.8301
200	1.632281	3.8328
200.5	1.632793	3.8354
201	1.633305	3.8381
201.5	1.633815	3.8407
202	1.634324	3.8434
202.5	1.634833	3.846
203	1.63534	3.8486
203.5	1.635847	3.8513

204	1.636352	3.8539
204.5	1.636857	3.8565
205	1.63736	3.8592
205.5	1.637863	3.8618
206	1.638365	3.8644
206.5	1.638866	3.867
207	1.639365	3.8696
207.5	1.639864	3.8722
208	1.640362	3.8748
208.5	1.640859	3.8774
209	1.641355	3.88
209.5	1.64185	3.8826
210	1.642345	3.8852
210.5	1.642838	3.8877
211	1.64333	3.8903
211.5	1.643822	3.8929
212	1.644312	3.8955
212.5	1.644802	3.898
213	1.645291	3.9006
213.5	1.645779	3.9032
214	1.646266	3.9057
214.5	1.646752	3.9083
215	1.647237	3.9108
215.5	1.647722	3.9134
216	1.648205	3.9159
216.5	1.648688	3.9185
217	1.64917	3.921
217.5	1.64965	3.9235
218	1.65013	3.9261
218.5	1.65061	3.9286
219	1.651088	3.9311
219.5	1.651565	3.9336
220	1.652042	3.9362
220.5	1.652518	3.9387
221	1.652993	3.9412
221.5	1.653467	3.9437
222	1.65394	3.9462
222.5	1.654413	3.9487

223	1.654884	3.9512
223.5	1.655355	3.9537
224	1.655825	3.9562
224.5	1.656294	3.9587
225	1.656763	3.9612
225.5	1.65723	3.9637
226	1.657697	3.9662
226.5	1.658163	3.9686
227	1.658628	3.9711
227.5	1.659092	3.9736
228	1.659556	3.976
228.5	1.660018	3.9785
229	1.66048	3.981
229.5	1.660942	3.9834
230	1.661402	3.9859
230.5	1.661861	3.9884
231	1.66232	3.9908
231.5	1.662778	3.9933
232	1.663236	3.9957
232.5	1.663692	3.9981
233	1.664148	4.0006
233.5	1.664603	4.003
234	1.665057	4.0055
234.5	1.665511	4.0079
235	1.665963	4.0103
235.5	1.666415	4.0127
236	1.666866	4.0152
236.5	1.667317	4.0176
237	1.667767	4.02
237.5	1.668216	4.0224
238	1.668664	4.0248
238.5	1.669111	4.0272
239	1.669558	4.0296
239.5	1.670004	4.0321
240	1.670449	4.0345
240.5	1.670894	4.0369
241	1.671338	4.0392
241.5	1.671781	4.0416

242	1.672223	4.044
242.5	1.672665	4.0464
243	1.673106	4.0488
243.5	1.673547	4.0512
244	1.673986	4.0536
244.5	1.674425	4.0559
245	1.674863	4.0583
245.5	1.675301	4.0607
246	1.675738	4.0631
246.5	1.676174	4.0654
247	1.676609	4.0678
247.5	1.677044	4.0702
248	1.677478	4.0725
248.5	1.677911	4.0749
249	1.678344	4.0772
249.5	1.678776	4.0796
250	1.679207	4.0819
250.5	1.679638	4.0843
251	1.680068	4.0866
251.5	1.680497	4.089
252	1.680926	4.0913
252.5	1.681354	4.0936
253	1.681781	4.096
253.5	1.682208	4.0983
254	1.682634	4.1006
254.5	1.683059	4.103
255	1.683484	4.1053
255.5	1.683908	4.1076
256	1.684331	4.1099
256.5	1.684754	4.1122
257	1.685176	4.1145
257.5	1.685597	4.1169
258	1.686018	4.1192
258.5	1.686438	4.1215
259	1.686858	4.1238
259.5	1.687277	4.1261
260	1.687695	4.1284
260.5	1.688113	4.1307

261	1.68853	4.133
261.5	1.688946	4.1353
262	1.689362	4.1376
262.5	1.689777	4.1399
263	1.690192	4.1421
263.5	1.690606	4.1444
264	1.691019	4.1467
264.5	1.691432	4.149
265	1.691844	4.1513
265.5	1.692255	4.1535
266	1.692666	4.1558
266.5	1.693076	4.1581
267	1.693486	4.1604
267.5	1.693895	4.1626
268	1.694303	4.1649
268.5	1.694711	4.1671
269	1.695119	4.1694
269.5	1.695525	4.1717
270	1.695931	4.1739
270.5	1.696337	4.1762
271	1.696742	4.1784
271.5	1.697146	4.1807
272	1.69755	4.1829
272.5	1.697953	4.1852
273	1.698356	4.1874
273.5	1.698758	4.1896
274	1.699159	4.1919
274.5	1.69956	4.1941
275	1.69996	4.1963
275.5	1.70036	4.1986
276	1.700759	4.2008
276.5	1.701158	4.203
277	1.701556	4.2053
277.5	1.701953	4.2075
278	1.70235	4.2097
278.5	1.702746	4.2119
279	1.703142	4.2141
279.5	1.703537	4.2164

280	1.703932	4.2186	285	1.707849	4.2406	290	1.711712	4.2624	295	1.715523	4.284
280.5	1.704326	4.2208	285.5	1.708237	4.2428	290.5	1.712095	4.2646	295.5	1.715901	4.2862
281	1.70472	4.223	286	1.708625	4.245	291	1.712478	4.2668	296	1.716279	4.2883
281.5	1.705113	4.2252	286.5	1.709013	4.2472	291.5	1.71286	4.2689	296.5	1.716656	4.2905
282	1.705505	4.2274	287	1.7094	4.2493	292	1.713242	4.2711	297	1.717033	4.2926
282.5	1.705897	4.2296	287.5	1.709787	4.2515	292.5	1.713624	4.2733	297.5	1.717409	4.2948
283	1.706289	4.2318	288	1.710173	4.2537	293	1.714005	4.2754	298	1.717785	4.2969
283.5	1.706679	4.234	288.5	1.710558	4.2559	293.5	1.714385	4.2776	298.5	1.718161	4.2991
284	1.70707	4.2362	289	1.710943	4.2581	294	1.714765	4.2797	299	1.718535	4.3012
284.5	1.707459	4.2384	289.5	1.711328	4.2602	294.5	1.715144	4.2819	299.5	1.71891	4.3034

Table A2 - Image potential

$$\eta_C = 1 + 0.3475\Psi_I^{0.3802} 0 < \Psi_I \leq 266$$

$$\eta_{FM} = 1 + 1.2534\Psi_I^{0.5} \quad 0 < \Psi_I \leq 266$$

Ψ_I	η_C	η_{FM}	11	1.877641	5.1568	22	2.166423	6.8786	33	2.365141	8.1998
0.5	1.180912	1.8863	11.5	1.894369	5.2502	22.5	2.176832	6.945	33.5	2.372968	8.2541
1	1.270874	2.2534	12	1.910606	5.3417	23	2.187079	7.0107	34	2.380713	8.3081
1.5	1.33833	2.5351	12.5	1.926385	5.4312	23.5	2.19717	7.0757	34.5	2.388376	8.3616
2	1.393737	2.7725	13	1.941735	5.5189	24	2.207111	7.14	35	2.39596	8.4148
2.5	1.44137	2.9817	13.5	1.956683	5.605	24.5	2.216907	7.2036	35.5	2.403467	8.4675
3	1.483478	3.1709	14	1.971253	5.6895	25	2.226562	7.2666	36	2.410899	8.5199
3.5	1.521411	3.3448	14.5	1.985467	5.7725	25.5	2.236081	7.329	36.5	2.418258	8.572
4	1.556059	3.5067	15	1.999345	5.8541	26	2.245469	7.3907	37	2.425545	8.6237
4.5	1.588038	3.6587	15.5	2.012906	5.9344	26.5	2.25473	7.4519	37.5	2.432761	8.675
5	1.617798	3.8026	16	2.026166	6.0133	27	2.263867	7.5125	38	2.439909	8.726
5.5	1.645681	3.9393	16.5	2.03914	6.091	27.5	2.272886	7.5725	38.5	2.44699	8.7767
6	1.671947	4.07	17	2.051844	6.1676	28	2.281789	7.632	39	2.454005	8.827
6.5	1.696808	4.1954	17.5	2.064289	6.243	28.5	2.290579	7.6909	39.5	2.460956	8.877
7	1.72043	4.316	18	2.076488	6.3174	29	2.299261	7.7493	40	2.467845	8.9267
7.5	1.742954	4.4324	18.5	2.088452	6.3908	29.5	2.307837	7.8073	40.5	2.474671	8.9761
8	1.764493	4.545	19	2.100192	6.4631	30	2.31631	7.8647	41	2.481438	9.0252
8.5	1.785146	4.6541	19.5	2.111717	6.5345	30.5	2.324683	7.9217	41.5	2.488146	9.074
9	1.804995	4.76	20	2.123037	6.605	31	2.332959	7.9782	42	2.494795	9.1224
9.5	1.824111	4.863	20.5	2.13416	6.6747	31.5	2.34114	8.0343	42.5	2.501389	9.1707
10	1.842556	4.9634	21	2.145093	6.7435	32	2.349229	8.0899	43	2.507926	9.2186
10.5	1.860384	5.0613	21.5	2.155845	6.8114	32.5	2.357229	8.145	43.5	2.514409	9.2662

44	2.520839	9.3136	63	2.733586	10.948	82	2.90379	12.349	101	3.04728	13.596
44.5	2.527217	9.3607	63.5	2.738513	10.987	82.5	2.907862	12.384	101.5	3.050779	13.627
45	2.533543	9.4075	64	2.743413	11.027	83	2.911915	12.418	102	3.054266	13.658
45.5	2.539819	9.4541	64.5	2.748285	11.066	83.5	2.915952	12.453	102.5	3.05774	13.689
46	2.546046	9.5004	65	2.75313	11.105	84	2.91997	12.487	103	3.061202	13.72
46.5	2.552224	9.5465	65.5	2.757947	11.143	84.5	2.923971	12.521	103.5	3.064651	13.751
47	2.558354	9.5923	66	2.762739	11.182	85	2.927955	12.555	104	3.068089	13.781
47.5	2.564437	9.6379	66.5	2.767503	11.221	85.5	2.931922	12.589	104.5	3.071514	13.812
48	2.570475	9.6833	67	2.772242	11.259	86	2.935872	12.623	105	3.074927	13.843
48.5	2.576467	9.7284	67.5	2.776956	11.297	86.5	2.939806	12.657	105.5	3.078329	13.873
49	2.582415	9.7732	68	2.781644	11.335	87	2.943722	12.69	106	3.081719	13.904
49.5	2.58832	9.8179	68.5	2.786307	11.373	87.5	2.947623	12.724	106.5	3.085097	13.934
50	2.594181	9.8623	69	2.790946	11.411	88	2.951507	12.757	107	3.088463	13.964
50.5	2.600001	9.9065	69.5	2.79556	11.449	88.5	2.955375	12.791	107.5	3.091818	13.995
51	2.605779	9.9505	70	2.80015	11.486	89	2.959228	12.824	108	3.095162	14.025
51.5	2.611516	9.9943	70.5	2.804717	11.523	89.5	2.963064	12.857	108.5	3.098494	14.055
52	2.617214	10.038	71	2.80926	11.561	90	2.966885	12.89	109	3.101816	14.085
52.5	2.622871	10.081	71.5	2.813779	11.598	90.5	2.970691	12.923	109.5	3.105126	14.115
53	2.628491	10.124	72	2.818276	11.635	91	2.974481	12.956	110	3.108425	14.145
53.5	2.634072	10.167	72.5	2.822751	11.672	91.5	2.978256	12.989	110.5	3.111713	14.175
54	2.639615	10.21	73	2.827202	11.708	92	2.982016	13.021	111	3.11499	14.205
54.5	2.645121	10.253	73.5	2.831632	11.745	92.5	2.985761	13.054	111.5	3.118256	14.234
55	2.650592	10.295	74	2.83604	11.781	93	2.989492	13.087	112	3.121512	14.264
55.5	2.656026	10.337	74.5	2.840427	11.818	93.5	2.993208	13.119	112.5	3.124757	14.293
56	2.661425	10.379	75	2.844792	11.854	94	2.996909	13.151	113	3.127992	14.323
56.5	2.666789	10.421	75.5	2.849136	11.89	94.5	3.000596	13.184	113.5	3.131216	14.352
57	2.672119	10.462	76	2.853459	11.926	95	3.004269	13.216	114	3.13443	14.382
57.5	2.677416	10.504	76.5	2.857761	11.962	95.5	3.007928	13.248	114.5	3.137633	14.411
58	2.682679	10.545	77	2.862043	11.998	96	3.011573	13.28	115	3.140826	14.44
58.5	2.687909	10.586	77.5	2.866305	12.033	96.5	3.015204	13.312	115.5	3.14401	14.47
59	2.693107	10.627	78	2.870547	12.069	97	3.018821	13.344	116	3.147183	14.499
59.5	2.698274	10.668	78.5	2.874769	12.104	97.5	3.022425	13.376	116.5	3.150346	14.528
60	2.703409	10.708	79	2.878972	12.14	98	3.026015	13.407	117	3.153499	14.557
60.5	2.708513	10.749	79.5	2.883155	12.175	98.5	3.029592	13.439	117.5	3.156642	14.586
61	2.713587	10.789	80	2.88732	12.21	99	3.033155	13.47	118	3.159776	14.615
61.5	2.718631	10.829	80.5	2.891465	12.245	99.5	3.036706	13.502	118.5	3.162899	14.643
62	2.723645	10.869	81	2.895592	12.28	100	3.040243	13.533	119	3.166014	14.672
62.5	2.72863	10.908	81.5	2.8997	12.315	100.5	3.043768	13.564	119.5	3.169118	14.701

120	3.172213	14.729
120.5	3.175299	14.758
121	3.178375	14.786
121.5	3.181442	14.815
122	3.1845	14.843
122.5	3.187549	14.872
123	3.190588	14.9
123.5	3.193619	14.928
124	3.19664	14.956
124.5	3.199653	14.984
125	3.202657	15.013
125.5	3.205652	15.041
126	3.208638	15.068
126.5	3.211616	15.096
127	3.214585	15.124
127.5	3.217545	15.152
128	3.220497	15.18
128.5	3.223441	15.207
129	3.226376	15.235
129.5	3.229303	15.263
130	3.232221	15.29
130.5	3.235132	15.317
131	3.238034	15.345
131.5	3.240928	15.372
132	3.243814	15.4
132.5	3.246692	15.427
133	3.249562	15.454
133.5	3.252424	15.481
134	3.255278	15.508
134.5	3.258125	15.535
135	3.260964	15.562
135.5	3.263795	15.589
136	3.266618	15.616
136.5	3.269434	15.643
137	3.272242	15.67
137.5	3.275043	15.696
138	3.277836	15.723
138.5	3.280622	15.75

139	3.283401	15.776
139.5	3.286172	15.803
140	3.288936	15.829
140.5	3.291692	15.856
141	3.294442	15.882
141.5	3.297184	15.909
142	3.29992	15.935
142.5	3.302648	15.961
143	3.305369	15.987
143.5	3.308083	16.014
144	3.310791	16.04
144.5	3.313491	16.066
145	3.316184	16.092
145.5	3.318871	16.118
146	3.321551	16.144
146.5	3.324224	16.17
147	3.326891	16.196
147.5	3.329551	16.221
148	3.332204	16.247
148.5	3.334851	16.273
149	3.337491	16.299
149.5	3.340125	16.324
150	3.342752	16.35
150.5	3.345373	16.376
151	3.347988	16.401
151.5	3.350596	16.426
152	3.353197	16.452
152.5	3.355793	16.477
153	3.358382	16.503
153.5	3.360965	16.528
154	3.363542	16.553
154.5	3.366113	16.578
155	3.368678	16.604
155.5	3.371236	16.629
156	3.373789	16.654
156.5	3.376335	16.679
157	3.378876	16.704
157.5	3.381411	16.729

158	3.383939	16.754
158.5	3.386462	16.779
159	3.388979	16.804
159.5	3.39149	16.829
160	3.393996	16.853
160.5	3.396496	16.878
161	3.39899	16.903
161.5	3.401478	16.927
162	3.403961	16.952
162.5	3.406438	16.977
163	3.408909	17.001
163.5	3.411375	17.026
164	3.413835	17.05
164.5	3.41629	17.075
165	3.418739	17.099
165.5	3.421183	17.124
166	3.423622	17.148
166.5	3.426055	17.172
167	3.428483	17.196
167.5	3.430905	17.221
168	3.433322	17.245
168.5	3.435734	17.269
169	3.438141	17.293
169.5	3.440542	17.317
170	3.442938	17.341
170.5	3.445329	17.365
171	3.447715	17.389
171.5	3.450095	17.413
172	3.452471	17.437
172.5	3.454842	17.461
173	3.457207	17.485
173.5	3.459567	17.509
174	3.461923	17.532
174.5	3.464273	17.556
175	3.466619	17.58
175.5	3.468959	17.603
176	3.471295	17.627
176.5	3.473626	17.651

177	3.475952	17.674
177.5	3.478273	17.698
178	3.480589	17.721
178.5	3.482901	17.745
179	3.485208	17.768
179.5	3.48751	17.792
180	3.489807	17.815
180.5	3.4921	17.838
181	3.494388	17.862
181.5	3.496671	17.885
182	3.49895	17.908
182.5	3.501224	17.931
183	3.503494	17.955
183.5	3.505759	17.978
184	3.508019	18.001
184.5	3.510275	18.024
185	3.512527	18.047
185.5	3.514774	18.07
186	3.517016	18.093
186.5	3.519254	18.116
187	3.521488	18.139
187.5	3.523717	18.162
188	3.525942	18.185
188.5	3.528163	18.207
189	3.530379	18.23
189.5	3.532591	18.253
190	3.534799	18.276
190.5	3.537002	18.298
191	3.539201	18.321
191.5	3.541396	18.344
192	3.543587	18.366
192.5	3.545773	18.389
193	3.547956	18.412
193.5	3.550134	18.434
194	3.552308	18.457
194.5	3.554478	18.479
195	3.556643	18.502
195.5	3.558805	18.524

196	3.560963	18.546
196.5	3.563116	18.569
197	3.565266	18.591
197.5	3.567411	18.613
198	3.569553	18.636
198.5	3.571691	18.658
199	3.573824	18.68
199.5	3.575954	18.702
200	3.57808	18.725
200.5	3.580201	18.747
201	3.582319	18.769
201.5	3.584433	18.791
202	3.586544	18.813
202.5	3.58865	18.835
203	3.590752	18.857
203.5	3.592851	18.879
204	3.594946	18.901
204.5	3.597037	18.923
205	3.599125	18.945
205.5	3.601208	18.967
206	3.603288	18.988
206.5	3.605364	19.01
207	3.607437	19.032
207.5	3.609506	19.054
208	3.611571	19.076
208.5	3.613632	19.097
209	3.61569	19.119
209.5	3.617744	19.141
210	3.619795	19.162
210.5	3.621842	19.184
211	3.623886	19.205
211.5	3.625925	19.227
212	3.627962	19.249
212.5	3.629995	19.27
213	3.632024	19.292
213.5	3.63405	19.313

214	3.636072	19.334
214.5	3.638091	19.356
215	3.640106	19.377
215.5	3.642118	19.399
216	3.644126	19.42
216.5	3.646131	19.441
217	3.648133	19.463
217.5	3.650131	19.484
218	3.652126	19.505
218.5	3.654117	19.526
219	3.656106	19.547
219.5	3.65809	19.569
220	3.660072	19.59
220.5	3.66205	19.611
221	3.664025	19.632
221.5	3.665996	19.653
222	3.667965	19.674
222.5	3.66993	19.695
223	3.671891	19.716
223.5	3.67385	19.737
224	3.675805	19.758
224.5	3.677757	19.779
225	3.679706	19.8
225.5	3.681652	19.821
226	3.683594	19.841
226.5	3.685533	19.862
227	3.68747	19.883
227.5	3.689403	19.904
228	3.691332	19.925
228.5	3.693259	19.945
229	3.695183	19.966
229.5	3.697103	19.987
230	3.699021	20.007
230.5	3.700935	20.028
231	3.702847	20.049
231.5	3.704755	20.069

232	3.70666	20.09
232.5	3.708563	20.111
233	3.710462	20.131
233.5	3.712358	20.152
234	3.714251	20.172
234.5	3.716142	20.193
235	3.718029	20.213
235.5	3.719913	20.233
236	3.721795	20.254
236.5	3.723673	20.274
237	3.725549	20.295
237.5	3.727421	20.315
238	3.729291	20.335
238.5	3.731158	20.356
239	3.733022	20.376
239.5	3.734883	20.396
240	3.736741	20.416
240.5	3.738596	20.437
241	3.740449	20.457
241.5	3.742298	20.477
242	3.744145	20.497
242.5	3.745989	20.517
243	3.74783	20.537
243.5	3.749669	20.557
244	3.751504	20.577
244.5	3.753337	20.597
245	3.755167	20.618
245.5	3.756995	20.638
246	3.758819	20.658
246.5	3.760641	20.677
247	3.76246	20.697
247.5	3.764277	20.717
248	3.766091	20.737
248.5	3.767902	20.757
249	3.76971	20.777
249.5	3.771516	20.797

250	3.773319	20.817
250.5	3.775119	20.836
251	3.776917	20.856
251.5	3.778712	20.876
252	3.780504	20.896
252.5	3.782294	20.916
253	3.784081	20.935
253.5	3.785866	20.955
254	3.787648	20.975
254.5	3.789427	20.994
255	3.791204	21.014
255.5	3.792978	21.033
256	3.79475	21.053
256.5	3.796519	21.073
257	3.798286	21.092
257.5	3.80005	21.112
258	3.801811	21.131
258.5	3.80357	21.151
259	3.805327	21.17
259.5	3.807081	21.19
260	3.808832	21.209
260.5	3.810581	21.229
261	3.812328	21.248
261.5	3.814072	21.267
262	3.815813	21.287
262.5	3.817553	21.306
263	3.819289	21.325
263.5	3.821024	21.345
264	3.822756	21.364
264.5	3.824485	21.383
265	3.826212	21.403
265.5	3.827937	21.422
266	3.829659	21.441

Appendix B – Singly and Doubly Charged Cluster Coordinates (Angstrom) and Single Point Electronic Energy (A.U)

Singly charged Cluster coordinates (Angstrom) and single point electronic energy (A.U)

NaI

Na 0.00 0.00 0.00
Na 0.00 5.95 0.01

--
NaI2_4

--
I 2.74 0.00 0.00
I -1.95 0.00 0.00
Na -4.95 0.00 0.00
Na 0.58 2.05 0.00
Na 0.58 -2.05 0.00

--
NaI2_5

--
I -2.10 0.00 0.00
I 2.10 0.00 0.00
Na 0.00 -2.36 0.22
Na 0.00 0.99 -2.16
Na 0.00 1.38 1.93

--
NaI3_1

--
I 0.94 -2.54 0.06
I -2.67 0.46 0.06
I 1.73 2.09 0.06
Na 0.00 0.00 1.75
Na -2.01 -2.43 -0.89
Na 3.11 -0.53 -0.89
Na -1.09 2.96 -0.89

--
NaI3_2

--
I -6.03 0.00 0.00
I 6.03 0.00 0.00
I 0.00 0.00 0.00
Na 2.98 0.00 0.00
Na -2.98 0.00 0.00
Na -8.94 0.00 0.00
Na 8.94 0.00 0.00

--
NaI3_4

--
I 2.72 0.00 0.00
I -1.57 -2.15 0.00
I -1.56 2.15 0.00
Na 0.03 0.00 1.78
Na 5.69 0.00 0.00
Na 0.03 0.00 -1.78
Na -3.79 0.00 0.00

NaI1 -11.73
NaI2_1 -23.44
NaI2_4 -23.44
NaI2_5 -23.44
NaI3_1 -35.17
NaI3_4 -35.15
NaI3_2 -35.14
NaI4_1 -46.89
NaI4_2 -46.88
NaI4_3 -46.85
NaI4_new -46.88
NaI5_2 -58.61
NaI5_1 -58.60
NaI6_3 -70.34
NaI6_1 -70.34
NaI6_2 -70.34
NaI6_4 -70.32
NaI7_2 -82.06
NaI7_3 -82.06
NaI7_1 -82.05
NaI8_1 -93.78
NaI8_3 -93.78
NaI8_2 -93.78
NaI8_2_2 -93.77
NaI9_3 -105.50
NaI9_1 -105.50
NaI9_2 -105.50
NaI9_4 -105.49
NaI9_5 -105.49
NaI10_1 -117.23
NaI11_4 -128.95
NaI11_1 -128.95
NaI11_5 -128.95
NaI12_3 -140.67
NaI12_1 -140.67
NaI12_2 -140.66
NaI13_1 -152.42
NaI13_2 -152.39

--
NaI1

--
I 0.00 0.00 0.00
Na 0.00 0.00 2.96
Na 0.00 0.00 -2.96

--
NaI2_1

--
I 0.00 3.03 0.00
I 0.00 -3.03 0.00
Na 0.00 -5.95 0.01

--
NaI4_1

--
I -0.25 3.28 -0.04
I 0.25 -3.28 -0.04
I 3.29 0.25 0.07
I -3.29 -0.25 0.07
Na 3.26 -2.81 -0.11
Na 2.81 3.26 -0.16
Na -3.26 2.81 -0.11
Na -2.81 -3.26 -0.16
Na 0.00 0.00 0.21

--
NaI4_2

--
I -1.20 -1.19 2.48
I 2.75 0.02 0.01
I -1.22 2.74 -0.22
I -1.17 -1.57 -2.27
Na 0.38 1.43 2.07
Na 0.40 1.09 -2.26
Na 0.42 -2.52 0.20
Na -2.85 -0.01 -0.01
Na 5.75 0.03 0.01

--
NaI4_3

--
I 8.62 2.69 0.00
I -2.87 -0.89 0.00
I 2.87 0.89 0.00
Na 0.00 0.00 0.00
Na 5.71 1.77 0.00
Na 11.39 3.56 0.00
Na -5.71 -1.78 0.00
I -8.62 -2.68 0.00
Na -11.39 -3.55 0.00

--
NaI4_new

--
I -2.21 -2.26 -0.23
I 2.95 0.00 -1.77
I 1.33 0.00 2.16
I -2.20 2.26 -0.22
Na 0.88 -2.06 -0.48
Na 0.88 2.06 -0.48
Na -3.58 0.00 -1.84
Na -1.86 0.00 2.03
Na 4.28 0.00 1.04

--
NaI5_1

--
I -0.80 -2.58 -0.81
I 3.43 -2.08 1.09
I 3.44 2.08 -1.08
I -5.62 0.00 0.00
I -0.81 2.58 0.79
Na -3.85 2.17 1.04
Na -3.85 -2.17 -1.04
Na 1.48 -4.28 0.31
Na 1.05 0.00 0.00
Na 1.48 4.28 -0.32
Na 5.40 0.00 0.01

--
NaI5_2

--
I 0.34 2.41 -0.86
I -1.51 0.00 2.88
I -3.77 0.00 -1.24
I 4.20 0.00 0.34
I 0.34 -2.41 -0.86
Na 3.44 -2.77 -0.80
Na 3.44 2.77 -0.80
Na -1.00 0.00 -2.55
Na 1.14 0.00 1.32
Na -2.56 -2.09 0.78
Na -2.56 2.09 0.78

--
NaI6_1

--
I 0.00 2.37 2.19
I 3.79 0.37 -0.02
I 0.00 -2.80 -2.43
I -3.79 0.38 -0.03
I -0.01 -2.42 2.79
I 0.01 2.03 -2.49
Na -2.13 -0.51 -2.53
Na -0.01 -4.22 0.30
Na 2.14 -0.51 -2.53
Na 2.09 2.94 -0.21
Na 2.13 -0.15 2.58
Na -2.08 2.95 -0.21
Na -2.14 -0.14 2.57

--
NaI6_2

--
I -2.59 -0.97 1.80
I 2.14 -1.76 1.79
I 3.05 1.14 -1.93
I -2.52 2.07 -1.92
I -0.54 -3.22 -1.92
I 0.46 2.73 1.79
Na 0.00 0.00 3.30

Na 3.28 1.22 1.14
Na -2.70 2.23 1.15
Na 2.25 -1.86 -1.63
Na -0.58 -3.45 1.15
Na -2.74 -1.02 -1.63
Na 0.48 2.87 -1.63

--
NaI6_3

--
I 1.08 2.72 -1.65
I 1.81 -2.30 -1.65
I -1.08 -2.72 1.65
I -1.81 2.30 1.65
I 2.90 0.42 1.65
I -2.90 -0.42 -1.65
Na -3.37 -0.49 1.59
Na -1.26 -3.17 -1.58
Na 2.11 -2.67 1.58
Na 0.00 0.00 0.00
Na 1.26 3.17 1.58
Na -2.11 2.67 -1.58
Na 3.37 0.49 -1.59

--
NaI6_4

--
I 0.13 -0.03 2.49
I -3.56 1.65 0.00
I 2.96 2.81 0.00
I 3.71 -1.91 0.00
I -2.57 -3.06 0.00
I 0.13 -0.03 -2.49
Na -2.82 -0.89 2.16
Na -2.82 -0.88 -2.16
Na -0.04 1.99 0.00
Na 3.30 0.42 -2.05
Na 0.60 -2.33 0.00
Na 3.30 0.42 2.04
Na -5.42 4.00 0.00

--
NaI7_1

--
I 4.36 -1.38 -0.01
I -0.01 -3.43 0.00
I -4.37 -1.36 0.02
I 0.02 -0.20 3.40
I -0.03 -0.20 -3.41
Na 2.10 -2.07 -2.07
Na -2.14 -2.10 -2.07
Na -2.11 -2.06 2.07
Na 2.12 -2.10 2.07
Na 0.03 2.67 2.09
I -2.30 3.26 0.02
I 2.32 3.25 -0.02

Na -0.01 2.67 -2.09
Na 4.90 1.63 -0.01
Na -4.88 1.66 0.01

--
NaI7_2

--
I -0.74 0.00 2.45
I 1.38 3.51 0.00
I 1.38 -3.51 0.00
I -3.36 -3.16 0.00
I -3.35 3.17 0.00
I -0.74 0.00 -2.45
I 4.63 0.00 0.00
Na -1.07 3.12 2.10
Na -1.07 3.12 -2.10
Na -3.13 0.00 0.00
Na 1.36 0.00 0.00
Na 4.43 3.04 -0.01
Na 4.42 -3.05 0.00
Na -1.08 -3.12 -2.11
Na -1.08 -3.12 2.10

--
NaI7_3

--
I 1.23 -0.24 2.79
I 1.23 2.54 -1.18
I -2.80 0.23 -2.59
I -2.80 -2.35 1.10
I 1.23 -2.30 -1.60
I -2.80 2.13 1.49
I 5.01 0.00 0.00
Na -1.86 3.13 -1.46
Na 3.07 2.01 1.41
Na -4.60 0.00 0.00
Na -1.86 -0.30 3.44
Na -0.49 0.00 0.00
Na -1.86 -2.83 -1.98
Na 3.07 -2.22 1.04
Na 3.07 0.21 -2.44

--
NaI8

--
I 0.00 4.27 1.82
I 2.33 2.33 -1.74
I -2.33 -2.33 -1.74
I -4.28 0.00 1.81
I -2.33 2.33 -1.74
I 0.00 -4.27 1.82
I 4.28 0.00 1.81
I 2.33 -2.33 -1.74
Na 2.65 2.64 1.55
Na 4.44 0.00 -1.33
Na -2.65 2.64 1.55
Na 0.00 4.43 -1.33
Na 0.00 0.00 -2.22
Na -2.65 -2.64 1.55
Na 0.00 -4.43 -1.33
Na 2.65 -2.64 1.55
Na -4.44 0.00 -1.33

--
NaI8_2

--
I -3.17 -2.92 -1.79
I -3.24 0.10 1.84
I 0.18 3.31 1.66
I -0.03 -3.31 1.66
I -2.97 3.10 -1.79
Na -3.76 0.12 -1.43
Na -2.96 3.22 1.36
Na 0.05 -0.01 2.44
Na -3.16 -3.03 1.36
Na -0.15 -3.68 -1.57
I 2.86 -2.87 -2.00
Na 3.81 -0.11 -2.92
Na 0.08 3.69 -1.56
I 3.04 2.70 -1.99
I 3.27 -0.10 2.39
Na 3.27 2.73 1.18
Na 3.10 -2.93 1.18

--
NaI8_2_2

--
I -3.02 -2.75 -1.99
I -3.23 -0.01 2.59
I -0.01 3.25 1.54
I 0.01 -3.25 1.55
I -3.03 2.73 -1.99
Na -4.00 -0.01 -2.91
Na -3.12 2.75 1.21
Na 0.00 0.00 2.75
Na -3.11 -2.76 1.21
Na 0.01 -3.54 -1.62
I 3.03 -2.74 -1.99
Na 4.00 0.01 -2.92
Na -0.01 3.54 -1.63
I 3.02 2.75 -1.99
I 3.23 0.01 2.59
Na 3.11 2.76 1.21
Na 3.12 -2.75 1.21

--
NaI8_3

--
I 0.00 -0.13 -2.08
I -2.39 -3.27 0.52
I 2.29 1.15 2.24
I 0.00 4.34 -0.39
I -4.78 0.34 -1.61
I -2.29 1.15 2.24
I 4.78 0.34 -1.61
I 2.39 -3.27 0.52
Na -2.70 -1.77 -2.35
Na 0.00 -5.14 1.11
Na -2.34 2.31 -0.94
Na -4.52 -0.82 1.28
Na 0.00 -0.86 1.16
Na 0.00 3.33 2.56
Na 2.34 2.31 -0.94
Na 2.70 -1.77 -2.35
Na 4.52 -0.82 1.28

--
NaI9_1

--
I 4.69 2.39 -1.05
I 3.11 -0.01 2.73
I -0.35 -2.92 1.06
I -0.35 2.91 1.08
I 4.68 -2.38 -1.06
Na 5.71 0.00 0.68
Na 2.76 -2.90 1.29
Na -0.20 -0.01 2.65
Na 2.76 2.89 1.31
Na -1.19 2.48 -1.99
I 0.29 0.01 -3.16
I -4.30 2.60 -1.43
Na 3.43 0.01 -2.74
Na -5.66 0.01 -2.28
Na -1.19 -2.47 -2.00
I -4.30 -2.59 -1.44
I -3.33 -0.01 3.23
Na -3.52 -2.66 1.62
Na -3.52 2.65 1.64

--
NaI9_2

--
I -0.20 -1.58 3.00
I 3.48 1.30 -2.45
I -3.44 1.49 -2.83
I -3.44 1.70 2.71
I 3.47 1.48 2.35
I -0.20 3.39 -0.13
I -3.44 -3.20 0.12
I 3.48 -2.77 0.11
I -0.20 -1.81 -2.87
Na -3.46 -1.61 -2.56
Na -3.46 3.02 -0.12
Na -3.46 -1.41 2.67
Na -0.26 1.64 2.61
Na -0.26 -3.08 0.12
Na -0.27 1.44 -2.72
Na 2.87 -1.83 -2.91
Na 4.97 0.01 0.00
Na 2.86 3.44 -0.13
Na 2.86 -1.60 3.04

--
NaI9_3

--
I -0.03 -1.33 -2.76
I -3.19 1.26 2.63
I 3.31 1.42 2.96
I 3.31 1.86 -2.71
I -3.19 1.65 -2.40
I -0.03 3.07 0.23
I 3.31 -3.29 -0.25
I -3.20 -2.91 -0.22
I -0.03 -1.74 2.53
Na -3.27 -1.92 2.80
Na -3.27 3.38 0.26
Na -3.28 -1.46 -3.05
Na -1.55 0.00 0.00
Na 0.13 1.53 3.19
Na 0.13 2.00 -2.92
Na 0.13 -3.53 -0.27
Na 3.23 -1.64 2.40
Na 3.23 -1.26 -2.62
Na 3.23 2.92 0.22

--
NaI9_4

--
I -0.11 0.00 -1.52
I -2.05 2.41 2.14
I 2.67 -2.35 1.73
I 4.47 -0.01 -2.02
I 0.06 4.63 -1.53
I 2.68 2.34 1.73
I 0.05 -4.63 -1.53
I -4.72 0.01 -1.10
I -2.06 -2.41 2.14
Na -7.06 0.00 -2.96
Na -2.08 2.41 -1.09
Na -3.99 0.00 2.15
Na 2.30 2.29 -1.62
Na 0.39 4.47 1.57
Na 0.39 0.00 1.84
Na 4.72 -0.01 1.07
Na 2.29 -2.29 -1.62
Na -2.09 -2.40 -1.09
Na 0.38 -4.47 1.57

--
NaI9_5

--
I 0.36 -2.65 2.16
I 2.12 1.65 2.16
I -2.95 4.30 -1.05
I -5.16 -1.03 -1.01
I -2.49 1.02 2.17
I -2.27 -4.69 -1.06
I 5.25 0.39 -1.01
I 1.67 4.93 -1.06
Na 3.01 -1.22 0.76
Na 3.95 3.06 -0.06
Na -2.57 -1.99 0.76
Na 0.00 0.00 3.77
Na -0.44 3.21 0.75
Na -4.82 -3.71 -2.40
Na -0.83 5.98 -2.44
Na 5.66 -2.29 -2.37
Na -4.63 1.88 -0.04
Na 0.68 -4.93 -0.09
I 3.46 -3.92 -1.04

--
NaI10_1

--
I 0.09 0.00 -1.27
I -5.74 0.00 -1.61
I -1.90 0.00 3.04
I 4.51 0.00 0.88
I 3.25 3.21 -2.40
I -2.81 3.49 -0.17
I 1.39 3.33 2.00
I 3.26 -3.20 -2.40
I -2.81 -3.50 -0.17
I 1.40 -3.33 2.00
Na -5.45 -3.04 -1.67
Na -5.46 3.04 -1.67
Na -2.84 0.00 -0.09
Na -1.61 -3.13 2.78
Na 0.38 3.23 -1.13
Na -1.61 3.13 2.78
Na 1.37 0.00 1.87
Na 4.25 3.12 0.54
Na 3.28 0.00 -2.25
Na 0.38 -3.23 -1.14
Na 4.25 -3.12 0.55

--
NaI11_4

--
I 1.32 0.00 -1.46
I -5.03 0.01 -1.77
I -4.72 -3.02 1.78
I 4.86 -0.01 2.05
I 4.70 3.19 -1.43
I -1.67 3.36 -1.76
I -4.70 3.03 1.78
I 1.29 3.19 1.96
I 4.68 -3.20 -1.43
I -1.69 -3.36 -1.75
I 1.28 -3.19 1.96
Na 4.54 -3.15 1.67
Na 4.56 3.14 1.67
Na 4.75 -0.01 -1.34
Na 1.70 0.00 1.80
Na 1.56 -3.22 -1.42
Na -1.74 -3.89 1.45
Na -5.42 0.01 1.52
Na -4.82 -3.13 -1.37
Na -4.80 3.15 -1.37
Na -1.78 0.00 -2.23
Na -1.72 3.90 1.45
Na 1.57 3.21 -1.43

--
NaI11_1

--
I -0.06 0.00 -0.83
I -3.96 -2.39 0.73
I 0.00 2.41 3.24
I 4.21 2.94 -1.70
I -4.00 2.33 0.74
I -3.96 -0.03 -3.40
I -0.25 4.67 -1.06
I 4.27 -2.87 -1.69
I 0.04 -2.42 3.23
I -0.17 -4.67 -1.07
I 3.84 0.04 1.90
Na 2.46 -5.09 -2.64
Na 5.22 0.04 -0.98
Na 2.36 5.12 -2.66
Na 1.88 2.27 0.49
Na 1.92 -2.24 0.49
Na 1.80 0.01 4.26
Na -2.18 2.17 -1.98
Na -1.86 4.41 1.70
Na -1.93 -0.02 1.93
Na -2.14 -2.20 -1.99
Na -1.79 -4.44 1.68
Na -5.54 -0.05 -0.72

--
NaI11_5

--
I -1.20 0.23 -1.45
I 5.17 1.78 -1.28
I 2.07 0.72 2.16
I -4.55 -1.19 1.79
I -3.56 -3.76 -2.09
I 2.60 -2.18 -1.97
I 5.85 -2.19 1.36
I -0.38 -3.41 1.48
I -5.31 2.34 -1.37
I 1.08 4.22 -0.97
I -2.30 2.90 2.26
Na -2.30 3.20 -1.04
Na -5.30 1.87 1.70
Na -4.41 -0.73 -1.55
Na -1.41 -0.32 1.84
Na -3.49 -4.07 1.00
Na -0.55 -2.94 -1.82
Na 2.70 -2.72 1.29
Na 5.64 -1.49 -1.68
Na 5.22 0.76 1.81
Na 1.88 0.88 -1.16
Na 0.68 3.57 2.13
Na 3.91 4.48 -2.16

--
NaI12_3

--
I -1.54 2.80 -1.18
I 1.54 -2.80 1.18
I -4.93 -3.04 1.27
I -4.93 0.41 -3.27
I 1.54 0.38 -3.01
I -1.54 -2.42 -1.83
I -4.93 2.62 1.99
I 1.54 2.42 1.83
I -1.54 -0.38 3.01
I 4.93 -0.41 3.27
I 4.93 -2.62 -1.99
I 4.93 3.04 -1.28
Na 4.81 -2.68 1.12
Na 4.81 0.37 -2.89
Na 4.81 2.32 1.76
Na 1.77 -0.45 3.52
Na 1.77 -2.82 -2.14
Na -1.77 -3.27 1.37
Na 0.00 0.00 0.00
Na -1.77 2.83 2.14
Na -4.81 -0.37 2.88
Na -4.81 -2.32 -1.76
Na -4.81 2.68 -1.12
Na -1.77 0.45 -3.52
Na 1.77 3.27 -1.37

--
NaI12_1

--
I 0.00 0.00 -0.49
I 4.88 0.01 -0.17
I 0.00 -0.68 4.28
I -4.88 0.03 -0.17
I -2.58 -2.83 -3.21
I 2.36 -3.66 1.44
I 2.57 -2.84 -3.21
I -2.38 -3.64 1.44
I -2.37 3.51 -2.37
I 2.35 3.02 2.39
I 2.39 3.50 -2.37
I -2.33 3.03 2.39
Na 0.01 4.64 -3.97
Na -4.46 3.11 0.09
Na -4.50 -3.12 -0.81
Na -2.33 -0.39 1.92
Na -2.61 0.18 -2.48
Na 0.01 3.13 0.11
Na 0.01 2.46 4.44
Na -0.01 -3.31 -1.24
Na -0.01 -3.76 3.46
Na 2.32 -0.41 1.92
Na 2.62 0.16 -2.48
Na 4.47 3.09 0.10
Na 4.49 -3.14 -0.81

--
NaI12_2

--
I -1.29 4.34 0.06
I 1.59 2.91 -3.24
I -1.56 -2.92 -3.25
I -4.34 -1.29 0.04
I -2.90 1.57 -3.26
I 1.29 -4.33 0.08
I 4.34 1.29 0.08
I 2.93 -1.58 -3.24
I -1.94 -3.54 3.29
I 3.54 -1.92 3.31
I 1.91 3.55 3.30
I -3.58 1.93 3.27
Na -3.93 -1.15 3.27
Na 1.14 -3.89 3.31
Na 3.90 1.16 3.31
Na -1.17 3.90 3.28
Na -3.48 1.88 0.09
Na 1.89 3.48 0.11
Na 3.48 -1.88 0.13
Na -1.89 -3.47 0.11
Na 1.28 -4.25 -3.04
Na -4.24 -1.27 -3.07
Na 0.02 -0.01 -3.53
Na 4.27 1.26 -3.04
Na -1.25 4.24 -3.06

--
NaI13_1

--
I 0.00 0.00 0.00
I -3.30 1.35 3.13
I -3.41 -1.55 -2.92
I 3.30 -1.35 -3.13
I 3.41 1.55 2.92
I 3.49 -2.92 1.34
I -3.22 -3.12 1.55
I 0.19 -1.57 4.47
I 0.08 -4.47 -1.57
I 3.22 3.12 -1.55
I -3.49 2.92 -1.34
I -0.08 4.47 1.57
I -0.19 1.57 -4.47
Na -3.05 -4.27 -1.37
Na -3.30 1.37 -4.08
Na -3.30 -0.10 0.10
Na -0.05 -1.43 -2.97
Na -3.20 4.09 1.57
Na -0.13 2.97 -1.43
Na 2.95 1.56 -4.27
Na 3.20 -4.09 -1.57
Na 0.13 -2.97 1.43
Na -2.95 -1.56 4.27
Na 3.30 -1.37 4.08
Na 0.05 1.43 2.97
Na 3.30 0.10 -0.10
Na 3.05 4.27 1.37

--
NaI13_2

--
I -1.34 0.00 -1.18
I 5.82 3.21 0.85
I 5.82 -3.21 0.85
I -0.48 -3.34 2.28
I -0.48 3.33 2.29
I -3.88 0.00 2.89
I -7.12 0.01 -2.17
I -4.40 3.49 -0.36
I -4.40 -3.49 -0.37
I 2.57 0.00 1.53
I 5.14 0.00 -2.62
I 1.87 3.35 -1.85
I 1.87 -3.35 -1.85
Na 5.04 -3.11 -2.15
Na 5.78 0.00 0.72
Na 5.04 3.12 -2.15
Na 2.70 -3.22 1.37
Na 1.99 0.00 -1.76
Na -1.12 -3.23 -0.89
Na -1.12 3.23 -0.88
Na -3.55 3.13 2.72
Na -4.41 0.00 -0.32
Na -6.87 -3.04 -2.14
Na -6.84 3.05 -2.17
Na -3.55 -3.14 2.72
Na 2.70 3.22 1.37
Na -0.55 0.00 2.15

KI

KI1 -67.64
KI2 -107.30
KI2_1 -107.30
KI2_2 -107.29
KI3 -146.98
KI3_4 -146.96
KI3_3 -146.95
KI4_1 -186.65
KI4_2 -186.64
KI4_3 -186.63
KI4_5 -186.60
KI5 -226.31
KI5_3 -226.31
KI5_1 -226.30
KI6_2 -265.99
KI6_1 -265.98
KI6_3 -265.98
KI6_5 -265.97
KI7_1 -305.66
KI7 -305.66
KI7_4 -305.65
KI7_3 -305.65
KI8 -345.33
KI8_3 -345.33
KI9 -385.01
KI9_2 -385.00
KI10 -424.67
KI11 -464.34
KI11_2 -464.34
KI11_3 -464.34
KI12_2 -504.02
KI12_3 -504.02
KI12_4 -504.01
KI13 -543.72
KI13_2 -543.69

--
KI1

--
I 0.00 0.00 0.00
K 0.00 0.00 3.31
K 0.00 0.00 -3.31

--
KI2

--
I 2.18 0.00 0.00
I -2.18 0.00 0.00
K 0.00 -2.63 -0.93
K 0.00 2.12 -1.82
K 0.00 0.51 2.74

--
KI2_1

--
I 0.00 0.00 -3.37
I 0.00 0.00 3.37
K 0.00 0.00 6.65
K 0.00 0.00 0.00
K 0.00 0.00 -6.65

--
KI2_2

--
I 3.17 0.00 0.00
I -1.88 0.00 0.00
K -5.24 0.00 -0.01
K 0.82 2.38 0.00
K 0.82 -2.38 0.00

--
KI3

--
I -1.64 -2.37 0.09
I -1.23 2.61 0.09
I 2.87 -0.24 0.09
K 2.05 2.95 -0.98
K 0.00 0.00 2.17
K 1.53 -3.25 -0.98
K -3.58 0.30 -0.98

--
KI3_4

--
I -2.94 -0.02 0.00
I 1.83 -2.25 0.00
I 1.80 2.26 0.00
K 4.46 0.02 0.00
K -0.06 -0.01 -2.06
K -0.05 -0.01 2.06
K -6.27 0.01 0.00

--
KI3_3

--
I 6.72 0.00 0.00
I -6.72 0.00 0.00
I 0.00 0.01 0.00
K -9.99 -0.01 0.00
K -3.34 0.01 0.00
K 9.99 -0.01 0.00
K 3.34 0.01 0.00

--
KI4_1

--
I -0.22 -3.55 -0.05
I 0.22 3.57 -0.02
I -3.59 0.22 0.10
I 3.59 -0.23 0.10
K -3.19 3.60 -0.24
K 0.00 0.01 0.48
K 3.61 3.18 -0.22
K 3.19 -3.61 -0.21
K -3.62 -3.19 -0.18

--
KI4_2

--
I 2.49 2.37 -0.12
I -3.22 0.00 -2.00
I -1.58 0.00 2.12
I 2.49 -2.37 -0.12
K -0.93 -2.39 -0.69
K 4.37 0.00 -1.80
K 1.92 0.00 2.48
K -0.93 2.39 -0.69
K -4.92 0.00 1.04

--
KI4_3

--
I 1.42 -2.94 0.41
I 1.43 1.82 2.34
I -2.86 0.01 0.00
I 1.44 1.11 -2.75
K -6.23 0.01 0.00
K -0.42 -1.08 2.67
K -0.39 2.86 -0.40
K -0.41 -1.77 -2.28
K 3.43 -0.01 0.00

--
KI4_5

--
I -10.05 0.39 0.00
I 3.35 -0.14 0.00
I -3.35 0.13 0.00
I 10.05 -0.39 0.00
K 13.32 -0.51 0.00
K 6.68 -0.26 0.00
K 0.00 0.00 0.00
K -6.68 0.26 0.00
K -13.32 0.52 0.00

--
KI5

--
I 0.41 -2.64 -0.74
I -3.99 0.00 -1.63
I -2.06 0.00 3.03
I 4.49 0.00 0.45
I 0.41 2.64 -0.74
K -2.99 2.45 0.69
K -2.99 -2.45 0.69
K -0.79 0.00 -2.87
K 1.14 0.00 1.73
K 3.84 -3.21 -0.64
K 3.84 3.21 -0.64

--
KI5_3

--
I 0.44 2.95 0.00
I -2.87 0.00 2.51
I -2.87 0.00 -2.51
I 3.90 0.00 0.00
I 0.44 -2.95 0.00
K -3.11 2.46 0.00
K -3.11 -2.46 0.00
K 0.59 0.00 2.16
K 0.59 0.00 -2.17
K 3.84 3.47 0.00
K 3.84 -3.47 0.00

--
KI5_1

--
I -0.99 -2.95 -0.61
I 3.77 -2.34 0.88
I 3.77 2.34 -0.88
I -6.15 0.00 0.00
I -0.98 2.95 0.61
K 6.07 0.00 0.01
K 1.05 0.00 0.00

K 1.61 4.91 -0.43
K -4.36 2.62 1.08
K -4.37 -2.62 -1.09
K 1.61 -4.91 0.42

--
KI6_2

--
I 3.21 -0.20 -1.73
I -1.78 -2.68 -1.73
I -3.21 0.20 1.73
I 1.78 2.68 1.73
I 1.43 -2.88 1.73
I -1.43 2.88 -1.73
K 3.83 -0.24 1.85
K -2.13 -3.20 1.85
K -1.71 3.44 1.85
K 0.00 0.00 0.00
K 2.13 3.20 -1.85
K 1.71 -3.44 -1.85
K -3.83 0.24 -1.85

--
KI6_1

--
I -0.02 -2.37 2.50
I -4.15 -0.43 0.00
I 0.02 2.90 -2.81
I 4.14 -0.49 0.00
I 0.02 2.88 2.82
I -0.02 -2.35 -2.51
K 2.43 0.37 -2.91
K 2.33 -3.42 -0.01
K 2.42 0.36 2.91
K -2.37 -3.39 -0.01
K -2.42 0.40 2.91
K -2.42 0.41 -2.91
K 0.04 4.85 0.01

--
KI6_3

--
I 0.22 -2.98 1.88
I 2.47 1.68 1.88
I -0.26 3.57 -2.11
I -2.97 -2.01 -2.11
I 3.23 -1.56 -2.11
I -2.69 1.30 1.88
K -3.01 1.45 -1.90
K -0.29 3.96 1.30
K 2.76 1.88 -1.90
K -3.28 -2.23 1.31
K 0.00 0.00 3.75
K 3.57 -1.73 1.30
K 0.24 -3.33 -1.90

--
KI6_5

--
I -0.26 0.13 2.68
I 3.95 -1.47 0.00
I -3.08 -3.23 0.00
I -4.35 1.76 0.00
I 2.53 3.54 0.00
I -0.26 0.13 -2.68
K 6.28 -3.92 0.00
K 3.01 1.21 2.48
K 3.01 1.21 -2.49
K 0.24 -2.17 0.00
K -3.73 -0.71 -2.40
K -3.72 -0.71 2.40
K -0.97 2.68 0.00

--
KI7_1

--
I 1.40 -1.13 2.85
I 1.41 3.03 -0.45
I -3.05 1.02 -2.56
I -3.05 -2.73 0.40
I 1.40 -1.90 -2.40
I -3.05 1.71 2.16
I 5.47 0.00 0.00
K 3.43 1.76 2.23
K 3.44 1.05 -2.64
K -2.00 3.87 -0.57
K -0.52 0.00 0.00
K 3.43 -2.81 0.41
K -2.01 -2.43 -3.06
K -5.25 0.00 0.00
K -2.01 -1.44 3.63

--
KI7

--
I -0.97 0.00 2.65
I 1.51 3.75 0.00
I 1.51 -3.75 0.00
I -3.63 -3.54 0.00
I -3.63 3.55 0.00
I -0.96 0.00 -2.65
I 5.07 0.00 0.00
K -1.16 3.50 -2.43
K -1.16 3.50 2.43
K -3.63 0.00 0.00
K -1.16 -3.50 -2.43
K 1.46 0.00 0.00
K 4.95 3.40 0.00
K 4.94 -3.41 0.00
K -1.16 -3.50 2.43

--
KI7_4

--
I 4.55 -1.91 0.19
I -0.36 -3.12 1.31
I -5.09 -0.85 0.57
I 0.98 1.37 3.49
I -0.70 -1.81 -3.33
I -2.15 2.95 -0.31
I 2.78 3.07 -1.67
K 1.84 -3.34 -1.48
K -0.15 1.62 -2.97
K 5.53 1.13 -1.04
K 2.46 -1.75 3.03
K 0.92 3.95 1.17
K -3.06 -3.16 -1.05
K -2.00 0.03 2.13
K -5.57 2.36 -0.46

--
KI7_3

--
I -4.82 -1.43 0.01
I 0.00 -3.61 0.00
I 4.82 -1.44 -0.01
I -0.03 -0.27 -3.78
I 0.02 -0.27 3.78
I 2.55 3.45 -0.02
I -2.54 3.45 0.02
K 0.02 2.94 2.38
K -0.01 2.95 -2.38
K 5.57 1.90 -0.01
K 2.43 -2.37 2.36
K 2.41 -2.34 -2.37
K -2.41 -2.34 2.37
K -2.43 -2.36 -2.36
K -5.57 1.91 0.01

--
KI8

--
I -4.73 0.00 1.91
I -2.57 2.57 -1.79
I 2.57 -2.57 -1.79
I 0.00 -4.72 1.91
I -2.57 -2.57 -1.79
I 4.73 -0.01 1.91
I 0.00 4.72 1.91
I 2.57 2.57 -1.79
K 0.01 4.96 -1.60
K -4.97 0.01 -1.60
K 0.00 0.00 -2.17
K -3.04 3.04 1.82
K 3.05 3.04 1.83
K 4.97 0.00 -1.60
K 3.04 -3.04 1.82
K -3.05 -3.04 1.82
K 0.00 -4.96 -1.60

--
KI8_3

--
I 0.00 0.14 -2.32
I 2.57 3.48 0.68
I -2.53 -1.45 2.32
I 0.00 -4.83 -0.53
I 5.25 -0.27 -1.75
I 2.53 -1.45 2.32
I -5.25 -0.27 -1.75
I -2.57 3.48 0.68
K 0.00 -3.87 2.82
K 2.62 -2.62 -1.22
K 5.02 0.86 1.54
K 0.00 0.83 1.26
K 2.95 2.09 -2.64
K -2.63 -2.62 -1.22
K -5.02 0.86 1.54
K -2.95 2.09 -2.64
K 0.00 5.65 1.51

--
KI9

--
I -0.03 -0.11 3.37
I -3.42 0.10 -3.17
I 3.60 0.12 -3.58
I 3.60 -3.16 1.69
I -3.42 -2.79 1.49
I -0.03 -2.86 -1.78
I 3.60 3.05 1.89
I -3.42 2.69 1.67
I -0.03 2.97 -1.59
K -3.63 3.35 -1.79
K -3.62 -0.12 3.81
K -3.62 -3.24 -2.01
K -1.50 0.00 0.00
K 0.11 3.42 2.12
K 3.59 -0.11 3.36
K 3.58 2.97 -1.59
K 3.59 -2.85 -1.77
K 0.12 -3.55 1.90
K 0.12 0.13 -4.02

--
KI9_2

--
I -0.27 -2.95 -2.34
I 3.67 2.34 1.85
I -3.73 2.73 2.16
I -3.73 -3.24 1.28
I 3.67 -2.77 1.10
I -0.27 -0.55 3.72
I -3.73 0.51 -3.44
I 3.67 0.43 -2.95
I -0.27 3.50 -1.39
K -3.85 3.22 -1.28
K -3.85 -0.51 3.43
K -3.85 -2.72 -2.15
K -0.20 2.68 2.12
K -0.20 0.50 -3.38
K -0.20 -3.18 1.26
K 3.13 -0.58 3.91
K 3.13 3.68 -1.46
K 5.55 0.00 0.00
K 3.14 -3.10 -2.46

--
KI10

--
I -0.17 0.01 -1.43
I 6.29 0.04 -1.74
I 1.89 -0.01 3.36
I -5.01 -0.03 0.82
I -3.58 -3.56 -2.65
I 3.15 -3.73 -0.08
I -1.56 -3.67 2.06
I -3.62 3.56 -2.62
I 3.10 3.76 -0.08
I -1.60 3.64 2.10
K 6.17 -3.37 -1.72
K 6.07 3.44 -1.81
K 1.68 3.50 3.19
K 3.08 0.01 -0.06
K 1.71 -3.51 3.18
K -0.31 -3.58 -1.37
K -1.60 -0.02 2.02
K -0.36 3.59 -1.33
K -4.85 3.48 0.64
K -3.66 -0.01 -2.64
K -4.81 -3.53 0.61

--
KI11

--
I -0.11 0.00 -0.90
I -4.38 -2.58 0.65
I -0.08 2.63 3.55
I 4.70 3.15 -1.79
I -4.34 2.63 0.65
I -4.29 0.02 -3.81
I -0.08 5.15 -1.09
I 4.66 -3.21 -1.79
I -0.12 -2.62 3.56
I -0.15 -5.14 -1.08
I 4.10 -0.02 2.16
K 2.77 -5.81 -2.86
K 5.87 -0.04 -0.92
K 2.85 5.78 -2.85
K 2.05 2.49 0.56
K 1.87 -0.01 4.84
K 2.02 -2.52 0.56
K -2.13 -4.95 1.89
K -2.28 -2.47 -2.32
K -2.22 0.01 2.10
K -2.25 2.49 -2.32
K -2.06 4.98 1.88
K -6.21 0.04 -0.87

--
KI11_2

--
I -1.37 0.22 -1.65
I 5.67 1.77 -1.35
I 2.21 0.68 2.38
I -5.08 -1.16 1.83
I -4.07 -4.09 -2.29
I 2.83 -2.54 -2.03
I 6.34 -2.53 1.55
I -0.63 -3.77 1.56
I -5.73 2.78 -1.53
I 1.35 4.51 -1.01
I -2.49 3.22 2.39
K 4.47 4.84 -2.47
K -2.33 3.63 -1.26
K 0.84 3.95 2.48
K -5.88 2.25 1.92
K -4.94 -0.68 -1.86
K -1.57 -0.32 1.98
K 2.06 0.86 -1.28
K 5.76 0.80 2.12
K 6.24 -1.85 -1.88
K 2.83 -3.15 1.59
K -0.66 -3.32 -2.10
K -4.10 -4.48 1.18

--
KI11_3

--
I -1.53 0.00 -1.69
I 5.57 -0.02 -1.80
I 5.17 3.34 1.92
I -5.36 0.02 2.13
I -5.21 -3.53 -1.57
I 1.86 -3.65 -1.80
I 5.13 -3.35 1.93
I -1.51 -3.55 2.04
I -5.18 3.56 -1.58
I 1.89 3.63 -1.80
I -1.48 3.55 2.04
K -5.10 3.54 1.90
K -5.33 0.02 -1.61
K -5.14 -3.50 1.91
K -1.69 3.58 -1.70
K -1.84 0.00 1.91
K -1.72 -3.58 -1.69
K 1.89 4.46 1.73
K 1.96 -0.01 -2.33
K 5.41 3.49 -1.59
K 1.85 -4.48 1.73
K 5.38 -3.53 -1.58
K 6.12 -0.01 1.84

--
KI12_2

--
I 0.00 0.02 -0.60
I 5.33 0.14 -0.24

I 0.02 -1.18 4.59
I -5.33 -0.08 -0.25
I -2.82 -2.95 -3.71
I 2.66 -4.09 1.22
I 2.96 -2.84 -3.70
I -2.49 -4.19 1.21
I -2.66 4.03 -2.23
I 2.49 3.07 2.88
I 2.49 4.13 -2.23
I -2.62 2.96 2.88
K 2.84 0.50 -2.81
K 5.18 -3.35 -1.09
K 4.91 3.54 0.39
K -0.11 5.59 -3.99
K -0.08 3.43 0.38
K 2.56 -0.57 2.04
K 0.08 -3.61 -1.63
K -2.86 0.40 -2.81
K -0.05 2.27 5.19
K -2.54 -0.68 2.04
K -5.03 -3.55 -1.11
K 0.09 -4.57 3.52
K -5.06 3.34 0.39

--
KI12_3

--
I -1.68 -2.02 -2.61
I 1.68 2.02 2.61
I -5.36 2.21 2.84
I -5.36 -3.57 0.49
I 1.68 -3.27 0.45
I -1.68 -1.25 3.06
I -5.36 1.36 -3.33
I 1.68 1.25 -3.05
I -1.68 3.27 -0.45
I 5.36 3.57 -0.49
I 5.36 -1.36 3.33
I 5.36 -2.21 -2.84
K 5.31 -3.32 0.45
K 5.31 2.05 2.65
K 5.31 1.26 -3.10
K 1.87 -1.51 3.70
K 1.87 -2.45 -3.16
K 1.88 3.96 -0.54
K 0.00 0.00 0.00
K -1.87 -3.96 0.54
K -1.87 2.45 3.16
K -1.87 1.51 -3.70
K -5.31 -1.26 3.10
K -5.31 -2.05 -2.65
K -5.31 3.32 -0.45

--
KI12_4

--
I 4.92 -0.44 0.08
I 2.35 -2.78 -3.51
I -2.33 2.80 -3.50
I 0.43 4.91 0.09
I 2.80 2.35 -3.49
I -4.91 0.43 0.07
I -0.43 -4.91 0.06
I -2.78 -2.33 -3.52
I -2.85 3.37 3.64
I -3.40 -2.86 3.62
I 2.84 -3.40 3.63
I 3.38 2.83 3.64
K -0.41 -4.60 3.66
K 4.59 -0.41 3.68
K 0.39 4.58 3.69
K 2.85 -3.40 0.10
K -4.60 0.39 3.67
K -3.39 -2.85 0.09
K -0.43 -4.93 -3.43
K 3.39 2.84 0.12
K 4.95 -0.42 -3.41
K 0.01 0.01 -3.76
K -2.85 3.39 0.11
K -4.94 0.45 -3.42
K 0.44 4.96 -3.40

--
KI13

--
I 0.00 0.00 0.00
I -3.59 -1.16 -3.56
I -3.75 1.15 3.39
I 3.59 1.16 3.56
I 3.75 -1.15 -3.39
I 3.69 3.49 -1.07
I -3.65 3.47 -1.24
I 0.10 2.33 -4.63
I -0.06 4.63 2.32
I 3.65 -3.47 1.24
I -3.69 -3.49 1.07
I 0.06 -4.63 -2.32
I -0.10 -2.32 4.63
K -3.61 -2.23 4.35
K 3.41 -2.21 4.51
K -0.02 -3.47 1.15
K 3.57 -4.42 -2.14
K -3.45 -4.44 -2.30
K -0.08 1.15 3.47
K 3.66 0.01 0.08
K 3.45 4.44 2.30
K -3.66 -0.01 -0.08
K -3.57 4.42 2.14
K 0.02 3.47 -1.15
K -3.41 2.21 -4.51
K 0.08 -1.15 -3.47
K 3.61 2.23 -4.35

--
KI13_2

--
I 1.40 0.00 -1.25
I -6.45 -3.56 0.91
I -6.45 3.56 0.92
I 0.52 3.65 2.46
I 0.52 -3.66 2.45
I 4.17 0.00 3.22
I 7.78 0.01 -2.42
I 4.85 -3.75 -0.37
I 4.85 3.75 -0.36
I -2.93 0.00 1.69
I -5.74 0.00 -2.78
I -2.14 -3.67 -1.98
I -2.14 3.67 -1.98
K 7.62 -3.40 -2.40
K 7.60 3.41 -2.41
K 4.83 0.00 -0.33
K 3.93 -3.51 3.09
K 3.93 3.51 3.09
K 1.24 -3.60 -1.07
K 0.53 0.00 2.41
K 1.24 3.59 -1.06
K -2.22 0.00 -1.91
K -3.00 -3.60 1.62
K -2.99 3.60 1.62
K -5.66 -3.49 -2.47
K -6.49 0.00 0.88
K -5.65 3.50 -2.47

RbI
RbI1 -59.10
RbI2 -94.48
RbI2_1 -94.48
RbI2_2 -94.48
RbI3 -129.88
RbI3_3 -129.86
RbI3_4 -129.87
RbI4_1 -165.28
RbI4_2 -165.27
RbI4_3 -165.26
RbI4_4 -165.27
RbI4_5 -165.23
RbI5 -200.67
RbI5_1 -200.65
RbI5_3 -200.67
RbI6_1 -236.06
RbI6_2 -236.06
RbI6_3 -236.06
RbI6_5 -236.05
RbI7 -271.46
RbI7_1 -271.46
RbI7_3 -271.45
RbI7_4 -271.45
RbI8 -306.86
RbI8_3 -306.85
RbI9 -342.26
RbI9_2 -342.25
RbI10 -377.65
RbI11 -413.05
RbI11_2 -413.04
RbI11_3 -413.04
RbI12_2 -448.45
RbI12_3 -448.44
RbI12_4 -448.44
RbI13 -483.87
RbI13_2 -483.84

--
RbI1

--
I 0.00 0.00 0.00
Rb 0.00 0.00 3.49
Rb 0.00 0.00 -3.49

--
RbI2

--
I 2.22 0.00 0.00
I -2.22 0.00 0.00
Rb 0.00 -2.03 2.17
Rb 0.00 2.89 0.68
Rb 0.00 -0.86 -2.84

--
RbI2_1

--
I -3.11 -0.65 -1.60
I 3.11 0.65 1.60
Rb 6.14 1.29 3.15
Rb 0.00 0.00 0.00
Rb -6.14 -1.29 -3.15

--
RbI2_2

--
I 3.60 0.00 0.00
I -1.63 0.00 0.00
Rb -5.16 0.00 0.00
Rb 1.17 -2.55 0.00
Rb 1.17 2.55 0.00

--
RbI3

--
I -2.34 1.83 0.15
I 2.76 1.11 0.15
I -0.42 -2.94 0.15
Rb 2.99 -2.34 -1.01
Rb 0.00 0.00 2.39
Rb -3.52 -1.42 -1.01
Rb 0.53 3.75 -1.01

--
RbI3_4

--
I -2.97 0.00 0.00
I 2.03 -2.30 0.00
I 2.02 2.30 0.00
Rb 4.85 0.01 0.00
Rb 0.04 0.00 2.20
Rb 0.04 0.00 -2.20
Rb -6.48 0.00 0.00

--
RbI3_3

--
I 7.10 0.00
I -7.10 0.00
I 0.00 0.01
Rb -10.55 -0.01
Rb -3.53 0.01
Rb 3.53 0.01
Rb 10.55 -0.01

--
RbI4_1

--
I 0.32 -3.72 -0.02
I -0.32 3.73 0.00
I -3.74 -0.33 0.12
I 3.74 0.32 0.12
Rb 0.00 0.00 0.53
Rb -3.89 3.26 -0.20
Rb -3.27 -3.88 -0.22
Rb 3.89 -3.26 -0.19
Rb 3.27 3.88 -0.24

--
RbI4_2

--
I -2.64 -2.44 0.00
I 3.24 0.00 -2.25
I 1.76 0.00 2.04
I -2.64 2.44 0.01
Rb 5.23 0.00 0.81
Rb 0.91 -2.54 -0.82
Rb 0.91 2.54 -0.82
Rb -4.78 0.00 -1.62
Rb -1.88 0.00 2.74

--
RbI4_3

--
I -1.70 0.06 3.07
I -1.68 -2.69 -1.48
I 2.79 0.00 0.01
I -1.69 2.63 -1.59
Rb 6.35 0.00 0.00
Rb 0.25 -2.62 1.59
Rb 0.25 2.69 1.48
Rb -3.85 -0.01 -0.01
Rb 0.26 -0.06 -3.06

--
RbI4_5

--
I -10.63 -0.08 0.00
I 3.54 0.03 0.00
I -3.54 -0.03 0.00
I 10.63 0.08 0.00
Rb -14.08 -0.10 0.00
Rb -7.06 -0.05 0.00
Rb 0.00 0.00 0.00
Rb 7.06 0.06 0.00
Rb 14.08 0.09 0.00

--
RbI5

--
I 0.38 -2.76 -0.66
I -4.13 0.00 -1.85
I -2.42 0.00 3.07
I 4.57 0.00 0.62
I 0.38 2.75 -0.66
Rb 3.98 -3.40 -0.47
Rb 3.98 3.40 -0.47
Rb 1.04 0.00 1.97
Rb -0.71 0.00 -3.00
Rb -3.28 -2.61 0.61
Rb -3.28 2.61 0.61

--
RbI5_3

--
I 0.37 3.07 0.00
I -3.10 0.00 2.59
I -3.11 0.00 -2.59
I 3.93 0.00 0.00
I 0.37 -3.07 0.00
Rb 3.94 3.65 0.00
Rb 0.54 0.00 -2.31
Rb 3.94 -3.65 0.00
Rb 0.54 0.00 2.30
Rb -3.38 -2.62 0.00
Rb -3.38 2.62 0.00

--
RbI5_1

--
I 1.11 3.14 -0.56
I -3.87 2.45 0.88
I -3.87 -2.44 -0.88
I 6.44 0.00 0.00
I 1.10 -3.14 0.56
Rb 4.66 -2.84 1.10
Rb -1.64 -5.20 -0.50
Rb -6.33 0.00 0.00
Rb -1.01 0.00 0.00
Rb -1.64 5.20 0.50

Rb 4.67 2.84 -1.10

--
RbI6_2

--
I 3.77 0.85 -0.15
I -0.69 3.05 -2.52
I -3.77 -0.85 -0.17
I 1.16 -2.18 2.69
I 0.68 -2.96 -2.63
I -1.15 2.08 2.77
Rb 3.41 -2.97 -0.18
Rb -2.90 -2.99 -3.04
Rb -2.42 -1.40 3.30
Rb 0.00 0.01 -0.43
Rb 2.42 1.28 3.34
Rb 2.89 3.10 -2.93
Rb -3.41 2.98 -0.06

--
RbI6_1

--
I 2.44 0.01 2.60
I 0.50 -4.32 -0.01
I -3.05 -0.01 -2.92
I 0.46 4.32 0.00
I -3.04 -0.02 2.93
I 2.43 0.02 -2.60
Rb -0.44 2.56 -3.08
Rb 3.59 2.49 0.00
Rb -0.43 2.55 3.09
Rb 3.61 -2.46 -0.01
Rb -0.40 -2.56 3.08
Rb -5.16 -0.02 0.01
Rb -0.41 -2.56 -3.08

--
RbI6_3

--
I -0.04 -3.10 1.88
I 2.71 1.52 1.88
I 0.05 3.74 -2.26
I -3.27 -1.83 -2.26
I 3.22 -1.92 -2.26
I -2.67 1.59 1.88
Rb -3.04 1.81 -2.08
Rb -3.66 -2.05 1.32
Rb -0.04 -3.54 -2.07
Rb 0.00 0.00 3.90
Rb 3.60 -2.14 1.33
Rb 3.09 1.73 -2.07
Rb 0.05 4.19 1.32

--
RbI6_5

--
I 0.44 0.19 -2.78
I -4.12 -1.12 0.00
I 3.11 -3.53 0.00
I 4.84 1.51 0.00
I -2.22 3.94 0.00
I 0.44 0.19 2.78
Rb -6.82 -3.43 0.00
Rb -2.92 1.57 -2.65
Rb -2.92 1.57 2.65
Rb 1.39 2.81 0.00
Rb -0.31 -2.22 0.00
Rb 4.01 -0.99 -2.56
Rb 4.01 -0.99 2.56

--
RbI7_1

--
I 1.53 -0.58 3.15
I 1.53 3.02 -1.07
I -3.16 0.51 -2.78
I -3.16 -2.67 0.94
I 1.53 -2.43 -2.08
I -3.16 2.15 1.84
I 5.72 0.00 0.00
Rb -2.06 -3.14 -2.68
Rb 3.66 0.55 -2.98
Rb 3.66 -2.86 1.01
Rb -0.47 0.00 0.00
Rb -2.05 3.89 -1.38
Rb 3.66 2.31 1.97
Rb -2.06 -0.75 4.06
Rb -5.56 0.00 0.00

--
RbI7

--
I -1.14 0.00 2.76
I 1.49 3.91 0.00
I 1.50 -3.90 0.00
I -3.85 -3.73 0.00
I -3.86 3.72 0.00
I -1.14 0.00 -2.76
I 5.22 0.01 0.00
Rb -1.29 3.69 2.59
Rb -1.29 3.69 -2.59
Rb -3.95 0.00 0.00
Rb 1.42 0.00 0.00
Rb -1.28 -3.70 -2.59
Rb -1.28 -3.69 2.59
Rb 5.13 -3.58 -0.01
Rb 5.12 3.60 0.00

--
RbI7_3

--
I 5.05 -1.48 -0.01
I 0.00 -3.75 0.00
I -5.05 -1.48 0.01
I 0.02 -0.31 3.96
I -0.02 -0.31 -3.96
I -2.66 3.58 0.01
I 2.66 3.58 -0.02
Rb 0.01 3.09 2.53
Rb -0.01 3.09 -2.53
Rb 5.88 2.03 -0.01
Rb 2.57 -2.51 2.50
Rb 2.55 -2.49 -2.51
Rb -2.55 -2.49 2.51
Rb -2.57 -2.51 -2.50
Rb -5.88 2.03 0.01

--
RbI7_4

--
I 4.83 -1.83 0.18
I -0.22 -3.25 1.47
I -5.27 -1.06 0.67
I 1.05 1.55 3.60
I -0.73 -2.06 -3.36
I -2.38 2.97 -0.34
I 2.76 3.22 -1.84
Rb 0.83 4.23 1.14
Rb -2.06 0.00 2.29
Rb -5.96 2.27 -0.45
Rb -3.12 -3.54 -0.93
Rb -0.28 1.58 -3.14
Rb 2.72 -1.69 3.23
Rb 2.06 -3.55 -1.48
Rb 5.78 1.36 -1.20

--
RbI8

--
I -4.94 0.17 1.99
I -2.60 2.79 -1.81
I 2.60 -2.79 -1.81
I -0.17 -4.94 1.99
I -2.79 -2.60 -1.81
I 4.94 -0.17 1.99
I 0.17 4.94 1.99
I 2.79 2.60 -1.81
Rb 3.35 3.12 1.97
Rb 0.18 5.23 -1.69
Rb -3.12 3.34 1.97
Rb -5.23 0.18 -1.69
Rb -3.35 -3.12 1.97
Rb 0.00 0.00 -2.16
Rb 3.12 -3.35 1.97
Rb 5.23 -0.18 -1.69
Rb -0.18 -5.23 -1.69

--
RbI8_3

--
I 0.00 0.13 2.46
I -2.67 3.53 -0.79
I 2.65 -1.70 -2.33
I 0.00 -5.13 0.70
I -5.48 -0.28 1.83
I -2.65 -1.70 -2.33
I 5.48 -0.28 1.83
I 2.67 3.53 -0.79
Rb 0.00 5.82 -1.75
Rb -5.27 0.78 -1.66
Rb -2.76 -2.81 1.42
Rb 2.76 -2.81 1.42
Rb -3.09 2.23 2.77
Rb 0.00 0.74 -1.31
Rb 5.27 0.78 -1.66
Rb 3.09 2.23 2.77
Rb 0.00 -4.26 -2.86

--
RbI9

--
I 0.00 2.38 2.61
I -3.54 -2.22 -2.43
I 3.77 -2.51 -2.76
I 3.79 -1.13 3.54
I -3.52 -0.99 3.15
I -0.01 -3.45 0.76
I 3.78 3.64 -0.81
I -3.53 3.22 -0.70
I -0.02 1.07 -3.37
Rb 3.78 1.08 -3.42
Rb 3.79 -3.51 0.76
Rb 3.80 2.41 2.64
Rb 0.13 -2.88 -3.16
Rb 0.14 4.18 -0.92
Rb -3.79 1.22 -3.82
Rb -3.77 2.71 2.98
Rb -3.78 -3.92 0.87
Rb -1.50 0.00 0.00
Rb 0.15 -1.29 4.07

--
RbI9_2

--
I -0.36 -2.02 -3.38
I 3.77 1.58 2.65
I -3.96 1.86 3.11
I -3.97 -3.63 0.05
I 3.77 -3.09 0.04
I -0.36 -1.92 3.44
I -3.96 1.77 -3.16
I 3.77 1.50 -2.70
I -0.35 3.94 -0.06
Rb 5.81 0.00 0.00
Rb 3.24 4.18 -0.06
Rb -0.26 1.75 -3.14
Rb 3.23 -2.14 -3.59
Rb 3.23 -2.04 3.65
Rb -0.26 1.84 3.09
Rb -4.11 3.69 -0.05
Rb -4.13 -1.79 3.21
Rb -0.27 -3.60 0.05
Rb -4.13 -1.88 -3.16

--
RbI10

--
I 0.26 0.00 -1.54
I -6.55 0.01 -1.61
I -1.73 0.00 3.55
I 5.38 -0.01 0.62
I 3.80 3.74 -2.88
I -3.17 3.90 0.00
I 1.83 3.83 2.08
I 3.77 -3.73 -2.92
I -3.19 -3.90 0.01
I 1.83 -3.85 2.06
Rb -6.39 3.59 -1.68
Rb -6.44 -3.59 -1.60
Rb -3.12 0.00 0.02
Rb -1.57 3.69 3.39
Rb -1.57 -3.70 3.40
Rb 0.38 -3.79 -1.48
Rb 0.40 3.80 -1.47
Rb 3.86 0.01 -2.97
Rb 5.21 -3.70 0.46
Rb 1.86 -0.01 2.01
Rb 5.22 3.69 0.50

--
RbI11

--
I 0.11 0.00 -0.94
I 4.58 2.73 0.56
I 0.21 -2.75 3.73
I -4.93 -3.33 -1.77
I 4.57 -2.75 0.55
I 4.41 0.00 -4.06
I 0.07 -5.41 -1.11
I -4.92 3.35 -1.77
I 0.21 2.74 3.73
I 0.09 5.41 -1.11
I -4.22 0.01 2.36
Rb -6.19 0.01 -0.82
Rb -3.02 6.14 -2.91
Rb -2.10 2.64 0.65
Rb -2.11 -2.63 0.65
Rb -3.04 -6.13 -2.91
Rb 2.30 -2.63 -2.52
Rb 2.31 2.62 -2.52
Rb -1.84 0.00 5.17
Rb 2.40 -0.01 2.15
Rb 6.53 -0.01 -1.05
Rb 2.25 -5.24 1.95
Rb 2.27 5.24 1.95

--
RbI11_2

--
I -1.47 0.22 -1.75
I 5.97 1.58 -1.31
I 2.24 0.57 2.52
I -5.46 -1.04 1.78
I -4.45 -4.18 -2.45
I 2.85 -2.83 -2.05
I 6.44 -2.92 1.69
I -0.91 -3.98 1.59
I -5.88 3.10 -1.71
I 1.59 4.62 -1.01
I -2.57 3.43 2.41
Rb -6.17 2.58 1.91
Rb -5.25 -0.57 -2.09
Rb -4.59 -4.60 1.19
Rb -2.30 3.87 -1.41
Rb -1.75 -0.32 2.05
Rb -0.83 -3.53 -2.25
Rb 0.96 4.09 2.65
Rb 2.16 0.77 -1.33
Rb 2.75 -3.49 1.73
Rb 4.91 4.88 -2.50
Rb 5.99 0.58 2.36
Rb 6.47 -2.23 -1.91

--
RbI11_3

--
I -1.63 0.00 -1.84
I 5.84 -0.01 -1.75
I 5.32 3.50 2.08
I -5.66 0.01 2.10
I -5.46 -3.71 -1.72
I 1.98 -3.81 -1.82
I 5.30 -3.50 2.09
I -1.66 -3.74 2.05
I -5.45 3.73 -1.71
I 1.99 3.79 -1.83
I -1.64 3.74 2.06
Rb -5.45 3.72 1.94
Rb -5.62 0.01 -1.82
Rb -5.46 -3.71 1.93
Rb -1.78 3.78 -1.86
Rb -1.96 0.00 1.94
Rb -1.79 -3.77 -1.86
Rb 1.89 4.75 1.85
Rb 2.07 -0.01 -2.41
Rb 1.87 -4.76 1.86
Rb 5.69 3.69 -1.60
Rb 6.39 0.00 2.07
Rb 5.67 -3.70 -1.59

--
RbI12_2

--
I 0.00 0.05 -0.66
I 5.57 0.12 -0.28
I 0.03 -1.72 4.64
I -5.57 -0.09 -0.30
I -2.99 -2.79 -4.11

I 2.78 -4.43 0.85
I 3.11 -2.67 -4.12
I -2.59 -4.54 0.85
I -2.77 4.40 -1.94
I 2.61 2.85 3.28
I 2.60 4.51 -1.93
I -2.74 2.75 3.27
Rb -0.12 6.25 -3.63
Rb 5.18 3.63 0.74
Rb 2.98 0.77 -2.95
Rb 5.48 -3.47 -1.47
Rb 2.69 -0.84 2.04
Rb -0.07 3.53 0.72
Rb -3.00 0.66 -2.96
Rb 0.08 -3.69 -2.05
Rb 0.10 -5.20 3.24
Rb -5.33 -3.68 -1.47
Rb -2.66 -0.95 2.04
Rb -5.32 3.42 0.72
Rb -0.05 1.82 5.66

--
RbI12_3

--
I -1.77 -2.43 2.44
I 1.77 2.43 -2.44
I -5.61 2.65 -2.66
I -5.61 0.98 3.62
I 1.77 0.90 3.32
I -1.77 3.33 0.88
I -5.61 -3.63 -0.96
I 1.77 -3.33 -0.88
I -1.77 -0.90 -3.33
I 5.61 -0.98 -3.62
I 5.61 3.63 0.96
I 5.61 -2.65 2.66
Rb 5.59 0.93 3.42
Rb 5.59 2.51 -2.52
Rb 5.59 -3.44 -0.91
Rb 1.96 4.08 1.09
Rb 1.96 -1.10 -4.07
Rb 1.96 -2.98 2.99
Rb -0.01 0.00 0.00
Rb -1.96 1.10 4.08
Rb -1.95 2.98 -2.99
Rb -1.96 -4.08 -1.09
Rb -5.59 -2.51 2.52
Rb -5.59 -0.93 -3.44
Rb -5.59 3.44 0.91

--
RbI12_4

--
I 2.36 4.60 0.11
I 3.63 1.15 -3.64
I -3.61 -1.18 -3.64
I -4.61 2.36 0.10
I -1.16 3.60 -3.66
I -2.36 -4.60 0.14
I 4.61 -2.36 0.14
I 1.18 -3.63 -3.62
I -4.42 -1.40 3.83
I 1.41 -4.38 3.86
I 4.40 1.44 3.84
I -1.43 4.42 3.82
Rb 4.33 -2.21 3.94
Rb 4.67 -2.40 -3.53
Rb 4.42 1.43 0.15
Rb 2.21 4.36 3.91
Rb 2.40 4.64 -3.56
Rb -1.43 4.42 0.12
Rb 0.01 -0.02 -3.93
Rb 1.43 -4.42 0.17
Rb -2.23 -4.32 3.94
Rb -2.38 -4.68 -3.54
Rb -4.42 -1.42 0.14
Rb -4.36 2.24 3.90
Rb -4.65 2.37 -3.57

--
RbI13

--
I 0.00 0.00 0.00
I 3.42 -4.20 0.35
I -4.05 -3.14 1.80
I -3.42 4.20 -0.35
I 4.05 3.14 -1.80
I -0.53 2.68 -4.69
I -1.16 -4.66 -2.53
I 2.89 -1.52 -4.34
I -4.58 -0.46 -2.89
I 1.16 4.66 2.53
I 0.53 -2.68 4.69
I 4.58 0.46 2.88
I -2.89 1.52 4.33
Rb -4.71 -3.98 -1.74
Rb -3.09 -2.07 5.21
Rb -0.31 -3.68 1.08
Rb -3.75 0.53 0.73
Rb -4.11 3.09 -3.82
Rb -0.84 -0.99 -3.61
Rb 2.48 -5.00 -3.13
Rb 3.09 2.07 -5.21
Rb 3.75 -0.53 -0.73
Rb 4.11 -3.10 3.82
Rb 0.32 3.68 -1.08
Rb 0.84 0.99 3.62
Rb -2.48 5.00 3.13
Rb 4.72 3.98 1.74

--
RbI13_2

--
I 1.38 0.00 -1.26
I -6.81 -3.75 0.94
I -6.83 3.73 0.97
I 0.50 3.84 2.57
I 0.50 -3.83 2.58
I 4.29 0.01 3.40
I 8.02 -0.01 -2.60
I 5.04 -3.91 -0.33
I 5.03 3.91 -0.36
I -3.18 0.00 1.84
I -6.10 0.00 -2.86
I -2.33 -3.84 -2.02
I -2.35 3.85 -2.01
Rb -6.92 -0.01 0.97
Rb -6.01 -3.69 -2.63
Rb -6.03 3.69 -2.60
Rb -3.22 3.79 1.77
Rb -2.42 0.00 -1.94
Rb -3.21 -3.80 1.76
Rb 0.47 0.01 2.58
Rb 1.25 -3.78 -1.12
Rb 1.24 3.79 -1.13
Rb 4.07 3.71 3.28
Rb 4.99 0.00 -0.32
Rb 4.07 -3.69 3.31
Rb 7.90 -3.60 -2.55
Rb 7.88 3.58 -2.59

CsI

CsI1 -51.14
CsI2 -82.53
CsI2_1 -82.53
CsI2_2 -82.53
CsI3 -113.95
CsI3_3 -113.92
CsI4_1 -145.36
CsI4_4 -145.35
CsI4_3 -145.34
CsI4_2 -145.34
CsI5 -176.76
CsI5_2 -176.76
CsI6 -208.17
CsI6_1 -208.17
CsI6_3 -208.17
CsI7_1 -239.58
CsI7 -239.58
CsI8_2 -270.99
CsI9 -302.41
CsI9_2 -302.39
CsI10_1 -333.81
CsI10_3 -333.80
CsI11 -365.22
CsI11_2 -365.22
CsI11_3 -365.21
CsI12_2 -396.63
CsI12_3 -396.63
CsI12_4 -396.63
CsI13 -428.07
CsI13_2 -428.04

--
CsI1

--
Cs 0.00 0.00 3.70
I 0.00 0.00 0.00
Cs 0.00 0.00 -3.70

--
CsI2

--
Cs -3.05 -0.96 0.00
Cs 0.69 3.12 0.00
Cs 2.36 -2.16 0.00
I 0.00 0.00 -2.28
I 0.00 0.00 2.28

--
CsI2_1

--
Cs 8.15 -5.79 -0.75
I 5.69 -3.07 -0.54
Cs 3.16 -0.27 -0.31
Cs -1.84 5.25 0.12
I 0.62 2.53 -0.09

--
CsI2_2

--
Cs 0.49 -1.41 -0.55
I 4.22 -1.46 -0.39
Cs 4.55 2.23 0.07
Cs -1.96 5.35 0.13
I 0.57 2.56 -0.08

--
CsI3

--
Cs 0.00 0.00 2.62
I 2.56 -1.75 0.18
I -2.80 -1.34 0.18
Cs 3.65 1.74 -1.05
Cs -0.31 -4.02 -1.05
Cs -3.33 2.28 -1.05
I 0.24 3.09 0.18

--
CsI3_3

--
Cs 11.22 -0.02 0.00
I 7.55 -0.01 0.00
I -7.55 0.02 0.00
Cs 3.75 -0.02 0.00
Cs -11.22 0.03 0.00
Cs -3.75 0.00 0.00
I 0.00 -0.01 0.00

--
CsI4_1

--
Cs -4.11 -3.52 -0.20
I -0.30 -3.91 -0.06
Cs 0.00 0.01 0.61
Cs -3.52 4.08 -0.23
I 0.30 3.94 0.02
I -3.94 0.29 0.15
I 3.95 -0.30 0.17
Cs 3.53 -4.09 -0.20
Cs 4.10 3.51 -0.25

--
CsI4_4

--
Cs 5.20 -0.01 -1.56
I 2.80 2.53 0.08
I -3.36 -0.01 -2.45
Cs -5.58 0.01 0.71
Cs 1.89 0.01 2.99
Cs -0.92 2.71 -0.96
I -1.91 0.01 2.01
Cs -0.92 -2.72 -0.94
I 2.80 -2.52 0.09

--
CsI4_3

--
Cs -4.07 -0.41 2.14
I -2.66 2.95 0.58
I -0.43 -1.20 3.52
Cs 5.24 0.70 -3.33
Cs -1.95 1.08 -2.71
Cs 0.78 2.19 2.14
I 1.98 0.31 -1.42
Cs 0.33 -3.15 0.29
I -3.10 -2.28 -1.22

--
CsI4_2

--
Cs -2.59 0.00 -2.82
I -2.81 -2.67 0.01
I 1.87 0.00 -2.34
Cs 5.07 0.00 0.00
Cs -2.52 0.00 2.84
Cs 0.93 -3.18 -0.02
I 1.86 0.00 2.33
Cs 0.93 3.18 -0.02
I -2.81 2.67 0.01

--
CsI5

--
I -0.36 2.90 -0.62
Cs 3.56 2.81 0.56
Cs -4.17 3.65 -0.38
Cs 0.64 -0.01 -3.17
I 4.29 0.00 -2.05
Cs -0.98 0.00 2.19
I 2.75 0.01 3.16
I -4.70 0.00 0.71
I -0.36 -2.91 -0.60
Cs -4.17 -3.65 -0.36
Cs 3.56 -2.81 0.57

--
CsI5_2

--
I 0.33 3.21 0.00
Cs -3.65 2.82 0.00
Cs 4.10 3.87 0.00
Cs 0.52 0.00 2.47
I -3.34 0.00 2.70
Cs 0.51 0.00 -2.48
I -3.35 0.00 -2.70
I 4.03 0.00 0.00
I 0.33 -3.21 0.00
Cs 4.10 -3.87 0.00
Cs -3.65 -2.82 0.00

--
CsI6

--
Cs 3.50 2.88 -3.14
Cs -3.21 3.60 -0.12
Cs -3.49 -2.86 -3.16
I 4.05 0.39 -0.17
I -0.28 3.30 -2.66
Cs -2.75 -1.13 3.51
I -4.04 -0.39 -0.19
Cs 3.21 -3.60 -0.14
I 0.94 -2.35 2.85
Cs 0.00 0.00 -0.47
I 0.29 -3.28 -2.69
I -0.95 2.33 2.86
Cs 2.73 1.10 3.52

--
CsI6_1

--
Cs 2.32 1.21 -3.42
Cs -3.02 3.18 -0.13
Cs -3.01 -2.71 -3.14
I 3.84 0.91 0.36
I 0.04 4.15 -2.31
Cs -2.51 -1.07 3.25
I -4.18 -0.52 -0.22
Cs 2.83 -3.04 -0.05
I 0.89 -2.94 3.30
Cs 2.14 4.49 0.89
I 0.81 -2.36 -3.29
I -0.58 2.54 3.09
Cs 2.63 0.38 4.13

```
---------------------------------- Cs 0.27 -5.54 -1.82 Cs 5.56 3.92 0.53 I -5.85 -0.94 1.77 Cs 4.26 -5.26 -1.19
--                                 Cs 3.29 3.63 2.13   Cs 0.38 -4.02 -1.57 Cs -0.99 -3.78 -2.40 Cs 5.71 -1.23 5.33
CsI6_3                             I 5.20 0.26 2.08    I 3.99 -3.95 -3.05 I -4.86 -4.32 -2.62 ----------------------------------
---------------------------------- I -0.26 5.20 2.08   I -3.38 -4.10 0.03 I 2.93 -3.13 -2.11 --
--                                 I 2.71 2.99 -1.86   I 1.93 -4.05 2.17  I 6.64 -3.26 1.89  CsI12_3
Cs 2.85 0.90 -3.60                 Cs -0.27 5.54 -1.82 Cs -6.80 -3.81 -1.75 I -1.17 -4.22 1.65 ----------------------------------
Cs -3.40 3.32 0.28                 Cs 5.54 0.27 -1.82  Cs -1.67 -3.92 3.63 Cs 6.79 -2.60 -1.94 --
Cs -2.39 -0.85 -3.21               ---------------------------------- Cs 5.54 -3.93 0.52 Cs 2.72 -3.79 1.90 I 1.88 -2.89 -2.17
I 3.91 0.78 0.29                   --                                 ---------------------------------- Cs -5.09 -4.77 1.23 Cs 5.92 -3.04 -2.28
I -0.52 2.85 -2.51                 CsI9                               --                                 Cs 6.28 0.47 2.59  Cs -2.06 -3.58 -2.71
Cs -2.52 -1.21 3.33                ---------------------------------- CsI10_3                           Cs -2.29 4.13 -1.55 Cs 2.05 3.60 2.71
I -4.41 -0.36 0.05                 --                                 ---------------------------------- I -6.12 3.44 -1.86  I -1.88 2.90 2.18
Cs 2.76 -3.26 0.04                 I 0.04 3.18 1.94                   --                                 I 1.84 4.78 -1.04  I 5.91 3.16 2.36
I 0.97 -2.88 3.46                  Cs 4.07 3.26 1.96                  I -1.93 -0.65 2.78                 I -2.66 3.66 2.48  Cs 2.05 0.54 -4.47
Cs 1.79 4.08 0.43                  Cs -3.95 3.66 2.26                 Cs 0.15 -4.07 1.99                 Cs 5.38 4.99 -2.61 I 5.91 0.47 -3.93
I 1.11 -2.50 -3.38                 Cs 0.13 -3.90 -2.38                Cs -4.53 2.40 2.74                 Cs 1.09 4.29 2.84  I -1.88 0.44 -3.59
I -0.63 2.55 3.12                  I -3.72 -2.95 -1.77                Cs -0.21 0.92 -0.64                Cs -6.51 2.91 1.97 I 1.88 3.34 -1.42
Cs 2.69 0.48 4.12                  I 3.97 -3.36 -2.08                 I -2.91 4.10 -0.41                 ---------------------------------- Cs 0.02 0.01 0.01
---------------------------------- Cs 0.21 -0.11 4.55                 I 6.90 -0.06 -1.27                 --                                 Cs -2.05 4.13 -1.76
--                                 I 4.05 -0.11 3.89                  I 2.06 -2.61 -1.64                 CsI11_3                            Cs 5.91 3.50 -1.50
CsI7_1                             I -3.66 -0.07 3.49                 Cs -4.90 -2.55 0.33                ---------------------------------- Cs 2.06 -4.14 1.77
---------------------------------- I 0.01 -3.28 1.79                  I -2.61 -5.70 -0.19                --                                 I 5.92 -3.63 1.55
--                                 Cs -1.54 0.00 0.01                 I -7.14 0.66 0.51                  I -1.75 -0.01 -2.01                I -1.87 -3.34 1.41
Cs 3.90 2.55 2.01                  Cs -3.98 -3.74 2.08                I -3.03 -0.88 -2.95                Cs -5.97 0.00 -2.00                I 1.88 -0.44 3.61
Cs -2.14 4.08 -1.64                Cs 4.05 -3.37 1.80                 Cs 0.50 5.88 -0.43                 Cs 2.20 0.03 -2.46                 Cs -2.06 -0.55 4.45
Cs -2.15 -3.46 -2.71               Cs 0.15 4.01 -2.19                 Cs -5.49 2.15 -2.68                Cs -2.05 -0.01 2.01                Cs 5.92 -0.45 3.78
I 1.65 -0.48 3.35                  I 3.99 3.45 -1.91                  Cs -1.14 -4.24 -3.44               I 6.18 0.02 -1.73                  Cs -5.92 3.03 2.30
I 1.66 3.14 -1.26                  I -3.70 3.05 -1.62                 Cs 1.34 0.51 4.82                  I 5.49 3.67 2.24                   Cs -5.93 0.47 -3.75
Cs -5.87 0.00 0.00                 I -0.04 0.09 -3.73                 I 3.34 -2.61 3.75                  I -5.98 -0.01 2.12                 Cs -5.91 -3.52 1.48
I -3.29 0.42 -2.94                 Cs -4.04 0.11 -4.23                I 2.00 3.46 2.34                   Cs -1.89 -4.01 -2.05               I -5.92 -0.50 3.91
Cs 3.90 -3.01 1.21                 Cs 4.00 0.09 -3.86                 I 2.59 3.30 -2.55                  I -5.77 -3.94 -1.86                I -5.91 3.65 -1.53
I -3.29 -2.75 1.10                 ---------------------------------- Cs 5.37 3.10 0.33                  I 2.11 -3.98 -1.88                 I -5.92 -3.16 -2.38
Cs -0.46 0.00 0.00                 --                                 Cs 5.48 -3.12 0.59                 I 5.56 -3.73 2.20                  ----------------------------------
I 1.65 -2.66 -2.09                 CsI9_2                             Cs 4.12 0.00 -3.97                 I -1.80 -3.97 2.08                 --
I -3.29 2.34 1.83                  ---------------------------------- ---------------------------------- Cs 6.03 -3.91 -1.69                CsI12_4
Cs -2.15 -0.62 4.35                --                                 --                                 Cs 1.94 -5.11 1.98                 ----------------------------------
Cs 3.90 0.46 -3.22                 I 0.22 3.54 2.18                   CsI11                              Cs -5.82 -3.96 2.02                --
I 6.02 0.00 0.00                   Cs 4.21 3.34 2.00                  ---------------------------------- Cs 6.72 -0.02 2.30                 I -5.39 -0.79 0.09
---------------------------------- Cs -3.59 3.81 2.38                 --                                 Cs -1.90 3.99 -2.05                Cs 3.98 -2.97 0.15
--                                 Cs 0.02 -3.26 -1.97                I 0.02 -0.14 -0.98                 I -5.78 3.93 -1.85                 Cs -3.98 2.96 0.19
CsI7                               I -4.20 -2.74 -1.60                Cs 2.91 -2.29 -2.72                I 2.10 4.05 -1.88                  Cs 0.04 0.09 -4.04
---------------------------------- I 3.94 -3.26 -2.03                 Cs -2.86 2.08 0.73                 I -1.80 3.95 2.10                  I -3.19 2.48 -3.78
--                                 Cs 0.11 -0.09 3.84                 Cs 0.10 -2.60 2.26                 Cs 6.03 3.94 -1.63                 I 3.27 -2.32 -3.82
I -1.33 -0.10 2.89                 I 4.03 -0.10 3.77                  I -3.72 5.06 -1.79                 Cs 1.91 5.14 1.98                  Cs -2.96 -3.98 0.07
Cs -1.15 -4.01 2.77                I -4.13 -0.07 3.30                 I -2.88 -0.41 3.94                 Cs -5.82 3.93 2.02                 I 0.79 -5.39 0.05
Cs -1.70 3.81 2.77                 I 0.20 -3.64 2.00                  I 3.08 -4.71 0.50                  ---------------------------------- I -2.36 -3.14 -3.88
Cs 1.42 0.10 0.01                  Cs -6.41 0.01 0.11                 Cs 2.70 2.30 0.73                  --                                 Cs -5.46 -0.73 -3.82
I 1.23 4.20 0.02                   Cs -3.61 -3.90 2.20                I 5.72 0.18 -1.16                  CsI12_2                            Cs 0.84 -5.41 -3.86
I 1.80 -3.99 0.01                  Cs 4.19 -3.46 1.84                 I -0.17 4.40 2.56                  ---------------------------------- Cs 2.96 3.98 0.27
Cs -4.28 -0.30 -0.03               Cs 0.04 3.35 -1.81                 I 3.31 5.34 -1.79                  --                                 I 5.39 0.78 0.22
I -3.81 -4.22 -0.04                I 3.95 3.34 -1.87                  I 2.89 -0.19 3.94                  I 0.20 -0.06 0.65                  I -0.79 5.39 0.24
I -4.35 3.64 -0.03                 I -4.19 2.84 -1.47                 Cs -0.25 6.58 -0.76                Cs 0.29 -3.76 2.30                 I 2.44 3.31 -3.72
I -1.28 -0.09 -2.91                I 0.12 0.10 -4.14                  Cs -0.08 1.87 5.53                 Cs -0.04 3.46 -1.52                Cs -0.77 5.57 -3.66
Cs -1.66 3.81 -2.79                Cs -3.69 0.12 -4.38                Cs 5.66 -2.21 2.04                 Cs 0.06 -2.00 -3.01                Cs 5.54 0.89 -3.69
Cs -1.11 -4.00 -2.80               Cs 4.11 0.09 -3.98                 Cs 6.40 3.52 -3.04                 I 0.17 5.69 1.84                   I 3.88 -3.02 4.06
I 5.43 0.38 0.03                   ---------------------------------- Cs -2.70 -2.46 -2.76                I -0.08 1.48 -5.04                 I 2.88 3.82 4.18
Cs 5.09 4.18 0.03                  --                                 I 0.19 -4.61 -4.33                 I 0.38 -5.61 -1.23                 I -3.96 2.83 4.10
Cs 5.62 -3.43 0.03                 CsI10_1                            I -5.71 -0.26 -1.16                Cs -4.03 -0.21 0.94                I -2.97 -4.00 3.98
---------------------------------- ---------------------------------- I -2.71 -4.91 0.46                 I -3.56 -3.94 2.36                 Cs 0.70 -5.22 4.09
--                                 --                                 Cs -6.67 3.02 -3.02                I -4.03 3.36 -1.37                 Cs 5.10 0.65 4.25
CsI8_2                             I 0.29 0.00 -1.60                  Cs -5.48 -2.65 2.02                I -3.68 2.30 4.06                  Cs -0.79 5.04 4.27
---------------------------------- Cs 4.08 0.00 -3.19                 Cs 0.26 -6.92 -1.20                I -3.93 -2.12 -2.86                Cs -5.18 -0.83 4.13
--                                 Cs -3.31 0.01 0.04                 ---------------------------------- Cs -3.84 5.50 1.90                 ----------------------------------
I -5.20 -0.26 2.08                 Cs 1.98 -0.01 2.14                 --                                 Cs -4.03 1.32 -4.69                --
Cs 3.63 -3.29 2.13                 I -6.90 0.01 -1.73                 CsI11_2                            Cs -3.63 -5.61 -1.12               CsI13
Cs -3.63 3.29 2.13                 I -1.80 0.00 3.76                  ---------------------------------- Cs 0.17 2.30 3.95                  ----------------------------------
Cs 0.00 0.00 -2.11                 I 5.67 -0.01 0.61                  --                                 Cs 4.15 0.11 0.29                  --
I -2.99 2.71 -1.86                 Cs 0.40 4.02 -1.55                 I -1.58 0.22 -1.89                 I 4.38 -3.39 2.40                  I 0.00 0.00 0.00
I 2.99 -2.71 -1.86                 I 4.00 3.95 -3.04                  Cs -5.60 -0.46 -2.33               I 4.07 3.58 -1.69                  Cs 2.70 1.28 -2.77
Cs -3.29 -3.63 2.13                I -3.37 4.11 0.02                  Cs 2.28 0.71 -1.43                 I 4.28 2.07 3.88                   Cs -2.70 -1.28 2.77
I 0.26 -5.20 2.08                  I 1.95 4.04 2.18                   Cs -1.92 -0.32 2.13                I 4.17 -1.87 -3.17                 Cs 2.91 0.05 2.85
I -2.71 -2.99 -1.86                Cs -6.78 3.83 -1.78                I 6.32 1.45 -1.31                  Cs 4.07 5.49 1.73                  Cs -2.91 -0.06 -2.86
Cs -5.54 -0.27 -1.82               Cs -1.66 3.93 3.63                 I 2.29 0.50 2.64                   Cs 3.84 1.57 -5.08                 I 0.21 -1.22 5.60
```

I -5.58 -1.33 -0.08
I -0.21 1.22 -5.60
I 5.58 1.32 0.08
Cs 0.93 -3.87 -0.88
I 3.61 -2.58 -3.63
I -1.76 -5.12 1.89
I 3.82 -3.80 1.97
I -1.97 -3.90 -3.71
Cs 1.10 -4.92 4.59
Cs -4.51 -5.02 -0.92
Cs 0.70 -2.55 -6.28
Cs 6.31 -2.45 -0.77
Cs -0.93 3.88 0.88
I 1.76 5.12 -1.89
I -3.61 2.58 3.63
I 1.97 3.90 3.71
I -3.82 3.79 -1.97
Cs -0.70 2.55 6.28
Cs -6.31 2.45 0.77
Cs -1.10 4.92 -4.58
Cs 4.51 5.02 0.93

--
CsI13_2

--
I 1.38 0.00 -1.29
Cs 0.44 0.03 2.76
Cs -7.40 -0.01 1.08
Cs 1.26 -4.02 -1.18
Cs 1.27 4.03 -1.23
I -7.25 -3.97 1.01
I -7.27 3.94 0.99
I 0.49 4.07 2.70
I 0.50 -4.01 2.75
Cs 5.21 0.00 -0.36
I 4.48 0.04 3.58
I 8.43 -0.05 -2.74
I 5.26 -4.11 -0.33
I 5.29 4.11 -0.40
Cs 8.29 -3.87 -2.73
Cs 8.38 3.77 -2.70
Cs 4.29 3.97 3.47
Cs 4.29 -3.88 3.54
Cs -2.62 0.00 -2.02
I -3.43 0.01 1.97
I -6.53 -0.02 -2.96
I -2.55 -4.06 -2.05
I -2.56 4.05 -2.09
Cs -6.43 -3.94 -2.79
Cs -6.45 3.90 -2.80
Cs -3.46 4.04 1.91
Cs -3.44 -4.02 1.94

--

Doubly charged Clusters' coordinates

NaI

NaI16-NaNa " - 187.574898222"
NaI16-NaNa-3 " - 187.550195355"
NaI16-NaNa-2 " - 187.541829550"
NaI17-NaNa " - 199.302771454"
NaI18-NaNa-4 " - 211.034439606"
NaI18-NaNa " - 211.007512446"
NaI18-NaNa-3 " - 211.005421226"
NaI18-NaNa-2 " - 210.992844202"
NaI19-NaNa " - 222.737520639"
NaI19-NaNa-2 " - 222.726680403"
NaI20-NaNa-2 " - 234.477046796"
NaI20-NaNa " - 234.470753857"
NaI21-NaNa-4 " - 246.214775975"
NaI21-NaNa-3 " - 246.204471685"
NaI21-NaNa " - 246.190837488"
NaI21-NaNa-2 " - 246.182691221"
NaI22-NaNa-4 " - 257.938705701"
NaI22-NaNa-3 " - 257.937235833"
NaI22-NaNa-2 " - 257.918374040"
NaI22-NaNa " - 257.913192242"
NaI23-NaNa-2 " - 269.654095955"
NaI23-NaNa " - 269.638691630"
NaI24-NaNa-3 " - 281.366911331"
NaI24-NaNa " - 281.351419889"
NaI24-NaNa2 " - 281.351417214"
NaI25-NaNa-2 " - 293.081728217"
NaI25-NaNa " - 293.076825806"
NaI26-NaNa " - 304.818075184"

--
NaI16-NaNa

--
I 1.24 0.17 0.00
I -2.15 1.30 3.28
I 4.56 -1.20 3.31
I 4.55 -1.20 -3.31
I -2.14 1.30 -3.28
I 2.60 3.07 -3.24
I 2.61 3.07 3.24
I -1.10 4.72 0.00
I 5.88 1.85 0.00
I 0.28 -3.06 -3.38
I 0.29 -3.06 3.38
I -2.71 -2.18 0.00
I 3.38 -4.29 0.00
I -5.93 -1.87 3.03
I -5.92 -1.86 -3.04
I -5.34 2.59 0.00
Na -5.94 -2.74 0.00
Na -5.40 1.14 -2.88
Na -4.13 5.40 0.02
Na -5.41 1.13 2.88
Na -2.78 -2.22 -3.29
Na -0.36 3.93 -3.07
Na -0.36 3.92 3.08
Na -2.78 -2.22 3.29
Na -1.98 1.03 0.00
Na 1.48 -0.08 -3.28
Na 2.90 2.97 0.00
Na 1.49 -0.09 3.28
Na 0.37 -3.10 0.00
Na 3.29 -4.12 -3.19
Na 5.60 1.77 -3.18
Na 5.61 1.77 3.18
Na 3.29 -4.13 3.18
Na 4.59 -1.23 0.00

--
NaI16-NaNa-3

--
I 1.96 0.76 0.00
I -1.16 4.13 -0.02
I 5.26 4.10 -0.02
I 5.57 -2.55 0.01
I -0.88 -2.99 0.02
I 2.21 -2.96 -3.31
I -1.26 0.60 -3.33
I 5.17 0.81 -3.33
I 2.21 -2.93 3.33
I -1.26 0.63 3.33
I 5.17 0.83 3.32
I -5.70 2.84 3.01
I -4.21 -3.36 -3.21
I -5.70 2.80 -3.04
I -4.21 -3.33 3.24
I -4.60 -0.15 0.00
Na -4.81 -0.25 3.27
Na -4.24 -3.43 0.02
Na -4.80 -0.28 -3.27
Na -6.54 2.45 -0.01
Na -1.14 -2.98 3.27
Na -1.14 -3.02 -3.24
Na -2.73 3.45 -2.75
Na -2.73 3.48 2.72
Na -1.40 0.24 0.00
Na 2.27 -3.12 0.01
Na 1.88 0.16 -3.28
Na 1.93 3.92 -0.02
Na 1.88 0.19 3.28
Na 5.33 -2.49 3.21
Na 5.33 -2.52 -3.19
Na 6.35 3.65 -2.99
Na 6.36 3.66 2.96
Na 5.10 0.60 0.00

--
NaI16-NaNa-2

--
I -2.47 0.37 -1.63
I 1.97 1.58 -3.45
I -5.87 -1.19 1.93
I 0.51 -1.42 2.41
I -2.59 1.76 3.40
I -2.12 5.04 -2.09
I 1.20 2.98 0.87
I -5.84 3.20 0.21
I -2.51 -4.27 0.70
I 1.13 -2.86 -2.13
I -5.86 -2.92 -2.50
I 6.07 -1.86 -3.33
I 3.62 1.13 4.73
I 5.88 3.71 -0.61
I 3.82 -4.65 1.83
I 4.66 -0.41 0.55
Na 5.24 -3.37 -0.64
Na 3.69 -1.79 3.36
Na 4.68 2.47 2.10
Na 6.58 0.84 -1.73
Na 0.87 -4.31 0.92
Na 0.68 1.55 3.84
Na 3.00 4.03 -1.58
Na 3.15 -1.34 -4.13
Na 1.56 -0.03 -0.39
Na -2.62 -1.39 2.46
Na -2.06 3.05 0.49
Na -1.00 2.51 -3.51
Na -2.03 -2.75 -2.03
Na -5.60 -4.03 0.60
Na -5.71 1.82 3.09
Na -5.00 5.76 -1.37
Na -7.56 -4.09 -4.71
Na -5.58 0.20 -0.96

--
NaI17-NaNa

--
I -1.70 0.00 0.00
I 1.69 2.30 -2.50
I -5.14 2.38 -2.32
I -5.12 -2.39 2.34
I 1.70 -2.30 2.48
I -1.91 0.01 4.71
I -1.63 4.64 0.00
I 1.70 2.29 2.48
I -5.13 2.38 2.34
I -1.63 -4.64 0.00
I -1.93 0.00 -4.70
I 1.70 -2.30 -2.50
I -5.14 -2.38 -2.32
I 6.27 0.00 2.50
I 4.79 4.66 -0.01
I 4.79 -4.66 -0.01
I 6.28 0.00 -2.48
Na 4.88 -2.84 -2.51
Na 4.87 -2.85 2.49
Na 4.87 2.85 2.50
Na 4.87 2.84 -2.51
Na 1.57 -4.60 -0.02
Na 1.15 0.00 4.62
Na 1.57 4.60 -0.01
Na 1.13 0.00 -4.63
Na 1.49 0.00 -0.01
Na -1.86 -2.34 2.35
Na -1.86 2.35 2.34
Na -1.87 2.34 -2.34
Na -1.87 -2.34 -2.34
Na -4.86 -4.52 0.01
Na -5.10 0.00 4.43
Na -4.87 4.52 0.01
Na -5.12 0.00 -4.42
Na -5.13 0.00 0.01
Na 8.11 0.01 0.02

--
NaI18-NaNa-4

--
I -2.00 -0.20 0.01
I 1.19 2.72 1.67
I -4.89 1.24 3.60
I -5.47 -3.21 -1.33
I 0.93 -1.63 -3.59
I -1.07 -4.76 -0.45
I -0.57 -0.41 4.59
I 2.26 -1.82 1.13
I -3.91 -3.35 3.10
I -3.67 -0.08 -4.31
I -2.99 4.37 0.54
I -0.05 2.98 -3.08
I -6.42 1.42 -0.83
I 3.04 6.00 -0.83
I 5.08 -3.55 -2.05
I 5.41 1.31 2.82
I 4.28 1.37 -1.94
I 8.18 -2.08 1.18
Na 8.22 0.08 3.37
Na 7.82 -4.38 -0.80
Na 2.32 0.38 3.57
Na -3.59 -1.09 5.30
Na -0.89 -2.54 2.08
Na 5.27 -0.95 0.35
Na 1.87 -3.95 -1.29
Na -4.06 -5.28 0.60
Na 4.17 3.64 0.92
Na 4.06 -1.19 -3.82
Na 1.05 0.60 -0.89
Na -2.46 -2.45 -2.32
Na -1.87 1.94 2.58
Na -5.15 -0.96 1.12
Na -5.88 3.45 1.54
Na -6.54 -0.80 -3.08
Na -3.37 2.16 -1.83
Na 0.02 5.13 -0.22
Na -0.79 0.63 -5.08
Na 2.95 4.07 -3.18

--
NaI18-NaNa

--
I -1.85 0.00 -0.13
I 1.40 -3.41 0.06
I -5.22 -3.33 -0.44
I -5.23 3.34 -0.20
I 1.40 3.41 0.27
I -1.60 3.45 -3.31
I -1.60 -3.23 -3.53
I 1.75 0.10 -3.33
I -4.98 0.13 -3.68
I -2.10 3.24 3.37
I -2.09 -3.46 3.14
I 1.05 -0.11 3.52
I -5.47 -0.11 2.99
I 4.33 -3.30 3.73
I 4.98 3.55 -2.73
I 5.00 -3.39 -2.89
I 4.33 3.09 3.92
I 4.84 0.00 0.39
Na 6.65 -5.64 -4.01
Na 6.62 5.82 -3.82
Na 1.52 -3.11 -3.08
Na 4.84 0.08 -2.73
Na 1.51 3.29 -2.88
Na -1.72 0.11 -3.40
Na -4.78 -3.02 -3.54
Na -4.78 3.26 -3.31
Na -5.21 0.00 -0.32
Na -5.22 -3.26 2.74
Na -5.23 3.04 2.97
Na -1.94 -3.30 -0.14
Na -2.19 -0.11 3.22
Na -1.94 3.30 0.08
Na 1.14 -3.35 3.43
Na 1.38 -0.01 0.27
Na 4.52 -3.19 0.64
Na 4.30 -0.10 3.90
Na 4.51 3.16 0.83
Na 1.14 3.14 3.63

--
NaI18-NaNa-3

--
I 2.18 0.00 0.03
I -0.20 1.88 -3.63
I 4.37 -2.94 -2.96
I 4.71 -1.94 3.65
I -0.47 2.84 2.92
I 0.09 -2.02 3.79
I -0.28 -3.17 -2.71
I -2.40 -0.24 0.12
I 2.35 -4.84 0.81
I 4.56 2.70 2.77
I 4.60 1.71 -3.52
I 1.61 5.15 -0.82
I 7.08 -0.34 -0.04
I -5.28 1.10 3.35
I -5.51 -0.52 -3.17
I -3.13 4.26 -0.87
I -8.75 -0.40 0.43
I -5.56 -3.86 -0.32
Na -7.92 -2.43 -1.88
Na -8.40 0.40 3.31
Na -3.44 -2.85 -2.37
Na 2.17 -5.14 -2.35
Na 0.03 -2.52 0.49
Na -5.59 -0.72 0.33
Na -2.31 -0.10 3.43
Na 2.45 -4.17 3.90
Na -3.34 1.66 -2.92
Na -3.59 3.44 2.12
Na -0.27 2.19 -0.37
Na 2.33 0.26 3.30
Na 1.92 -0.72 -3.24
Na 4.59 -2.51 0.34
Na 6.63 -0.75 -3.19
Na 6.82 0.32 3.07
Na 4.82 1.87 -0.35
Na 2.31 3.75 -3.72
Na 2.13 4.63 2.35
Na -1.14 6.47 -1.52

--
NaI18-NaNa-2

--
I 1.81 0.07 -0.03
I -1.35 -1.58 3.08
I 5.31 -1.51 2.65
I 4.99 1.47 -3.11
I -1.71 1.53 -2.93
I 1.58 4.46 -1.27
I 1.86 1.58 4.31
I -1.84 3.03 1.65
I 6.31 2.90 1.24
I 1.49 -1.43 -4.54
I 1.80 -4.50 1.41
I -1.50 -3.07 -1.45
I 5.04 -3.10 -1.80
I -4.66 -4.54 1.59
I -5.27 4.23 -1.32
I -4.80 1.08 4.66
I -4.94 -1.70 -4.19
I -5.03 -0.18 0.18
Na 9.34 3.08 1.26
Na -7.50 6.10 -2.05
Na -1.65 1.27 4.53
Na 4.91 1.33 3.89
Na 1.25 2.87 1.49
Na -5.01 2.47 1.87
Na -1.81 4.24 -1.30
Na 4.66 4.07 -1.42
Na -4.71 -1.77 3.12
Na -4.92 1.04 -2.74
Na -1.70 -0.18 0.09
Na 1.55 1.43 -3.00
Na 1.85 -1.57 2.86
Na 5.03 -0.25 -0.33
Na 4.89 -4.35 1.14
Na 4.60 -1.45 -4.49
Na 1.68 -3.02 -1.57
Na -1.52 -4.49 1.51
Na -1.79 -1.58 -4.31
Na -4.82 -3.18 -1.30

--
NaI19-NaNa

--
I 2.07 -0.41 0.00
I -0.87 0.81 -3.29
I 5.25 -1.60 -3.34
I 5.26 -1.58 3.34
I -0.87 0.82 3.29
I 0.88 -3.53 3.29
I 0.87 -3.54 -3.27
I -2.53 -3.27 0.01
I 4.09 -4.74 0.01
I 3.35 2.74 3.34
I 3.34 2.73 -3.35
I 0.57 4.22 0.00
I 6.50 1.49 -0.01
I -2.62 5.15 -3.19
I -5.11 -1.04 3.29
I -5.11 -1.05 -3.29
I -2.61 5.15 3.19
I -3.97 2.02 0.00
I -7.47 -3.36 0.00
Na -7.92 -2.24 -2.99
Na -7.92 -2.22 2.98
Na -4.90 -5.22 0.01
Na -1.96 -2.15 -3.26
Na -4.87 -0.96 0.00
Na -1.96 -2.14 3.26
Na 1.08 -3.54 0.01
Na 3.95 -4.45 -3.15
Na 3.96 -4.43 3.16
Na 5.26 -1.57 0.00
Na 6.23 1.44 -3.17
Na 6.23 1.45 3.16
Na 2.23 -0.35 -3.30
Na 3.48 2.74 -0.01
Na 2.23 -0.34 3.30
Na 0.37 4.05 -3.27
Na -0.69 1.31 0.00
Na -3.75 2.25 -3.24
Na -2.55 5.32 0.00
Na -3.75 2.26 3.24
Na 0.38 4.06 3.27

--
NaI19-NaNa-2

--
I 1.75 0.55 -0.02
I -0.01 -2.48 2.93
I 5.59 0.81 2.88
I 3.83 3.37 -3.07
I -1.70 0.27 -2.92
I -0.77 5.00 -1.30
I 1.21 1.63 4.62
I -2.79 2.23 2.07
I 3.19 4.67 1.57
I 2.66 -1.00 -4.60
I 4.20 -3.45 1.39
I 0.81 -3.97 -1.66
I 6.26 -0.40 -1.58
I -1.47 -6.59 1.40
I -5.97 0.94 -1.18
I -4.25 -1.63 4.48
I -2.95 -4.11 -4.33
I -3.69 -2.81 0.02
I -5.44 5.51 -0.55
Na -3.02 7.02 -1.86
Na -7.62 3.45 -1.68
Na -4.63 4.66 2.39
Na -1.46 -0.22 4.69
Na -5.00 -0.52 1.70
Na -3.06 2.50 -1.17
Na 0.50 2.92 1.79
Na 4.00 3.12 4.29
Na 2.45 5.56 -1.33
Na 4.73 2.05 -0.04
Na 6.81 -1.69 1.30
Na 5.29 0.76 -4.35
Na 2.79 -0.91 2.91
Na 3.53 -2.23 -1.58
Na 1.27 1.43 -3.13
Na 1.34 -5.15 1.40
Na -0.70 -1.60 -0.15
Na -2.86 -4.20 2.95
Na -2.19 -5.49 -1.49
Na -4.33 -1.71 -2.90
Na -0.13 -2.74 -4.50

--
NaI20-NaNa-2

--
I -2.30 -0.42 0.01
I 0.27 2.55 2.29
I -4.53 -1.32 4.08
I -4.97 -3.69 -2.18
I -0.31 0.71 -4.27
I -0.25 -3.87 -2.44
I 0.35 -2.04 4.18
I 2.46 -0.96 -0.02
I -2.48 -4.87 1.63
I -4.99 0.70 -3.71
I -4.42 3.10 2.39
I -2.20 4.12 -1.72
I -7.08 -0.24 0.31
I 0.47 6.98 1.03
I 4.73 -0.28 -3.92
I 4.87 2.63 2.08
I 2.56 3.65 -1.97
I 7.42 -0.54 -0.09
I 5.08 -1.65 3.90
I 5.24 -4.43 -1.77
Na 7.18 0.63 2.82
Na 7.12 -2.17 -2.86
Na 5.24 -2.73 0.82
Na 2.61 0.41 2.89
Na 4.86 1.31 -0.97
Na 2.77 -2.80 -2.87
Na -0.17 -2.81 0.64
Na -2.46 -3.61 4.48
Na -2.65 -5.71 -1.47
Na -4.77 -2.51 0.89
Na -6.63 0.94 3.20
Na -7.11 -1.40 -2.64
Na -2.27 0.75 3.09
Na -4.69 1.85 -0.64
Na -2.55 -1.59 -3.14
Na -1.94 5.00 1.59
Na 0.10 1.58 -0.99
Na 2.60 4.74 1.49
Na 0.37 6.04 -1.87
Na 2.59 1.80 -4.65
Na -2.76 2.66 -4.51
Na 2.93 -2.96 5.67

--
NaI20-NaNa

--
I -2.14 -0.63 -0.09
I 0.79 0.16 3.25
I -4.47 -3.33 2.88
I -5.38 -1.46 -3.50
I 0.04 2.26 -3.03
I -0.74 -2.15 -4.37
I 0.44 -4.75 1.90
I 2.61 -1.86 -1.22
I -3.08 -5.02 -1.40
I -4.46 3.01 -2.27
I -3.81 1.22 4.13
I -1.63 3.99 1.21
I -6.85 0.11 0.66
I 1.58 4.71 4.43
I 4.62 1.54 -3.75
I 5.28 -0.21 2.58
I 0.86 6.62 -1.65
I 3.14 3.11 0.36
I 7.39 -1.51 -1.43
Na 7.42 -2.29 1.77
Na 7.51 0.49 -3.89
Na 5.12 -3.72 -1.47
Na 2.71 -2.16 2.12
Na 4.83 0.61 -0.56
Na 1.78 -0.17 -4.01
Na -0.46 -3.13 -1.28
Na -2.71 -5.60 1.66
Na -3.47 -3.79 -4.34
Na -4.96 -2.38 -0.35
Na -6.27 -0.73 3.65
Na -6.96 1.08 -2.38
Na -2.06 -1.22 3.13
Na -4.22 2.08 0.90
Na -2.69 0.44 -3.25
Na -1.09 3.05 4.27
Na 0.25 1.59 0.23
Na 3.33 2.30 3.53
Na 1.18 5.76 1.41
Na 2.61 4.23 -2.65
Na -1.80 4.91 -1.94
I 5.23 -4.73 1.51
Na 2.91 -6.53 2.48

--
NaI21-NaNa-4

--
I 2.29 -0.39 0.08
I 0.00 -3.90 2.50
I 4.80 0.75 3.91
I 4.65 3.00 -2.31
I 0.00 -1.76 -4.06
I 0.01 2.75 -2.45
I 0.00 0.85 4.16
I -2.29 -0.39 0.08
I 2.32 4.25 1.69
I 4.80 -1.41 -3.87
I 4.84 -3.61 2.48
I 2.57 -4.83 -1.48
I 7.13 -0.27 0.01
I -4.80 -1.41 -3.87
I -4.85 -3.60 2.48
I -2.58 -4.83 -1.47
I -7.13 -0.25 0.00
I -4.81 0.77 3.90
I -4.64 3.01 -2.33
Na -7.01 -1.32 2.97
Na -6.86 0.83 -2.97
Na -4.71 1.87 0.74
Na -2.45 -1.48 3.17
Na -4.80 -2.48 -0.70
Na -2.41 0.68 -3.10
Na 0.00 1.89 0.79
Na 2.56 2.75 4.48
Na 2.28 5.06 -1.84
Na 4.71 1.86 0.75
Na 7.00 -1.34 2.98
Na 6.88 0.83 -2.96
Na 2.44 -1.48 3.17
Na 4.80 -2.48 -0.70
Na 2.42 0.68 -3.10
Na 2.62 -5.58 1.55
Na 0.00 -2.78 -0.80
Na -2.64 -5.58 1.57
Na -2.63 -3.59 -4.35
Na 2.63 -3.58 -4.37
I -2.32 4.25 1.68
I 0.01 7.22 -1.44
Na 0.01 6.47 1.50
Na -2.26 5.07 -1.85
Na -2.56 2.76 4.47

--
NaI21-NaNa-3

--
I -2.08 -0.28 0.08
I 0.43 -3.45 -2.25
I -5.04 -0.02 -3.67
I -4.82 2.98 2.19
I 0.87 -0.80 3.99
I -0.14 3.44 1.96
I -0.40 0.63 -4.28
I 2.45 0.47 -0.53
I -2.99 4.04 -2.12
I -4.04 -1.20 4.24
I -4.09 -4.22 -1.64
I -1.20 -4.62 2.20
I -6.81 -0.99 0.51
I 1.30 -7.59 -0.81
I 5.51 0.13 3.04
I 5.01 -2.62 -2.90
I 3.46 -3.90 1.51
I 6.95 1.33 -1.26
I 4.44 4.40 1.56
Na 7.51 -0.82 -3.45
Na 7.02 2.61 1.77
Na 4.21 3.18 -1.38
Na 2.12 -1.06 -3.43
Na 5.11 -1.21 0.11
Na 2.61 1.86 2.58
Na -0.25 2.28 -1.31
Na -3.09 2.18 -4.73
Na -2.83 5.27 1.17
Na -4.89 1.46 -0.72
Na -6.64 -2.41 -2.31
Na -6.55 0.54 3.26
Na -2.32 -1.72 -2.91
Na -4.07 -2.68 1.23
Na -2.19 1.21 3.00
Na -1.42 -5.92 -1.15
Na 0.59 -2.09 0.78
Na 3.13 -5.16 -1.74
Na 1.45 -6.42 1.98
Na 3.75 -2.13 4.15
Na -1.48 -2.80 4.79
I 1.70 4.83 -2.24

I -1.01 7.71 0.40
Na -0.95 6.57 -2.45
Na 1.62 6.00 0.88

--
NaI21-NaNa

--
I 0.00 4.25 -3.27
I -2.45 -0.54 -3.71
I 2.30 6.19 1.12
I -2.30 1.79 2.47
I 2.30 1.79 2.47
I 2.45 -0.54 -3.71
I 0.00 -1.45 0.17
I 4.57 2.92 -1.55
I -2.30 6.19 1.12
I -4.56 2.92 -1.55
I -7.29 -1.14 -3.08
I -2.34 -2.55 4.29
I -2.34 -5.00 -1.94
I -6.96 1.50 2.52
I -4.77 -1.94 0.51
I 0.00 -6.02 2.07
I 2.34 -5.00 -1.94
I 2.33 -2.55 4.29
Na 0.00 -6.94 -0.99
Na 0.00 -4.60 4.95
Na 2.28 -3.87 1.23
Na 0.00 -2.89 -2.78
Na -2.28 -3.87 1.23
Na 0.00 -0.49 3.38
Na 2.71 0.32 -0.46
Na 5.31 0.99 -3.97
Na 4.85 3.65 1.66
Na 2.61 5.30 -1.92
Na 0.00 8.21 1.79
Na 0.00 1.32 -4.44
Na -2.61 5.31 -1.92
Na 0.00 3.96 2.04
Na -5.31 0.99 -3.97
Na -2.71 0.32 -0.46
Na -4.85 -3.11 -2.55
Na -7.53 -0.26 -0.03
Na -4.65 -0.47 3.46
Na -4.85 3.65 1.66
I 4.77 -1.95 0.51
I 7.29 -1.15 -3.08
I 6.96 1.50 2.52
Na 7.52 -0.26 -0.03
Na 4.65 -0.47 3.46
Na 4.85 -3.11 -2.55

--
NaI21-NaNa-2

--
I 1.45 -3.01 1.51
I -2.77 0.05 3.19
I 4.37 -4.90 -1.97
I -1.05 -1.47 -3.06
I 3.27 -0.53 -2.08
I 2.12 0.47 4.56
I 0.01 1.80 0.14
I 6.01 -1.91 2.64
I -0.28 -5.95 -1.80
I -2.03 -4.43 4.31
I -3.66 -3.51 0.15
I -7.12 -1.18 2.08
I -1.90 2.92 -4.29
I -3.89 4.47 1.82
I -5.50 -2.48 -3.98
I -4.75 1.13 -1.17
I -1.01 6.45 -1.33
I 0.72 5.32 2.94
I 2.61 4.00 -3.13
Na -1.89 6.92 1.69
Na -0.05 5.48 -4.22
Na 1.48 4.72 -0.21
Na -1.40 2.86 2.89
Na -3.03 3.84 -1.33
Na 0.65 1.31 -3.10
Na 2.60 0.09 1.14
Na 4.59 -1.25 5.29
Na 5.92 -2.13 -2.90
Na 4.40 -4.12 1.10
Na 2.35 -7.22 -2.77
Na -0.39 -1.81 4.16
Na -1.26 -5.18 1.36
Na 1.35 -3.14 -1.83
Na -4.65 -2.80 3.22
Na -2.29 -0.59 -0.07
Na -5.61 1.56 1.96
Na -6.42 -1.81 -0.97
Na -3.81 0.18 -4.16
Na -3.04 -4.10 -2.94
I 4.75 2.60 1.25
I 7.62 0.33 -1.99
Na 7.30 0.56 1.06
Na 5.08 2.27 -2.14
Na 3.07 3.49 3.82

--
NaI22-NaNa-4

--
I -2.31 0.00 0.00
I 0.00 -3.26 -2.34
I -4.81 0.89 -3.91
I -4.69 3.47 2.18
I 0.00 -1.14 4.18
I 0.00 3.26 2.33
I 0.00 1.14 -4.18
I 2.31 0.00 0.00
I -2.35 4.54 -1.86
I -4.80 -0.88 3.91
I -4.68 -3.47 -2.18
I -2.35 -4.54 1.86
I -7.12 -0.01 0.00
I 0.00 -7.64 -1.08
I 4.81 -0.88 3.91
I 4.68 -3.47 -2.18
I 2.35 -4.54 1.86
I 7.12 0.00 0.00
I 4.81 0.89 -3.91
I 4.68 3.47 2.18
Na 6.90 -1.29 -2.88
Na 6.90 1.29 2.88
Na 4.74 2.16 -0.82
Na 2.43 -1.23 -3.07
Na 4.75 -2.16 0.82
Na 2.42 1.23 3.07
Na 0.00 2.24 -0.87
Na -2.61 2.92 -4.58
Na -2.30 5.52 1.58
Na -4.75 2.16 -0.82
Na -6.89 -1.30 -2.89
Na -6.90 1.29 2.88
Na -2.42 -1.23 -3.07
Na -4.75 -2.17 0.82
Na -2.42 1.23 3.07
Na -2.29 -5.52 -1.59
Na 0.00 -2.24 0.87
Na 2.29 -5.52 -1.59
Na 0.00 -6.74 1.82
Na 2.61 -2.92 4.58
Na -2.61 -2.92 4.58
I 2.35 4.53 -1.86
I 0.00 7.64 1.09
Na 0.00 6.74 -1.82
Na 2.29 5.52 1.58
Na 2.61 2.92 -4.58

--
NaI22-NaNa-3

--
I -2.30 0.00 0.40
I 0.00 -2.25 -3.01
I -4.63 2.39 -3.05
I -4.85 2.30 3.58
I 0.00 -2.50 3.83
I 0.00 2.50 3.83
I 0.00 2.26 -3.01
I 2.30 0.00 0.40
I -2.34 4.90 0.38
I -4.85 -2.30 3.57
I -4.63 -2.39 -3.05
I -2.34 -4.90 0.38
I -7.10 0.00 0.14
I 0.00 -6.76 -3.52
I 4.85 -2.30 3.58
I 4.63 -2.39 -3.05
I 2.34 -4.90 0.38
I 7.10 0.00 0.14
I 4.63 2.39 -3.05
I 4.85 2.30 3.58
Na 6.74 0.00 -3.02
Na 7.03 0.00 3.29
Na 4.73 2.32 0.21
Na 2.36 0.00 -2.98
Na 4.74 -2.32 0.21
Na 2.47 0.00 3.65
Na 0.00 2.41 0.28
Na -2.28 4.57 -3.24
Na -2.60 4.38 3.49
Na -4.73 2.32 0.21
Na -6.74 0.00 -3.02
Na -7.03 0.00 3.29
Na -2.36 0.00 -2.98
Na -4.74 -2.32 0.21
Na -2.47 0.00 3.65
Na -2.28 -4.57 -3.25
Na 0.00 -2.42 0.28
Na 2.28 -4.57 -3.24
Na 0.00 -6.94 -0.49
Na 2.60 -4.38 3.49
Na -2.60 -4.38 3.49
I 2.34 4.90 0.38
I 0.00 6.76 -3.52
Na 0.00 6.94 -0.49
Na 2.60 4.38 3.49
Na 2.28 4.57 -3.24

--
NaI22-NaNa-2

--
I 2.36 -0.74 0.00
I -0.01 1.59 -3.40
I 5.03 -2.61 -3.20
I 5.03 -2.61 3.21
I -0.01 1.60 3.40
I 0.03 -3.52 3.27
I 0.03 -3.53 -3.27
I -2.34 -0.77 0.00
I 2.50 -5.96 0.00
I 4.68 2.07 3.33
I 4.68 2.07 -3.33
I 2.33 4.11 0.00
I 7.35 0.06 0.00
I -0.03 6.41 -3.22
I -4.72 2.04 3.33
I -4.72 2.04 -3.32
I -0.03 6.41 3.22
I -2.38 4.08 0.00
I -7.35 -0.02 0.00
I -4.99 -2.65 -3.21
I -4.99 -2.65 3.21
Na -7.03 -0.07 -3.19
Na -7.03 -0.08 3.19
Na -5.19 -2.33 0.00
Na -2.56 -0.34 -3.26
Na -4.85 2.13 0.00
Na -2.55 -0.34 3.26
Na 0.02 -3.04 0.00
Na 2.90 -4.84 -3.02
Na 2.90 -4.84 3.03
Na 5.22 -2.28 0.00
Na 7.03 0.00 -3.19
Na 7.02 0.00 3.19
Na 2.54 -0.33 -3.27
Na 4.81 2.16 0.00
Na 2.54 -0.33 3.27
Na 2.19 4.22 -3.26
Na -0.01 1.80 0.00
Na -2.24 4.20 -3.26
Na -0.03 6.45 0.00
Na -2.24 4.20 3.26
Na 2.19 4.23 3.26
I -2.44 -5.97 0.00
Na 0.03 -7.80 -0.01
Na -2.83 -4.86 3.03
Na -2.84 -4.85 -3.03

--
NaI22-NaNa

--
I -1.24 -1.81 0.26
I -2.25 1.61 3.21
I -2.29 -4.80 3.49
I -0.47 -5.34 -2.72
I -0.58 1.23 -3.35
I 2.61 -1.86 -2.45
I 1.57 -1.42 4.60
I 2.13 1.42 0.81
I 2.46 -4.90 1.39
I -3.77 -2.06 -3.95
I -5.70 -1.61 2.39
I -4.70 1.32 -0.95
I -4.68 -5.19 -0.56
I -5.36 4.86 1.97
I 2.51 4.66 -2.84
I 1.22 4.96 3.65
I -3.81 4.46 -4.21
I -1.29 4.76 -0.26
I 5.23 4.78 1.04
I 5.88 1.35 -2.34
Na 4.02 6.27 3.52
Na 5.57 4.57 -2.22
Na 5.40 1.50 0.79
Na 0.81 1.74 3.77
Na 1.84 4.64 0.33
Na 2.53 1.41 -2.68
Na 1.99 -1.75 0.80
Na 0.73 -4.50 4.05
Na 2.69 -5.14 -2.14
Na -1.58 -5.07 0.27
Na -5.43 -4.76 2.49
Na -3.59 -5.18 -3.57
Na -2.65 -1.56 3.20
Na -4.74 -1.89 -0.81
Na -0.66 -2.02 -3.07
Na -5.55 1.73 2.15
Na -1.54 1.48 -0.18
Na -2.34 4.91 2.77
Na -4.61 4.66 -1.14
Na -0.77 4.53 -3.51
Na -3.82 1.29 -4.11
I 5.76 -1.44 2.16
I 5.89 -4.81 -2.08
Na 5.65 -4.41 0.94
Na 5.78 -1.82 -3.02
Na 4.61 -1.49 4.99

--
NaI23-NaNa-2

--
I -2.30 -0.47 0.25
I 0.12 -2.89 -2.90
I -4.75 1.49 -3.39
I -4.76 2.32 3.24
I 0.11 -2.51 3.94
I -0.10 2.27 3.36
I -0.07 1.64 -3.47
I 2.33 -0.27 0.25
I -2.59 4.26 -0.35
I -4.72 -2.38 3.76
I -4.55 -3.25 -2.81
I -2.14 -5.29 0.80
I -7.08 -0.55 0.18
I 0.32 -7.40 -2.87
I 4.91 -1.96 3.76
I 4.81 -2.85 -2.81
I 2.59 -5.09 0.80
I 7.10 0.06 0.18
I 4.61 1.89 -3.39
I 4.55 2.72 3.24
Na 6.80 -0.37 -2.93
Na 6.83 0.54 3.31
Na 4.60 2.20 -0.04
Na 2.42 -0.56 -3.06
Na 4.88 -2.38 0.43
Na 2.42 0.23 3.52
Na -0.09 2.00 -0.01
Na -2.49 3.73 -3.48
Na -2.44 4.58 2.99
Na -4.77 1.80 -0.04
Na -6.74 -0.95 -2.93
Na -6.85 -0.04 3.31
Na -2.36 -0.77 -3.06
Na -4.65 -2.79 0.43
Na -2.42 0.02 3.52
Na -2.08 -5.30 -2.77
Na 0.12 -2.74 0.45
Na 2.52 -5.11 -2.77
Na 0.31 -7.28 0.17
Na 2.80 -4.18 3.83
Na -2.43 -4.41 3.84
I 2.22 4.47 -0.35
I -0.28 6.41 -3.84
I -0.30 6.91 2.73
Na -0.28 6.48 -0.35
Na 2.04 4.78 2.98
Na 2.16 3.93 -3.48
Na -0.39 8.90 -5.52

--
NaI23-NaNa

--
I 1.67 -1.68 0.31
I -2.12 -1.66 3.11

I 4.31 -2.91 3.88
I 5.41 -1.85 -2.48
I -1.02 -0.80 -3.55
I 2.51 1.97 -2.51
I 1.64 1.29 4.16
I -1.24 2.02 0.30
I 5.51 1.29 1.34
I 1.65 -4.59 -3.60
I 0.52 -5.57 2.93
I -1.97 -4.60 -0.77
I 4.38 -5.72 0.10
I -5.75 -4.51 1.90
I -4.07 2.69 -3.60
I -5.29 1.84 2.93
I -4.69 -3.68 -4.39
I -4.93 -0.82 -0.77
I -4.52 5.61 0.10
I -1.80 4.88 3.88
I -0.51 5.70 -2.48
Na -4.96 4.94 3.18
Na -3.73 5.73 -2.98
Na -1.36 5.26 0.65
Na -2.12 1.53 3.44
Na -4.69 2.31 -0.33
Na -0.91 2.35 -2.98
Na 1.94 1.53 0.80
Na 4.57 0.13 4.21
Na 5.53 1.23 -1.95
Na 4.78 -2.57 0.65
Na 3.61 -5.99 3.18
Na 4.68 -4.99 -2.97
Na 0.98 -2.42 3.44
Na 1.13 -5.11 -0.33
Na 2.06 -1.44 -2.98
Na -2.68 -4.94 2.39
Na -1.73 -1.35 -0.26
Na -5.43 -1.43 2.39
Na -5.24 -4.11 -1.25
Na -4.34 -0.59 -3.96
Na -1.61 -4.08 -3.96
I 2.56 5.04 1.34
I 6.13 4.80 -2.07
Na 5.61 4.40 1.08
Na 2.51 5.08 -1.95
Na 1.22 4.42 4.21
Na 7.98 6.23 -3.99

--
NaI24-NaNa-3

--
I 0.00 2.33 0.00
I 1.96 0.00 3.59
I -2.65 4.70 3.15
I -2.13 4.66 -3.52
I 2.62 0.00 -3.25
I -1.96 0.00 -3.59
I -2.63 0.00 3.25
I 0.00 -2.33 0.00
I -4.72 2.44 -0.37
I 2.66 4.69 -3.15
I 2.14 4.66 3.52
I 4.73 2.42 0.37
I 0.01 7.07 0.00
I 6.59 -0.01 3.91
I 2.65 -4.70 -3.15
I 2.13 -4.67 3.52
I 7.35 -0.01 -2.69
I 4.72 -2.43 0.37
I -0.01 -7.07 -0.01
I -2.66 -4.70 3.15
I -2.14 -4.66 -3.53
Na -0.22 -6.73 3.13
Na 0.21 -6.73 -3.15
Na -2.31 -4.70 -0.21
Na -0.26 -2.39 3.31
Na 2.30 -4.70 0.21
Na 0.25 -2.39 -3.30
Na -2.34 0.00 -0.24
Na -4.75 2.34 2.81
Na -4.33 2.26 -3.69
Na -2.30 4.71 -0.21
Na -0.20 6.73 3.14
Na 0.22 6.73 -3.14
Na -0.25 2.39 3.31
Na 2.31 4.70 0.20
Na 0.26 2.39 -3.31
Na 4.34 2.25 3.70
Na 2.34 0.00 0.24
Na 4.33 -2.26 3.70
Na 6.77 -0.01 0.80
Na 4.75 -2.33 -2.81
Na 4.75 2.32 -2.80
I -4.73 -2.42 -0.37
I -7.34 0.00 2.69
I -6.59 0.01 -3.91
Na -6.77 0.01 -0.80
Na -4.34 -2.25 -3.70
Na -4.75 -2.33 2.80
Na -10.03 0.00 4.02
Na 10.05 0.00 -3.99

--
NaI24-NaNa

--
I 0.06 2.35 0.00
I 2.38 0.00 3.42
I -2.24 4.74 3.33
I -2.25 4.74 -3.33
I 2.38 0.00 -3.42
I -2.23 0.00 -3.42
I -2.23 0.00 3.42
I 0.06 -2.35 0.00
I -4.74 2.44 0.00
I 2.56 4.67 -3.36
I 2.56 4.67 3.35
I 4.79 2.43 0.00
I 0.18 7.11 0.00
I 7.07 0.00 3.22
I 2.57 -4.67 -3.35
I 2.57 -4.66 3.36
I 7.06 0.00 -3.22
I 4.79 -2.43 0.00
I 0.18 -7.11 0.01
I -2.24 -4.74 3.33
I -2.24 -4.75 -3.32
Na 0.26 -6.76 3.15
Na 0.26 -6.76 -3.14
Na -2.10 -4.79 0.00
Na 0.24 -2.40 3.30
Na 2.54 -4.70 0.00
Na 0.23 -2.41 -3.30
Na -2.15 0.00 0.00
Na -4.29 2.37 3.19
Na -4.29 2.37 -3.19
Na -2.10 4.78 0.00
Na 0.25 6.76 3.14
Na 0.25 6.76 -3.15
Na 0.23 2.41 3.31
Na 2.53 4.70 0.00
Na 0.23 2.40 -3.30
Na 4.84 2.23 3.24
Na 2.55 0.00 0.00
Na 4.84 -2.23 3.24
Na 7.08 0.00 0.00
Na 4.84 -2.23 -3.24
Na 4.84 2.23 -3.24
I -4.74 -2.44 0.00
I -6.91 0.00 3.46
I -6.90 -0.01 -3.46
Na -6.72 0.00 0.00
Na -4.29 -2.38 -3.18
Na -4.29 -2.37 3.19
Na -8.91 0.01 5.70
Na -8.89 -0.02 -5.72

--
NaI24-NaNa2

--
I -0.06 -2.35 0.00
I -2.38 0.00 3.42
I 2.25 -4.74 3.33
I 2.25 -4.74 -3.33
I -2.37 0.00 -3.42
I 2.23 0.00 -3.41
I 2.22 0.00 3.42
I -0.06 2.35 0.00
I 4.74 -2.44 0.00
I -2.56 -4.66 -3.36
I -2.56 -4.67 3.36
I -4.79 -2.43 0.00
I -0.18 -7.11 0.00
I -7.07 0.00 3.21
I -2.56 4.67 -3.36
I -2.57 4.66 3.36
I -7.06 0.00 -3.22
I -4.79 2.43 0.00
I -0.19 7.12 0.00
I 2.24 4.74 3.33
I 2.24 4.74 -3.32
Na -0.26 6.76 3.15
Na -0.26 6.76 -3.14
Na 2.10 4.79 0.00
Na -0.24 2.40 3.30
Na -2.54 4.70 0.00
Na -0.23 2.41 -3.30
Na 2.14 0.00 0.00
Na 4.29 -2.37 3.18
Na 4.29 -2.37 -3.19
Na 2.10 -4.78 0.00
Na -0.25 -6.76 3.14
Na -0.25 -6.76 -3.15
Na -0.23 -2.41 3.31
Na -2.54 -4.71 0.00
Na -0.23 -2.40 -3.30
Na -4.84 -2.23 3.24
Na -2.55 0.00 0.00
Na -4.84 2.23 3.24
Na -7.08 0.00 0.00
Na -4.84 2.23 -3.24
Na -4.84 -2.23 -3.24
I 4.74 2.44 0.01
I 6.90 0.00 3.46
I 6.90 0.01 -3.46
Na 6.72 0.00 0.00
Na 4.29 2.37 -3.18
Na 4.29 2.37 3.19
Na 8.91 0.00 5.70
Na 8.90 0.02 -5.71

--
NaI25-NaNa-2

--
I 1.05 -2.41 0.00
I 2.74 0.37 -3.40
I -0.94 -5.06 -3.31
I -0.94 -5.06 3.31
I 2.75 0.37 3.40
I -1.80 -0.40 3.31
I -1.80 -0.40 -3.30
I -0.02 2.27 0.00
I -3.73 -3.16 0.00
I 3.81 -4.21 3.37
I 3.81 -4.21 -3.37
I 5.62 -1.61 0.00
I 1.87 -7.03 0.00
I 7.36 1.22 -3.22
I 2.08 4.99 3.35
I 2.08 4.99 -3.35
I 7.36 1.22 3.22
I 4.68 3.19 0.00
I -0.66 7.03 0.00
I -2.69 4.26 -3.28
I -2.69 4.26 3.28
Na -0.53 6.67 -3.16
Na -0.53 6.67 3.15
Na -2.50 4.39 0.00
Na 0.21 2.36 -3.30
Na 2.07 5.03 0.00
Na 0.21 2.36 3.30
Na -1.47 -0.59 0.00
Na -3.45 -3.13 -3.25
Na -3.45 -3.12 3.26
Na -0.77 -5.12 0.00
Na 1.86 -6.65 -3.15
Na 1.86 -6.65 3.15
Na 1.12 -2.40 -3.31
Na 3.84 -4.29 0.00
Na 1.12 -2.40 3.31
Na 5.60 -1.40 -3.25
Na 2.98 0.38 0.00
Na 4.78 3.00 -3.25
Na 7.40 1.21 0.00
Na 4.78 3.01 3.25
Na 5.60 -1.40 3.25
I -5.34 2.10 0.00
I -6.35 -1.13 -3.29
I -6.35 -1.13 3.29
Na -6.09 -1.08 0.00
Na -4.27 1.55 3.28
Na -4.27 1.54 -3.28
Na -9.37 -1.54 -2.98
Na -9.37 -1.53 2.99
Na -8.37 2.57 -0.01
I -9.59 -0.36 0.00

--
NaI25-NaNa

--
I 1.91 0.06 0.78
I -1.32 -2.51 3.34
I 2.83 2.26 5.08
I 5.13 2.68 -2.22
I 0.70 -2.17 -3.24
I 0.52 2.47 -3.07
I -1.49 2.02 3.51
I -2.60 -0.12 -0.52
I 1.83 4.71 1.08
I 5.24 -2.31 -1.89
I 3.10 -2.51 4.75
I 2.12 -4.64 0.75
I 6.18 0.21 2.35
I -1.09 -7.16 3.00
I -3.81 -2.48 -4.48
I -5.74 -2.78 1.94
I 0.74 -6.88 -3.14
I -2.55 -4.80 -0.70
I -7.18 -0.29 -1.85
I -5.94 2.02 2.10
I -4.05 2.31 -4.31
Na -7.76 -0.46 1.28
Na -5.97 -0.21 -4.76
Na -5.03 2.06 -1.06
Na -3.68 -0.35 2.66
Na -4.83 -2.58 -1.25
Na -1.78 -0.06 -3.69
Na -0.56 2.24 0.34
Na 0.49 4.43 4.36
Na 2.48 4.69 -2.01
Na 3.79 2.36 2.07
Na 4.97 -0.08 5.38
Na 6.93 0.29 -0.67
Na 0.79 -0.24 4.17
Na 4.05 -2.29 1.67
Na 2.73 0.11 -2.37
Na 0.90 -4.87 3.82
Na -0.37 -2.48 0.13
Na -3.35 -4.99 2.47
Na -0.20 -7.03 -0.05
Na -1.50 -4.70 -3.75
Na 2.66 -4.58 -2.37
I -2.90 4.57 -0.34
I -1.68 6.62 3.67
I 0.18 7.22 -2.61
Na -0.74 6.65 0.72
Na -1.96 4.47 -3.36
Na -3.77 4.29 2.90
Na 7.68 2.67 -4.01
I 9.07 0.13 -3.05
Na 7.93 -2.71 -3.43
Na -0.07 9.99 -3.73

--
NaI26-NaNa

--
I -1.71 2.22 -0.17
I -2.76 -0.90 -3.50
I 0.03 4.95 -3.53
I -0.54 5.44 3.09
I -3.27 -0.53 3.28
I 1.03 1.05 3.55
I 1.76 0.45 -3.09
I 0.14 -2.16 0.25
I 2.74 3.83 0.16
I -5.04 3.78 2.83
I -4.51 3.39 -3.84
I -6.13 0.72 -0.45
I -3.30 6.66 -0.58
I -7.09 -2.57 -3.56
I -1.81 -4.93 3.65
I -1.08 -5.27 -3.02
I -7.62 -2.18 2.82
I -4.35 -3.84 -0.04
I 1.64 -6.59 0.78
I 3.97 -4.11 -2.64
I 2.71 -3.32 4.07
Na 1.68 -6.49 -2.36
Na 1.07 -6.08 3.90
Na 2.93 -3.64 0.83
Na 0.02 -2.28 -3.02
Na -1.45 -5.13 0.37
Na -0.41 -1.98 3.58
Na 1.14 0.92 0.20
Na 2.84 3.53 -3.12
Na 2.28 4.01 3.38
Na -0.38 5.23 -0.22
Na -2.97 6.13 -3.68
Na -3.52 6.52 2.59
Na -1.57 2.08 -3.46
Na -4.78 3.64 -0.51

Na -2.08 2.48 3.13
Na -5.86 0.35 -3.65
Na -3.22 -0.76 -0.08
Na -4.24 -3.85 -3.27
Na -7.39 -2.36 -0.37
Na -4.79 -3.47 3.19
Na -6.35 0.72 2.80
I 4.90 -0.92 0.79
I 5.89 2.31 -2.78
I 5.43 2.63 3.79
Na 5.56 2.37 0.47
Na 3.83 -0.33 3.93
Na 4.68 -0.74 -2.55
Na 8.85 1.45 -2.53
Na 8.46 3.11 3.54
Na 8.01 -1.33 0.53
I 8.93 1.69 0.76
I 8.14 -1.75 -2.59
Na 6.86 -4.35 -3.71

KI

KI14-KK2 " -
611.307795505"
KI15-KK2 " -
650.989879300"
KI16-KK2 " -
690.691057219"
KI17-KK3 " -
730.334668618"
KI18-KK-4 " -
770.052397648"
KI18-KK2 " -
770.028091044"
KI18-KK-2 " -
770.010002899"
KI19-KK-2 " -
809.691243180"
KI20-KK-2 " -
849.391545820"
KI20-2KK " -
849.386762128"
KI21-KK-4 " -
889.083924340"
KI21-KK-3 " -
889.070678236"
KI21-KK2 " -
889.061472968"
KI21-KK " -
889.050801304"
KI21-KK-2 " -
889.044123935"
KI22-KK-3 " -
928.753546694"
KI22-KK-2 " -
928.730184464"
KI22-KK " -
928.725602986"
KI22-KK-5 " -
928.713538913"
KI23-KK-2 " -
968.422517429"
KI23-KK " -
968.405297260"
KI24-KK-3 " -
1008.08733972"
KI24-KK2 " -
1008.07129067"
KI25-KK-2 " -
1047.74872937"

--

KI14-KK2

--
I 4.08 0.60 -2.92
I -1.06 -2.69 -2.64
I -0.73 2.90 2.26
I 5.34 2.33 1.86
I 3.71 -4.21 -1.05
I 0.99 -1.57 2.11
I 7.68 -1.40 0.65
I 1.57 5.76 -1.26
I -1.15 2.04 -3.21
K 1.99 3.42 -3.74
K -1.89 4.83 -0.87
K -2.98 -0.46 -4.84
K 7.02 1.63 -1.30
K 2.44 4.49 1.81
K 7.85 0.58 3.57
K 2.28 -2.38 -3.71
K 7.09 -4.69 -0.46
K 3.97 -0.88 0.49
K 0.23 -4.60 0.33
K -1.44 0.09 -0.11
K -0.30 0.34 4.74
K -4.44 -2.99 3.70
K -4.41 2.28 3.04
K -6.82 1.19 -1.37
K -4.55 -3.59 -1.35
I -6.05 -1.34 -3.66
I -3.57 -0.14 5.54
I -3.03 -5.22 1.39
I -5.15 3.93 0.01
I -4.81 -0.73 0.94

--
KI15-KK2

--
I 3.25 0.00 -2.52
I -1.74 -2.44 -3.17
I 6.76 2.70 0.18
I -0.29 2.46 1.79
I 3.87 0.00 3.26
I 2.56 -5.21 -1.42
I -0.29 -2.46 1.79
I 6.76 -2.70 0.18
I 2.56 5.21 -1.42
I -1.74 2.44 -3.17
K 5.83 6.05 -0.53
K 1.59 2.90 -3.88
K -1.37 4.99 -0.52
K -3.90 0.00 -4.67
K 6.75 0.00 -2.10
K 3.07 2.36 0.73
K 7.26 0.00 2.64
K 1.59 -2.90 -3.88
K 5.83 -6.05 -0.53
K 3.06 -2.36 0.73
K -1.37 -4.99 -0.52
K -1.91 0.00 -0.36
K 0.49 0.00 4.39
K -3.72 -2.58 3.45
K -3.72 2.58 3.45
K -6.69 2.59 -0.69
K -6.69 -2.59 -0.69
I -6.92 0.00 -3.07
I -2.72 0.00 5.65
I -4.56 -4.88 0.86
I -4.56 4.88 0.86
I -5.12 0.00 1.28

--
KI16-KK2

--
I 1.35 0.13 0.00
I -1.08 5.00 0.02
I 6.25 2.18 0.01
I 3.81 -4.67 -0.02
I -3.02 -2.47 -0.01
I 0.39 -3.45 -3.67
I 2.79 3.37 -3.59
I -2.32 1.32 -3.64
I 4.94 -1.22 -3.64
I 0.39 -3.49 3.64
I 2.79 3.34 3.62
I -2.32 1.29 3.65
I 4.94 -1.26 3.63
K 6.14 2.04 3.55
K 3.77 -4.60 3.52
K 1.53 -0.10 3.66
K -2.99 -2.55 3.65
K -0.49 4.33 3.57
K 4.96 -1.24 -0.01
K 0.42 -3.48 -0.02
K 3.77 -4.56 -3.56
K 2.90 3.41 0.01
K 6.14 2.08 -3.53
K 1.53 -0.07 -3.66
K -0.49 4.36 -3.54
K -2.18 1.09 0.01
K -3.00 -2.51 -3.67
K -5.97 1.28 -3.16
K -6.55 -3.38 -0.01
K -5.96 1.25 3.17
K -4.41 6.13 0.03
I -6.48 -2.10 -3.26
I -6.48 -2.13 3.25
I -5.63 2.92 0.01

--
KI17-KK3

--
I 3.25 -0.18 0.93
I -1.89 -0.33 2.98
I 6.43 0.10 -2.49
I -1.05 -0.13 -2.85
I 2.37 3.67 -2.94
I 1.54 3.19 4.28
I -0.74 5.21 0.23
I 4.61 5.57 0.64
I 2.73 -3.48 -3.40
I 1.99 -3.99 3.93
I -0.83 -4.69 -0.09
I 6.04 -4.40 0.57
K 4.77 -6.05 3.44
K 6.18 -3.55 -3.04
K 2.43 -3.63 0.23
K -0.88 -3.92 -3.56
K -1.72 -4.22 3.27
K 6.64 -0.96 0.86
K 2.57 0.01 -2.92
K 5.87 3.62 -2.24
K 1.45 -0.42 4.08
K 3.78 5.83 4.07
K 1.96 3.01 0.71
K -2.05 3.42 3.18
K -2.99 -1.82 -0.23
K -1.40 3.44 -2.89
K -6.55 3.31 -0.49
K -4.81 -0.04 -3.92
K -6.77 -3.90 -0.78
K -5.64 -0.26 3.02
I -5.10 -3.71 2.33
I -4.79 3.45 -3.52

I -5.50 3.25 2.85
I -4.39 -3.50 -3.36
I -6.36 -0.28 -0.59
K 1.89 6.91 -1.36

--
KI18-KK-4

--
I -2.23 -0.23 0.04
I 1.28 2.96 1.93
I -5.41 1.11 4.02
I -5.92 -3.53 -1.60
I 1.00 -1.57 -3.99

I -1.12 -5.20 -0.66
I -0.66 -0.63 5.02
I 2.48 -1.96 1.14
I -4.24 -3.86 3.26
I -4.09 0.06 -4.70
I -3.42 4.71 0.86
I -0.18 3.41 -3.24
I -7.06 1.50 -0.83
I 3.21 6.65 -0.70
I 5.65 -3.65 -2.36
I 5.97 1.35 3.13
I 4.60 1.68 -2.11
I 8.97 -2.28 1.27
K 9.10 -0.01 3.84
K 8.68 -4.79 -1.01
K 2.57 0.33 3.98
K -3.98 -1.51 5.89
K -0.91 -2.89 2.19
K 5.80 -0.95 0.29
K 2.13 -4.26 -1.59
K -4.42 -5.97 0.45
K 4.59 4.00 1.14
K 4.48 -1.06 -4.37
K 1.10 0.75 -0.96
K -2.60 -2.60 -2.69
K -2.08 2.03 2.95
K -5.65 -1.19 1.20
K -6.65 3.67 1.92
K -7.28 -0.85 -3.44
K -3.73 2.45 -1.93
K -0.14 5.71 0.01
K -0.94 0.95 -5.69
K 3.15 4.70 -3.50

--
KI18-KK2

--
I -2.09 0.00 -0.16
I 1.49 -3.73 0.29
I -5.75 -3.66 -0.55
I -5.75 3.66 -0.55
I 1.49 3.73 0.29
I -1.65 3.66 -3.79
I -1.65 -3.66 -3.78
I 2.02 0.00 -3.44
I -5.30 0.00 -4.21
I -2.53 3.67 3.50
I -2.53 -3.66 3.50
I 1.00 0.00 3.99
I -6.19 0.00 3.06
K -6.02 -3.52 2.98
K -6.02 3.52 2.97
K -2.57 0.00 3.52
K 1.01 3.62 4.00
K 1.01 -3.62 4.00
K -5.76 0.00 -0.55
K -2.14 3.66 -0.10

K -5.20 3.51 -4.02
K -2.14 -3.66 -0.10
K -5.20 -3.52 -4.02
K -1.71 0.00 -3.76
K 1.81 -3.56 -3.22
K 1.48 0.00 0.40
K 1.81 3.56 -3.22
K 5.47 0.00 -2.77
K 4.96 3.54 0.93
K 4.58 0.00 4.53
K 4.96 -3.54 0.93
I 4.55 -3.55 4.37
I 5.59 3.78 -2.83
I 5.59 -3.78 -2.83
I 4.55 3.55 4.37
I 5.24 0.00 0.72
K 7.51 6.36 -3.96
K 7.51 -6.36 -3.97

--
KI18-KK-2

--
I 1.92 0.10 -0.01
I -1.45 -2.32 3.10
I 5.87 -1.94 2.65
I 5.34 2.24 -3.17
I -2.01 2.01 -2.91
I 1.52 5.06 -0.75
I 2.03 0.98 4.93
I -2.10 2.87 2.26
I 6.79 2.98 1.69
I 1.64 -0.82 -5.15
I 2.15 -5.07 0.77
I -1.65 -3.20 -2.08
I 5.61 -2.87 -2.43
I -4.98 -5.40 1.03
I -5.98 4.62 -0.64
I -5.23 0.32 5.24
I -5.47 -1.30 -4.79
I -5.54 -0.45 0.21
K 10.22 2.87 1.44
K -8.65 6.69 -0.98
K -1.72 0.57 5.19
K 5.48 0.95 4.58
K 1.34 2.93 2.09
K -5.60 2.31 2.40
K -2.19 4.78 -0.74
K 5.01 4.92 -0.97
K -5.14 -2.61 3.18
K -5.57 1.49 -2.73
K -1.88 -0.29 0.08
K 1.57 2.09 -3.05
K 2.08 -2.16 2.89
K 5.47 0.01 -0.35
K 5.61 -4.85 0.53
K 5.12 -0.73 -5.21
K 1.89 -3.01 -2.22
K -1.48 -5.28 0.91
K -1.96 -1.11 -4.99
K -5.32 -3.47 -1.92

--
KI19-KK-2

--
I -2.00 -0.49 -0.05
I 0.15 2.76 3.22
I -6.18 -0.68 3.18
I -4.41 -3.54 -3.34
I 1.88 -0.26 -3.16
I 0.53 -5.36 -1.33
I -1.39 -1.81 4.96

I 3.00 -2.32 2.26
I -3.74 -4.99 1.70
I -2.90 1.12 -5.00
I -4.51 3.90 1.54
I -0.71 4.41 -1.81
I -6.89 0.69 -1.72
I 1.80 7.22 1.56
I 6.56 -1.18 -1.34
I 4.77 1.65 4.90
I 3.38 4.40 -4.76
I 4.19 3.11 0.02
I 5.63 -5.93 -0.54
K 2.96 -7.81 -1.81
K 8.33 -4.05 -1.99
K 5.13 -4.96 2.86
K 1.64 0.09 5.08
K 5.66 0.50 1.77
K 3.33 -2.85 -1.30
K -0.60 -3.24 1.79
K -4.58 -3.35 4.77
K -3.07 -6.16 -1.50
K -5.32 -2.08 -0.04
K -7.55 2.12 1.47
K -5.97 -0.65 -4.83
K -3.00 1.09 3.22
K -3.79 2.59 -1.75
K -1.39 -1.63 -3.40
K -1.39 5.73 1.56
K 0.88 1.72 -0.15
K 3.34 4.59 3.31
K 2.61 6.07 -1.68
K 4.95 1.74 -3.17
K 0.19 2.98 -4.98

--
KI20-KK-2

--
I -2.53 -0.44 -0.02
I 0.34 2.59 2.75
I -5.05 -1.89 4.27
I -5.48 -3.66 -2.83
I -0.28 1.35 -4.56
I -0.36 -3.94 -3.06
I 0.26 -2.66 4.30
I 2.70 -1.05 -0.16
I -2.83 -5.49 1.21
I -5.44 1.26 -3.98
I -4.76 3.08 3.01
I -2.31 4.69 -1.42
I -7.75 -0.17 0.29
I 0.62 7.52 1.85
I 5.25 0.14 -4.28
I 5.42 2.47 2.62
I 2.90 4.21 -1.71
I 8.09 -0.78 -0.12
I 5.44 -2.36 4.11
I 5.65 -4.60 -2.59
K 3.07 -3.97 6.00
K 7.94 0.14 3.26
K 7.91 -2.07 -3.45
K 5.62 -3.26 0.60
K -2.86 -4.56 4.56
K -3.03 -6.13 -2.30
K 2.81 0.07 3.24
K 5.37 1.49 -0.89
K 2.91 -2.62 -3.58
K -0.20 -3.15 0.45
K 3.02 4.99 2.16
K 2.96 2.61 -4.97
K 0.16 1.84 -0.89
K -2.38 0.40 3.52
K -2.78 -1.30 -3.64
K -5.29 -2.79 0.69
K -7.35 0.75 3.66
K -7.89 -1.11 -3.12
K -5.05 2.18 -0.48
K -2.11 5.33 2.32
K -3.02 3.56 -4.73
K 0.51 6.91 -1.51

--
KI20-2KK

--
I 2.43 -0.58 -0.10
I -0.16 2.62 -3.25
I 5.90 -1.30 -3.94
I 5.13 -3.61 2.97
I -0.86 0.17 3.59
I -0.17 -5.13 2.02
I 0.81 -2.21 -4.78
I -2.77 -1.91 -1.30
I 3.54 -5.34 -1.72
I 4.18 1.24 4.49
I 4.81 3.49 -2.43
I 1.64 4.42 1.42
I 7.55 0.33 0.64
K 7.71 1.50 -2.70
K 7.06 -0.74 3.96
K 4.56 2.40 1.03
K 1.19 3.24 4.82
K 1.86 5.54 -2.04
K 5.57 -2.45 -0.52
K 2.24 -1.53 3.39
K 3.31 -6.25 1.64
K 2.87 0.68 -3.58
K 3.90 -3.97 -4.99
K 0.56 -3.36 -1.36
K -2.02 -0.09 -4.45
K -0.38 1.71 0.28
K -2.88 -2.47 2.34
K -5.37 0.63 -0.52
K -3.80 2.36 4.02
K -1.48 6.35 1.75
K -3.14 4.64 -2.83
I -1.18 7.28 -1.66
I -5.80 -0.45 2.88
I -5.20 1.66 -4.02
I -1.82 5.03 5.03
I -3.56 3.42 0.55
K -8.09 -2.85 1.93
K -8.45 0.45 -4.23
I -5.37 -5.27 1.57
I -8.00 -1.83 -1.57
K -2.84 -7.30 2.76
K -5.40 -4.19 -1.80

--
KI21-KK-4

--
I 2.51 -0.41 0.09
I 0.00 -4.18 2.88
I 5.24 0.97 4.22
I 5.09 3.12 -2.73
I 0.00 -2.13 -4.37
I 0.00 2.99 -2.79
I 0.00 1.18 4.48
I -2.51 -0.41 0.08
I 2.54 4.76 1.67
I 5.28 -1.74 -4.17
I 5.29 -3.81 2.85
I 2.83 -5.34 -1.40
I 7.82 -0.25 0.03
I -5.27 -1.74 -4.17
I -5.29 -3.81 2.85
I -2.82 -5.34 -1.40
I -7.82 -0.25 0.02
I -5.24 0.97 4.22
I -5.09 3.11 -2.73
I -2.54 4.76 1.66
I 0.00 7.88 -1.85
K 7.76 -1.34 3.37
K 7.64 0.76 -3.36
K 2.93 -4.23 -4.73
K 2.91 -6.18 1.98
K 5.28 -2.74 -0.66
K 5.14 2.13 0.73
K 2.59 -1.48 3.56
K 2.57 0.57 -3.48
K 0.00 -3.05 -0.74
K -2.92 -6.17 1.99
K -2.92 -4.23 -4.72
K 2.86 3.31 4.90
K 2.57 5.52 -2.28
K 0.00 2.15 0.78
K -2.57 0.57 -3.48
K -2.59 -1.48 3.55
K -5.28 -2.74 -0.66
K 0.00 7.30 1.50
K -2.86 3.31 4.90
K -2.57 5.52 -2.28
K -5.14 2.13 0.73
K -7.76 -1.34 3.37
K -7.64 0.75 -3.36

--
KI21-KK-3

--
I -2.32 -0.31 0.07
I 0.48 -3.72 -2.53
I -5.56 0.05 -4.03
I -5.28 3.15 2.52
I 0.88 -0.97 4.34
I -0.18 3.80 2.18
I -0.51 0.83 -4.66
I 2.70 0.54 -0.58
I -3.32 4.50 -2.23
I -4.47 -1.44 4.61
I -4.55 -4.58 -1.94
I -1.33 -5.11 2.28
I -7.46 -1.09 0.53
I 1.46 -8.25 -1.07
I 5.98 0.11 3.38
I 5.53 -2.74 -3.26
I 3.76 -4.28 1.60
I 7.65 1.39 -1.28
I 4.88 4.75 1.77
K 8.40 -0.83 -3.86
K 7.80 2.82 2.07
K 4.67 3.50 -1.54
K 2.35 -1.04 -3.86
K 5.62 -1.38 0.13
K 2.81 1.98 2.87
K -0.30 2.54 -1.36
K -3.50 2.57 -5.25
K -3.20 5.79 1.40
K -5.38 1.65 -0.77
K -7.43 -2.61 -2.64
K -7.29 0.50 3.67
K -2.55 -1.84 -3.26
K -4.48 -3.03 1.31
K -2.32 1.22 3.36
K -1.60 -6.47 -1.42
K 0.63 -2.27 0.82
K 3.52 -5.57 -2.07
K 1.61 -7.15 2.15
K 4.10 -2.45 4.66
K -1.68 -3.28 5.33
I 1.83 5.38 -2.31
I -1.11 8.47 0.53
K -1.06 7.33 -2.72
K 1.85 6.65 1.16

--
KI21-KK2

--
I -2.55 -0.70 0.00
I 0.17 1.60 3.72
I -5.39 -2.88 3.67
I -5.40 -2.88 -3.66
I 0.17 1.59 -3.72
I 0.04 -3.98 -3.77
I 0.04 -3.97 3.77
I 2.58 -1.28 0.00
I -3.06 -5.77 0.00
I -4.98 2.23 -3.66
I -4.98 2.23 3.65
I -2.28 4.50 0.00
I -7.79 -0.15 0.00
K -7.63 -0.07 3.54
K -7.64 -0.08 -3.53
K -5.03 2.26 0.00
K -2.21 4.55 -3.62
K -2.21 4.56 3.61
K -5.47 -2.89 0.00
K -2.69 -0.49 -3.66
K -3.22 -5.57 -3.49
K -2.68 -0.49 3.66
K -3.22 -5.57 3.50
K -0.30 -3.45 0.00
K 2.62 -0.95 3.56
K 0.15 1.82 0.00
K 5.39 1.55 0.00
K 2.87 4.15 -3.63
K 0.52 6.90 0.00
K 2.88 4.16 3.62
I 0.52 6.74 3.55
I 5.28 1.43 -3.64
I 5.28 1.43 3.64
I 0.52 6.73 -3.56
I 2.97 4.10 0.00
K 7.75 -1.04 -3.54
K 7.75 -1.03 3.54
I 7.96 -1.09 0.00
I 5.22 -3.66 3.62
K 2.83 -5.50 5.27
K 2.62 -0.95 -3.56
K 5.40 -3.50 0.00
K 2.83 -5.51 -5.26
I 5.22 -3.67 -3.61

--
KI21-KK

--
I 0.00 4.95 -3.54
I -2.71 -0.51 -4.04
I 2.48 6.74 1.48
I -2.55 1.81 2.82
I 2.55 1.81 2.82
I 2.71 -0.51 -4.04
I 0.00 -1.64 0.18
I 4.81 3.33 -1.65
I -2.48 6.74 1.48
I -4.82 3.33 -1.65
I -7.96 -1.13 -3.38
I -2.54 -3.05 4.63
I -2.53 -5.47 -2.25
I -7.56 1.56 2.70
I -5.32 -2.23 0.50
I 0.00 -6.76 2.08
I 2.53 -5.47 -2.25
I 2.54 -3.05 4.63
K 0.00 -7.77 -1.32
K 0.00 -5.40 5.37
K 2.55 -4.36 1.23
K 0.00 -3.06 -3.16
K -2.55 -4.36 1.23
K 0.00 -0.67 3.72
K 3.02 0.34 -0.47
K 5.83 1.34 -4.38
K 5.24 4.06 1.91
K 2.88 6.17 -2.02
K 0.00 8.98 2.55
K 0.00 1.66 -4.80
K -2.88 6.17 -2.01
K 0.00 4.20 2.35
K -5.83 1.34 -4.38
K -3.02 0.34 -0.47
K -5.27 -3.38 -2.96
K -8.49 -0.52 0.03
K -5.11 -0.72 3.85
K -5.24 4.06 1.91
I 5.32 -2.22 0.50
I 7.96 -1.13 -3.38
I 7.56 1.56 2.70
K 8.49 -0.52 0.03
K 5.11 -0.72 3.85
K 5.27 -3.38 -2.96

--
KI21-KK-2

--
I 1.25 -3.31 1.76
I -3.10 0.38 3.46
I 4.27 -5.82 -1.96
I -1.36 -1.70 -3.29
I 3.57 -0.96 -2.26
I 2.23 0.81 4.92
I 0.17 1.95 0.06
I 6.00 -2.04 3.06
I -0.80 -6.62 -1.72
I -2.53 -4.50 4.92
I -4.37 -3.59 0.34
I -7.90 -0.59 2.34
I -1.86 3.12 -4.83
I -3.74 5.22 1.85
I -6.22 -2.50 -4.26
I -5.14 1.51 -1.33
I -0.49 6.99 -1.74
I 1.27 5.97 2.94
I 3.12 3.97 -3.75
K -1.44 7.88 1.53
K 0.35 5.86 -4.99
K 2.19 4.96 -0.44
K -1.10 3.26 3.20
K -2.92 4.28 -1.56
K 0.82 1.16 -3.50
K 2.96 -0.07 1.28
K 4.64 -1.38 6.17
K 6.27 -3.08 -3.26
K 4.48 -4.75 1.41
K 1.97 -8.39 -2.79
K -0.53 -1.70 4.60
K -1.82 -5.63 1.68
K 1.22 -3.63 -1.91
K -5.37 -2.58 3.73
K -2.55 -0.53 -0.03
K -6.01 2.36 2.11
K -7.26 -1.54 -1.00

K -4.19 0.35 -4.65
K -3.66 -4.53 -3.04
I 5.34 2.73 1.11
I 8.26 -0.49 -2.06
K 8.03 0.27 1.28
K 5.76 1.99 -2.57
K 3.82 3.97 4.10

--
KI22-KK-3

--
I -2.53 0.00 0.38
I 0.00 -2.54 -3.34
I -5.10 2.59 -3.38
I -5.29 2.49 3.90
I 0.00 -2.78 4.13
I 0.00 2.77 4.13
I 0.00 2.54 -3.34
I 2.53 0.00 0.38
I -2.55 5.39 0.42
I -5.29 -2.49 3.90
I -5.10 -2.59 -3.38
I -2.55 -5.39 0.42
I -7.74 0.00 0.15
I 0.00 -7.45 -3.83
I 5.29 -2.49 3.90
I 5.10 -2.59 -3.38
I 2.55 -5.39 0.42
I 7.74 0.00 0.15
I 5.10 2.59 -3.38
I 5.29 2.49 3.90
I 2.55 5.39 0.42
I 0.00 7.45 -3.82
K -2.89 -4.91 3.92
K 2.89 -4.91 3.92
K 2.62 0.00 3.99
K 7.78 0.00 3.66
K 2.89 4.91 3.92
K -2.89 4.91 3.92
K -7.78 0.00 3.65
K -2.62 0.00 3.99
K 0.00 -7.78 -0.44
K 5.18 -2.59 0.21
K 0.00 -2.66 0.29
K 5.18 2.59 0.21
K 0.00 2.66 0.29
K -5.18 2.59 0.21
K -5.18 -2.59 0.21
K 0.00 7.77 -0.44
K -2.58 5.07 -3.61
K 2.58 5.06 -3.61
K -2.56 0.00 -3.36
K -7.52 0.00 -3.38
K -2.58 -5.06 -3.61
K 2.56 0.00 -3.36
K 7.52 0.00 -3.38
K 2.58 -5.06 -3.61

--
KI22-KK-2

--
I -2.59 -0.77 0.00
I 0.00 1.89 3.72
I -5.49 -2.84 3.56
I -5.48 -2.84 -3.57
I 0.00 1.89 -3.71
I -0.01 -3.69 -3.65
I -0.01 -3.68 3.66
I 2.59 -0.78 0.00
I -2.61 -6.32 0.01
I -5.13 2.20 -3.64
I -5.13 2.20 3.64
I -2.57 4.60 0.00
I -8.03 -0.05 -0.01
I 0.01 7.10 3.57
I 5.14 2.19 -3.64
I 5.15 2.19 3.63
I 0.01 7.11 -3.55
I 2.58 4.59 0.00
I 8.02 -0.08 -0.01
I 5.48 -2.85 3.56
I 5.47 -2.86 -3.57
I 2.59 -6.32 0.01
K -0.01 -8.63 0.01
K 3.12 -5.35 -3.47
K -3.14 -5.35 -3.47
K -3.14 -5.34 3.48
K -5.66 -2.65 0.00
K -7.79 -0.05 -3.56
K -7.80 -0.05 3.55
K 3.12 -5.34 3.48
K -0.01 -3.32 0.00
K -2.69 -0.41 -3.65
K -5.23 2.31 0.00
K -2.69 -0.41 3.64
K 5.65 -2.67 0.00
K 2.69 -0.42 -3.64
K 2.70 -0.41 3.64
K 0.00 2.04 0.00
K -2.51 4.68 -3.62
K -2.51 4.68 3.62
K 0.01 7.23 0.01
K 2.52 4.68 -3.62
K 2.52 4.67 3.62
K 5.24 2.31 0.00
K 7.79 -0.08 -3.56
K 7.80 -0.07 3.55

--
KI22-KK

--
I 2.25 0.89 0.24
I 1.00 -2.89 3.48
I 5.11 2.99 3.78
I 3.78 4.46 -3.16
I -0.23 -1.56 -3.71
I -1.21 3.32 -2.69
I -0.31 2.27 4.89
I -2.78 -0.05 0.82
I 1.04 5.99 1.38
I 4.71 -0.53 -4.32
I 6.03 -1.98 2.69
I 3.38 -4.18 -1.01
I 7.40 1.81 -0.62
I 1.75 -7.70 2.28
I -5.19 -2.68 -3.15
I -4.24 -3.72 3.98
I 0.69 -6.45 -4.62
I -1.80 -5.18 -0.32
I -7.66 -1.12 1.12
I -6.14 2.37 -2.60
I -3.94 4.72 2.44
I -2.34 7.91 -2.34
K -7.70 -3.27 3.88
K -7.99 -0.69 -2.51
K -4.58 -3.13 0.34
K -2.22 -4.65 -3.91
K -1.11 -5.88 3.13
K 1.26 -7.18 -1.21
K 3.95 -4.96 2.46
K 2.74 -3.59 -4.54
K 0.42 -2.29 -0.18
K -3.13 0.28 -2.97
K -1.84 -1.04 4.14
K -5.76 2.00 0.89
K -4.15 5.19 -3.56
K -0.73 2.85 0.94
K 1.80 1.39 -3.44
K 5.40 -1.25 -0.84
K 3.18 -0.08 3.61
K -3.12 4.14 5.73
K -2.23 7.56 1.06
K 0.85 6.33 -2.50
K 2.29 4.79 4.48
K 4.50 3.74 0.25
K 6.60 2.41 -4.02
K 7.94 0.99 2.77

--
KI22-KK-5

--
I 0.53 -3.88 1.09
I 2.21 -0.63 -3.55
I -1.82 -6.54 -2.67
I 2.86 0.72 3.56
I -2.00 -0.82 4.28
I -2.73 -1.60 -2.95
I -0.53 1.86 -0.08
I -4.80 -4.00 1.26
I 4.49 -4.21 4.46
I 3.30 -5.59 -2.79
I 5.66 -1.91 0.02
K 1.04 -7.84 -4.22
K 6.21 -5.74 6.98
K 3.94 -4.86 0.71
K 6.02 -0.93 3.41
K 5.31 -2.46 -3.55
K -2.12 -6.17 0.80
K 1.21 -2.29 4.20
K -5.03 -2.60 4.61
K 0.28 -3.45 -2.59
K -4.92 -4.40 -2.63
K -2.75 -0.92 0.65
K -0.80 1.39 -3.76
K 2.74 0.34 -0.10
K -0.40 2.55 3.50
K 1.41 5.04 -0.83
K 4.78 3.87 2.78
K 7.62 1.36 -0.77
K 4.21 2.48 -4.34
I 7.11 0.47 -4.16
I 1.60 5.52 2.80
I 1.18 4.34 -4.41
I 7.78 1.94 2.75
I 4.56 3.32 -0.80
K -1.39 7.36 2.52
K -1.80 6.24 -4.45
I -1.64 7.01 -0.99
I -3.81 3.37 -3.97
I -3.46 4.56 3.24
I -7.80 -0.66 4.14
I -7.74 -2.39 -2.72
I -5.69 1.19 0.24
K -3.54 4.00 -0.40
K -6.27 2.44 3.54
K -5.80 0.50 -3.32
K -7.90 -1.67 0.72

--
KI23-KK-2

--
I 0.49 -2.55 0.26
I 3.05 0.07 -3.31
I -1.97 -5.17 -3.61
I -2.35 -5.20 3.70
I 3.03 0.06 4.17
I -2.30 -0.05 3.83
I -2.05 -0.04 -3.63
I 0.38 2.57 0.26
I -4.76 -2.73 -0.07
I 2.74 -5.27 3.95
I 3.23 -5.07 -3.31
I 5.81 -2.47 0.60
I 0.49 -7.75 0.13
I 7.98 0.18 -3.48
I 2.50 5.38 3.96
I 3.01 5.21 -3.30
I 5.70 2.72 0.61
I 0.14 7.77 0.14
I -2.19 5.08 -3.60
I -2.58 5.08 3.70
K 0.35 7.54 -3.37
K -0.18 7.66 3.65
K -2.33 5.09 0.08
K 0.47 2.59 -3.41
K 2.82 5.28 0.30
K 0.09 2.62 3.90
K -2.20 -0.05 0.14
K -4.46 -2.66 -3.61
K -4.88 -2.66 3.63
K -2.10 -5.19 0.07
K 0.68 -7.51 -3.37
K 0.16 -7.66 3.64
K 0.58 -2.56 -3.42
K 3.05 -5.15 0.30
K 0.21 -2.62 3.90
K 5.64 -2.47 -3.35
K 3.04 0.07 0.37
K 5.53 2.71 -3.34
K 8.15 0.18 -0.08
K 4.99 3.04 4.08
K 5.12 -2.82 4.08
I -4.88 2.52 -0.07
I -7.28 -0.15 -3.83
I -7.39 -0.17 3.44
K -7.22 -0.16 -0.04
K -4.99 2.43 3.63
K -4.57 2.47 -3.60
K -10.14 -0.19 -5.68

--
KI23-KK

--
I 0.13 2.60 0.32
I 3.14 -0.41 3.31
I -0.87 5.56 4.30
I -2.70 5.65 -2.71
I 1.46 -0.19 -3.93
I -3.46 0.46 -2.68
I -2.06 0.28 4.60
I -0.56 -2.54 0.32
I -5.05 3.29 1.58
I 2.28 4.86 -3.94
I 4.02 4.67 3.16
I 5.20 1.95 -0.95
I 1.08 7.78 0.15
I 8.06 -1.08 1.94
I 0.93 -5.28 -3.94
I 2.65 -5.55 3.17
I 6.43 -0.86 -4.98
I 4.51 -3.25 -0.94
I -1.00 -7.79 0.16
I -2.30 -5.13 4.31
I -4.09 -4.74 -2.70
K -0.02 -7.77 3.56
K -1.74 -7.43 -3.27
K -3.15 -5.00 0.79
K 0.50 -2.75 3.81
K 1.80 -5.45 -0.39
K -1.19 -2.46 -3.29
K -2.60 0.35 0.92
K -3.53 3.50 4.86
K -5.30 3.41 -2.09
K -1.73 5.65 0.78
K 2.03 7.51 3.55
K 0.27 7.63 -3.28
K 1.21 2.53 3.81
K 3.17 4.79 -0.40
K -0.50 2.69 -3.29
K 6.08 1.75 2.55
K 2.44 -0.32 -0.35
K 5.41 -3.28 2.56
K 7.35 -0.98 -1.55
K 3.74 -3.05 -4.48
K 4.41 1.96 -4.48
I -5.73 -1.85 1.59
I -8.39 1.09 -2.15
K -7.73 1.03 1.36
K -6.00 -1.91 -2.08
K -4.31 -2.43 4.87
K -10.86 1.34 -4.51

--
KI24-KK-3

--
I 0.00 -2.58 0.00
I 2.03 0.00 -4.01
I -3.07 -5.15 -3.31
I -2.13 -5.13 3.96
I 3.06 0.00 3.39
I -2.03 0.00 4.01
I -3.06 0.00 -3.39
I 0.00 2.58 0.00
I -5.18 -2.65 0.64
I 3.06 -5.16 3.31
I 2.13 -5.13 -3.97
I 5.17 -2.65 -0.64
I 0.00 -7.75 0.00
I 7.07 0.00 -4.56
I 3.07 5.16 3.31
I 2.13 5.13 -3.97
I 8.22 0.00 2.64
I 5.18 2.65 -0.64
I 0.00 7.75 0.00
I -3.06 5.16 -3.31
I -2.13 5.13 3.96
K -0.42 7.51 -3.49
K 0.43 7.51 3.49
K -2.56 5.17 0.34
K -0.46 2.59 -3.64
K 2.56 5.17 -0.35
K 0.46 2.59 3.64
K -2.56 0.00 0.36
K -5.45 -2.58 -2.89
K -4.60 -2.55 4.29
K -2.56 -5.17 0.34
K -0.43 -7.51 -3.49
K 0.42 -7.51 3.49
K -0.46 -2.59 -3.64
K 2.56 -5.17 -0.34
K 0.46 -2.59 3.64
K 4.60 -2.55 -4.30
K 2.56 0.00 -0.36
K 4.60 2.55 -4.29
K 7.50 0.00 -1.10
K 5.45 2.58 2.89
K 5.45 -2.58 2.89
I -5.17 2.65 0.64

I -8.22 0.00 -2.63
I -7.06 0.00 4.56
K -7.50 0.00 1.10
K -4.60 2.55 4.29
K -5.45 2.58 -2.89
K -11.34 0.00 -3.96
K 11.33 0.00 3.98

--
KI24-KK2

--
I -0.16 -2.59 0.00
I -2.73 0.00 3.73
I 2.38 -5.20 3.66
I 2.38 -5.20 -3.66
I -2.73 0.00 -3.73
I 2.39 0.00 -3.73
I 2.39 0.00 3.73
I -0.16 2.59 0.00
I 5.08 -2.66 0.00
I -2.84 -5.14 -3.67
I -2.84 -5.14 3.67
I -5.37 -2.66 0.00
I -0.23 -7.79 0.00
I -7.82 0.01 3.56
I -2.84 5.14 -3.67
I -2.84 5.14 3.67
I -7.82 0.00 -3.56
I -5.37 2.66 0.00
I -0.22 7.79 0.00
I 2.39 5.19 3.66
I 2.39 5.19 -3.66
I 5.08 2.65 0.00
I 7.53 0.00 3.77
I 7.53 -0.01 -3.78
K 9.76 0.00 6.35
K 9.75 0.00 -6.36
K 7.38 0.00 0.00
K 4.74 -2.62 3.56
K 4.74 -2.62 -3.55
K 2.31 -5.23 0.00
K -0.31 -7.54 3.52
K -0.31 -7.54 -3.51
K 4.75 2.61 3.55
K 4.75 2.61 -3.55
K 2.31 0.00 0.00
K -0.29 -2.60 3.66
K -0.29 -2.60 -3.66
K -2.87 -5.17 0.00
K -0.29 2.60 3.66
K 2.32 5.22 0.00
K -0.29 2.60 -3.66
K -2.87 0.00 0.00
K -5.39 -2.54 3.61
K -5.39 -2.54 -3.61
K -7.92 0.01 0.00
K -5.39 2.55 3.61
K -5.39 2.55 -3.61
K -2.86 5.17 0.00
K -0.30 7.54 3.52
K -0.30 7.54 -3.52

--
KI25-KK-2

--
I 1.21 -2.66 0.00
I 3.13 0.42 -3.71
I -1.01 -5.54 -3.65
I -1.00 -5.54 3.64
I 3.12 0.42 3.71
I -1.92 -0.46 3.62
I -1.92 -0.45 -3.62
I 0.08 2.52 0.00
I -4.01 -3.46 0.00
I 4.17 -4.64 3.67
I 4.18 -4.64 -3.67
I 6.25 -1.75 0.00
I 2.04 -7.70 0.00
I 8.14 1.32 -3.55
I 2.32 5.49 3.66
I 2.33 5.49 -3.66
I 8.13 1.32 3.56
I 5.26 3.50 0.00
I -0.70 7.68 0.00
I -2.86 4.67 -3.63
I -2.86 4.67 3.63
I -5.70 2.28 0.00
I -6.95 -1.22 -3.60
I -6.94 -1.23 3.60
I -10.35 -0.32 0.00
K -10.36 -1.66 -3.33
K -9.09 3.02 -0.01
K -10.36 -1.65 3.34
K -6.66 -1.20 0.00
K -3.83 -3.45 -3.64
K -4.69 1.69 -3.69
K -4.69 1.69 3.69
K -2.74 4.74 0.00
K -0.56 7.44 -3.53
K -0.57 7.44 3.53
K -3.83 -3.45 3.64
K -1.60 -0.62 0.00
K 0.27 2.55 3.66
K 0.27 2.55 -3.66
K 2.35 5.53 0.00
K 5.31 3.39 -3.61
K 5.31 3.39 3.62
K 3.33 0.42 0.00
K 1.22 -2.59 -3.67
K 1.22 -2.59 3.67
K -0.89 -5.60 0.00
K 2.05 -7.42 -3.52
K 2.05 -7.42 3.52
K 4.27 -4.72 0.00
K 6.21 -1.63 3.62
K 6.22 -1.63 -3.62
K 8.26 1.33 0.00

RbI

"RbI14-RR-2 " " " -542.92
RbI14-RR2 " -
542.919337130"
RbI14-RR-3 " -
542.897518358"
RbI15-RR2 " -
578.322163885"
RbI16-RR2 " " " " -613.75
RbI16-RbRb-3 " -
613.718266952"
RbI17-RbRb " -
649.149329824"
RI17-RR3 " -
649.115752693"
RbI18-RR2 " " -684.53
RbI19-RbRb-2 " -
719.919936213"
RbI20-2RR " " -755.34
RbI21-RbRb-2 " -
790.720625105"
RbI21-RbRb " -
790.726901004"
RbI22-RbRb-4 " -
826.155520881"
RbI22-RR-2 " -
826.130439048"
RbI22-RR " -
826.126447746"
RbI22-RbRb-5 " -
826.114499396"
RbI22-RR2 " -
790.738202542"
RbI23-RbRb-2 " -
861.547924985"
RbI24-RbRb-3 " -
896.937812588"
RbI24-RbRb " -
896.922039113"

--
RbI14-RR-2

--
I -2.26 2.11 -2.75
I 3.26 1.62 -3.01
I -8.29 -0.19 0.42
I -1.91 -1.82 1.45
I -4.44 2.94 2.35
I 1.17 6.54 -1.47
I 0.99 2.57 1.99
I -4.98 -2.96 -2.66
I 0.45 -2.69 -3.51
I 6.26 -3.54 -2.19
I 0.75 -0.97 6.03
I 6.28 2.07 2.07
I 0.59 -6.43 0.97
I 3.63 -2.34 1.81
Rb 2.01 10.02 -1.06
Rb 0.67 3.92 -4.13
Rb -1.71 4.42 0.27
Rb -8.05 2.44 2.85
Rb -8.48 -3.17 -1.58
Rb -4.61 0.09 -0.28
Rb -2.60 -1.09 -4.75
Rb -1.72 0.89 4.11
Rb 3.89 3.84 -0.02
Rb 1.12 -0.46 -0.42
Rb -1.85 -4.67 -1.10
Rb 3.98 -1.80 -4.40
Rb 0.61 -3.85 3.66
Rb 3.58 0.61 4.24
Rb 7.02 -1.19 0.55
Rb 3.97 -5.60 -0.14

--
RbI14-RR2

--
I 4.62 0.78 -2.86
I -1.94 -2.27 -2.86
I -0.53 2.98 2.71
I 5.86 1.54 2.45
I 3.11 -4.16 -1.82
I 0.65 -1.68 1.80
I 7.77 -2.30 0.41
I 2.52 5.82 -0.72
I -0.40 2.17 -3.36
I -6.72 -0.46 -3.82
I -3.70 -0.34 5.77
I -3.81 -5.20 1.09
I -4.47 3.68 -0.17
I -5.71 -0.52 1.23
Rb -0.23 -0.05 4.96
Rb -5.14 -3.14 3.83
Rb -4.47 2.43 3.42
Rb -2.10 0.40 -0.05
Rb -1.12 5.07 -0.58
Rb -5.48 -3.21 -1.59
Rb -7.52 1.79 -1.09
Rb -3.44 0.52 -4.94
Rb -0.44 -4.68 -0.26
Rb 3.07 4.13 2.44
Rb 4.00 -1.21 0.41
Rb 8.16 -0.99 3.85
Rb 6.63 -5.05 -1.82
Rb 7.68 1.28 -0.92
Rb 1.53 -1.26 -3.70
Rb 2.86 3.93 -3.78

--
RbI14-RR-3

--
I -0.01 2.53 -2.59
I 2.79 -2.24 -1.84
I -2.80 1.54 2.08
I -0.05 6.18 1.47
I 5.56 2.32 -2.57
I 2.77 1.59 2.09
I -5.59 2.24 -2.59
I -2.75 -2.28 -1.85
I 0.05 -6.71 -1.10
I -0.02 0.49 6.57
I 5.29 -3.12 2.80
I -5.25 -3.20 2.78
I 0.02 -3.23 2.87
Rb 8.78 2.63 -4.13
Rb 2.62 0.42 -4.40
Rb 2.68 4.11 -0.58
Rb -0.08 9.39 3.07
Rb -8.81 2.52 -4.15
Rb -2.74 4.06 -0.59
Rb -2.61 0.38 -4.41
Rb -0.03 3.07 4.03
Rb 5.29 -0.51 0.29
Rb 0.01 -0.56 0.22
Rb -5.29 -0.60 0.26
Rb 0.04 -4.19 -3.77
Rb -2.69 -1.51 4.87
Rb 2.69 -1.47 4.89
Rb 2.72 -5.11 0.90
Rb -2.65 -5.16 0.89
I 0.02 -1.33 -6.29

--
RbI15-RR2

--
I 3.38 0.00 -2.57
I -1.83 -2.53 -3.32
I 6.99 2.82 0.30
I -0.43 2.55 1.92
I 3.95 0.00 3.49
I 2.63 -5.44 -1.46
I -0.43 -2.55 1.92
I 6.99 -2.82 0.31
I 2.63 5.44 -1.46
I -1.83 2.53 -3.32
I -7.26 0.00 -3.17
I -2.99 0.00 5.95
I -4.84 -5.06 0.85
I -4.84 5.06 0.85
I -5.55 0.00 1.40
Rb 6.04 -6.35 -0.42
Rb 7.52 0.00 2.91
Rb 6.04 6.35 -0.42
Rb 7.06 0.00 -2.11
Rb 3.10 2.45 0.80
Rb 3.10 -2.45 0.80
Rb 0.40 0.00 4.68
Rb 1.67 -3.03 -4.10
Rb 1.67 3.04 -4.10
Rb -1.47 5.23 -0.56
Rb -4.11 0.00 -4.93
Rb -4.03 2.72 3.66
Rb -1.48 -5.22 -0.56
Rb -4.03 -2.72 3.66
Rb -7.21 -2.73 -0.68
Rb -7.21 2.73 -0.67
Rb -2.17 0.00 -0.36

--
RbI16-RR2

--
I -1.43 0.12 0.00
I 1.27 5.11 0.00
I -6.44 2.49 0.00
I -4.18 -4.79 0.00
I 3.09 -2.74 0.00
I -0.56 -3.70 3.83
I -2.80 3.55 3.78
I 2.46 1.22 3.84
I -5.22 -1.16 3.81
I -0.56 -3.70 -3.83
I -2.80 3.55 -3.78
I 2.45 1.22 -3.84
I -5.22 -1.16 -3.81
I 6.69 -2.44 3.38
I 6.69 -2.44 -3.38
I 5.94 2.85 0.00
Rb 4.78 6.28 0.00
Rb 6.29 1.12 3.33
Rb 6.77 -3.86 0.00
Rb 6.29 1.12 -3.33
Rb 3.04 -2.83 -3.85
Rb 0.67 4.51 -3.78
Rb 0.67 4.51 3.78
Rb 3.04 -2.82 3.85
Rb 2.30 1.02 0.00
Rb -0.56 -3.71 0.00
Rb -1.59 -0.10 -3.85
Rb -2.88 3.64 0.00
Rb -1.59 -0.09 3.85
Rb -4.15 -4.73 3.73
Rb -4.15 -4.73 -3.72
Rb -6.37 2.35 -3.73
Rb -6.37 2.36 3.73
Rb -5.27 -1.16 0.00

--
RbI16-RbRb-3

--
I 2.14 0.73 0.00
I -1.23 4.55 -0.01
I 6.26 4.32 -0.01
I 6.16 -3.25 0.01
I -1.37 -3.43 0.01
I 2.33 -3.43 -3.78
I -1.69 0.69 -3.85
I 5.85 0.69 -3.79
I 2.33 -3.41 3.80
I -1.69 0.70 3.84
I 5.85 0.71 3.79
I -6.63 3.38 3.34
I -5.09 -3.83 -3.71
I -6.63 3.37 -3.36
I -5.09 -3.81 3.73
I -5.64 -0.14 0.00
Rb -5.71 -0.20 3.84

Rb -5.25 -3.97 0.01
Rb -5.70 -0.22 -3.84
Rb -8.02 2.82 -0.01
Rb -1.48 -3.56 3.82
Rb -1.48 -3.59 -3.81
Rb -3.13 4.18 -3.24
Rb -3.14 4.20 3.22
Rb -1.85 0.35 0.00
Rb 2.32 -3.68 0.01
Rb 2.01 0.23 -3.84
Rb 2.41 4.45 -0.01
Rb 2.01 0.25 3.84
Rb 6.01 -3.19 3.76
Rb 6.01 -3.21 -3.75
Rb 7.55 3.91 -3.53
Rb 7.55 3.93 3.51
Rb 5.83 0.43 0.00

--
RbI17-RbRb

--
I 1.88 0.00 0.00
I -1.89 -2.68 -2.90
I 5.86 -2.72 -2.68
I 5.86 2.73 2.68
I -1.89 2.68 2.92
I 2.24 0.00 5.42
I 1.97 -5.35 0.00
I -1.89 -2.68 2.92
I 5.86 -2.72 2.68
I 1.96 5.35 0.00
I 2.23 0.00 -5.42
I -1.89 2.68 -2.91
I 5.86 2.72 -2.68
I -6.92 0.00 3.02
I -5.50 -5.04 0.00
I -5.51 5.03 0.00
I -6.91 0.00 -3.03
Rb -5.57 3.43 -3.25
Rb -5.57 3.43 3.25
Rb -5.57 -3.43 3.25
Rb -5.57 -3.44 -3.25
Rb -1.76 5.30 0.01
Rb -1.37 0.00 5.48
Rb -1.75 -5.30 0.01
Rb -1.38 0.00 -5.47
Rb -1.91 0.00 0.00
Rb 2.08 2.72 2.73
Rb 2.08 -2.72 2.73
Rb 2.07 -2.72 -2.73
Rb 2.07 2.72 -2.74
Rb 5.73 5.30 0.00
Rb 5.96 0.00 5.21
Rb 5.74 -5.29 0.00
Rb 5.95 0.00 -5.22
Rb 5.85 0.00 0.00
Rb -8.96 0.01 -0.01

--
RI17-RR3

--
I 3.39 -0.28 0.92
I -1.99 -0.36 3.14
I 6.61 0.06 -2.69
I -1.22 -0.10 -3.03
I 2.42 3.86 -3.07
I 1.67 3.28 4.47
I -0.75 5.46 0.28
I 4.82 5.75 0.63
I 2.73 -3.66 -3.64
I 2.06 -4.28 4.02
I -0.98 -4.89 -0.15
I 6.25 -4.68 0.45
I -5.38 -3.85 2.45
I -5.12 3.68 -3.58
I -5.75 3.43 3.05
I -4.74 -3.59 -3.47
I -6.73 -0.24 -0.55
Rb -7.00 3.54 -0.41
Rb -5.94 -0.25 3.26
Rb -7.23 -4.04 -0.76
Rb -1.86 -4.49 3.42
Rb -3.20 -1.85 -0.23
Rb -5.19 0.04 -4.10
Rb -2.13 3.60 3.38
Rb -1.54 3.67 -3.02
Rb 1.53 -0.52 4.27
Rb -1.07 -4.10 -3.80
Rb 4.97 -6.46 3.47
Rb 2.47 -3.86 0.15
Rb 2.59 0.01 -3.14
Rb 2.03 3.09 0.72
Rb 6.96 -1.08 0.82
Rb 6.36 -3.77 -3.34
Rb 6.12 3.77 -2.44
Rb 4.04 6.04 4.26
Rb 1.98 7.27 -1.41

--
RbI18-RR2

--
I -2.25 0.00 -0.22
I 1.49 -3.91 0.46
I -6.04 -3.84 -0.86
I -6.04 3.84 -0.85
I 1.49 3.91 0.47
I -1.58 3.84 -3.99
I -1.58 -3.84 -3.99
I 2.25 0.00 -3.40
I -5.36 0.00 -4.65
I -2.94 3.84 3.58
I -2.94 -3.84 3.58
I 0.75 0.00 4.32
I -6.73 0.00 2.89
I 4.44 -3.73 4.88
I 5.97 3.96 -2.61
I 5.97 -3.95 -2.61
I 4.44 3.72 4.88
I 5.37 0.00 1.12
Rb 8.05 6.65 -3.75
Rb 8.05 -6.64 -3.75
Rb 5.12 3.73 1.31
Rb 4.48 0.00 5.10
Rb 5.12 -3.74 1.31
Rb 5.85 0.00 -2.53
Rb 0.74 3.81 4.35
Rb 0.74 -3.82 4.34
Rb 1.46 0.00 0.59
Rb 2.04 3.75 -3.20
Rb 2.04 -3.75 -3.21
Rb -2.30 3.84 -0.16
Rb -2.97 0.00 3.61
Rb -2.30 -3.84 -0.17
Rb -1.62 0.00 -3.98
Rb -5.29 3.71 -4.47
Rb -5.29 -3.70 -4.48
Rb -6.08 0.00 -0.86
Rb -6.58 -3.71 2.83
Rb -6.58 3.71 2.84

--
RbI19-RbRb-2

--
I -2.10 -0.59 -0.05
I -0.11 3.03 3.37
I -6.45 -1.10 3.31
I -4.34 -4.04 -3.44
I 1.97 -0.04 -3.29
I 0.95 -5.48 -1.34
I -1.39 -1.87 5.19
I 3.29 -2.03 2.40
I -3.54 -5.41 1.83
I -3.13 0.89 -5.26
I -5.09 3.79 1.53
I -1.12 4.61 -1.96
I -7.29 0.20 -1.84
I 1.23 7.77 1.55
I 6.95 -0.64 -1.36
I 4.79 2.24 5.13
I 3.17 4.87 -5.02
I 4.10 3.70 0.01
I 6.32 -5.60 -0.43
Rb 3.71 -7.86 -1.74
Rb 9.05 -3.51 -2.00
Rb 5.78 -4.58 3.14
Rb 1.63 0.37 5.37
Rb 5.89 1.11 1.87
Rb 3.71 -2.64 -1.31
Rb -0.39 -3.33 1.90
Rb -4.60 -3.77 5.04
Rb -2.74 -6.69 -1.50
Rb -5.45 -2.55 -0.03
Rb -8.15 1.69 1.48
Rb -6.21 -1.19 -5.09
Rb -3.28 1.02 3.37
Rb -4.20 2.44 -1.89
Rb -1.30 -1.84 -3.53
Rb -2.00 5.99 1.56
Rb 0.76 1.95 -0.14
Rb 3.08 5.22 3.45
Rb 2.21 6.64 -1.84
Rb 5.06 2.27 -3.32
Rb -0.05 3.11 -5.27

--
RbI20-2RR

--
I 2.58 -0.57 -0.13
I -0.17 2.90 -3.32
I 6.14 -1.25 -4.22
I 5.43 -3.85 2.95
I -0.84 0.17 3.81
I -0.14 -5.35 2.00
I 0.81 -2.15 -5.04
I -2.91 -1.85 -1.35
I 3.68 -5.52 -1.96
I 4.48 1.16 4.68
I 5.08 3.73 -2.50
I 1.79 4.64 1.59
I 7.95 0.33 0.60
I -1.18 7.72 -1.54
I -6.02 -0.45 3.10
I -5.50 1.94 -4.08
I -1.75 5.21 5.44
I -3.67 3.68 0.74
I -5.59 -5.43 1.54
I -8.38 -1.75 -1.57
Rb -2.95 -7.66 2.73
Rb -8.46 -2.94 2.07
Rb -5.67 -4.25 -1.97
Rb -8.94 0.73 -4.30
Rb -5.62 0.80 -0.44
Rb -2.98 -2.57 2.45
Rb -3.92 2.46 4.37
Rb -2.17 0.10 -4.65
Rb -3.30 5.03 -2.81
Rb -1.45 6.71 2.04
Rb 2.02 5.91 -2.02
Rb -0.36 1.83 0.35
Rb 1.39 3.32 5.15
Rb 2.99 0.85 -3.77
Rb 4.86 2.52 1.10
Rb 8.12 1.64 -2.90
Rb 7.51 -0.90 4.07
Rb 5.86 -2.56 -0.67
Rb 4.03 -4.03 -5.39
Rb 2.39 -1.69 3.51
Rb 0.57 -3.44 -1.49
Rb 3.50 -6.62 1.54

--
RbI21-RbRb-2

--
I 1.34 -3.37 1.85
I -3.25 0.39 3.67
I 4.50 -6.03 -2.01
I -1.53 -1.88 -3.42
I 3.68 -0.96 -2.45
I 2.33 1.10 5.04
I 0.06 2.09 -0.03
I 6.26 -1.84 3.16
I -0.74 -7.00 -1.68
I -2.47 -4.68 5.27
I -4.54 -3.88 0.50
I -8.25 -0.74 2.63
I -2.18 3.15 -5.11
I -4.00 5.41 1.92
I -6.58 -2.86 -4.28
I -5.51 1.42 -1.32
I -0.76 7.27 -1.98
I 1.21 6.37 2.89
I 3.02 4.16 -4.13
Rb -1.71 8.30 1.46
Rb 0.06 6.08 -5.41
Rb 2.14 5.26 -0.64
Rb -1.16 3.44 3.35
Rb -3.23 4.37 -1.66
Rb 0.70 1.15 -3.76
Rb 3.06 0.07 1.25
Rb 4.92 -1.09 6.46
Rb 6.53 -3.17 -3.52
Rb 4.78 -4.82 1.52
Rb 2.19 -8.85 -2.80
Rb -0.46 -1.68 4.88
Rb -1.79 -5.95 1.88
Rb 1.27 -3.81 -1.99
Rb -5.55 -2.78 4.08
Rb -2.69 -0.63 0.03
Rb -6.36 2.40 2.30
Rb -7.68 -1.81 -0.87
Rb -4.58 0.19 -4.83
Rb -3.84 -4.94 -3.05
I 5.49 3.06 0.96
I 8.53 -0.39 -2.26
Rb 8.39 0.55 1.22
Rb 5.89 2.19 -2.89
Rb 3.99 4.43 4.13

--
RbI21-RbRb

--
I 0.00 5.25 -3.65
I -2.84 -0.50 -4.23
I 2.57 7.01 1.66
I -2.69 1.80 3.02
I 2.69 1.80 3.02
I 2.84 -0.50 -4.23
I 0.00 -1.78 0.19
I 4.98 3.51 -1.68
I -2.57 7.02 1.66
I -4.98 3.51 -1.68
I -8.31 -1.14 -3.53
I -2.65 -3.34 4.82
I -2.63 -5.74 -2.43
I -7.88 1.54 2.80
I -5.60 -2.39 0.50
I 0.00 -7.18 2.08
I 2.63 -5.74 -2.43
I 2.65 -3.34 4.82
Rb 0.00 -8.21 -1.51
Rb 0.00 -5.84 5.57
Rb 2.68 -4.65 1.24
Rb 0.00 -3.19 -3.38
Rb -2.68 -4.65 1.24
Rb 0.00 -0.80 3.92
Rb 3.18 0.32 -0.47
Rb 6.10 1.49 -4.59
Rb 5.48 4.22 2.06
Rb 3.02 6.55 -2.03
Rb 0.00 9.37 2.87
Rb 0.00 1.82 -5.03
Rb -3.01 6.55 -2.03
Rb 0.00 4.32 2.58
Rb -6.10 1.49 -4.59
Rb -3.18 0.32 -0.47
Rb -5.52 -3.55 -3.17
Rb -8.96 -0.66 0.06
Rb -5.36 -0.88 4.06
Rb -5.48 4.22 2.06
I 5.59 -2.39 0.50
I 8.31 -1.14 -3.53
I 7.88 1.54 2.80
Rb 8.96 -0.66 0.06
Rb 5.36 -0.88 4.06
Rb 5.52 -3.55 -3.17

--
RbI22-RbRb-4

--
I -2.66 0.00 0.00
I 0.00 -3.58 -2.96
I -5.53 1.44 -4.37
I -5.39 3.66 2.92
I 0.00 -1.81 4.65
I 0.00 3.58 2.97
I 0.00 1.81 -4.65
I 2.66 0.00 0.00
I -2.68 5.40 -1.68
I -5.53 -1.44 4.37
I -5.39 -3.65 -2.92
I -2.69 -5.40 1.68
I -8.11 0.01 0.00
I 0.00 -8.64 -1.94
I 5.52 -1.44 4.37
I 5.39 -3.65 -2.92
I 2.69 -5.41 1.68
I 8.11 0.00 0.00
I 5.53 1.44 -4.37
I 5.39 3.65 2.92
I 2.69 5.40 -1.68
I 0.01 8.65 1.93
Rb 3.07 -3.96 5.13
Rb -0.01 -8.08 1.59
Rb 2.74 -6.21 -2.40
Rb 5.43 -2.63 0.72
Rb 8.06 1.13 3.53

Rb 8.07 -1.14 -3.53
Rb -3.07 -3.96 5.13
Rb 2.71 1.05 3.71
Rb 0.00 -2.69 0.78
Rb -2.75 -6.21 -2.40
Rb 5.43 2.62 -0.72
Rb 2.71 -1.06 -3.72
Rb 2.74 6.21 2.40
Rb 0.00 2.69 -0.78
Rb -2.71 -1.05 -3.72
Rb 3.07 3.95 -5.13
Rb -2.71 1.05 3.71
Rb -5.43 -2.62 0.72
Rb -8.06 1.14 3.53
Rb -2.74 6.21 2.40
Rb -5.43 2.63 -0.72
Rb -8.07 -1.13 -3.53
Rb 0.01 8.08 -1.60
Rb -3.07 3.96 -5.13

--
RbI22-RR-2

--
I -2.73 -0.71 0.00
I 0.00 2.09 3.89
I -5.73 -2.91 3.74
I -5.73 -2.91 -3.74
I 0.00 2.10 -3.89
I 0.00 -3.76 -3.84
I 0.00 -3.77 3.84
I 2.73 -0.71 0.00
I -2.71 -6.51 0.00
I -5.38 2.35 -3.80
I -5.39 2.35 3.81
I -2.71 4.93 0.00
I -8.39 -0.04 0.00
I 0.00 7.51 3.74
I 5.39 2.35 -3.80
I 5.38 2.34 3.81
I 0.00 7.52 -3.73
I 2.71 4.93 0.00
I 8.39 -0.04 0.00
I 5.73 -2.92 3.74
I 5.73 -2.91 -3.75
I 2.70 -6.51 -0.01
Rb 0.00 -8.98 -0.01
Rb 3.28 -5.57 3.68
Rb 8.20 -0.02 3.75
Rb 5.90 -2.77 0.00
Rb 8.20 -0.01 -3.74
Rb 3.28 -5.55 -3.70
Rb 2.80 -0.38 3.85
Rb 5.49 2.48 0.01
Rb 2.80 -0.36 -3.84
Rb 2.67 4.99 3.82
Rb -3.28 -5.56 -3.69
Rb -5.90 -2.78 0.00
Rb -3.28 -5.56 3.69
Rb -8.20 -0.02 3.74
Rb -8.19 -0.02 -3.75
Rb -2.67 5.00 -3.82
Rb 2.67 5.00 -3.81
Rb -2.80 -0.37 -3.84
Rb 0.00 7.70 0.00
Rb 0.00 -3.38 0.00
Rb -2.67 5.00 3.82
Rb -2.81 -0.37 3.85
Rb -5.49 2.49 0.00
Rb 0.00 2.24 0.00

--
RbI22-RR

--
I 2.53 0.40 0.22
I 0.39 -3.14 3.67
I 5.85 2.09 3.93
I 4.86 3.69 -3.41
I -0.48 -1.71 -3.91
I -0.51 3.58 -2.94
I 0.21 2.42 5.02
I -2.86 0.47 0.75
I 2.34 5.93 1.30
I 4.82 -1.64 -4.47
I 5.76 -3.19 2.94
I 2.66 -5.07 -0.95
I 7.99 0.32 -0.61
I 0.20 -8.22 2.54
I -5.84 -1.78 -3.40
I -5.19 -2.87 4.11
I -0.53 -6.91 -4.74
I -2.89 -5.02 -0.32
I -8.08 0.41 1.00
I -5.75 3.60 -2.90
I -3.01 5.58 2.49
I -0.78 8.47 -2.60
Rb -8.67 -1.73 3.95
Rb -8.33 0.86 -2.81
Rb -5.48 3.22 0.78
Rb -3.15 6.07 -4.01
Rb -0.74 8.20 0.98
Rb -2.33 4.89 5.98
Rb -3.09 0.82 -3.22
Rb -5.36 -2.34 0.27
Rb -2.16 -0.63 4.29
Rb -0.14 3.05 0.89
Rb 7.39 1.01 -4.22
Rb 5.40 2.92 0.22
Rb 3.37 4.58 4.64
Rb 8.38 -0.55 2.97
Rb 3.19 -0.64 3.83
Rb 5.32 -2.44 -0.79
Rb 3.06 -5.88 2.74
Rb -2.42 -5.79 3.35
Rb -0.13 -7.75 -1.15
Rb -3.19 -4.46 -4.12
Rb 2.20 -4.41 -4.70
Rb -0.02 -2.50 -0.19
Rb 2.20 0.94 -3.67
Rb 2.24 6.26 -2.76

--
RbI22-RbRb-5

--
I 0.89 -4.00 0.93
I 2.27 -0.29 -3.83
I -1.44 -6.82 -3.02
I 3.00 0.90 3.68
I -1.92 -1.16 4.45
I -2.84 -1.72 -3.11
I -0.74 1.97 -0.05
I -4.69 -4.55 1.25
I 5.14 -4.19 4.38
I 3.79 -5.44 -3.23
I 6.04 -1.49 -0.19
Rb 1.59 -7.93 -4.81
Rb 7.16 -5.79 6.89
Rb 4.53 -4.77 0.45
Rb 6.44 -0.60 3.41
Rb 5.64 -2.00 -3.97
Rb -1.72 -6.61 0.65
Rb 1.56 -2.44 4.28
Rb -4.95 -3.25 4.85
Rb 0.48 -3.43 -2.89
Rb -4.87 -4.87 -2.86
Rb -2.85 -1.12 0.68
Rb -1.06 1.58 -3.92
Rb 2.79 0.61 -0.17
Rb -0.57 2.54 3.77
Rb 1.03 5.48 -0.74
Rb 4.72 4.40 2.96
Rb 7.84 2.11 -0.93
Rb 4.08 3.16 -4.58
I 7.26 1.25 -4.49
I 1.24 5.84 3.08
I 0.74 4.86 -4.50
I 8.00 2.61 2.78
I 4.46 3.90 -0.82
Rb -2.03 7.58 2.92
Rb -2.52 6.64 -4.45
I -2.31 7.29 -0.77
I -4.36 3.44 -3.98
I -3.93 4.42 3.59
I -7.98 -1.37 4.44
I -7.97 -2.96 -2.80
I -6.11 0.86 0.39
Rb -4.06 3.97 -0.23
Rb -6.78 2.06 3.90
Rb -6.24 0.27 -3.39
Rb -8.14 -2.37 0.83

--
RbI22-RR2

--
I -2.69 -0.70 0.00
I 0.15 1.78 3.89
I -5.62 -3.03 3.83
I -5.62 -3.03 -3.83
I 0.15 1.78 -3.89
I 0.08 -4.08 -3.95
I 0.08 -4.08 3.95
I 2.73 -1.22 0.00
I -3.14 -6.01 0.00
I -5.27 2.32 -3.83
I -5.27 2.32 3.82
I -2.46 4.78 0.00
I -8.17 -0.20 0.00
I 0.45 7.13 3.73
I 5.52 1.62 -3.81
I 5.52 1.62 3.81
I 0.45 7.13 -3.73
I 3.04 4.43 0.00
I 8.32 -0.99 0.00
I 5.48 -3.70 3.80
I 5.48 -3.70 -3.80
Rb 3.02 -5.68 5.57
Rb 8.15 -0.93 3.73
Rb 5.68 -3.56 0.00
Rb 8.15 -0.94 -3.73
Rb 3.02 -5.68 -5.57
Rb 5.63 1.79 0.00
Rb 2.74 -0.89 3.75
Rb -0.27 -3.54 0.00
Rb 2.74 -0.89 -3.75
Rb -3.32 -5.85 3.68
Rb 2.98 4.48 3.83
Rb 0.13 2.00 0.00
Rb 2.98 4.48 -3.83
Rb -3.32 -5.85 -3.68
Rb -2.81 -0.49 -3.85
Rb -5.72 -3.05 0.00
Rb -2.81 -0.49 3.85
Rb -8.05 -0.13 3.72
Rb -2.42 4.83 3.81
Rb -5.33 2.38 0.00
Rb 0.45 7.35 0.00
Rb -2.42 4.83 -3.81
Rb -8.05 -0.13 -3.72

--
RbI23-RbRb-2

--
I 0.53 -2.68 0.26
I 3.02 0.04 -3.64
I -2.33 -5.40 -3.61
I -2.21 -5.42 4.05
I 3.50 0.04 4.16
I -2.16 -0.03 4.17
I -2.40 -0.03 -3.64
I 0.45 2.69 0.26
I -5.01 -2.81 0.26
I 3.11 -5.53 3.96
I 3.10 -5.35 -3.67
I 6.13 -2.63 0.25
I 0.48 -8.11 0.14
I 8.13 0.11 -4.15
I 2.96 5.61 3.97
I 2.96 5.43 -3.66
I 6.05 2.79 0.25
I 0.26 8.12 0.15
I -2.47 5.34 -3.60
I -2.35 5.35 4.06
Rb 0.21 7.93 -3.56
Rb 0.18 8.06 3.86
Rb -2.38 5.36 0.25
Rb 0.30 2.69 -3.61
Rb 3.06 5.51 0.13
Rb 0.42 2.73 4.11
Rb -2.28 -0.03 0.31
Rb -4.96 -2.77 -3.47
Rb -4.88 -2.76 4.16
Rb -2.24 -5.42 0.24
Rb 0.42 -7.92 -3.56
Rb 0.39 -8.05 3.85
Rb 0.37 -2.68 -3.61
Rb 3.21 -5.43 0.12
Rb 0.49 -2.73 4.10
Rb 5.69 -2.67 -3.88
Rb 3.24 0.04 0.20
Rb 5.61 2.82 -3.88
Rb 8.59 0.12 -0.60
Rb 5.60 3.16 3.96
Rb 5.68 -3.01 3.96
I -5.08 2.68 0.27
I -7.89 -0.09 -3.54
I -7.48 -0.10 4.09
Rb -7.59 -0.10 0.44
Rb -4.95 2.63 4.16
Rb -5.02 2.64 -3.47
Rb -10.99 -0.11 -5.32

--
RbI24-RbRb-3

--
I 0.00 2.71 0.00
I 1.92 0.00 4.29
I -3.39 5.41 3.29
I -2.00 5.39 -4.26
I 3.41 0.00 -3.39
I -1.93 0.00 -4.29
I -3.40 0.00 3.38
I 0.00 -2.71 0.00
I -5.40 2.77 -0.94
I 3.39 5.40 -3.31
I 1.99 5.40 4.25
I 5.40 2.77 0.95
I 0.00 8.11 -0.02
I 7.13 0.00 5.14
I 3.39 -5.40 -3.31
I 1.99 -5.40 4.25
I 8.78 0.00 -2.30
I 5.40 -2.77 0.94
I 0.00 -8.11 -0.02
I -3.38 -5.41 3.29
I -2.00 -5.39 -4.26
Rb -0.65 -7.92 3.63
Rb 0.65 -7.91 -3.66
Rb -2.68 -5.42 -0.50
Rb -0.68 -2.71 3.80
Rb 2.68 -5.42 0.49
Rb 0.68 -2.70 -3.81
Rb -2.66 0.00 -0.51
Rb -5.89 2.72 2.76
Rb -4.61 2.70 -4.75
Rb -2.68 5.42 -0.50
Rb -0.65 7.92 3.63
Rb 0.65 7.91 -3.66
Rb -0.68 2.71 3.80
Rb 2.68 5.42 0.49
Rb 0.68 2.70 -3.81
Rb 4.59 2.70 4.75
Rb 2.66 0.00 0.50
Rb 4.59 -2.70 4.75
Rb 7.84 0.00 1.55
Rb 5.90 -2.71 -2.75
Rb 5.90 2.71 -2.75
I -5.40 -2.77 -0.94
I -8.76 0.00 2.35
I -7.15 0.00 -5.13
Rb -7.86 0.00 -1.53
Rb -4.61 -2.70 -4.75
Rb -5.89 -2.72 2.76
Rb -12.10 0.00 3.62
Rb 12.16 0.00 -3.46

--
RbI24-RbRb

--
I -0.29 2.73 0.00
I -3.00 0.00 -3.91
I 2.39 5.44 -3.84
I 2.39 5.44 3.84
I -2.99 0.00 3.91
I 2.41 0.00 3.91
I 2.41 0.00 -3.91
I -0.29 -2.73 0.00
I 5.22 2.76 0.00
I -3.07 5.40 3.84
I -3.07 5.40 -3.84
I -5.76 2.78 0.00
I -0.33 8.15 0.00
I -8.30 0.00 -3.73
I -3.07 -5.40 3.84
I -3.07 -5.39 -3.84
I -8.30 0.00 3.74
I -5.77 -2.78 0.00
I -0.34 -8.15 -0.01
I 2.39 -5.44 -3.84
I 2.39 -5.45 3.83
I 5.22 -2.77 0.00
I 7.81 0.00 -3.95
I 7.80 -0.01 3.96
Rb 10.17 0.01 -6.66
Rb 10.15 -0.01 6.68
Rb 7.67 0.00 0.00
Rb 4.90 2.75 -3.74
Rb 4.90 2.75 3.75
Rb 2.34 5.47 0.00
Rb -0.42 7.95 -3.71

Rb -0.41 7.95 3.70
Rb 4.90 -2.75 -3.75
Rb 4.90 -2.76 3.75
Rb 2.31 0.00 0.00
Rb -0.41 2.72 -3.85
Rb -0.41 2.72 3.85
Rb -3.13 5.44 0.00
Rb -0.41 -2.72 3.85
Rb -3.13 0.00 0.00
Rb -5.77 2.70 -3.80
Rb -5.77 2.70 3.81
Rb 2.33 -5.48 0.00
Rb -0.41 -2.72 -3.85
Rb -0.42 -7.94 -3.71
Rb -5.78 -2.69 -3.80
Rb -3.14 -5.44 0.00
Rb -0.42 -7.95 3.70
Rb -8.46 0.00 0.00
Rb -5.77 -2.69 3.81

CsI

CsI14-CC2 " " " -
479.162074927"
CsI15-CC2 " -
510.577207982"
CsI16-CC2 " " " -
542.015884637"
CsI16-CsCs-3 " " " -
541.986410814"
"CsI16-CsCs-2 " " -
541.982433120"
CsI17-CsCs " " " -
573.439966879"
CsI18-CsCs-4 " " " -
604.852844991"
CsI18-CC2 " " " -
604.831417986"
CsI19-CsCs " " " -
636.243999548"
CsI19-CsCs-2 " " " -
636.230472046"
CsI20-2CC " " -667.66
"CsI21-CsCs-3 " " -
699.085477126"
CsI21-CC2 " " " -
699.075981037"
"CsI21-CsCs " -699.06
CsI21-CsCs-2 " " -699.06
"CsI22-CsCs-4 " -730.51
CsI22-CsCs-5 " " " -
730.465994011"
CsI23-CsCs-2 " " " -
761.913709198"
CsI24-CsCs-3 " -
793.318442276"

--
CsI14-CC2

--
I 4.86 0.82 -3.04
I -2.08 -2.41 -3.02
I -0.68 3.10 2.87
I 6.15 1.65 2.63
I 3.29 -4.35 -1.91
I 0.65 -1.77 1.93
I 8.20 -2.28 0.41
I 2.64 6.02 -0.73
I -0.45 2.26 -3.53
I -7.14 -0.52 -4.04
I -4.03 -0.38 6.05
I -4.03 -5.46 1.18
I -4.79 3.79 -0.24
I -6.12 -0.58 1.28
Cs 8.64 -1.00 4.08
Cs 8.06 1.52 -0.95
Cs 7.06 -5.17 -2.02
Cs 4.19 -1.23 0.45
Cs 3.16 4.34 2.69
Cs 2.99 4.14 -4.04
Cs 1.60 -1.35 -3.96
Cs -0.45 -4.94 -0.26
Cs -0.32 -0.08 5.29
Cs -1.24 5.30 -0.63
Cs -2.27 0.37 -0.02
Cs -3.67 0.56 -5.22
Cs -4.84 2.57 3.59
Cs -8.07 1.85 -1.17
Cs -5.83 -3.44 -1.71
Cs -5.59 -3.35 4.06

--
CsI15-CC2

--
I 3.57 0.00 -2.67
I -1.89 -2.65 -3.51
I 7.29 2.97 0.41
I -0.56 2.68 2.06
I 4.09 0.00 3.74
I 2.73 -5.73 -1.51
I -0.56 -2.68 2.06
I 7.29 -2.97 0.41
I 2.73 5.73 -1.51
I -1.89 2.65 -3.51
I -7.58 0.00 -3.33
I -3.29 0.00 6.31
I -5.14 -5.29 0.84
I -5.14 5.29 0.84
I -6.02 0.00 1.52
Cs 6.31 -6.73 -0.31
Cs 7.48 0.00 -2.17
Cs 7.88 0.00 3.18
Cs 6.31 6.73 -0.31
Cs 3.18 -2.56 0.87
Cs 3.18 2.56 0.87
Cs 1.81 3.21 -4.36
Cs 1.81 -3.21 -4.36
Cs 0.34 0.00 5.01
Cs -1.56 -5.52 -0.61
Cs -4.37 -2.89 3.88
Cs -2.45 0.00 -0.38
Cs -4.37 2.89 3.88
Cs -1.56 5.52 -0.61
Cs -4.29 0.00 -5.28
Cs -7.75 2.89 -0.71
Cs -7.75 -2.89 -0.71

--
CsI16-CC2

--
I -1.52 0.10 0.00
I 1.43 5.30 0.00
I -6.68 2.79 0.00
I -4.59 -4.98 0.00
I 3.17 -3.05 0.00
I -0.73 -3.94 4.04
I -2.85 3.79 4.00
I 2.61 1.17 4.05
I -5.54 -1.10 4.02
I -0.73 -3.94 -4.04
I -2.85 3.79 -4.00
I 2.61 1.17 -4.05
I -5.54 -1.10 -4.02
I 6.97 -2.77 3.52
I 6.97 -2.77 -3.53
I 6.27 2.88 0.00
Cs 5.16 6.56 0.00
Cs 6.69 1.02 3.52
Cs 6.69 1.03 -3.52
Cs 7.02 -4.39 0.00
Cs 3.11 -3.10 4.09
Cs 3.11 -3.10 -4.09
Cs 2.45 0.97 0.00
Cs 0.86 4.73 4.04
Cs 0.86 4.73 -4.04
Cs -2.87 3.93 0.00
Cs -1.68 -0.08 -4.09
Cs -0.71 -4.00 0.00
Cs -1.68 -0.09 4.09
Cs -6.67 2.66 3.95
Cs -6.67 2.66 -3.95
Cs -5.59 -1.10 0.00
Cs -4.57 -4.94 -3.95
Cs -4.57 -4.94 3.95

--
CsI16-CsCs-3

--
I 2.21 0.71 0.00
I -1.30 4.74 -0.02
I 6.65 4.43 -0.03
I 6.40 -3.54 0.03
I -1.58 -3.64 0.02
I 2.38 -3.67 -3.97
I -1.87 0.70 -4.07
I 6.13 0.62 -4.00
I 2.37 -3.61 4.02
I -1.88 0.74 4.06
I 6.12 0.67 4.00
I -7.02 3.63 3.47
I -5.48 -4.05 -3.91
I -7.01 3.59 -3.52
I -5.49 -4.00 3.95
I -6.07 -0.15 0.00
Cs -6.11 -0.17 4.07
Cs -5.70 -4.21 0.02
Cs -6.10 -0.22 -4.08
Cs -8.60 3.00 -0.02
Cs -1.66 -3.79 4.07
Cs -1.65 -3.84 -4.03
Cs -3.31 4.45 -3.45
Cs -3.32 4.49 3.40
Cs -2.04 0.38 0.00
Cs 2.33 -3.93 0.03
Cs 2.06 0.21 -4.08
Cs 2.57 4.66 -0.03
Cs 2.05 0.27 4.08
Cs 6.27 -3.47 4.01
Cs 6.28 -3.53 -3.96
Cs 8.02 4.00 -3.76
Cs 8.01 4.05 3.71
Cs 6.13 0.35 0.00

--
CsI16-CsCs-2

--
I -3.23 0.55 -2.50
I 2.99 0.83 -4.05
I -6.79 -0.16 2.83
I 0.90 -1.56 3.43
I -2.50 2.71 4.18
I -0.81 5.45 -3.11
I 2.13 3.16 1.00
I -5.71 4.72 0.02
I -3.51 -4.55 1.85
I 0.53 -3.73 -2.12
I -7.61 -3.09 -1.96
I 6.99 -3.24 -3.88
I 5.13 1.62 5.55
I 6.94 4.25 -1.62
I 4.44 -5.35 2.11
I 6.46 -0.78 0.74
Cs 7.43 -4.52 -0.24
Cs 4.93 -2.10 4.32
Cs 6.34 3.02 2.08
Cs 7.20 0.61 -3.01
Cs 0.58 -5.23 1.69
Cs 1.40 2.29 4.83
Cs 3.21 4.80 -2.43
Cs 3.31 -3.15 -4.85
Cs 2.56 -0.68 -0.19
Cs -2.97 -1.22 4.02
Cs -1.78 3.27 0.26
Cs -0.62 2.01 -4.98
Cs -3.34 -3.32 -1.90
Cs -7.36 -3.93 1.99
Cs -6.22 3.65 3.84
Cs -4.04 7.42 -2.26
Cs -9.95 -4.67 -4.55
Cs -6.80 0.96 -0.99

--
CsI17-CsCs

--
I 1.90 -0.01 0.00
I -1.99 -2.50 3.55
I 6.06 -2.30 3.32
I 6.03 2.36 -3.28
I -1.99 2.46 -3.57
I 1.95 5.62 -0.98
I 1.97 0.99 5.61
I -2.02 3.54 2.47
I 6.02 3.33 2.33
I 2.01 -0.99 -5.61
I 2.02 -5.62 1.00
I -1.96 -3.58 -2.49
I 6.09 -3.27 -2.32
I -6.06 3.95 -0.72
I -6.01 0.70 3.94
I -5.98 -0.71 -3.92
I -6.04 -3.94 0.70
Cs -5.78 -4.51 -3.12
Cs -5.78 3.11 -4.51
Cs -5.82 4.49 3.11
Cs -5.81 -3.14 4.48
Cs -1.93 -1.00 -5.49
Cs -2.00 5.45 -0.99
Cs -1.99 0.96 5.46
Cs -1.94 -5.49 0.97
Cs -2.05 -0.04 -0.02
Cs 2.06 2.36 -3.36
Cs 2.03 3.38 2.37
Cs 2.08 -2.36 3.37
Cs 2.10 -3.38 -2.36
Cs 6.01 -0.92 -5.49
Cs 5.95 5.54 -0.94
Cs 5.96 0.99 5.52
Cs 6.02 -5.47 0.96
Cs 6.07 0.02 0.02
Cs -7.11 0.00 0.00

--
CsI18-CsCs-4

--
I -2.55 -0.27 0.07
I 1.31 3.25 2.34
I -6.09 0.90 4.51
I -6.49 -3.90 -1.97
I 1.10 -1.43 -4.45
I -1.20 -5.71 -0.97
I -0.83 -0.97 5.56
I 2.71 -2.12 1.19
I -4.68 -4.51 3.40
I -4.56 0.27 -5.17
I -4.00 5.10 1.26
I -0.34 3.98 -3.37
I -7.88 1.57 -0.84
I 3.33 7.43 -0.42
I 6.31 -3.70 -2.76
I 6.55 1.43 3.58
I 4.96 2.12 -2.23
I 9.88 -2.42 1.37
Cs 10.06 -0.05 4.38
Cs 9.66 -5.12 -1.32
Cs 2.78 0.23 4.53
Cs -4.50 -2.10 6.52
Cs -1.01 -3.33 2.32
Cs 6.38 -0.89 0.28
Cs 2.42 -4.57 -1.97
Cs -4.86 -6.77 0.18
Cs 5.00 4.50 1.54
Cs 4.98 -0.78 -4.96
Cs 1.14 0.95 -0.99
Cs -2.83 -2.75 -3.13
Cs -2.41 2.10 3.44
Cs -6.33 -1.49 1.28
Cs -7.60 3.85 2.37
Cs -8.13 -0.88 -3.91
Cs -4.23 2.81 -2.01
Cs -0.38 6.39 0.38
Cs -1.09 1.40 -6.31
Cs 3.34 5.52 -3.70

--
CsI18-CC2

--
I 2.43 0.00 -0.26
I -1.52 4.12 0.58
I 6.40 4.05 -1.07
I 6.40 -4.05 -1.07
I -1.52 -4.12 0.58
I 1.58 -4.05 -4.22
I 1.58 4.06 -4.21
I -2.45 0.00 -3.44
I 5.53 0.00 -5.04
I 3.29 -4.05 3.72
I 3.29 4.05 3.72
I -0.61 0.00 4.62
I 7.26 0.00 2.87
I -4.48 3.94 5.32
I -6.36 -4.18 -2.53
I -6.36 4.18 -2.53
I -4.48 -3.94 5.32
I -5.58 0.00 1.40
Cs -8.62 -7.05 -3.64
Cs -8.62 7.05 -3.64
Cs -6.25 0.00 -2.45
Cs -5.35 3.96 1.57
Cs -5.35 -3.96 1.57
Cs -4.53 0.00 5.59
Cs -0.58 -4.05 4.66
Cs -0.58 4.05 4.66
Cs -1.48 0.00 0.70
Cs -2.23 -3.98 -3.30

Cs -2.23 3.99 -3.29
Cs 1.60 0.00 -4.21
Cs 2.47 4.07 -0.21
Cs 2.47 -4.07 -0.21
Cs 3.33 0.00 3.79
Cs 7.14 -3.94 2.82
Cs 7.14 3.94 2.82
Cs 6.46 0.00 -1.08
Cs 5.49 -3.94 -4.89
Cs 5.49 3.94 -4.89

--
CsI19-CsCs

--
I -2.68 -0.50 0.00
I 0.90 1.22 3.99
I -6.39 -2.22 4.04
I -6.38 -2.24 -4.04
I 0.90 1.20 -3.99
I -0.97 -4.20 -4.01
I -0.98 -4.18 4.03
I 3.14 -3.50 0.01
I -4.63 -5.90 0.02
I -4.51 3.12 -4.05
I -4.52 3.13 4.03
I -1.09 5.21 -0.01
I -8.17 1.38 -0.01
I 2.64 6.47 3.92
I 6.23 -0.81 -3.98
I 6.23 -0.79 3.98
I 2.65 6.46 -3.93
I 4.52 3.03 0.00
I 9.07 -3.31 0.00
Cs 9.88 -2.02 3.70
Cs 9.88 -2.04 -3.71
Cs 6.13 -5.99 0.01
Cs 2.49 -2.37 4.14
Cs 5.92 -0.59 0.00
Cs 2.50 -2.39 -4.13
Cs -1.02 -4.18 0.01
Cs -4.65 -5.73 3.96
Cs -4.65 -5.75 -3.93
Cs -6.45 -2.25 0.00
Cs -8.06 1.38 3.93
Cs -8.04 1.36 -3.96
Cs -2.78 -0.46 4.09
Cs -4.62 3.27 -0.01
Cs -2.78 -0.48 -4.09
Cs -1.02 5.05 4.07
Cs 0.67 1.70 0.00
Cs 4.44 3.06 4.07
Cs 2.64 6.88 0.00
Cs 4.45 3.05 -4.07
Cs -1.01 5.04 -4.08

--
CsI19-CsCs-2

--
I -2.24 -0.62 -0.06
I -0.25 3.31 3.54
I -6.83 -1.27 3.48
I -4.48 -4.40 -3.60
I 2.09 0.08 -3.48
I 1.11 -5.66 -1.39
I -1.47 -1.92 5.49
I 3.48 -1.88 2.52
I -3.61 -5.75 1.97
I -3.30 0.78 -5.54
I -5.55 3.89 1.55
I -1.30 4.85 -2.10
I -7.72 0.02 -1.98
I 1.01 8.32 1.57
I 7.37 -0.46 -1.41
I 4.96 2.60 5.40
I 3.21 5.25 -5.33
I 4.21 4.11 -0.02
I 6.77 -5.63 -0.32
Cs 4.10 -8.17 -1.64
Cs 9.67 -3.46 -2.05
Cs 6.23 -4.43 3.45
Cs 1.65 0.55 5.69
Cs 6.25 1.47 1.96
Cs 3.98 -2.62 -1.38
Cs -0.33 -3.46 2.02
Cs -4.81 -4.04 5.37
Cs -2.75 -7.18 -1.53
Cs -5.71 -2.82 -0.03
Cs -8.74 1.60 1.51
Cs -6.54 -1.48 -5.42
Cs -3.55 1.08 3.56
Cs -4.51 2.48 -2.05
Cs -1.27 -2.04 -3.70
Cs -2.36 6.35 1.58
Cs 0.76 2.11 -0.14
Cs 3.06 5.72 3.64
Cs 2.13 7.15 -2.01
Cs 5.33 2.58 -3.52
Cs -0.12 3.23 -5.60

--
CsI20-2CC

--
I -2.77 -0.55 0.16
I 0.18 3.20 3.42
I -6.46 -1.21 4.54
I -5.77 -4.13 -2.97
I 0.83 0.16 -4.05
I 0.11 -5.63 -2.04
I -0.80 -2.11 5.34
I 3.07 -1.80 1.41
I -3.85 -5.75 2.22
I -4.81 1.10 -4.93
I -5.41 4.01 2.60
I -1.93 4.89 -1.78
I -8.43 0.33 -0.57
I 1.19 8.24 1.42
I 6.34 -0.50 -3.32
I 5.84 2.21 4.20
I 1.76 5.41 -5.89
I 3.84 3.96 -0.92
I 5.84 -5.70 -1.52
I 8.82 -1.75 1.65
Cs 9.51 0.94 4.46
Cs 5.95 -4.38 2.19
Cs 8.93 -3.14 -2.17
Cs 3.08 -8.11 -2.80
Cs 5.95 0.94 0.38
Cs 2.34 0.29 4.91
Cs -0.58 -3.55 1.62
Cs 3.11 -2.71 -2.59
Cs -3.72 -7.06 -1.45
Cs -4.19 -4.13 5.84
Cs 4.11 2.55 -4.74
Cs 3.50 5.45 2.83
Cs 0.37 1.96 -0.42
Cs -3.16 1.02 3.98
Cs -6.21 -2.68 0.82
Cs -2.54 -1.88 -3.66
Cs -8.02 -1.07 -4.22
Cs -8.63 1.79 3.11
Cs -5.19 2.67 -1.20
Cs -1.57 3.40 -5.53
Cs -2.19 6.34 2.02
Cs 1.47 7.12 -2.35

--
CsI21-CsCs-3

--
I -2.63 -0.35 0.04
I 0.57 -3.93 -3.03
I -6.19 0.25 -4.48
I -5.93 3.20 3.00
I 0.91 -1.34 4.74
I -0.34 4.13 2.63
I -0.65 1.26 -5.09
I 2.95 0.69 -0.62
I -3.78 5.10 -2.21
I -4.99 -1.95 4.98
I -5.04 -4.96 -2.48
I -1.43 -5.77 2.21
I -8.24 -1.32 0.47
I 1.72 -8.94 -1.60
I 6.53 0.04 3.78
I 6.16 -2.67 -3.76
I 4.16 -4.74 1.56
I 8.43 1.71 -1.28
I 5.30 5.18 2.21
Cs 9.38 -0.53 -4.32
Cs 8.61 3.12 2.52
Cs 5.11 4.06 -1.57
Cs 2.59 -0.83 -4.40
Cs 6.22 -1.46 0.10
Cs 3.00 2.07 3.32
Cs -0.43 2.91 -1.32
Cs -3.99 3.20 -5.75
Cs -3.75 6.32 1.90
Cs -6.04 1.85 -0.78
Cs -8.30 -2.81 -3.17
Cs -8.20 0.18 4.10
Cs -2.84 -1.86 -3.77
Cs -4.95 -3.51 1.24
Cs -2.62 1.12 3.84
Cs -1.74 -7.09 -2.00
Cs 0.70 -2.53 0.76
Cs 4.01 -5.95 -2.63
Cs 1.87 -8.04 2.08
Cs 4.54 -2.94 5.13
Cs -1.88 -4.03 5.78
I 1.89 6.15 -2.18
I -1.40 9.31 1.02
Cs -1.34 8.32 -2.69
Cs 1.94 7.38 1.73

--
CsI21-CC2

--
I 2.85 -0.68 0.00
I -0.15 1.97 -4.11
I 5.93 -3.19 -4.04
I 5.93 -3.19 4.04
I -0.14 1.97 4.11
I -0.08 -4.22 4.17
I -0.08 -4.22 -4.17
I -2.88 -1.18 0.00
I 3.28 -6.31 0.00
I 5.58 2.45 4.04
I 5.58 2.45 -4.04
I 2.61 5.11 0.00
I 8.63 -0.21 0.00
I -0.44 7.59 -3.94
I -5.82 1.76 4.03
I -5.83 1.76 -4.03
I -0.44 7.59 3.94
I -3.21 4.78 0.00
I -8.74 -1.01 0.00
I -5.75 -3.84 -4.02
I -5.75 -3.84 4.02
Cs -3.16 -5.93 -5.95
Cs 3.49 -6.19 -3.91
Cs 3.49 -6.19 3.91
Cs 6.04 -3.22 0.00
Cs 8.53 -0.15 -3.95
Cs 8.53 -0.14 3.95
Cs 5.65 2.56 0.00
Cs 2.94 -0.51 4.09
Cs 2.94 -0.51 -4.09
Cs 0.26 -3.69 0.00
Cs 2.59 5.15 -4.05
Cs -2.87 -0.87 -3.98
Cs -5.95 -3.75 0.00
Cs -8.62 -0.95 -3.95
Cs -8.62 -0.95 3.95
Cs -5.94 1.96 0.00
Cs -3.16 4.82 -4.06
Cs -2.87 -0.87 3.98
Cs -3.16 -5.94 5.95
Cs -0.13 2.19 0.00
Cs 2.59 5.15 4.05
Cs -0.44 7.87 0.00
Cs -3.16 4.82 4.07

--
CsI21-CsCs

--
I 0.00 5.57 -3.75
I -3.02 -0.53 -4.45
I 2.70 7.40 1.81
I -2.86 1.84 3.21
I 2.85 1.84 3.21
I 3.02 -0.53 -4.46
I 0.00 -1.92 0.20
I 5.19 3.73 -1.75
I -2.71 7.40 1.81
I -5.19 3.73 -1.75
I -8.74 -1.17 -3.71
I -2.78 -3.61 5.06
I -2.75 -6.09 -2.61
I -8.29 1.57 2.91
I -5.94 -2.58 0.52
I 0.00 -7.64 2.14
I 2.76 -6.09 -2.60
I 2.78 -3.61 5.06
Cs 0.00 -8.75 -1.66
Cs 0.00 -6.30 5.87
Cs 2.85 -4.97 1.27
Cs 0.00 -3.36 -3.61
Cs -2.85 -4.98 1.27
Cs 0.00 -0.89 4.17
Cs 3.38 0.31 -0.48
Cs 6.44 1.65 -4.85
Cs 5.78 4.45 2.21
Cs 3.20 7.02 -2.11
Cs 0.00 9.86 3.21
Cs 0.00 1.95 -5.26
Cs -3.21 7.02 -2.11
Cs 0.00 4.50 2.66
Cs -6.44 1.64 -4.86
Cs -3.39 0.31 -0.48
Cs -5.82 -3.76 -3.40
Cs -9.53 -0.80 0.08
Cs -5.67 -1.01 4.32
Cs -5.78 4.45 2.21
I 5.94 -2.58 0.52
I 8.74 -1.16 -3.71
I 8.29 1.57 2.91
Cs 9.53 -0.80 0.08
Cs 5.67 -1.00 4.31
Cs 5.82 -3.76 -3.40

--
CsI21-CsCs-2

--
I 1.35 -3.49 1.95
I -3.41 0.47 3.92
I 4.61 -6.44 -2.07
I -1.75 -2.04 -3.58
I 3.81 -1.07 -2.66
I 2.48 1.33 5.22
I 0.02 2.23 -0.12
I 6.52 -1.82 3.31
I -0.88 -7.44 -1.67
I -2.57 -4.85 5.66
I -4.87 -4.09 0.66
I -8.70 -0.68 2.92
I -2.41 3.28 -5.43
I -4.13 5.75 2.02
I -7.07 -3.05 -4.38
I -5.85 1.48 -1.33
I -0.80 7.65 -2.21
I 1.34 6.79 2.90
I 3.09 4.31 -4.52
Cs -1.76 8.84 1.43
Cs -0.03 6.39 -5.87
Cs 2.29 5.55 -0.82
Cs -1.13 3.67 3.53
Cs -3.40 4.58 -1.76
Cs 0.64 1.14 -4.05
Cs 3.20 0.12 1.24
Cs 5.22 -0.95 6.84
Cs 6.76 -3.50 -3.83
Cs 5.01 -5.03 1.62
Cs 2.20 -9.47 -2.83
Cs -0.43 -1.69 5.20
Cs -1.93 -6.29 2.09
Cs 1.23 -4.07 -2.09
Cs -5.86 -2.87 4.46
Cs -2.86 -0.68 0.08
Cs -6.68 2.64 2.50
Cs -8.20 -1.88 -0.78
Cs -4.97 0.18 -5.07
Cs -4.19 -5.29 -3.10
I 5.78 3.26 0.83
I 8.85 -0.57 -2.45
Cs 8.85 0.61 1.20
Cs 6.16 2.23 -3.23
Cs 4.33 4.81 4.22

--
CsI22-CsCs-4

--
I 2.81 0.00 0.00
I 0.00 -3.68 3.27
I 5.83 1.72 4.54
I 5.69 3.70 -3.25
I 0.00 -2.13 -4.83
I 0.00 3.68 -3.27
I 0.00 2.13 4.84
I -2.81 0.00 0.00
I 2.84 5.78 1.56
I 5.82 -1.72 -4.54
I 5.69 -3.70 3.25
I 2.84 -5.78 -1.56
I 8.55 0.00 -0.01
I 0.00 -9.04 2.37
I -5.83 -1.72 -4.54
I -5.69 -3.70 3.25
I -2.84 -5.78 -1.56

I -8.55 0.00 -0.01
I -5.83 1.72 4.54
I -5.69 3.71 -3.25
I -2.83 5.78 1.56
I 0.00 9.04 -2.36
Cs -3.25 -4.44 -5.29
Cs 0.00 -8.63 -1.40
Cs -2.92 -6.47 2.82
Cs -5.74 -2.82 -0.65
Cs -8.54 1.03 -3.81
Cs -8.55 -1.03 3.79
Cs 3.25 -4.44 -5.29
Cs -2.84 0.95 -3.99
Cs 0.00 -2.88 -0.72
Cs 2.92 -6.48 2.81
Cs -5.74 2.82 0.65
Cs -2.84 -0.95 3.99
Cs -2.92 6.48 -2.81
Cs 0.00 2.88 0.72
Cs 2.84 -0.95 3.99
Cs -3.25 4.43 5.29
Cs 2.84 0.95 -3.99
Cs 5.73 -2.82 -0.65
Cs 8.54 1.03 -3.81
Cs 2.92 6.47 -2.81
Cs 5.74 2.82 0.65
Cs 8.55 -1.03 3.79
Cs 0.00 8.63 1.42
Cs 3.25 4.43 5.29

--
CsI22-CsCs-5

--
I 1.16 -4.04 0.84
I 2.35 -0.03 -4.12
I -1.13 -7.18 -3.31
I 3.17 1.08 3.85
I -1.91 -1.42 4.68
I -2.97 -1.87 -3.32
I -0.93 2.10 -0.03
I -4.67 -5.06 1.25
I 5.69 -4.21 4.44
I 4.24 -5.41 -3.59
I 6.45 -1.16 -0.34
Cs 2.08 -8.18 -5.31
Cs 7.95 -5.86 7.06
Cs 5.05 -4.74 0.29
Cs 6.90 -0.31 3.50
Cs 6.01 -1.67 -4.35
Cs -1.38 -7.04 0.59
Cs 1.85 -2.54 4.46
Cs -4.97 -3.85 5.13
Cs 0.65 -3.47 -3.20
Cs -4.89 -5.36 -3.11
Cs -2.94 -1.34 0.71
Cs -1.29 1.74 -4.13
Cs 2.87 0.81 -0.21
Cs -0.72 2.58 4.04
Cs 0.74 5.92 -0.68
Cs 4.73 4.90 3.15
Cs 8.13 2.76 -1.07
Cs 4.03 3.75 -4.87
I 7.49 1.89 -4.85
I 0.97 6.19 3.36
I 0.39 5.34 -4.66
I 8.30 3.20 2.87
I 4.44 4.40 -0.86
Cs -2.59 7.88 3.31
Cs -3.15 7.06 -4.53
I -2.91 7.62 -0.61
I -4.87 3.53 -4.09
I -4.37 4.38 3.92
I -8.26 -2.00 4.73
I -8.26 -3.51 -2.97
I -6.51 0.55 0.48
Cs -4.57 4.00 -0.12
Cs -7.28 1.73 4.23
Cs -6.67 0.04 -3.55
Cs -8.46 -2.99 0.90

--
CsI23-CsCs-2

--
I -0.53 2.84 0.24
I -3.07 0.02 -3.98
I 2.70 5.66 -3.70
I 2.22 5.68 4.38
I -3.90 0.02 4.23
I 2.11 -0.01 4.48
I 2.71 -0.01 -3.72
I -0.55 -2.84 0.24
I 5.34 2.87 0.51
I -3.36 5.89 4.06
I -3.01 5.72 -3.99
I -6.44 2.89 0.03
I -0.37 8.57 0.14
I -8.43 0.04 -4.66
I -3.42 -5.87 4.06
I -3.07 -5.69 -3.99
I -6.47 -2.83 0.03
I -0.45 -8.56 0.13
I 2.65 -5.68 -3.70
I 2.17 -5.71 4.38
Cs -0.22 -8.41 -3.79
Cs -0.54 -8.55 4.07
Cs 2.40 -5.71 0.36
Cs -0.22 -2.83 -3.85
Cs -3.38 -5.77 0.00
Cs -0.69 -2.87 4.32
Cs 2.39 -0.01 0.42
Cs 5.46 2.85 -3.46
Cs 5.02 2.85 4.63
Cs 2.45 5.69 0.36
Cs -0.14 8.41 -3.79
Cs -0.46 8.55 4.08
Cs -0.20 2.83 -3.85
Cs -3.32 5.80 0.00
Cs -0.67 2.87 4.33
Cs -5.82 2.95 -4.34
Cs -3.44 0.01 0.06
Cs -5.85 -2.90 -4.34
Cs -9.11 0.04 -0.92
Cs -6.20 -3.24 3.98
Cs -6.17 3.30 3.99
I 5.31 -2.92 0.50
I 8.50 -0.03 -3.39
I 7.70 -0.04 4.64
Cs 8.03 -0.04 0.78
Cs 5.00 -2.90 4.63
Cs 5.43 -2.89 -3.47
Cs 11.90 -0.03 -5.11

--
CsI24-CsCs-3

--
I 0.00 2.87 0.00
I -1.91 0.00 -4.61
I 3.68 5.71 -3.37
I 1.94 5.70 4.55
I -3.74 0.00 3.43
I 1.91 0.00 4.61
I 3.73 0.00 -3.43
I 0.00 -2.87 0.00
I 5.68 2.92 1.19
I -3.69 5.71 3.37
I -1.94 5.70 -4.55
I -5.68 2.92 -1.19
I 0.00 8.57 0.00
I -7.37 0.00 -5.64
I -3.69 -5.71 3.37
I -1.94 -5.70 -4.55
I -9.37 0.00 2.19
I -5.68 -2.92 -1.19
I 0.00 -8.58 0.00
I 3.68 -5.71 -3.37
I 1.94 -5.70 4.55
Cs 0.83 -8.41 -3.85
Cs -0.83 -8.41 3.85
Cs 2.83 -5.73 0.61
Cs 0.86 -2.84 -4.01
Cs -2.82 -5.73 -0.61
Cs -0.86 -2.84 4.00
Cs 2.81 0.00 0.63
Cs 6.37 2.88 -2.72
Cs 4.71 2.88 5.20
Cs 2.83 5.73 0.61
Cs 0.83 8.41 -3.85
Cs -0.83 8.41 3.85
Cs 0.86 2.84 -4.01
Cs -2.83 5.73 -0.61
Cs -0.87 2.84 4.01
Cs -4.71 2.88 -5.20
Cs -2.81 0.00 -0.64
Cs -4.71 -2.88 -5.20
Cs -8.29 0.00 -1.87
Cs -6.37 -2.88 2.72
Cs -6.37 2.89 2.72